DEPARTAMENT D'ENGINYERIA ELÈCTRICA

UNIVERSITAT POLITÈCNICA DE CATALUNYA BARCELONATECH

Modeling and Characterization of Single-Phase and Three-Phase Transformers based on Minimum Information

Doctoral Thesis

Author: Gerardo de Jesús Martínez Figueroa

Directors: Felipe Córcoles López, Santiago Bogarra Rodríguez

Electrical Engineering Department (DEE)

Thesis presented to obtain the degree of doctorate

Universitat Politècnica de Catalunya (UPC)
Escuela Superior de Ingenierías Industrial, Aeroespacial y Audiovisual de Terrassa (ESEIAAT)

Terrassa, Spain, January 2024

Acknowledgments

Thanks to God.

I thank Dr. Felipe Córcoles and Dr. Santiago Bogarra for all their support, all their teachings and all their efforts during these four years of work. Thank you for having trusted me without even knowing me, thank you for your infinite patience.

Thanks to all the people who collaborated in any way with this work.

I thank my parents and my entire family for their support.

I thank to Ana all her love, support and patience.

I thank the National Council of Humanities, Sciences, and Technologies (CONAHCYT) from Mexico for scholarship grant no. 739523, to pursue my doctoral studies.

Abstract

The main objective of this thesis is to develop and validate simple but sufficiently accurate mathematical models for single-phase and three-phase transformers, by estimating their parameters from simple laboratory tests and field measurements, in particular, from the information obtained from the inrush current.

The energizing process of a transformer results in the generation of a high inrush current due to the saturation of the transformer core. This current can cause several problems, such as protections tripping and consequently being out of service. Clearing faults in the transmission network can also lead to transformer saturation. A part of this work aims to develop methodologies for the reduction of these high inrush currents.

In the literature, a great effort has been dedicated to the modeling, identification and analysis of electrical transformers. The representation of a transformer can be very complex due to the different types of core configurations and the large number of transformer parameters, as well as the fact that some of these parameters are nonlinear and even frequency dependent. These include core and coil configurations, self and mutual inductances among coils, dispersion fluxes, skin and proximity effects in coils, magnetic core saturation, hysteresis cycles, losses due to eddy currents, and capacitive effects.

The materials commonly used in transformer cores, like ferromagnetic materials, exhibit non-linear magnetic permeability, and usually work slightly saturated. The behavior of a non-linear core is given by the relationship between the magnetic field and magnetic induction, known as the magnetization or saturation curve. There are different ways to model the nonlinear operation of a magnetic core, ranging from finite elements to single-valued functions, through especially complex models such as Jiles-Atherton or Preisach hysteretic models.

This work is focused on low frequencies models (up to a few kHz), whose parameters reproduce in detail those situations in which the nonlinearity of the magnetic circuit significantly influences its dynamic behavior. For example, inrush current can be predicted, for which modeling or estimation of the residual flux is necessary. The adjustment of the parameters will be based on experimental measurements to which the developed adjustment algorithms will be applied. These measurements will be obtained both in specific laboratory tests and in transient connection records in transformers connected to the distribution network.

Although articles on transformers have been published for more than seventy years, the high number of current publications on their modeling and on the problems derived from their non-linear behavior is an indication that the issue has not been resolved satisfactorily and which is still relevant.

This document is structured as follows. The Introduction (Chapter 1) begins with an analysis of transformer operation and modeling. The primary issues arising in electrical power systems due to transformer nonlinearity are then mentioned. The chapter also states the reasons that underscore the importance and novelty of the proposed topic before outlining the main objectives.

Chapter 2 introduces a simplified single-phase transformer model based on a magnetic circuit, and focused on characterizing the inrush current and other core phenomena. Additionally, the chapter

provides a comprehensive analysis of the inrush current and how it is influenced by each transformer parameter.

In Chapter 3, the earlier model is expanded to incorporate core hysteresis, enabling the modeling and prediction of residual flux. This chapter also analyses the residual flux phenomenon and the de-energization trajectories, and also presents a simple smart switching strategy to avoid inrush currents.

Chapters 4 and Chapter 5 introduce methodologies for estimating saturation curves, including deep saturation from single-phase and three-phase three-legged transformers, respectively. These methodologies are based on the harmonic content of no-load currents and on the inrush currents.

Chapter 6 focuses on current transformers for protection, offering a comprehensive analysis of their saturation across various conditions, especially during inrush currents measurement. It details how each parameter affects to saturation. This chapter also explores briefly the estimation of the saturation curve of protection current transformers.

Chapter 7 summarizes the main contributions of the thesis and draws conclusions. Finally, several annexes present a portion of the work conducted throughout the thesis.

Keywords: inrush current, residual flux, single-phase transformer, three-legged transformer, current transformer, saturation curve, reluctance.

Resumen

El objetivo principal de esta tesis es desarrollar y validar modelos matemáticos simples pero suficientemente precisos para transformadores monofásicos y trifásicos, estimando sus parámetros a partir de pruebas de laboratorio simples y mediciones de campo, en particular, a partir de la información obtenida de la corriente de conexión.

El proceso de energización de un transformador resulta en la generación de una corriente de arranque elevada debido a la saturación del núcleo del transformador. Esta corriente puede causar varios problemas, como disparos de protecciones y, consecuentemente, dejar fuera de servicio al transformador. La corrección de fallas en la red de transmisión también puede llevar a la saturación del transformador. Una parte de este trabajo tiene como objetivo desarrollar metodologías para la reducción de estas corrientes de arranque elevadas.

En la literatura, se ha dedicado un gran esfuerzo a la modelización, identificación y análisis de transformadores eléctricos. La representación de un transformador puede ser muy compleja debido a los distintos tipos de configuraciones del núcleo y al gran número de parámetros del transformador, así como al hecho de que algunos de estos parámetros son no lineales e incluso dependientes de la frecuencia. Estos incluyen configuraciones de núcleo y bobina, inductancias propias y mutuas entre bobinas, flujos de dispersión, efecto pelicular y efecto proximidad en bobinas, saturación del núcleo magnético, ciclos de histéresis, pérdidas debidas a corrientes de Foucault y efectos capacitivos.

Los materiales comúnmente utilizados en los núcleos de transformadores, como los materiales ferromagnéticos, exhiben permeabilidad magnética no lineal y suelen trabajar ligeramente saturados. El comportamiento de un núcleo no lineal está dado por la relación entre el campo magnético y la inducción magnética, conocida como curva de magnetización o de saturación. Existen diferentes formas de modelar el funcionamiento no lineal de un núcleo magnético, desde elementos finitos hasta funciones unievaluadas, pasando por modelos especialmente complejos como los modelos de histéresis de Jiles-Atherton o Preisach.

Este trabajo se enfoca en modelos de baja frecuencia (hasta unos pocos kHz), cuyos parámetros reproducen en detalle aquellas situaciones en las que la no linealidad del circuito magnético influye significativamente en su comportamiento dinámico. Por ejemplo, la corriente de conexión puede ser predicha, para lo cual es necesaria la modelización o estimación del flujo residual. El ajuste de los parámetros se basará en mediciones experimentales a las cuales se aplicarán los algoritmos de ajuste desarrollados. Estas mediciones se obtendrán tanto en pruebas de laboratorio específicas como en registros transitorios de conexiones de transformadores conectados a la red de distribución.

Aunque se han publicado artículos sobre transformadores durante más de setenta años, el alto número de publicaciones actuales sobre su modelización y los problemas derivados de su comportamiento no lineal es una indicación de que el problema no se ha resuelto satisfactoriamente y que sigue siendo relevante.

Este documento está estructurado de la siguiente manera. La Introducción (Capítulo 1) comienza con un análisis del funcionamiento y la modelización del transformador. Luego profundiza en los problemas principales que surgen en los sistemas de energía eléctrica debido a la no linealidad del

transformador. En el capítulo también se exponen las razones que subrayan la importancia y novedad del tema propuesto antes de esbozar los objetivos principales.

El Capítulo 2 presenta un modelo simplificado de transformador monofásico basado en un circuito magnético y centrado en la caracterización de la corriente de conexión y otros fenómenos del núcleo. Además, el capítulo ofrece un análisis exhaustivo de la corriente de conexión y de cómo influye en ella cada parámetro del transformador.

En el Capítulo 3, el modelo anterior se amplía para incorporar la histéresis del núcleo, permitiendo la modelización y predicción del flujo residual. Este capítulo también analiza el fenómeno del flujo residual y las trayectorias de desenergización, y presenta una estrategia simple de conmutación inteligente para evitar corrientes de arranque.

Los Capítulos 4 y 5 presentan metodologías para estimar curvas de saturación, incluida la saturación profunda de transformadores monofásicos y trifásicos de tres columnas, respectivamente. Estas metodologías se basan en el contenido armónico de las corrientes de vacío y en las corrientes de conexión.

El Capítulo 6 se centra en los transformadores de corriente para protección y ofrece un análisis exhaustivo de su saturación en diversas condiciones, especialmente durante la medición de corrientes de conexión. Se detalla cómo afecta cada parámetro a la saturación. Este capítulo también explora brevemente la estimación de la curva de saturación de los transformadores de corriente para protección.

El Capítulo 7 resume las principales contribuciones de la tesis y presenta conclusiones. Finalmente, varios anexos presentan una parte del trabajo realizado a lo largo de la tesis.

Palabras clave: corriente de conexión, flujo residual, transformador monofásico, transformador de tres columnas, transformador de corriente, curva de saturación, reluctancia.

Table of Contents

List of Figures

List of Tables

List of Symbols

Symbols	Definition
B	Flux density
b_m	Magnetizing susceptance in per unit value
$e1$, $e2$	Primary and secondary induced voltages in a single-phase transformer
$e1a$, $e1b$, $e1c$	Primary induced voltages in a three-phase transformer
$e2a$, $e2b$, $e2c$	Secondary induced voltages in a three-phase transformer
f	Magnetic potential or frequency (depending on context)
f_d	Magnetic potential of the air path reluctance in a three-legged transformer
f_a, f_b, f_c	Magnetic potentials of the reluctances in a three-phase transformer
F_{k1}, F_{k3}, F_{k5}	Harmonics of the magnetic potential of the k-th reluctance
f_{KNEE}	Magnetic potential at which saturation begins (knee of the curve)
f_N	Transformer nominal frequency
g_{FE}	Conductance in per unit value
H	Magnetic field intensity
H_{EDDY}	Eddy-current component of the magnetic field intensity
H_{eff}	Effective magnetic field intensity
H_{EXC}	Excess component of the magnetic field intensity
H_H	Hysteresis component of the magnetic field intensity
I_1, I_3, I_5	Harmonics of the no-load current in a single phase transformer
i_0	RMS value of the no-load current in per unit
I_0	RMS value of the no-load current
i_1, i_2	Primary and secondary currents in a transformer
i_{1a}, i_{1b}, i_{1c}	Primary currents in a three-phase transformer
i_{2a}, i_{2b}, i_{2c}	Secondary currents in a three-phase transformer
i_{1m}	Magnetizing current in a single-phase transformer
i_{1ma}, i_{1mb}, i_{1mc}	Magnetizing currents in a three-phase transformer
I_{B1}, I_{B2}	Primary and secondary base currents
i_d, i_q, i_0	Currents in the dq0 reference frame
i_{EDDY}	Eddy current component
i_{EXCESS}	Excess current component
i_{FE}	Current due to total core losses
i_H	Hysteresis current component
I_{N1}, I_{N2}	Primary and secondary nominal currents
i_{PEAK}	First inrush current peak
i_{sc}	Current consumed during short-circuit test
I_{sc}	RMS value of current consumed during short-circuit test
K_1	Unsaturated slope of the saturation curve
K_2	Saturated slope of the saturation curve
k_{SAT}	Degree of saturation (parameter of the saturation curve)
L_{B1}, L_{B2}	Primary and secondary base inductances
l_{d1}, l_{d2}	Primary and secondary leakage inductances in per unit values
L_{d1}, L_{d2}	Primary and secondary leakage inductances
l_e	Effective length of the transformer core

L_m	Magnetizing inductance
m_3	Third-order central moment
M	Magnetization
M_{an}	Anhysteretic magnetization
M_{irr}	Irreversible component of magnetization
M_{rev}	Reversible component of magnetization
M_R	Remanence
N_1, N_2	Primary and secondary winding turns
p	Sharpness parameter of the saturation curve
P_{EDDY}	Classical eddy-current power losses
P_{EXCESS}	Excess power losses
P_H	Hysteresis power losses
P_T	Total power losses in unit volume per period
q	Instantaneous reactive power
Q	Average reactive power at each frequency period
Q_{MAX}	Maximum value of Q
r	Short-circuit resistance in per unit
r_1, r_2	Primary and secondary winding resistances in per unit values
R_1, R_2	Primary and secondary winding resistances
R_{B1}, R_{B2}	Primary and secondary base resistances
r_{FE}	Resistance to represent core losses en per unit
R_{FE}	Resistance to represent core losses
r_t	Transformation ratio
r_{tr}	Turns ratio
S_B	Base power
S_e	Cross-sectional area of the transformer core
S_N	Transformer nominal power
t	Time
t_0	Initial instant time
t_{SAT}	Saturation instant time
u_1, u_2	Primary and secondary voltages in a transformer
U_1, U_2	Primary and secondary RMS voltage values
u_{1a}, u_{1b}, u_{1c}	Primary voltages in a three-phase transformer
u_{2a}, u_{2b}, u_{2c}	Secondary voltages in a three-phase transformer
U_{B1}, U_{B2}	Primary and secondary base voltages
u_d, u_q, u_0	Voltages in the dq0 reference frame
U_{N1}, U_{N2}	Primary and secondary nominal voltages
U_{sc}	RMS supply voltage during short-circuit test
u_{sc}	RMS supply voltage during short-circuit test in per unit value
w_0	Power consumed during no-load test in per unit value
W_0	Power consumed during no-load test
W_{EDDY}	Classical eddy-current energy losses
W_{EXCESS}	Excess energy losses
W_H	Hysteresis energy losses
w_{sc}	Power consumed during short-circuit test in per unit value
W_{sc}	Power consumed during short-circuit test
W_T	Total energy losses in unit volume per period
x	Short-circuit reactance in per unit value
y_0	Magnitude of the no-load admittance in per unit value

z_0	Magnitude of the no-load impedance in per unit value
Z_B	Burden impedance in a current transformer
Z_{B1}, Z_{B2}	Primary and secondary base impedances
Z_M	Magnetizing impedance in a current transformer
z_{sc}	Magnitude of the short-circuit impedance in per unit value

Greek letters

α_E	Energization point-on-wave
α_D	De-energization point-on-wave
α_{RM}	Point-on-wave corresponding to maximum residual flux
ε_c	Composite error
λ_1, λ_2	Total fluxes linked by the primary and secondary windings
λ_{B1}, λ_{B2}	Base total flux
τ	Decay time
θ	Phase displacement
θ_1, θ_2	Boundary saturation angles
ϕ	Magnetic flux
ϕ_0	Initial flux
ϕ_d	Flux through the air path in a three-legged transformer
ϕ_a, ϕ_b, ϕ_c	Fluxes in a three-phase transformer
ϕ_B	Base flux
ϕ_{d1}, ϕ_{d2}	Primary and secondary leakage fluxes
ϕ_{i0}	Flux value when the no-load current is null
ϕ_{KNEE}	Saturation flux
ϕ_N	Nominal flux
ϕ_{PEAK}	Maximum inrush peak flux
ϕ_R	Residual flux
ϕ_{RM}	Maximum possible residual flux
ϕ_{STEADY}	Flux in steady-state assuming an infinite K_1
$\phi_{STEADY,K1}$	Flux in steady-state
$\phi_{STEADY,K2}$	Sinusoidal component of the flux during saturation intervals
ϕ_{T1}, ϕ_{T2}	Total fluxes per unit turn linked by the primary and secondary windings
ω	Angular frequency
ω_B	Base angular frequency
ω_N	Nominal angular frequency
χ_m	Incremental magnetic susceptibility

Other symbols

$\mathfrak{F}_1$, $\mathfrak{F}_2$	Primary and secondary magnetomotive forces
$\mathfrak{F}_{1a}$, $\mathfrak{F}_{1b}$, $\mathfrak{F}_{1c}$	Primary magnetomotive forces in a three-phase transformer
$\mathfrak{F}_{2a}$, $\mathfrak{F}_{2b}$, $\mathfrak{F}_{2c}$	Secondary magnetomotive forces in a three-phase transformer
$\mathfrak{F}_{1k}$, $\mathfrak{F}_{2k}$	Primary and secondary magnetomotive forces of the phase k

$\mathfrak{F}_B$	Base magnotomotive force
$\mathfrak{R}$	Magnetic reluctance
$\mathfrak{R}_d$	Magnetic reluctance of the air path in a three-legged transformer
$\mathfrak{R}_a$, $\mathfrak{R}_b$, $\mathfrak{R}_c$	Magnetic reluctances in a three-phase transformer
$\mathfrak{R}_B$	Base reluctance
$\mathfrak{R}_k$	Magnetic reluctance of the core leg k
$\mathfrak{L}_H$	Magnetic inductance (transferance) to model hysteresis losses
$\mathfrak{L}_E$	Magnetic inductance (transferance) to model eddy-current losses

Superscripts

'	Reduced to primary
pu	Reduced per unit

List of Abbreviations

Abbreviations	Definition
AC	Alternating current
CT	Current transformer
DAS	Data acquisition system
DC	Direct current
Dd	Delta-delta winding connection in three-phase transformers
Dy	Delta-wye winding connection in three-phase transformers
FPGA	Field-programmable gate array
HV	High voltage
LV	Low voltage
PDF	Preisach distribution function
pu	Per unit
RMS	Root mean square
THD	Total harmonic distortion
Yd	Ungrounded wye-delta winding connection in three-phase transformers
YNd	Grounded wye-delta winding connection in three-phase transformers
Yy	Ungrounded wye-wye winding connection in three-phase transformers
YNy	Grounded wye-wye winding connection in three-phase transformers

Chapter 1. Introduction

Power transformers are essential devices widely employed in electric power systems. Their energization or the process of restoring them after faults is an important subject, as they may drive the magnetic core of the transformer into saturation, causing high transient currents, known as inrush currents. These inrush currents can lead to undesirable events, such as wrong operation of protective relays, mechanical damage to the transformer windings, excessive stress on the insulation, and disturbances like voltage sags or harmonic distortion [1]-[7]. These disturbances can impact the power quality of the electric system and neighboring facilities [8]-[10].

In [2], issues related to the energization of large furnace power transformers in an industrial facility are discussed. Overvoltages may occur if the system is tuned to one of the harmonics of the inrush current. This can happen, e.g., when a large capacitor bank is installed in the system. Insulation failures due to the frequent switching of a no-load transformer are investigated in [3]. The mechanical forces in the winding caused by the inrush currents are compared with those from short-circuit currents. Other instances of disturbances caused by inrush currents are documented in [4]-[7].

It is necessary to predict the magnitudes of inrush currents and their durations for the proper design and operation of protective devices, preventing undesirable events [11]-[13]. Several analytical formulas have been proposed to calculate the initial peaks of inrush current and its rate decay [14]-[19], each one with different levels of simplicity and accuracy. For example, in [14], the primary winding resistance is not considered. Additionally, some formulas can provide an approximated waveform of the inrush currents [20]-[23], and different methods for computational simulation of the inrush currents are presented in [24]-[30]. Other analytical formulas have been suggested to compute an approximated evolution of the second harmonic [31]-[32], which is a distinctive characteristic commonly used as a criterion to discriminate inrush currents from fault currents [33]-[34].

A detailed prediction and estimation of inrush currents is possible by an accurate modeling of the transformer, particularly their nonlinear magnetizing core. An accurate representation of every transient situation demands a model valid for a frequency range from direct current (DC) to several MHz. However, this task is very complex, and not feasible in most cases. For this reason, transformer models are commonly developed to ensure accuracy within a specific range of frequencies. The accurate modeling up to 10 kHz, allows a correct prediction of inrush currents, as well as other low-frequency transients, such as ferroresonance or geomagnetic-induced currents. Different models suitable for inrush currents simulation are proposed in [35]-[44]. Some of these models have several parameters, which estimation requires detail transformer data that can be difficult to obtain.

Transformer modeling is a very broad subject. Even in a specific range of frequencies, there are different ways to model the nonlinear behavior of a transformer with different levels of detail. Saturation, hysteresis and eddy current losses are the main nonlinear effects to be considered in the modeling of an iron-core.

1.1. Objectives

1.2. Main objective

The main objective of this thesis is to develop and validate simple but sufficiently accurate mathematical models for single-phase and three-phase transformers, by estimating their parameters from different laboratory tests and, in particular, from the measurement of the inrush current. Value ranges for the parameters of these models will also be proposed to simulate the behavior of a true transformer.

1.3. Specific objectives

The specific objectives of this thesis are:

1. To estimate the parameters that define the linear and nonlinear behavior of a single-phase transformer using minimal data. Specifically, this involves utilizing the maximum value of the inrush current, the decay time constant, and the harmonic content of the no-load current.

2. To estimate the parameters defining the linear and nonlinear behavior of a three-phase transformer using the complete records of the inrush currents. This envolves measuring the temporal waveform of inrush currents.

3. To analyze the residual flux behavior and its de-energization trajectories.

4. To analyze the impact of residual flux and winding connections on the waveform of inrush currents.

5. To incorporate iron losses into the equivalent electrical circuit of the magnetic circuit.

6. To develop a methodology for reducing inrush current.

7. To analyze the current transformer saturation and to develop a simple model.

1.4. Thesis outline

The thesis work is structured as follows:

Chapter 2 introduces a simplified single-phase transformer model based on a magnetic circuit, and focused on characterizing the inrush current and other core phenomena. Additionally, the chapter provides a comprehensive analysis of the inrush current and how it is influenced by each transformer parameter.

In Chapter 3, the single-phase transformer model is improved to incorporate core hysteresis, enabling the modeling and prediction of residual flux. This chapter also analyses the de-energization trajectories and presents a simple smart switching strategy to avoid inrush currents. The proposed smart switching only requires two pieces of data (ϕ_{RM} and ϕ_{i0}, flux values of the static and dynamic loops when the respective currents are null), calculated from two simple no-load tests. It has a clear advantage over common approaches: no need to estimate or measure the residual flux during transformer de-energization or before each connection.

Chapters 4 and 5 introduce methodologies for estimating saturation curves, including deep saturation, from single-phase and three-phase three-legged transformers, respectively. Both methodologies are based on the harmonic content of no-load currents and on the inrush currents.

For both transformer types, there exists a distinctive pattern or signature that characterizes all potential inrush currents in a specific transformer. In single-phase transformers, this signature is the envelope of the waveform of the most severe case of inrush current. Conversely, in the case of three-legged transformers, the instantaneous reactive power shares common characteristics among all potential inrush transients in a given transformer, allowing it to be used as a distinctive signature.

Unlike other methodologies in literature, the proposal for three-legged transformers only requires terminal measurements (only one three-phase inrush test and only one three-phase no-load test) without breaking the winding connections and without knowledge of the residual flux. No special tests with specific winding connections are necessary.

Both methodologies are validated through multiple laboratory measurements, demonstrating its effectiveness by showing close agreement between measured and estimated inrush currents and no-load hysteresis loops.

Chapter 6 focuses on current transformers for protection, offering a comprehensive analysis of their saturation across various conditions, especially during inrush currents measurement. It details how each parameter affects to saturation. This chapter also explores briefly the modeling of protection current transformers and the estimation of the saturation curve based on minimum information provided by standards and/or the manufacturer.

Finally, Chapter 7 summarizes the main contributions of the thesis and draws conclusions. Finally, several annexes present a portion of the work conducted throughout the thesis.

1.5. Thesis publications

The author's publications in journals related to the thesis topic are listed below:

1. G. de J. Martínez-Figueroa, F. Córcoles and S. Bogarra, "A Novel Methodology to Estimate the Nonlinear Magnetizing Characteristic of Single-Phase Transformers Using Minimum Information," *IEEE Trans. Power Del.*, vol. 37, no. 4, pp. 2503-2513, Aug. 2022, doi: 10.1109/TPWRD.2021.3111709.

2. G. de J. Martínez-Figueroa, F. Córcoles-López, and S. Bogarra, "FPGA-Based Smart Sensor to Detect Current Transformer Saturation during Inrush Current Measurement," *Sensors*, vol. 23, no. 2, p. 744, Jan. 2023, doi: 10.3390/s23020744.

3. G. de J. Martínez-Figueroa, S. Bogarra, and F. Córcoles, "Smart Switching in Single-Phase Grid-Connected Photovoltaic Power Systems for Inrush Current Elimination," *Energies*, vol. 16, no. 20, p. 7211, Oct. 2023, doi: 10.3390/en16207211.

4. G. de J. Martínez-Figueroa, F. Córcoles and S. Bogarra, "Saturation Curve Estimation of

Three-Legged Three-Phase Transformers Using Inrush Current Waveforms," *IEEE Trans. Power Del.*, 2023, doi: 10.1109/TPWRD.2023.3334102.

1.6. Other publications

The author's publication in conference no related to the thesis topic is:

5. G. de J. Martínez-Figueroa, S. Bogarra, F. Córcoles, L. Sainz, L. Fernández and R. Sarrias "Real-Time Implementation of qZSC for MVDC to Microgrids Link," *20th International Conference on Renewable Energies and Power Quality (ICREPQ'22)*, Vigo, Spain, 27-29 July 2022, pp. 228-233, doi: 10.24084/repqj20.270.

Chapter 2. Single-Phase Transformer Model and Inrush Current Analysis

2.1. Introduction

This chapter presents a mathematical model of the single-phase two-winding transformer, suitable for simulating the inrush current with sufficient accuracy. The model is described by one electric equivalent circuit and a magnetic equivalent circuit. An important advantage of this model over others is that the parameters characterizing the saturation have a clear physical meaning. Analytical expressions for the flux and the inrush current are calculated from the model, as well as a simple analytical formulation to predict the maximum inrush current peak. Finally, it is also analyzed and discussed comprehensively the overall inrush current phenomenon and the influence of each parameter of the transformer.

2.2. Single-phase transformer model

The single-phase transformer depicted in Fig. 2.1 is modeled by the electric and magnetic equivalent circuits.

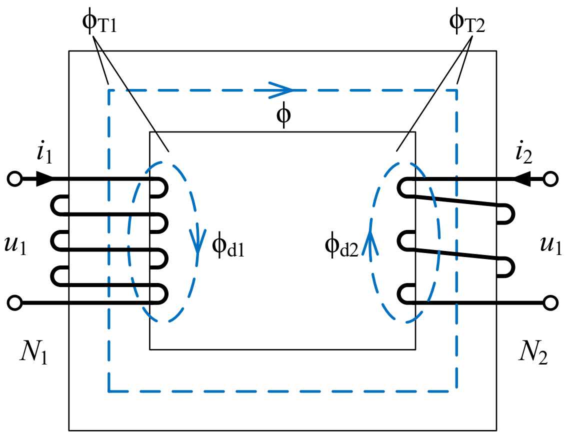

Fig. 2.1. Single-phase two-winding transformer.

The fluxes across both windings are:

- ϕ_{T1}: total flux per turn linked by the primary winding.
- ϕ_{d1}: flux per turn that passes only through the primary winding (leakage flux).
- ϕ: flux per turn through the primary and secondary windings (core flux).
- ϕ_{T2}: total flux per turn linked by the secondary winding.
- Φ_{d2}: flux per turn that passes only through the secondary winding (leakage flux).

It can be seen that

$$\begin{aligned} \phi_{T1} &= \phi + \phi_{d1} \\ \phi_{T2} &= \phi + \phi_{d2} \end{aligned} \tag{2.1}$$

and the total flux linked by each winding is

$$\begin{aligned} \lambda_1 &= N_1\phi_{T1} = N_1\left(\phi + \phi_{d1}\right) \\ \lambda_2 &= N_2\phi_{T2} = N_2\left(\phi + \phi_{d2}\right) \end{aligned} \tag{2.2}$$

2.2.1. Electric equivalent circuit

The electric equivalent circuit is depicted in Fig. 2.2. It incorporates the internal resistances of the windings, R_1 and R_2, the constant leakage inductances, L_{d1} and L_{d2}, and the induced primary and secondary voltages, e_1 and e_2, resulting from the core magnetic flux, ϕ. Since the leakage fluxes follow a path mainly surrounding the air, L_{d1} and L_{d2} can be considered linear inductances. The currents i_1 and i_2 represent the respective currents flowing through the primary and secondary windings.

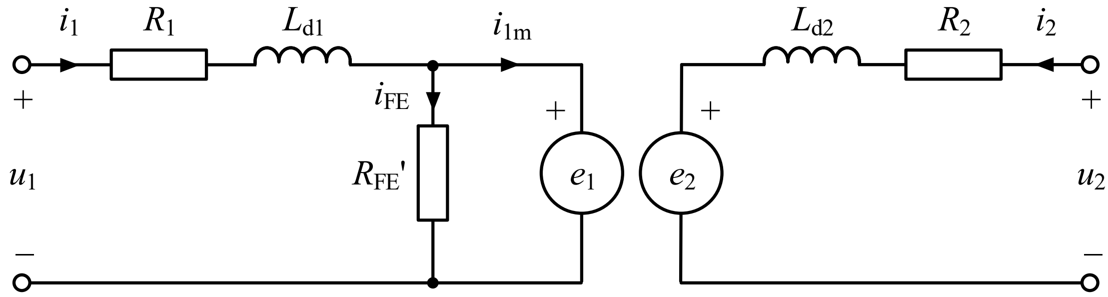

Fig. 2.2. Electric circuit of a single-phase transformer.

The iron-core losses are accounted for by adding a constant shunt resistance, R_{FE}', placed in parallel with e_1. This resistance incorporates both eddy current and hysteresis losses, and its value is valid only for the nominal frequency. This approach can be neglected for modeling inrush currents.

The electric relations of the transformer windings are

$$\begin{aligned} u_1 &= R_1 i_1 + L_{d1}\frac{\mathrm{d}i_1}{\mathrm{d}t} + e_1, \qquad e_1 = N_1\frac{\mathrm{d}\phi}{\mathrm{d}t} \\ u_2 &= R_2 i_2 + L_{d2}\frac{\mathrm{d}i_2}{\mathrm{d}t} + e_2, \qquad e_2 = N_2\frac{\mathrm{d}\phi}{\mathrm{d}t} \end{aligned} \tag{2.3}$$

where u_1, u_2, i_1, and i_2 are the voltages and currents of the primary/secondary windings, and N_1 and N_2 denote the number of primary and secondary winding turns, respectively.

The magnetizing current, i_{1m}, is the required current to generate the magnetic flux in the core. It is given by

$$i_{1\mathrm{m}} = i_1 - i_{\mathrm{FE}} = i_1 - \frac{N_1}{R_{\mathrm{FE}}'}\frac{\mathrm{d}\phi}{\mathrm{d}t} \tag{2.4}$$

where i_{FE} is the current through the resistance R_{FE}', which models the core losses.

2.2.2. Magnetic equivalent circuit

Fig. 2.3 depicts the magnetic equivalent circuit for a single-phase transformer. It includes the primary and secondary magnetomotive forces, $\mathfrak{F}_1$ and $\mathfrak{F}_2$, which depend on currents, i_{m} and i_2, respectively. The nonlinear behavior of the core is represented by a nonlinear reluctance, $\mathfrak{R}$, which depends on its own magnetic potential, f.

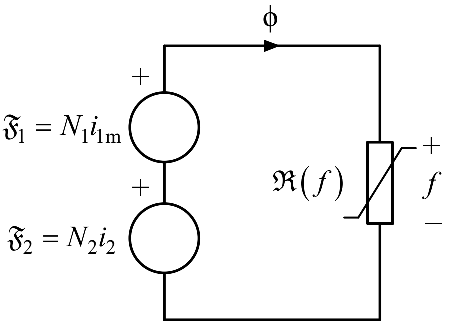

Fig. 2.3. Magnetic circuit of a single-phase transformer.

The magnetic circuit relation is

$$N_1 i_{1\mathrm{m}} + N_2 i_2 - f = 0 \tag{2.5}$$

2.2.3. Saturation curve

To represent the core nonlinear behavior, it is proposed a functional relationship between the magnetic potential in the core and the flux through it

$$f = \mathfrak{R}(f)\cdot\phi \tag{2.6}$$

The analytical single-valued function selected to model the nonlinear reluctance is [45]:

$$\mathfrak{R}(f)^{-1} = \frac{K_1}{\left(1+\left(\frac{|f|}{f_{\mathrm{KNEE}}}\right)^p\right)^{1/p}} + K_2 \tag{2.7}$$

where K_1, K_2, p and f_{KNEE}, are experimental parameters that allow this single-valued function to be fitted to the transformer saturation curve (ϕ–f), illustrated in Fig. 2.4. These four parameters have a clear physical meaning:

- K_1 and K_2 are defined by the slopes in the non-saturated and saturated regions of the curve, respectively. When expressed in pu, K_2 is equivalent to the air-core inductance.

- p influences the sharpness of the saturation knee.
- f_{KNEE} is the magnetic potential where saturation begins when the curve is approached by two slopes.

It is important to note that the graphic curve ϕ–f depicted in Fig. 2.4, represents an inverse reluctance. The reluctance of (2.7) is inversely proportional to the theoretical magnetizing inductance, L_{m}', as

$$L_{\mathrm{m}}' = \frac{N_1^2}{\mathfrak{R}} \tag{2.8}$$

if it were placed on the primary side of the electric circuit. This magnetizing inductance is not directly included into the model.

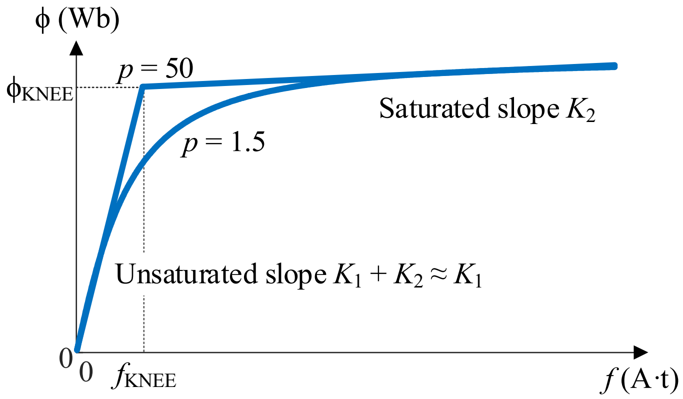

Fig. 2.4. Flux-magnetic potential characteristic of the proposed saturation curve for the following parameters: p = 1.5 and 50, $\mu_r = K_1/K_2 = 2000$.

Transformers are usually designed to operate at a point lightly below the knee point (f_{KNEE}, ϕ_{KNEE}). Due to this, a fifth parameter is introduced, the degree of saturation at rated flux, k_{SAT}, whose value can typically range from 0.4 to 1. With this parameter in mind, f_{KNEE} is defined as

$$k_{\mathrm{SAT}} = \frac{\sqrt{2}\cdot\phi_{\mathrm{N}}}{K_1 f_{\mathrm{KNEE}}} = \frac{\sqrt{2}\cdot\phi_{\mathrm{N}}}{\phi_{\mathrm{KNEE}}} \tag{2.9}$$

where ϕ_{N} is the RMS value of the nominal magnetic flux and ϕ_{KNEE} is the flux where saturation begins when the curve is approached by two slopes.

It is important to highlight that, depending on the p value, the knee point (f_{KNEE}, ϕ_{KNEE}), does not correspond exactly to the point where slight saturation begins, as illustrated in Fig. 2.4 for $p = 1.5$.

The saturation curve can be approached by less complex functions, useful in some cases. A first function, depicted in Fig. 2.5(a), is given by

$$f = \begin{cases} \dfrac{\phi - \phi_{\mathrm{S}}}{K_2} & \text{if } \phi \geq \phi_{\mathrm{KNEE}} \\ \dfrac{\phi}{K_1} & \text{if } |\phi| < \phi_{\mathrm{KNEE}} \\ \dfrac{\phi + \phi_{\mathrm{S}}}{K_2} & \text{if } \phi \geq -\phi_{\mathrm{KNEE}} \end{cases} \quad \rightarrow \quad \Re(\phi) = \frac{f}{\phi} = \begin{cases} \dfrac{1}{K_2}\left(1 - \dfrac{\phi_{\mathrm{S}}}{\phi}\right) & \text{if } \phi \geq \phi_{\mathrm{KNEE}} \\ \dfrac{1}{K_1} & \text{if } |\phi| < \phi_{\mathrm{KNEE}} \\ \dfrac{1}{K_2}\left(1 + \dfrac{\phi_{\mathrm{S}}}{\phi}\right) & \text{if } \phi \leq -\phi_{\mathrm{KNEE}} \end{cases} \tag{2.10}$$

where

$$\phi_{\mathrm{S}} = \left(1 - \frac{K_2}{K_1}\right)\phi_{\mathrm{KNEE}} \tag{2.11}$$

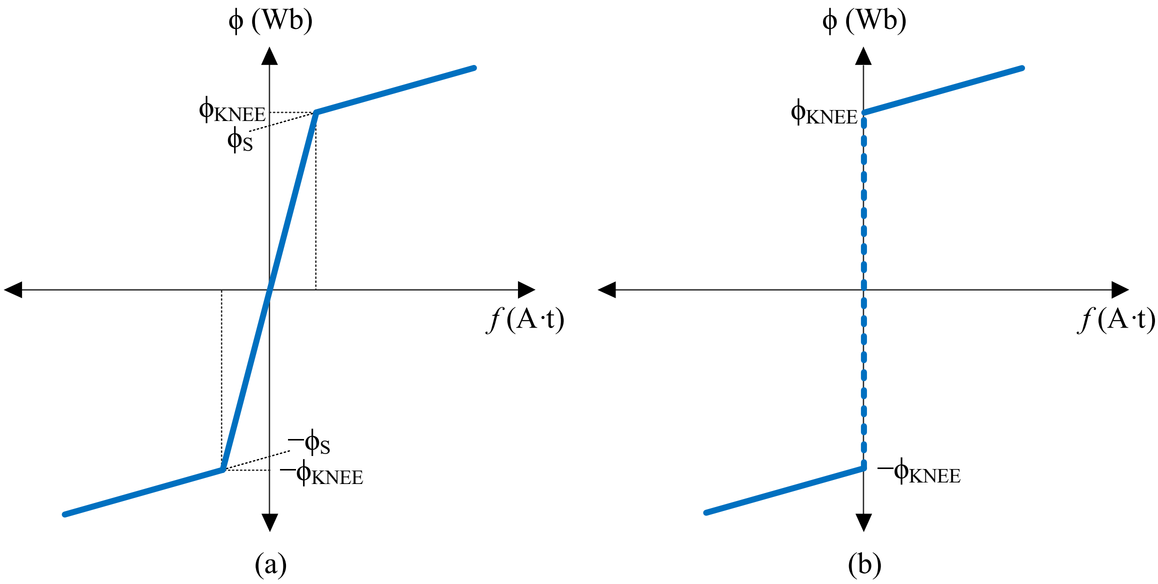

Fig. 2.5. Approximated saturation curves.

This function is represented by a piecewise linear curve composed only of two slopes, K_1 and K_2, representing the unsaturated and saturated regions, respectively. While this approach to model the saturation curve usually provides sufficient accuracy in predicting inrush current peaks, it is not suitable to accurately estimate the shape of the no-load current.

Another approximation of the saturation curve, as depicted in Fig. 2.5(b), considers an infinite slope in the unsaturated region, indicating that the magnetic potential is null in the absence of saturation. The function for this saturation curve is defined as

$$f = \begin{cases} \dfrac{\phi - \phi_{\mathrm{KNEE}}}{K_2} & \text{if } \phi \geq \phi_{\mathrm{KNEE}} \\ 0 & \text{if } |\phi| < \phi_{\mathrm{KNEE}} \\ \dfrac{\phi + \phi_{\mathrm{KNEE}}}{K_2} & \text{if } \phi \geq -\phi_{\mathrm{KNEE}} \end{cases} \quad \rightarrow \quad \Re(\phi) = \frac{f}{\phi} = \begin{cases} \dfrac{1}{K_2}\left(1 - \dfrac{\phi_{\mathrm{KNEE}}}{\phi}\right) & \text{if } \phi \geq \phi_{\mathrm{KNEE}} \\ 0 & \text{if } |\phi| < \phi_{\mathrm{KNEE}} \\ \dfrac{1}{K_2}\left(1 + \dfrac{\phi_{\mathrm{KNEE}}}{\phi}\right) & \text{if } \phi \leq -\phi_{\mathrm{KNEE}} \end{cases} \tag{2.12}$$

Usually, it is not possible to measure or estimate the true values of the magnetic reluctance, since the number of winding turns are unknown or not measurable. In Appendix A, it is explained how to eliminate the number of winding turns from the model equations, by a reduction to pu (per unit) or by a reduction to the primary or secondary sides.

2.3. No-load current

Assuming a single-phase transformer under no-load conditions (secondary winding unloaded, $i_2 = 0$) and supplied with a purely sinusoidal voltage, the primary current i_1 (no-load current) is very small. Furthermore, since the values of R_1 and L_{d1} are also typically small, it can be considered that

$$\begin{aligned} u_1 &\approx N_1 \frac{\mathrm{d}\phi}{\mathrm{d}t} \\ u_2 &= N_2 \frac{\mathrm{d}\phi}{\mathrm{d}t} \end{aligned} \tag{2.13}$$

The last equation indicates that the flux will be proportional to the derivative of the voltage, so if the voltage is purely sinusoidal, the flux will also be purely sinusoidal, shifted 90º behind the voltage. This will always be the case, regardless of whether the transformer is operating in the linear or nonlinear zone of the core saturation curve. Power transformers are typically designed to operate slightly above the knee point of the saturation curve, as can be seen in Fig. 2.6(a). Therefore, to achieve pure sinusoidal flux, the magnetizing current $i_{1m} = f / N_1$ (since $i_2 = 0$) cannot be sinusoidal; instead, it will have the typical bell shape waveform, as illustrated in Fig. 2.6(b). Since the effect of iron losses must also be considered, the resulting current i_1 is not perfectly symmetrical about the vertical axis, as exemplified in Fig. 2.6(b).

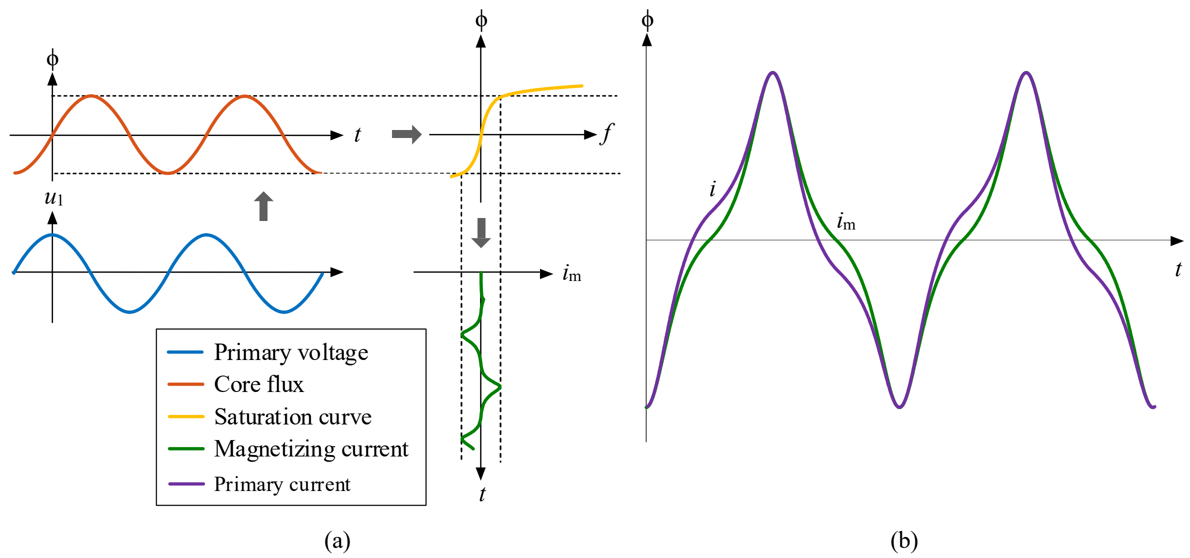

Fig. 2.6. (a) Steady-state operation of a no-load transformer and (b) typical waveforms of the magnetizing current and the no-load current.

The magnetizing current, being non-sinusoidal, exhibits harmonic distortion, specifically containing the first odd harmonics. As mentioned, the no-load current is further distorted due to core losses (resulting in a hysteresis loop). Specifically, the typical harmonic content of the no-load current is:

- Third harmonic, with amplitude between 10% and 60% of the fundamental component.
- Fifth harmonic, with amplitude between 0% and 30% of the fundamental component.
- Seventh harmonic, with amplitude between 0% and 20% of the fundamental component.

2.4. Inrush current

A slight increase in the flux beyond the knee point of the saturation curve, results in the saturation of the core. A DC flux component can be provoked by a sudden change in the primary voltage, which can be caused by the transformer energization or a fault restoration. The saturation of the core leads to a noticeable rise in primary current (several times the nominal current), as the slope in that region of the curve is very small.

As illustrated in Fig. 2.7(a), when a transformer is energized, the instantaneous magnitude of the flux at the instant of energization equals the residual flux, ϕ_R, which is the flux retained by the ferromagnetic core after de-energization due to hysteresis effects. Then, the core is driven into a deep asymmetrical saturation, which results in the typical inrush current waveform with a decay direct component shown in Fig. 2.7(b).

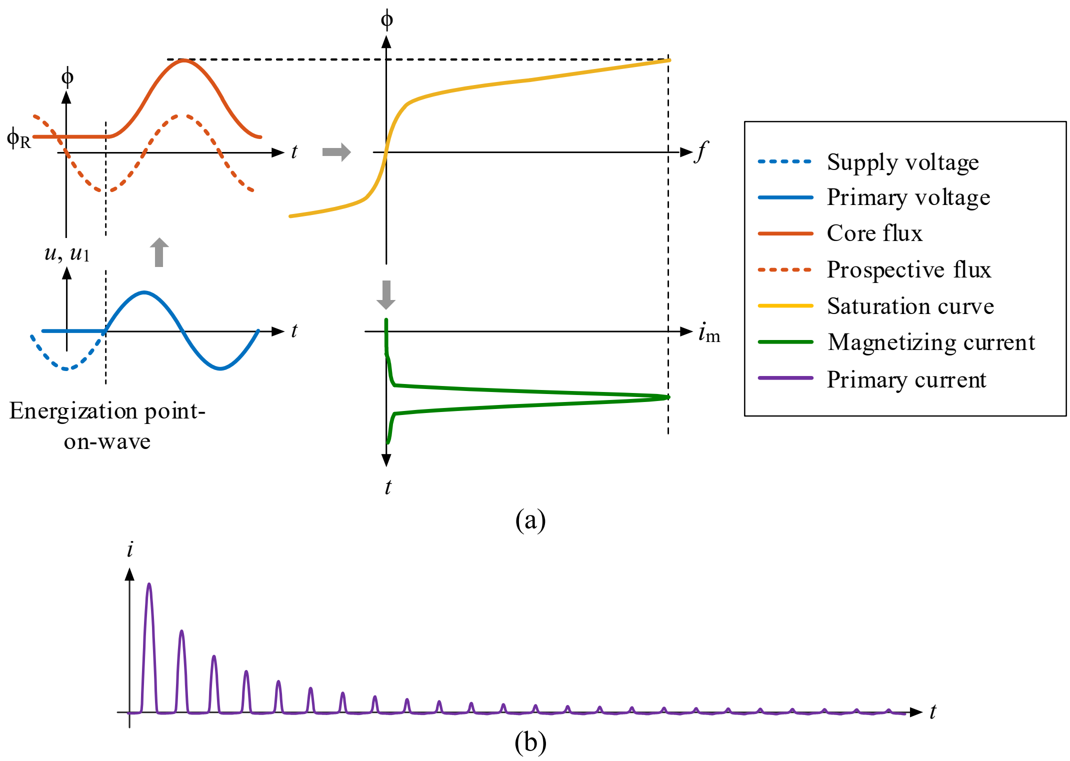

Fig. 2.7. (a)Inrush current generation after transformer energization and (b) typical inrush current waveform.

The offset (DC component) of the generated flux during the energization depends, mainly, on both the residual flux ϕ_R and the energization point-on-wave, α_E. The flux can reach a maximum theoretical value of two times the nominal flux peak plus the residual flux ($\phi_{MAX} = 2\sqrt{2}\cdot\phi_N + \phi_R$). After the flux reaches its maximum value, it begins to decay at a non-constant rate that depends on the own saturation curve, the primary winding impedance, and even the overall system supply impedance. In the following subsections, analytical expressions of the transient flux and the inrush current after the energization are developed. Furthermore, the influence of each transformer parameter on the inrush current is examined.

2.4.1. Theoretical calculation of inrush current

When a single-phase transformer is unloaded, there is no current through the secondary winding and the magnetomotive force $\mathfrak{F}_1$ of the magnetic circuit is directly equivalent to the magnetic potential f at the nonlinear reluctance $\mathfrak{R}$ (see Fig. 2.3). If the iron-core losses are neglected, the magnetic circuit equation leads to

$$\frac{N_1 i_1}{\mathfrak{R}(i_1)} = \phi \tag{2.14}$$

The expression (2.14) implies that the current in the primary winding depends on the concatenated flux through the core. Using the approach of saturation curve depicted in Fig. 2.5(a), (2.14) leads to

$$i_1(\phi) = \begin{cases} \dfrac{\phi - \phi_S}{N_1 K_2} & \text{if } \phi \geq \phi_{KNEE} \\ \dfrac{\phi}{N_1 K_1} & \text{if } |\phi| < \phi_{KNEE} \\ \dfrac{\phi + \phi_S}{N_1 K_2} & \text{if } \phi \geq -\phi_{KNEE} \end{cases} \tag{2.15}$$

Relationship (2.15) represents the primary current as a piecewise-defined function of the flux. To derive expressions for both flux and current as functions of time, it is necessary to solve the electric primary circuit, which is defined by the first equation in (2.3). The transformer exhibits three different behaviors: when $\phi \geq \phi_{KNEE}$, when $|\phi| < \phi_{KNEE}$, and when $\phi \geq -\phi_{KNEE}$. Next, the procedure for solving the electric primary circuit will be explained.

The first equation in (2.3) is a first-order linear ordinary differential equation. This equation involves two variables, i_1 and ϕ, both of which are dependent on a third independent variable, time. When deriving (2.15), the result is the derivative of the primary current as

$$\frac{\mathrm{d}i_1}{\mathrm{d}t} = \begin{cases} \dfrac{1}{N_1 K_1} \dfrac{\mathrm{d}\phi}{\mathrm{d}t} & \text{if } |\phi| < \phi_{KNEE} \\ \dfrac{1}{N_1 K_2} \dfrac{\mathrm{d}\phi}{\mathrm{d}t} & \text{if } |\phi| \geq \phi_{KNEE} \end{cases} \tag{2.16}$$

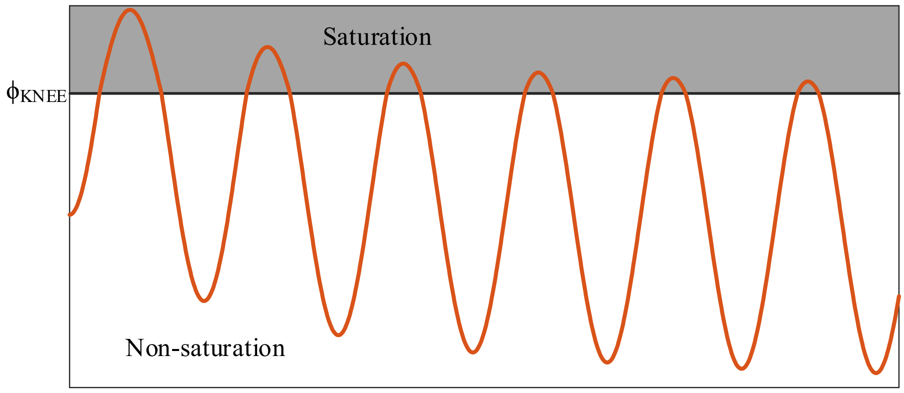

Fig. 2.8. Saturation and non-saturation of the flux.

First, for the case when $\phi \geq \phi_{KNEE}$ (see Fig. 2.8), next expression is obtained by substituting (2.15) and (2.16) in (2.3)

$$\sqrt{2}U_1 \cos(\omega t + \alpha_E) = R_1 \frac{\phi(t) - \phi_S}{N_1 K_2} + \left(\frac{L_{d1}}{N_1 K_2} + N_1\right) \frac{d\phi(t)}{dt} \tag{2.17}$$

where the primary voltage u_1 has been assumed to be purely sinusoidal as $\sqrt{2}U_1 \cos(\omega t + \alpha_E)$, where α_E is the energization point-on-wave assuming that the energization is produced at instant $t = 0$. Now, the first equation in (2.3) has been transformed into a differential equation with only one variable, the flux, which depends on the independent variable, the time. This equation can be rewritten as

$$N_1 K_2 \sqrt{2}U_1 \cos(\omega t + \alpha_E) + R_1 \phi_S = R_1 \phi(t) + \left(L_{d1} + N_1^2 K_2\right) \frac{d\phi(t)}{dt} \tag{2.18}$$

The solution of (2.18) consists of two parts, the solution of the homogeneous equation, and a particular solution.

First, the solution corresponding to the homogeneous equation of (2.18) must be found. The homogeneous equation is given by

$$R_1 \phi(t) + \left(L_{d1} + N_1^2 K_2\right) \frac{d\phi(t)}{dt} = 0 \tag{2.19}$$

This is a differential equation in which each of the variables, ϕ and t, that can be separated on either side of the equation by elementary algebra, yielding to

$$\frac{-\left(L_{d1} + N_1^2 K_2\right)}{R_1} \frac{d\phi}{\phi} = dt \tag{2.20}$$

By integrating both sides of the equation and rearranging, it can be obtained the solution to the homogeneous equation as

$$\phi_H(t) = C e^{\frac{-t}{\tau_{K2}}} \tag{2.21}$$

where

$$\tau_{\mathrm{K2}} = \frac{\left(L_{\mathrm{d1}} + N_1^{\,2} K_2\right)}{R_1} \tag{2.22}$$

By other hand, in (2.18), $R_1\phi_{\mathrm{S}}$ can be considered as a DC voltage source. In the presence of only a DC voltage source, after a certain time, the inductor ($L_{\mathrm{d1}} + N_1^{\,2}K_2$) in the circuit will behave only as a wire, so the flux will be constant and equal to ϕ_{S}, which is a part of the particular solution. Therefore, to determine the remaining part of the particular solution of (2.18), it is only necessary to solve the following equation

$$N_1 K_2 \sqrt{2} U_1 \cos\left(\omega t + \alpha_{\mathrm{E}}\right) = R_1 \phi\left(t\right) + \left(L_{\mathrm{d1}} + N_1^{\,2} K_2\right) \frac{\mathrm{d}\phi\left(t\right)}{\mathrm{d}t} \tag{2.23}$$

The solution is assumed to be of the form

$$\phi_{\mathrm{STEADY,K2}}(t) = \phi_1 \cos\left(\omega t + \alpha_{\mathrm{E}}\right) + \phi_2 \operatorname{sen}\left(\omega t + \alpha_{\mathrm{E}}\right) \tag{2.24}$$

where ϕ_1 and ϕ_2 are two unknown constants. By substituting (2.24) and its derivative in (2.23), it can be obtained

$$\begin{aligned} N_1 K_2 \sqrt{2} U_1 \cos\left(\omega t + \alpha_{\mathrm{E}}\right) = {} & \left[R_1 \phi_1 + \left(L_{\mathrm{d1}} + N_1^{\,2} K_2\right) \phi_2 \omega \right] \cos\left(\omega t + \alpha_{\mathrm{E}}\right) \\ & + \left[R_1 \phi_2 - \left(L_{\mathrm{d1}} + N_1^{\,2} K_2\right) \phi_1 \omega \right] \operatorname{sen}\left(\omega t + \alpha_{\mathrm{E}}\right) \end{aligned} \tag{2.25}$$

Equation (2.25) is fulfilled as long as the following expressions are fulfilled

$$\begin{aligned} & R_1 \phi_1 + \left(L_{\mathrm{d1}} + N_1^{\,2} K_2\right) \phi_2 \omega = N_1 K_2 \sqrt{2} U_1 \\ & R_1 \phi_2 - \left(L_{\mathrm{d1}} + N_1^{\,2} K_2\right) \phi_1 \omega = 0 \end{aligned} \tag{2.26}$$

The values of the constants ϕ_1 and ϕ_2 are obtained as

$$\begin{aligned} \phi_1 &= \frac{N_1 R_1 K_2 \sqrt{2} U_1}{R_1^{\,2} + \left(L_{\mathrm{d1}} + N_1^{\,2} K_2\right)^2 \omega^2} \\ \phi_2 &= \frac{\left(L_{\mathrm{d1}} + N_1 K_2\right) N_1 \omega K_2 \sqrt{2} U_1}{R_1^{\,2} + \left(L_{\mathrm{d1}} + N_1^{\,2} K_2\right)^2 \omega^2} \end{aligned} \tag{2.27}$$

By substituting these values in (2.24), the steady-state response is obtained as

$$\phi_{\mathrm{STEADY,K2}}\left(t\right) = \frac{N_1 K_2 \sqrt{2} U_1}{R_1^{\,2} + \left(L_{\mathrm{d1}} + N_1^{\,2} K_2\right)^2 \omega^2} \left[R_1 \cos\left(\omega t + \alpha_{\mathrm{E}}\right) + \left(L_{\mathrm{d1}} + N_1^{\,2} K_2\right) \omega \operatorname{sen}\left(\omega t + \alpha_{\mathrm{E}}\right) \right] \tag{2.28}$$

equivalent to

$$\phi_{\mathrm{STEADY,K2}}(t)=\frac{N_1K_2\sqrt{2}U_1}{\sqrt{R_1^{\,2}+\left(L_{\mathrm{d1}}+N_1^{\,2}K_2\right)^2\omega^2}}\cos\left(\omega t+\alpha_{\mathrm{E}}-\varphi\right) \tag{2.29}$$

where

$$\varphi=\arctan\left(\frac{\left(L_{\mathrm{d1}}+N_1^{\,2}K_2\right)\omega}{R_1}\right) \tag{2.30}$$

By combining the homogeneous solution and the particular solution, the general solution is obtained as

$$\phi(t)=C\mathrm{e}^{\frac{-t}{\tau_{\mathrm{K2}}}}+\phi_{\mathrm{STEADY}}(t)+\phi_{\mathrm{S}} \tag{2.31}$$

This solution is known as general because it contains an unknown constant C, whose value depends on the initial conditions, in this case, the conditions of the transformer when saturation is reached. At time $t = t_0$, it can be considered that $\phi(t_0) = \phi_0$. Substituting these values into (2.31) yields to

$$C=\left[\phi_0-\phi_{\mathrm{S}}-\phi_{\mathrm{STEADY,K2}}(t_0)\right]\mathrm{e}^{\frac{-(t-t_0)}{\tau_{\mathrm{K2}}}} \tag{2.32}$$

Substituting (2.32) into (2.31) yields the specific solution for (2.18), that is, the flux as a function of time when $\phi \geq \phi_{\mathrm{KNEE}}$

$$\phi(t)=\left[\phi_0-\phi_{\mathrm{S}}-\phi_{\mathrm{STEADY,K2}}(t_0)\right]\mathrm{e}^{\frac{-(t-t_0)}{\tau_{\mathrm{K2}}}}+\phi_{\mathrm{STEADY,K2}}(t)+\phi_{\mathrm{S}} \tag{2.33}$$

When $\phi \leq \phi_{\mathrm{KNEE}}$, the flux is given by

$$\phi(t)=\left[\phi_0+\phi_{\mathrm{S}}-\phi_{\mathrm{STEADY,K2}}(t_0)\right]\mathrm{e}^{\frac{-(t-t_0)}{\tau_{\mathrm{K2}}}}+\phi_{\mathrm{STEADY,K2}}(t)-\phi_{\mathrm{S}} \tag{2.34}$$

Finally, for the case when $|\phi| < \phi_{\mathrm{KNEE}}$, employing a similar process to solving (2.3), the flux is given by

$$\phi(t)=\left[\phi_0-\phi_{\mathrm{STEADY,K1}}(t_0)\right]\mathrm{e}^{\frac{-(t-t_0)}{\tau_{\mathrm{K1}}}}+\phi_{\mathrm{STEADY,K1}}(t) \tag{2.35}$$

where

$$\phi_{\mathrm{STEADY,K1}}(t) = \frac{N_1 K_1 \sqrt{2} U_1}{\sqrt{R_1^2 + \left(L_{\mathrm{d1}} + N_1^2 K_1\right)^2 \omega^2}} \cos\left(\omega t + \alpha_E - \beta\right)$$

$$\tau_{\mathrm{K1}} = \frac{\left(L_{\mathrm{d1}} + N_1^2 K_1\right)}{R_1} \tag{2.36}$$

$$\beta = \arctan\left(\frac{\left(L_{\mathrm{d1}} + N_1^2 K_1\right)\omega}{R_1}\right)$$

Each of the three previous equations determines the behavior of the transformer at different moments. It must be noted that the sub-indexes K1 and K2 have been used to distinguish between unsaturated or saturated conditions, respectively.

As it will be explained in detail later, the residual flux ϕ_R after a de-energization is never greater than the saturation flux ϕ_{KNEE}. Therefore, when a transformer is energized under normal conditions, it does not immediately enter into saturation. During the first instants of time, the flux will be less than the saturation flux, as illustrated in the example of Fig. 2.9. As long as this is the case, the flux will be determined by (2.35), where ϕ_0 corresponds to the residual flux $\phi_{0,1} = \phi_R$, and the initial time t_0 corresponds to the energization instant, which has been considered $t_{0,1} = 0$. After a certain amount of time, the flux may reach the saturation (positive or negative). Then, the initial flux ϕ_0 in (2.33) and (2.34) is always equal to ϕ_{KNEE} or $-\phi_{KNEE}$, respectively, while the initial time t_0 in both equations always corresponds to the saturation instant. When the flux drops beyond the saturation level, the equation (2.35) once again determines its behavior, but at this time ϕ_0 corresponds either to ϕ_{KNEE} or $-\phi_{KNEE}$, which is the same for all subsequent cycles, and t_0 corresponds to the de-saturation instant.

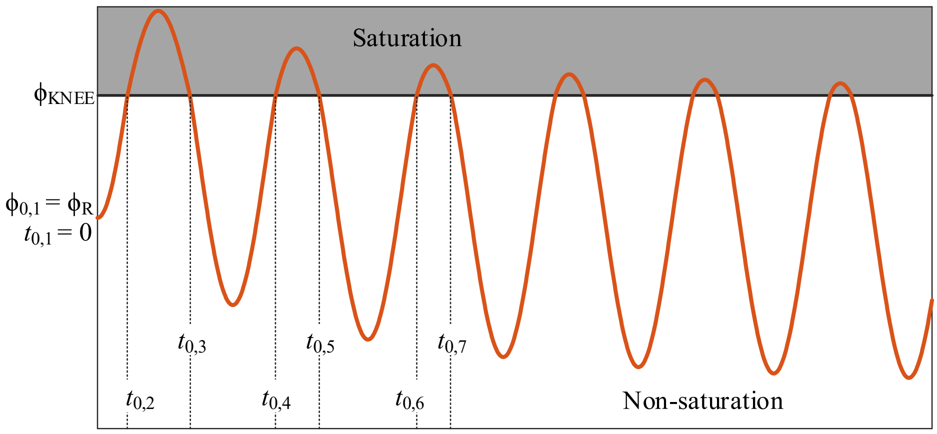

Fig. 2.9. Typical transient flux waveform.

The analytical expressions of the primary current, can be obtained by directly substituting the flux expressions, (2.33), (2.34) and (2.35), into (2.15), resulting in

$$\begin{aligned}
&\text{If } \phi(t) \geq \phi_{\text{KNEE}} && i_1(t) = \left[i_0 - i_{\text{STEADY,K2}}(t_0)\right] \mathrm{e}^{\frac{-(t-t_0)}{\tau_{\text{K2}}}} + i_{\text{STEADY,K2}}(t) \\
&\text{If } \left|\phi(t)\right| < \phi_{\text{KNEE}} && i_1(t) = \left[i_0 - i_{\text{STEADY,K1}}(t_0)\right] \mathrm{e}^{\frac{-(t-t_0)}{\tau_{\text{K1}}}} + i_{\text{STEADY,K1}}(t) \\
&\text{If } \phi(t) \leq \phi_{\text{KNEE}} && i_1(t) = \left[i_0 - i_{\text{STEADY,K2}}(t_0)\right] \mathrm{e}^{\frac{-(t-t_0)}{\tau_{\text{K2}}}} + i_{\text{STEADY,K2}}(t)
\end{aligned} \tag{2.37}$$

where

$$\begin{aligned}
i_{\text{STEADY,K2}}(t) &= \frac{\phi_{\text{STEADY,K2}}(t)}{N_1 K_2} \\
i_{\text{STEADY,K1}}(t) &= \frac{\phi_{\text{STEADY,K1}}(t)}{N_1 K_1}
\end{aligned} \tag{2.38}$$

At energization, the initial current, $i_{0,1}$, is not null with this model because the initial flux is not null; thus, $i_{0,1} = \phi_R / N_1 K_1$. For subsequent cycles, either saturation or desaturation, it corresponds to the current at the knee-point: $i_{0,n} = \phi_{\text{KNEE}} / N_1 K_1$ (where $n = 2,3,4...$). In contrast, the initial current at energization is null if the simplified saturation curve depicted in Fig. 2.5(b) is used. The corresponding equations for this simplified model can be obtained from the previous ones by imposing, without significant loss of accuracy, that $K_1 = \infty$ and $\phi_S = \phi_{\text{KNEE}}$.

The resulting flux expressions are given by:

$$\begin{aligned}
&\text{If } \phi(t) \geq \phi_{\text{KNEE}} && \phi(t) = \phi(t) = \phi_{\text{STEADY,K2}}(t) - \phi_{\text{STEADY,K2}}(t_0)\, \mathrm{e}^{\frac{-(t-t_0)}{\tau_{\text{K2}}}} + \phi_{\text{KNEE}} \\
&\text{If } \left|\phi(t)\right| < \phi_{\text{KNEE}} && \phi(t) = \phi_{\text{STEADY}}(t) - \phi_{\text{STEADY}}(t_0) + \phi_0 \\
&\text{If } \phi(t) \leq \phi_{\text{KNEE}} && \phi(t) = \phi(t) = \phi_{\text{STEADY,K2}}(t) - \phi_{\text{STEADY,K2}}(t_0)\, \mathrm{e}^{\frac{-(t-t_0)}{\tau_{\text{K2}}}} - \phi_{\text{KNEE}}
\end{aligned} \tag{2.39}$$

where

$$\phi_{\text{STEADY}}(t) = \sqrt{2}\phi_{\text{N}} \cos\left(\omega t + \alpha_{\text{E}} - \frac{\pi}{2}\right) \tag{2.40}$$

and ϕ_N is the nominal flux.

The corresponding current expressions are

$$\begin{aligned}
&\text{If } \phi(t) \geq \phi_{\text{KNEE}} && i_1(t) = \left[i_0 - i_{\text{STEADY,K2}}(t_0)\right] \mathrm{e}^{\frac{-(t-t_0)}{\tau_{\text{K2}}}} + i_{\text{STEADY,K2}}(t) \\
&\text{If } \left|\phi(t)\right| < \phi_{\text{KNEE}} && i_1(t) = 0 \\
&\text{If } \phi(t) \leq \phi_{\text{KNEE}} && i_1(t) = \left[i_0 - i_{\text{STEADY,K2}}(t_0)\right] \mathrm{e}^{\frac{-(t-t_0)}{\tau_{\text{K2}}}} + i_{\text{STEADY,K2}}(t)
\end{aligned} \tag{2.41}$$

The main difference with this approach is that the current during no-saturation conditions is zero; therefore, the energization flux (residual flux ϕ_R) involves an initial energization current that is null. Moreover, since the current during the non-saturation intervals is zero, the initial current $i_{0,n}$ previous to each saturation interval is also zero.

For simplicity, the source impedance has not been considered in the formulation of the inrush current, nor in the rest of the chapter. The source impedance has the same effects on the inrush current as R_1 and L_{d1}. Therefore, it can be considered as part of R_1 and L_{d1}.

2.4.2. Inrush current peak and decaying evolution

In this subsection, the derivation of an analytical formulation to calculate directly the maximum peak of the inrush current will be addressed. The overall evolution of the inrush current is also analyzed and discussed, as well as the influence of each transformer parameter.

Assuming $K_1 \approx \infty$ and $t_{0,1} = 0$, the flux at the first saturation instant, $t_{0,2}$, which from this point will be referred to as t_{SAT}, is given by

$$\left|\phi\left(t_{SAT}\right)\right| = \left|\phi_R + \sqrt{2}\phi_N \left[\cos\left(\omega t_{SAT} + \alpha_E - \frac{\pi}{2}\right) - \cos\left(\alpha_E - \frac{\pi}{2}\right)\right]\right| = \phi_{KNEE} \tag{2.42}$$

As $\phi_{KNEE} \geq \sqrt{2}\phi_N$, for saturation to occur in the positive direction, it must be fulfilled that

$$\frac{\phi_R}{\sqrt{2}\phi_N} - \cos\left(\alpha_E - \frac{\pi}{2}\right) \geq \frac{\phi_{KNEE}}{\sqrt{2}\phi_N} - 1 \tag{2.43}$$

while for saturation to occur in the negative direction, it must be fulfilled that

$$\frac{\phi_R}{\sqrt{2}\phi_N} - \cos\left(\alpha_E - \frac{\pi}{2}\right) \leq -\frac{\phi_{KNEE}}{\sqrt{2}\phi_N} + 1 \tag{2.44}$$

Therefore, (2.42) can be rewritten as

$$\begin{aligned} \phi\left(t_{SAT}\right) &= \phi_R + \sqrt{2}\phi_N \left[\cos\left(\omega t_{SAT} + \alpha_E - \frac{\pi}{2}\right) - \cos\left(\alpha_E - \frac{\pi}{2}\right)\right] \\ &= \begin{cases} \phi_{KNEE} & \text{if } -90^{\circ} - \theta_1 < \alpha_E < -90^{\circ} + \theta_1 \\ -\phi_{KNEE} & \text{if } 90^{\circ} - \theta_2 < \alpha_E < 90^{\circ} + \theta_2 \end{cases} \end{aligned} \tag{2.45}$$

where θ_1 and θ_2 are the boundary angles around –90° and 90°, respectively, where saturation occurs. These angles can be calculated as

$$\theta_1 = \pi - \arccos\left(\frac{+\phi_{KNEE} + \phi_R}{\sqrt{2}\phi_N} - 1\right)$$
$$\theta_2 = \arccos\left(\frac{-\phi_{KNEE} + \phi_R}{\sqrt{2}\phi_N} + 1\right) \tag{2.46}$$

With known values of α_E, ϕ_R, and ϕ_{KNEE}, (2.45) yields infinite solutions for ωt_{SAT}, as the cosine is a periodic function and its domain is the set of all real numbers. If the domain of the cosine is restricted to $[-\pi, \pi]$, only four different solutions can be obtained. Two solutions correspond to positive saturation, while the other two solutions correspond to negative saturation. In both cases, a solution corresponds to the angle at which the flux reaches saturation, and the other solution corresponds to the angle at which the flux drops beyond the saturation level, that is, the angle at which the core undergoes desaturation. The angle for positive saturation is given by

$$\omega t_{SAT} = -\arccos\left(\frac{+\phi_{KNEE} - \phi_R}{\sqrt{2}\phi_N} + \cos\left(\alpha_E - \frac{\pi}{2}\right)\right) - \alpha_E + \frac{\pi}{2} \tag{2.47}$$

while the angle for negative saturation is given by

$$\omega t_{SAT} = \arccos\left(\frac{-\phi_{KNEE} - \phi_R}{\sqrt{2}\phi_N} + \cos\left(\alpha_E - \frac{\pi}{2}\right)\right) - \alpha_E + \frac{\pi}{2} \tag{2.48}$$

From the previous equations, some insights can be deduced about inrush current. The saturation or the non-saturation of the transformer during the energization depends uniquely on the energization point-on-wave α_E, the residual flux ϕ_R, and the saturation flux level ϕ_{KNEE}. Fig. 2.10 shows t_{SAT}, as a function of ϕ_R and α_E for two different ϕ_{KNEE} values. In transformers with higher ϕ_{KNEE} values, it is more difficult to get saturation during energization, meaning there are fewer combinations of ϕ_R and α_E values that result into saturation. The empty spaces in both plots in Fig. 2.10 denote that the respective values of ϕ_R and α_E do not lead to saturation. Additionally, in Fig. 2.10, it can be observed that, for a given ϕ_R and α_E, a higher ϕ_{KNEE} results in a higher t_{SAT}, it takes more time to reach saturation.

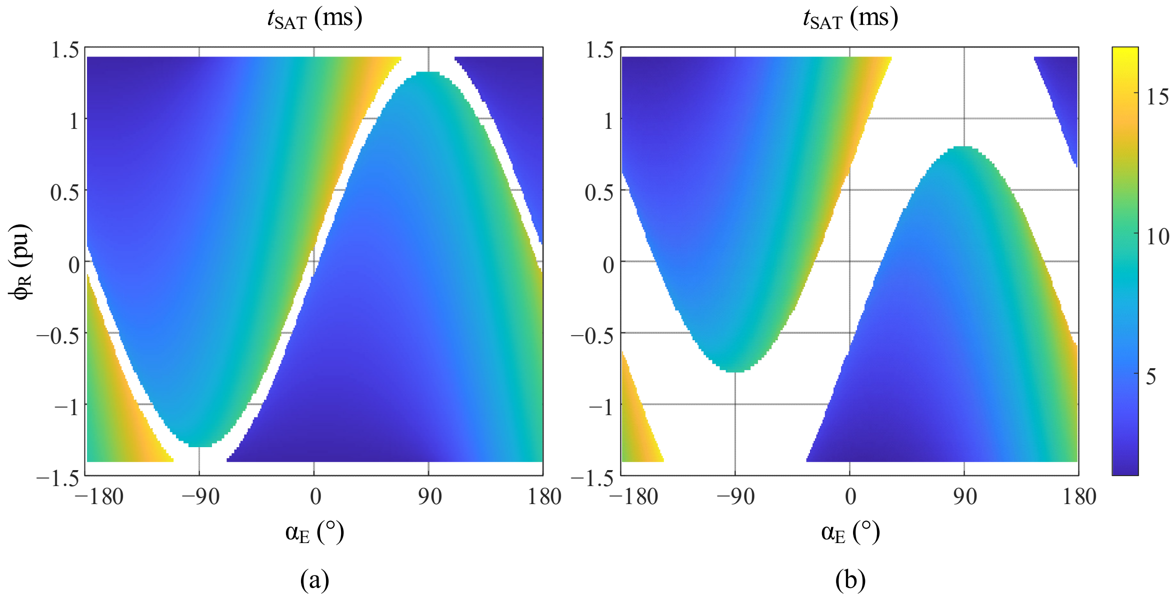

Fig. 2.10. First saturation time for different ϕ_{KNEE} values: (a) $\phi_{KNEE} = 1.05 \cdot \sqrt{2}\phi_N$ pu, and (b) $\phi_{KNEE} = 1.45 \cdot \sqrt{2}\phi_N$ pu.

It can be deduced from flux and current expressions, (2.39) and (2.41), that the flux and the current reach their maximum values, when the term $\cos(\omega t + \alpha_E - \varphi)$ is equal or very near to 1 and −1. Then, the time instant at which occurs the maximum peak of the inrush current, t_{PEAK}, can be approached as

$$t_{PEAK} \approx \begin{cases} \dfrac{-\alpha_E + \varphi}{\omega} & \text{if } -90^o - \theta_1 < \alpha_E < -90^o + \theta_1 \\ \dfrac{\pi - \alpha_E + \varphi}{\omega} & \text{if } 90^o - \theta_2 < \alpha_E < 90^o + \theta_2 \end{cases} \tag{2.49}$$

Therefore, the maximum peak of the inrush current can be approached as

$$|i_{PEAK}| \approx \hat{I}_{STEADY,K2}\left[1 + \left|\cos\left(\omega t_{SAT,1} + \alpha_E - \varphi\right)\right| e^{\frac{-R_1}{\left(L_{d1} + N_1^2 K_2\right)}\left(t_{PEAK} - t_{SAT}\right)}\right] \tag{2.50}$$

while the maximum peak of the flux can be approached as

$$|\phi_{PEAK}| \approx \hat{I}_{STEADY,K2}\left[1 + \left|\cos\left(\omega t_{SAT,1} + \alpha_E - \varphi\right)\right| e^{\frac{-R_1}{\left(L_{d1} + N_1^2 K_2\right)}\left(t_{PEAK} - t_{SAT}\right)}\right] + \phi_{KNEE} \tag{2.51}$$

where $\hat{I}_{STEADY,K2}$ is given by

$$\hat{I}_{STEADY,K2} = \frac{\sqrt{2}U_1}{\sqrt{R_1^2 + \left(L_{d1} + N_1^2 K_2\right)^2 \omega^2}} \tag{2.52}$$

A simpler approximation of the maximum peak of the inrush current can be obtained. Assuming that $t_{0,1} = 0$ and neglecting R_1 and L_{d1}, it can be considered that the flux at any time is given by

$$\phi(t) = \sqrt{2}\phi_N \left[\cos\left(\omega t + \alpha_E - \frac{\pi}{2} \right) - \cos\left(\alpha_E - \frac{\pi}{2} \right) \right] + \phi_R \tag{2.53}$$

Then, ϕ_{PEAK} can be approached as

$$\left|\phi_{PEAK}\right| = \sqrt{2}\phi_N + \left| \phi_R - \sqrt{2}\phi_N \cos\left(\alpha_E - \frac{\pi}{2} \right) \right| \tag{2.54}$$

and i_{PEAK} can be approached as

$$\left|i_{PEAK}\right| = \frac{\left|\phi_{PEAK}\right| - \phi_{KNEE}}{N_1 K_2} \tag{2.55}$$

The ϕ_{PEAK} and i_{PEAK} values obtained with this approach are not accurate and correspond only to ideal values, as they do not consider the voltage drop across the winding impedance. However, they are useful to understand the influence of ϕ_R and α_E. Fig. 2.11 shows the maximum peak of the flux (with the last approach) as a function of ϕ_R and α_E. It can be seen that the worst energization points-on-wave are −90° (voltage zero-crossing in positive direction) and 90° (voltage zero-crossing in negative direction) when ϕ_R is zero, resulting in positive and negative saturation, respectively. Conversely, the most favorable energization points-on-wave, when ϕ_R is zero or unknown, are 0° and 180°. If ϕ_R is known with a non-zero value, the worst and the most favorable energization points-on-wave are different; they vary as a function of ϕ_R. The most severe cases of inrush current happen when the core has the maximum ϕ_R and the energization occurs at the instant of voltage zero-crossing with a polarity that increases the flux in the core.

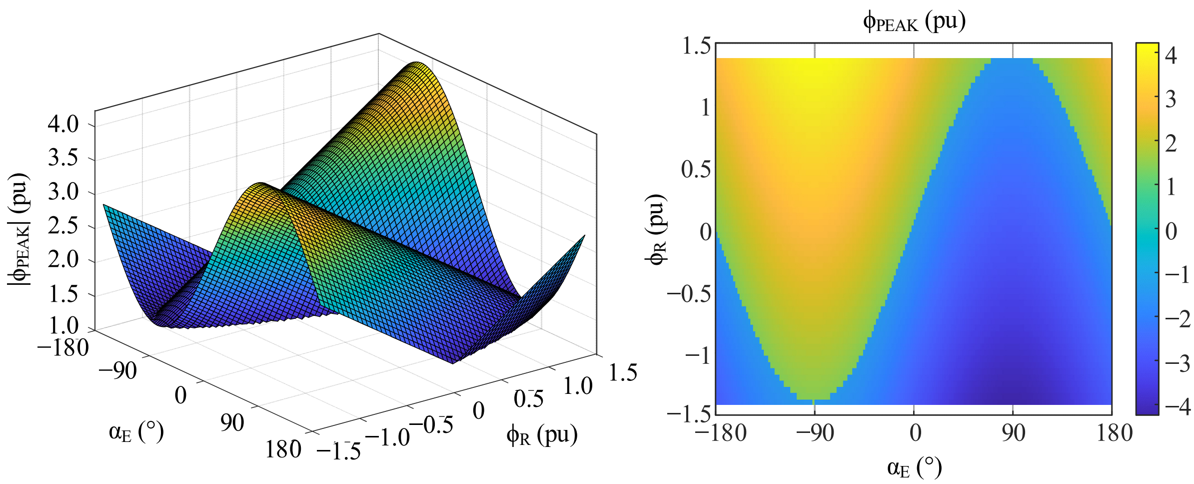

Fig. 2.11. Maximum peak of the transient flux as a function of the energization point-on-wave and the residual flux.

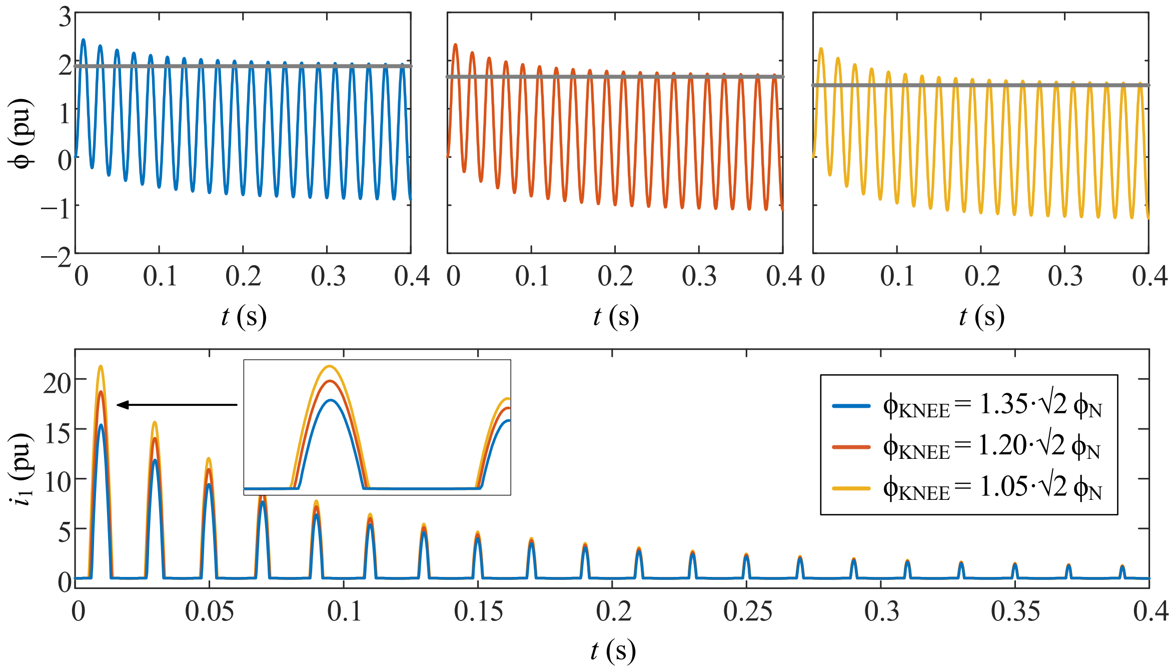

Fig. 2.12. Comparison of flux and inrush current for different saturation flux levels, ϕ_{KNEE}.

A comparison of transient flux and inrush current for different ϕ_{KNEE} values is illustrated in Fig. 2.12. According to (2.50) and (2.51), ϕ_{PEAK} and i_{PEAK} depend on the absolute value of $\cos(\omega t_{SAT} + \alpha_E - \varphi)$. As stated before, a higher ϕ_{KNEE} implies a higher t_{SAT}, resulting in a lower $\cos(\omega t_{SAT} + \alpha_E - \varphi)$. Consequently, a higher ϕ_{KNEE} leads to decreased ϕ_{PEAK} and i_{PEAK}, as shown in Fig. 2.12. It can also be observed that the difference between the final peaks for different ϕ_{KNEE} values is smaller than the difference between the initial peaks. Lastly, a lower ϕ_{KNEE} results in wider inrush current cycles due to a smaller t_{SAT}.

Based on flux and current expressions, (2.39) and (2.41), it is evident that higher resistance R_1 and higher leakage inductance L_{d1} reduce the initial peaks of the transient flux and, consequently, the initial peaks of the inrush current, as illustrated in Fig. 2.13 and Fig. 2.14, respectively. However, a proportional increment in L_{d1} has a more significant impact than the same proportional increment in R_1. The resistance R_1 also reduces the magnitude of the last peaks of the inrush current. It is responsible for damping the direct component of the flux and, consequently, for damping the inrush current, as shown in Fig. 2.13. However, the same effect is not observed for L_{d1}. A higher L_{d1} leads to a major opposition to current changes, as it is like a circuit inertia. Therefore, a higher L_{d1} results in a slower damping of the inrush current, as shown in Fig. 2.14.

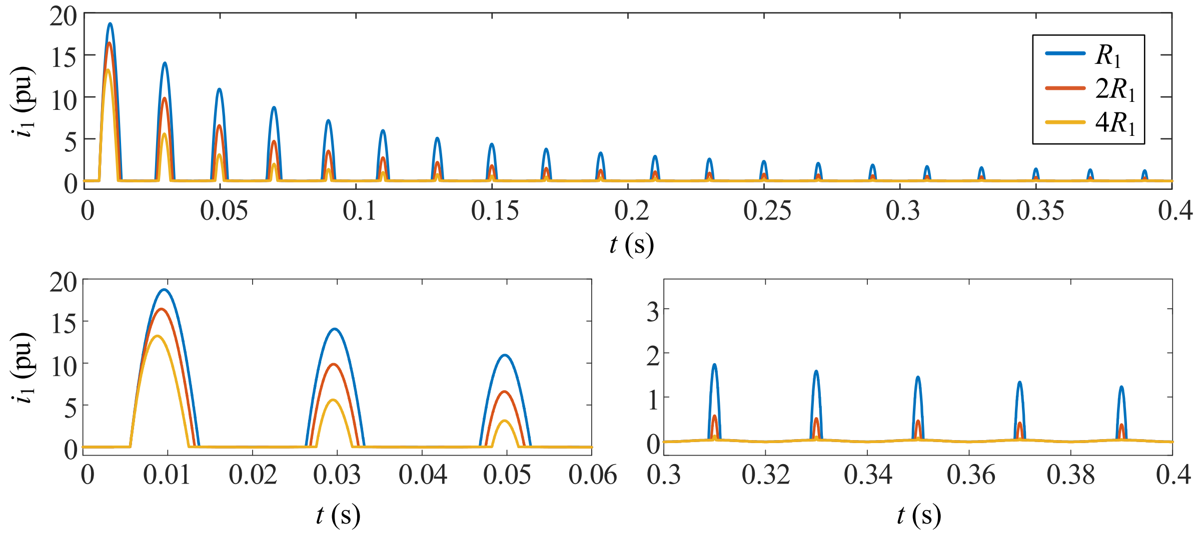

Fig. 2.13. Inrush current comparison for different R_1 values.

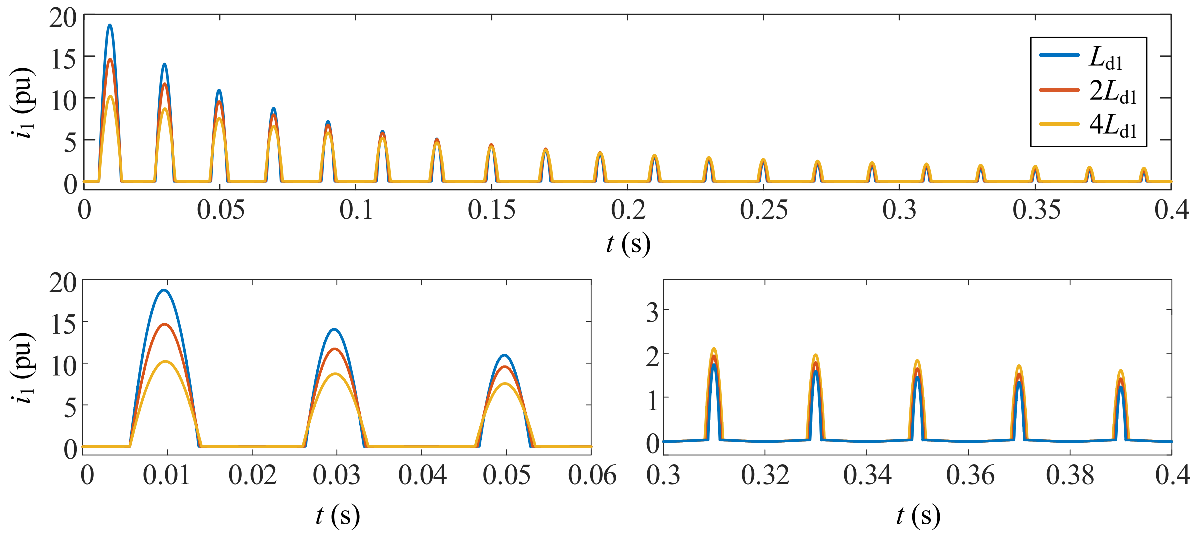

Fig. 2.14. Inrush current comparison for different L_{d1} values.

By other hand, some authors [16],[46] simplify the direct component as a decaying exponential, but this approach is erroneous. Assuming that $K_1 \approx \infty$ (or K_1 is very large), the damping of the inrush occurs only during the saturation intervals, as the current is zero (or very small) during no-saturation intervals. As illustrated in Fig. 2.15, the DC component of the flux (given by ϕ-ϕ_{STEADY}, since during steady-state conditions after inrush, the flux is equivalent to ϕ_{STEADY}) during no-saturation intervals remains constant. There is damping only during saturation intervals.

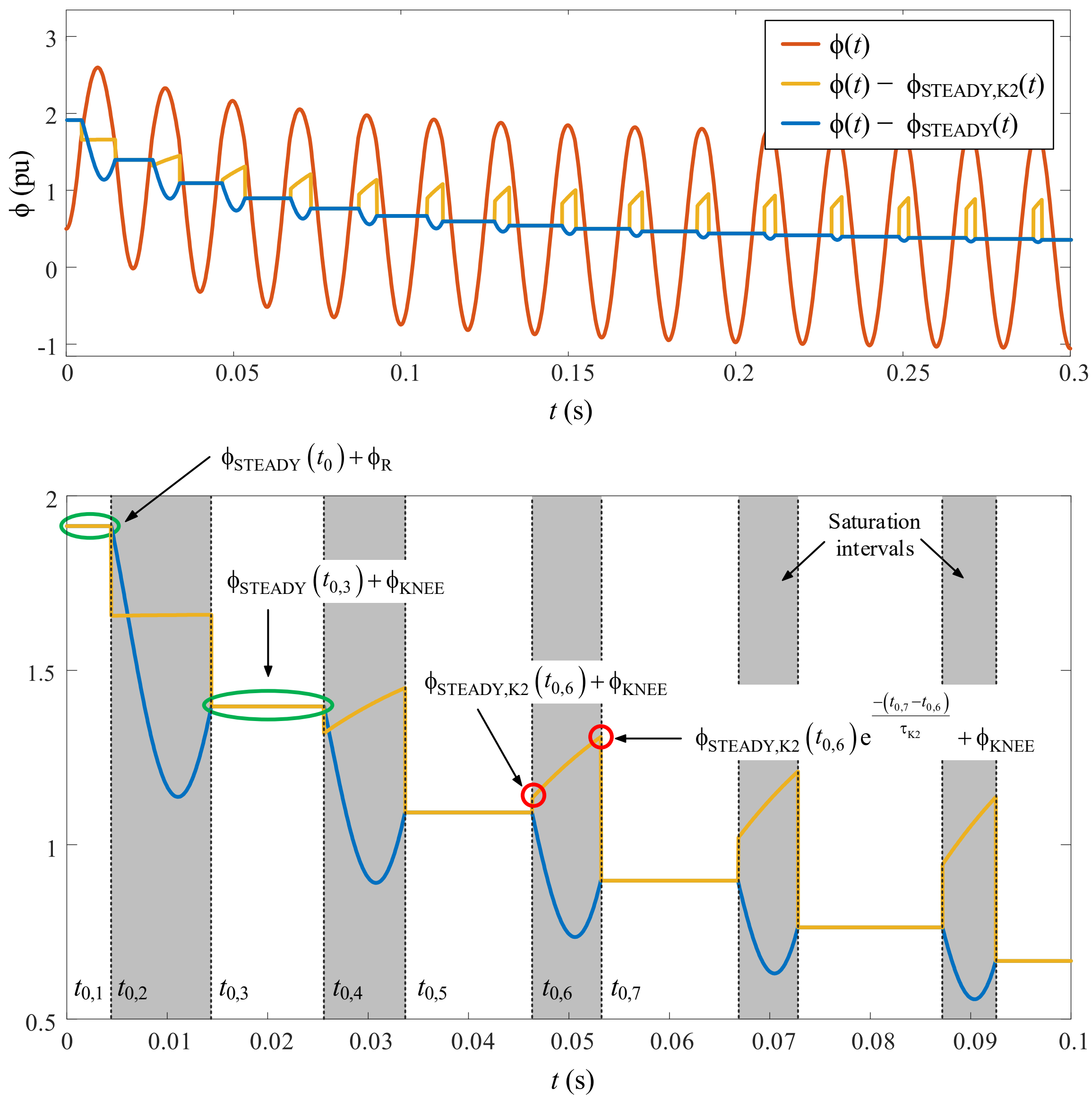

Fig. 2.15. Evolution of the flux and its components after energization.

The non-sinusoidal component during saturation intervals, $\phi(t)-\phi_{\text{STEADY,K2}}(t)=\phi_{\text{STEADY,K2}}(t_0)\mathrm{e}^{-(t-t_0)/\tau_{\text{K2}}}$, does exhibit an exponential evolution, as illustrated in Fig. 2.15, but this exponential does not encompass the entire evolution of the inrush. At the exact instant of saturation, the exponential term is equal to 1, and the initial value of the non-sinusoidal component for each saturation interval is determined only by the term $\phi_{\text{STEADY,K2}}(t_0)$, dependent on the corresponding saturation instant t_0. The saturation angle, ωt_0, is greater in each cycle, so the term $\phi_{\text{STEADY,K2}}(t_0) = \cos(\omega t_0 + \alpha_E - \varphi)$ gets closer to 1 with each cycle. In other words, the exponential term is reset at the beginning of every saturation intervals, and the overall inrush evolution is like an *extended* sinusoidal segment. It is important to note that, due to the exponential term, the inrush current cycles are not symmetrical around their peaks. In Fig. 2.13, it can also be seen that a higher R_1 results in narrower inrush current cycles, due to a faster decaying of the exponential term. In opposite, a higher L_{d1} results in wider inrush current cycles, as illustrated in Fig. 2.14.

The inductance during saturation intervals, $N_1^2K_2$, has exactly the same effects on the flux as L_{d1}. Fig. 2.16 illustrates the resulting fluxes and inrush currents for different K_2 values.

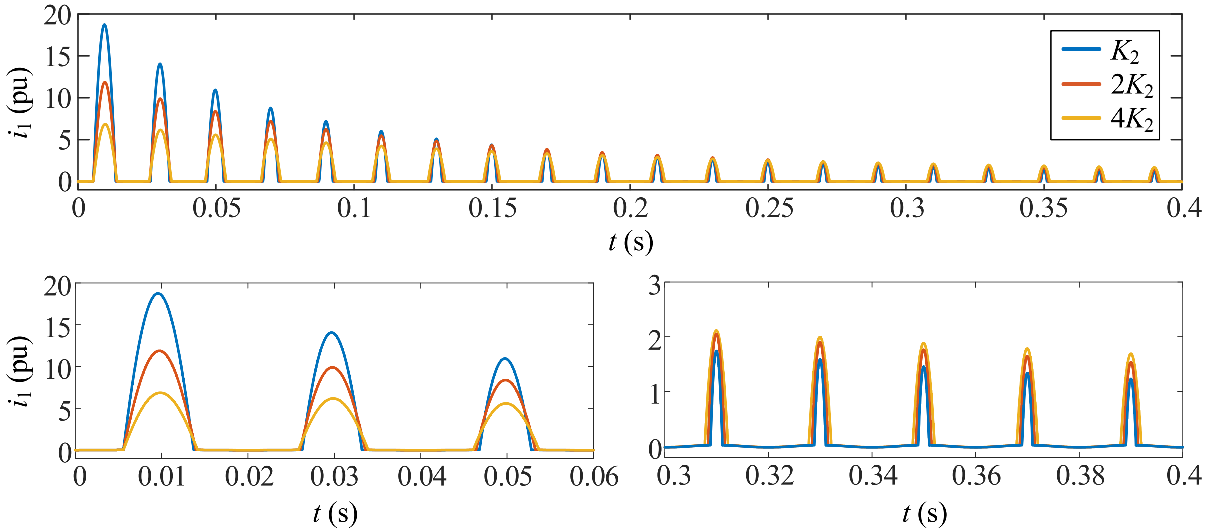

Fig. 2.16. Comparison of flux and inrush current for different K_2 values.

Finally, Table 2.1 and Table 2.2 summarize the influence of each parameter on the inrush current. As higher resistance R_1 reduces the first inrush current peak and higher leakage inductance L_{d1} reduce the decay time (inrush duration), τ, it is important to note that larger transformers present less severe inrush currents but with a longer duration (as larger transformers have more leakage inductance, as shown in Appendix C).

Table 2.1. Influence of each transformer parameter on the inrush current.

Parameter	Saturation / Non-saturation	First inrush current peak, i_{PEAK}	Decay time, τ
Winding resistance, R_1	No influence	Influence	Influence
Leakage Inductance, L_{d1}	No influence	Influence	Influence
Saturation slope, K_2	No influence	Influence	Influence
Saturation flux level, ϕ_{KNEE}	Influence	Influence	Influence
Non saturation slope, K_1	Negligible influence	No influence	No influence
Energization point-on-wave, α_E	Influence (depending on ϕ_R)	Influence (depending on ϕ_R)	Influence (depending on ϕ_R)
Residual flux, ϕ_R	Influence (depending on α_E)	Influence (depending on α_E)	Influence (depending on α_E)

Table 2.2. Influence of the main parameters on the inrush current peak and the decay time.

Parameter	First inrush current peak, i_{PEAK}	Decay time, τ
Winding resistance, R_1 ↑	≈	↓
Leakage Inductance, L_{d1} ↑	↓	↑

Chapter 3. Residual Flux and Inrush Current Elimination in Single-Phase Transformers

3.1. Introduction

As stated in previous chapter, there are several variables and parameters that influence the magnitude of the inrush current of a no-load transformer. These are the residual core flux, the magnitude of the supply voltage, the energization point-on-wave, the primary winding impedance, the magnetizing characteristic and even the impedance of the source. Of all these variables and parameters, the residual flux and the energization point-on-wave are, in practice, the only ones that can be controlled. The worst case of inrush current happens when the core has the maximum residual flux and the energization occurs at the instant of voltage zero-crossing with a polarity equal to that of the residual flux. Then, the most favorable switching angle depends on the existing residual flux, turning this variable the most critical. Therefore, this chapter is focused on switching angle and residual flux variables in order to eliminate the inrush current during energization.

The techniques for inrush current reduction in single-phase transformers can be classified into four general types: (1) external devices insertion [47]-[53], (2) methods that change the transformer design [54]-[57], (3) residual flux reduction [58]-[62], and (4) controlling the energization point-on-wave [63]-[67].

In the first approach, the most common technique is the resistor insertion in series with the transformer primary winding. This technique has the drawbacks of poor adaptability and increased losses during normal operation. Other proposals with better results are the insertion of diode bridges structures or superconducting fault current limiters, but, in general, these proposals require additional control circuitry outside the transformer, so they can be impractical or expensive. Techniques based on transformer design, such as reduced flux density designs, air-gaps, and low permeability iron core are more robust alternatives, but may be even more expensive and impractical (they result in larger transformers). Moreover, the inrush currents are not totally removed with some of these solutions [57].

The last two approaches are intricately linked to each other. When a transformer is de-energized, a residual flux can remain in the iron core due to the hysteresis characteristics of ferromagnetic materials. The determination of the most favorable energization point-on-wave, crucial for avoiding inrush current, relies on the value of this residual flux. The energization point-on-wave and the residual flux (in an indirect manner) are the only controllable parameters among all those on which the inrush current depends.

To achieve controlled energization, prior knowledge of the residual flux is essential. To address this challenge, there have been publications focusing on measuring and estimating the residual flux [68]-[75], as well as pre-setting a known residual flux value [76]. Since the residual flux can be different before each energization, it becomes necessary to consistently measure or estimate it before energizing the transformer using these approaches. This requires continuously acquiring signals and performing online calculations. Furthermore, most methodologies require specialized equipment and complex setups, typically implemented only in laboratories, resulting unsuitable for specific applications.

In this chapter, it is presented a smart switching for inrush current elimination. The smart switching avoids the need to measure or estimate the residual flux before each energization, which results into a more simple methodology than those of the literature. The no need to measure the residual flux is possible by using only two pieces of data (calculated from two no-load tests which characterize the static hysteresis loop and the de-energization flux trajectories): ϕ_{RM} and ϕ_{i0}, or the corresponding voltage points-on-wave α_{RM} and α_{i0}, along with understanding of the used breaker technology. Fig. 3.1 presents a comparison between the flowchart of common approaches and the proposed smart switching, while Fig. 3.2 provides a comparison between the experimental setups. It can be seen that the proposal is more simple and avoids the stage of measuring, eliminating or presetting the residual flux, with the corresponding saving of specific equipment and/or processing cost. Despite the proposed smart switching is applicable to SCR and IGBT breakers as well, the SCR breaker is a more cost-effective solution suitable for large power systems.

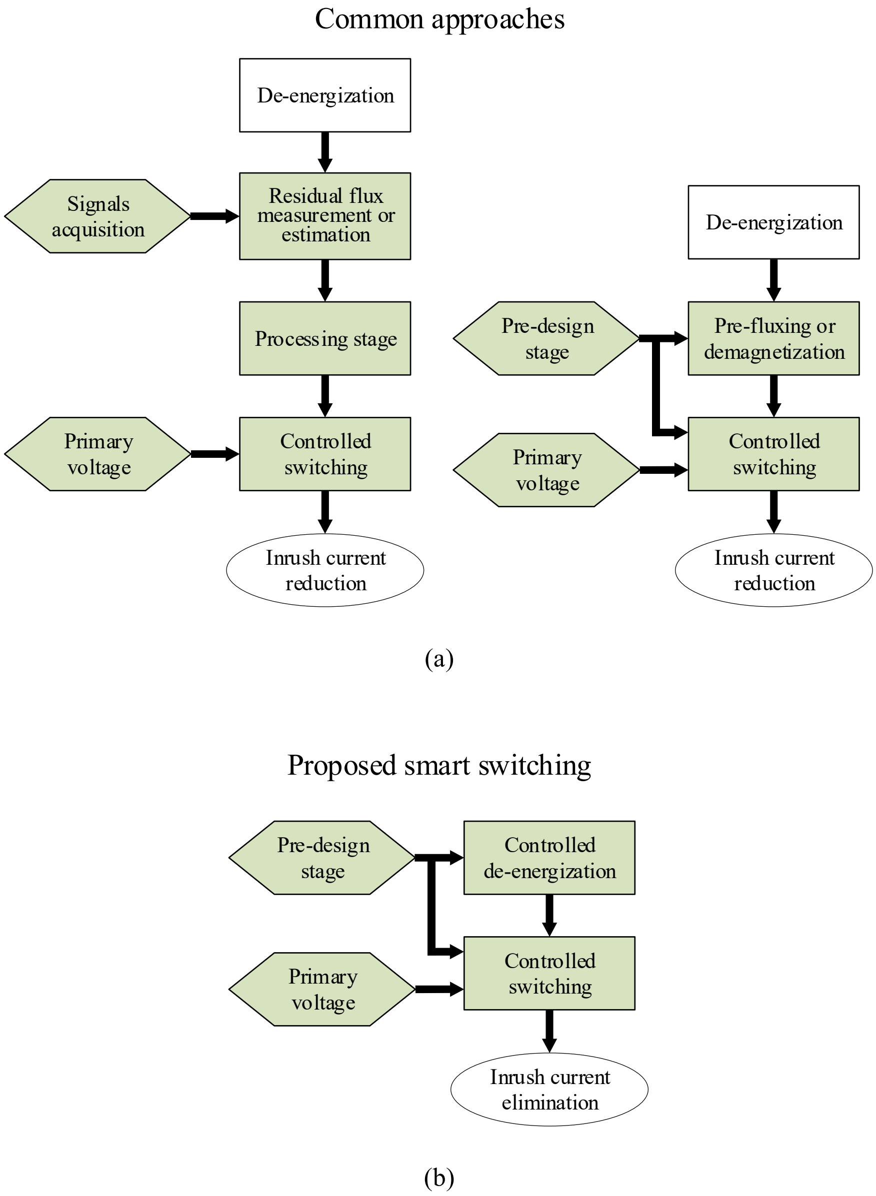

Fig. 3.1. Flowcharts of (a) common approaches for inrush current reduction and (b) the proposed smart switching for inrush current elimination.

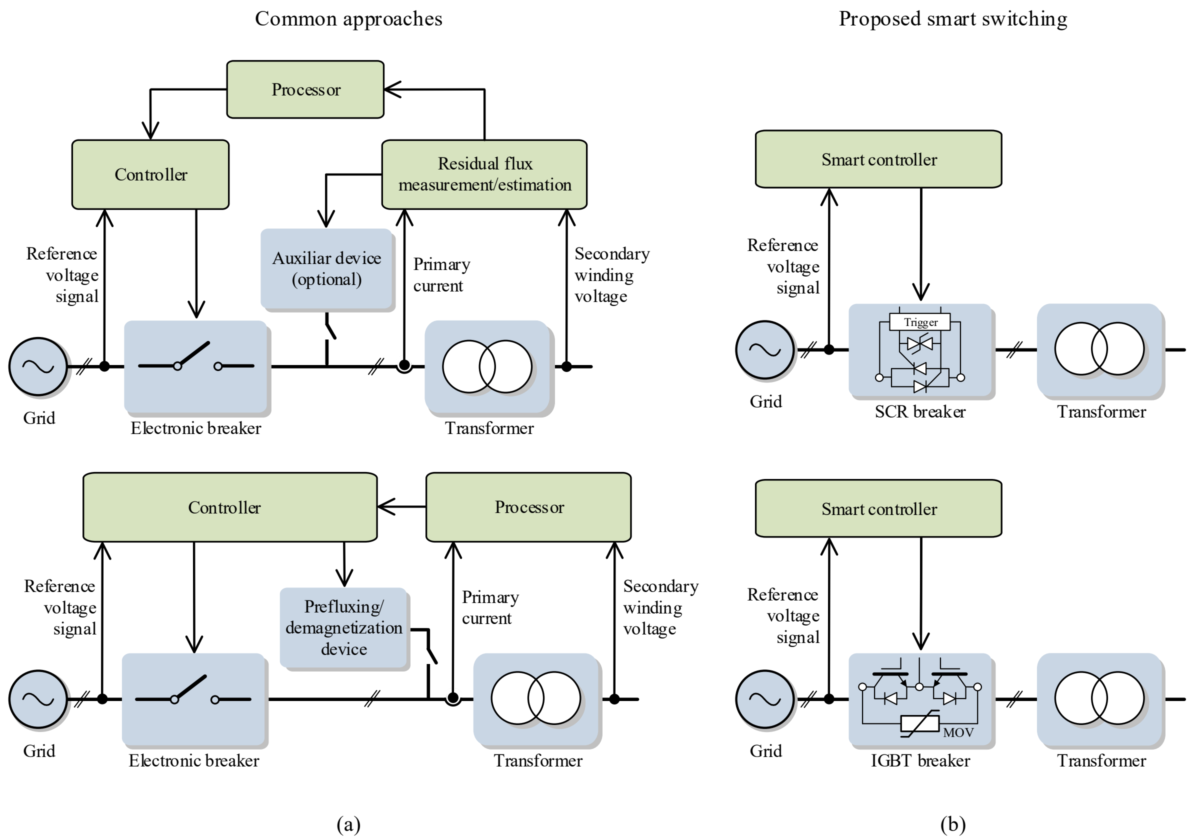

Fig. 3.2. Experimental setups of (a) common approaches for inrush current reduction and (b) the proposed smart switching for inrush current elimination.

This chapter also focuses on:

– A comprehensive analysis of the residual flux.

– The study of the de-energization trajectories.

– The presentation of a simple non-hysteretic model capable of store the residual flux value. This simple model avoids the use of complex hysteresis models like Jiles-Atherton and Preisach.

3.2. Hysteretic transformer model

The only way to characterize the residual flux after de-energization is with a correct iron core model incorporating hysteresis [77], which exhibits a memory-like or storage-like effect. Modeling a transformer iron core is complicated by its nonlinear magnetic characteristics. Saturation, hysteresis and eddy current losses are the main features to be taken into account. Saturation has been discussed previously; therefore, this section focuses on the last two features.

3.2.1. Hysteresis

In ferromagnetic materials, such as the iron used in transformer cores, the relationship between the magnetic field intensity, H, and the magnetization, M, is highly nonlinear and exhibits magnetic hysteresis [78]-[80]. This phenomenon occurs when an external magnetic field is applied to a ferromagnetic material and the magnetic dipoles align with it in the same direction, generating their own magnetic field. Moreover, M is not only a nonlinear function of H; it also depends on its previous states, that is, on its history. Each H value is associated with an infinite number of possible magnetizations; therefore, M is a multi-valued function of H, resulting into an M–H loop. After the magnetic field is removed, a portion of the alignment persists, effectively magnetizing the material. Hysteresis allows ferromagnetic materials to retain a magnetized state, known as remanence (M_R), when the applied magnetic field is no longer present. Once magnetized, the material will remain magnetized indefinitely, requiring an opposing magnetic field to demagnetize it.

The general relation among the flux density, B, M, and H, is

$$B = \mu_0 \left(H + M \right) \tag{3.1}$$

where μ_0 is the vacuum magnetic permeability. Then, an M–H loop can be represented also as a B–H loop, which is a more usual representation. This loop is commonly known as hysteresis loop.

The modeling of hysteresis can be approached at different scales of length. The basic physical principles of hysteresis can be treated at either an atomic or a macroscopic (ultra-millimeter) scale. For modeling a transformer iron-core, it is sufficient with a macroscopic scale. In macroscopic models, the magnetization is in general modeled as the global result of contributions from several magnetic domains. These models are not strictly based on a comprehensive analysis on the nature of the physical system; instead, they are primarily formulated to represent input-output relationships that are experimentally observed [81]. The most commonly used macroscopic hysteresis models are the Jiles-Atherton [82]-[83] and Preisach [84] models. Additionally, there exist other less commonly employed but more intricate models, such as Stoner-Wohlfarth [85] and Globus [86] models. In [87], it can be found a comprehensive comparison between these four hysteresis models, their advantages and their disadvantages. Many of the recent developed hysteresis models are actually extensions or combinations of them [88]-[101]. For instance, [101] discusses certain non-physical solutions that the original Jiles-Atherton model can produce, such as the non-closure of minor loops. Some modifications to the Jiles-Atherton model are also proposed to address these issues. An accurate hysteresis model must be capable of representing all the M–H loops and curves illustrated in Fig. 3.3 [87]. The slope of these curves is equivalent to the incremental magnetic susceptibility [102], χ_m.

When the iron-core is demagnetized, meaning that $H = 0$ and $M = 0$, and H is increased, the M–H curve follows what is known as the initial magnetization curve, whose initial susceptibility is different to zero. At first, this curve increases rapidly with the field and then approaches the magnetic saturation, M_s. When the magnetic field is reduced monotonically, the magnetization follows a different trajectory, known as the negative branch. At $H = 0$, the magnetization retains a non-zero remanence M_R. The remanence is the responsible of the residual flux in a transformer core after a de-energization. If the magnetic field continues to decrease, it eventually reaches negative saturation and then gradually increases back to positive saturation, following a new path called the positive branch. Then, a closed loop will be created, known as major loop [103], illustrated in Fig. 3.3. This loop represents the largest possible loop in which the endpoints reach saturation. Any other closed loop is referred to as a minor loop, with a further distinction between symmetric and asymmetric minor loops [104].

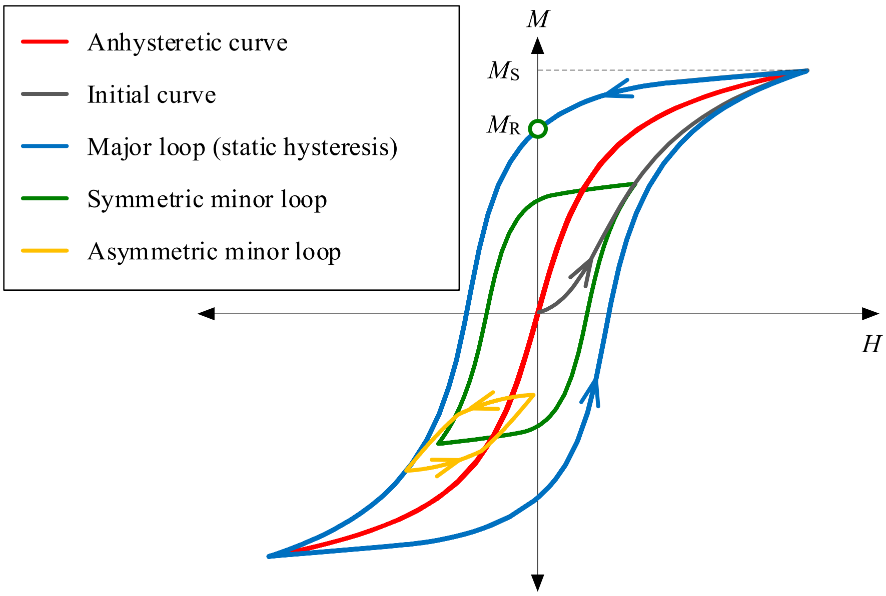

Fig. 3.3. Different types of hysteresis loops.

Symmetric minor loops are the closed loops within the major loop and centered with respect to the origin. They result from a cyclic H of lower magnitude than that which led to the major loop [105]. The shape of the symmetric minor loops is similar to the shape of the major loop. A set of different symmetric minor loops is depicted in Fig. 3.4. The tips of these loops are connected by the initial curve [87].

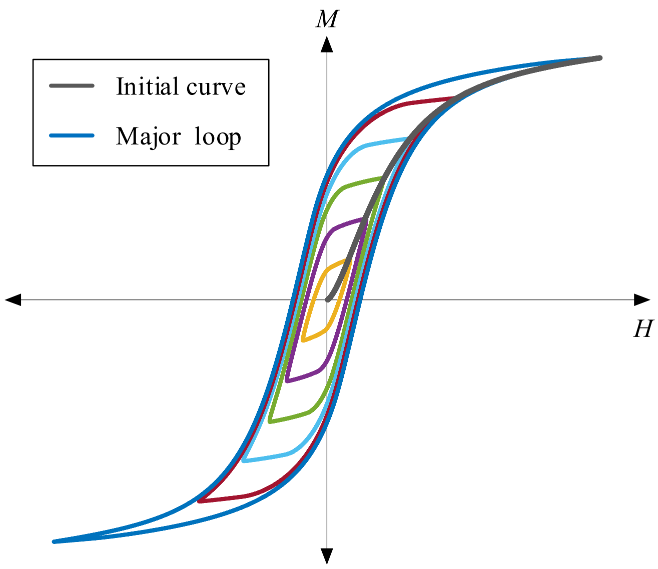

Fig. 3.4. Set of different symmetric minor loops.

Other important inner trajectories (inside the major loop) are the first-order reversal curves (FORCs), which determine the behavior of the asymmetric minor loops [104]. Each FORC starts on a branch of the major loop and ends at its opposite tip, as illustrated in Fig. 3.5. They are generated when, during the tracing of the descending or the ascending branch of the major loop, the direction of the magnetic field *H* is abruptly reversed. The shape of the reversal curve is uniquely determined by the last reversal point (red circles in Fig. 3.5). Conversely, if *H* is reversed once more before reaching the opposite tip of the major loop, an asymmetric minor loop is generated [106]. In general, asymmetric minor loops often result from partial demagnetization, changes in operating conditions, or transient states.

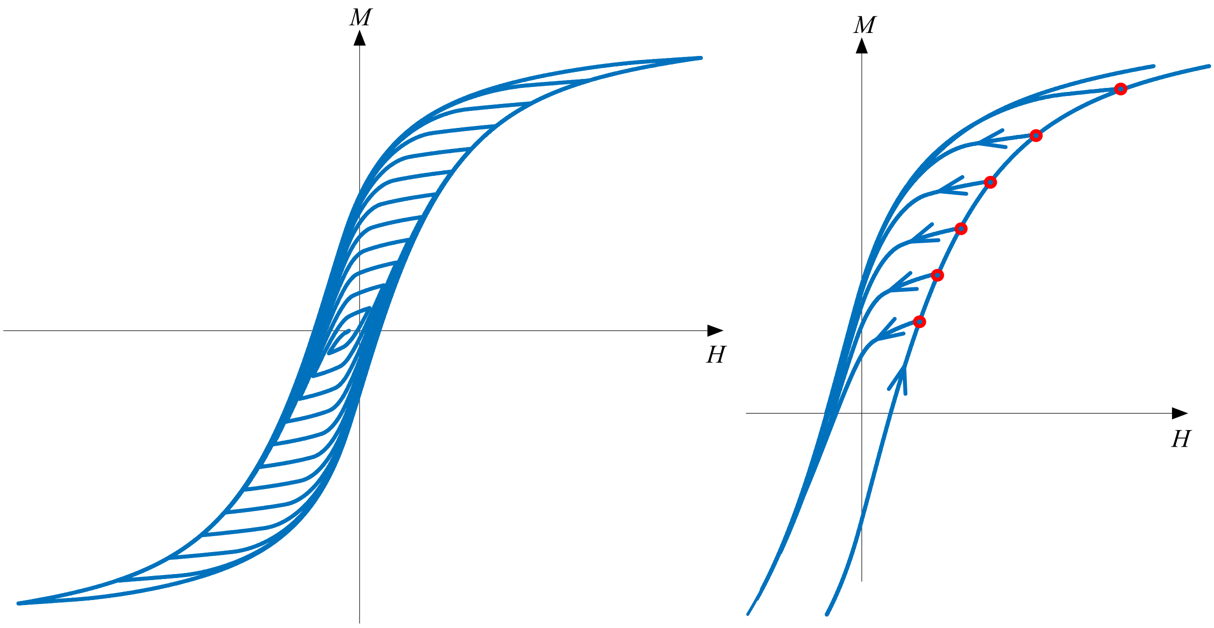

Fig. 3.5. Illustrative first-order reversal curves.

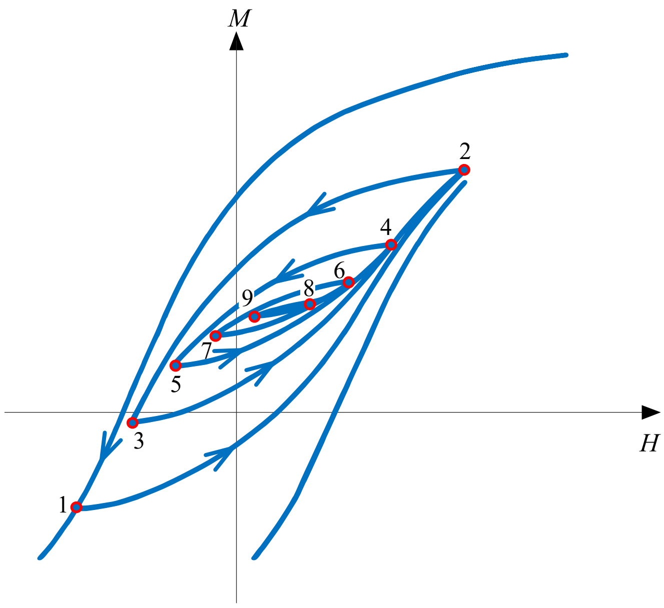

Fig. 3.6. Reversal curves and asymmetric minor loops.

Fig. 3.6 shows a set of reversal curves and asymmetric minor loops. They are obtained when, during the major loop tracing, the magnetic field *H* is then cycled at decreasing levels, beginning at point 1 an ending with a final reversal at point 9, followed by a positive increase to return to the major loop

[107]. Due to symmetry, each reversal curve tends to return to the reversal point immediately preceding the last [108]. For example, after point 2 the curve tends to return to point 1, and after point 5 the curve tends to return to point 4. It must be noted that the generated minor loops converge to a non-zero magnetization (near to point 9), which depends on the location of the first reversal at point 1. Thus, the symmetry of minor loops is not necessarily aligned with that of the major loop. Nevertheless, the incremental magnetic susceptibility following a reversal appears to have a slope similar to that in the saturated region of the major loop. During the tracing of a FORC, the curve can return to the major loop, or if H is reversed once again, a second-order reversal curve is described (for example, from point 2 to point 3) [104], [108].

The anhysteretic curve is the M–H relationship that, according to its own definition, would result if there were no hysteresis effect [87]. It is a single-valued function, and is also known as saturation curve. Unlike the other curves, the anhysteretic curve cannot be measured directly. Nonetheless, it can be estimated by several methodologies. This anhysteretic behavior is important because, if the saturation curve is defined, the model only requires the addition of hysteresis and losses.

3.2.2. Iron core losses

According to Bertotti [109], losses in a transformer iron core can be divided into three categories: hysteresis losses, classical eddy-current losses, and excess or anomalous losses. Next, these three categories are explained.

It is known that the flux–current loops of a transformer core are frequency dependent [110]. However, the mentioned Jiles-Atherton and Preisach hysteresis models, do not exhibit this frequency dependence [111]. Consequently, these hysteresis models are considered static. The term static indicates that the branches and reversal curves of hysteresis loops are solely determined by the past minimum and maximum values (tips and reversal points) of the input variable (flux in the case of a transformer), while the rate of input variation has no influence on the description of branches and reversal curves [103].

Hysteresis losses are caused by the magnetic hysteresis explained above, specifically due to cyclic magnetization and demagnetization of the iron core as current flows in both directions, representing an energy loss [112]. The energy lost depends on the coercive force needed to reverse the magnetic dipoles in the material, which is directly proportional to the area enclosed by the static hysteresis loop [113]. This area can be obtained through integration and is proportional to the square of the maximum flux density, B_{MAX}^2. Therefore, the hysteresis power losses per period in a transformer core are directly proportional to the product of frequency f and B_{MAX}^2 [114].

The flux–current loops in the transformers also depend due on the eddy currents in the core laminations. The eddy current losses can be estimated by applying the Faraday's law to a given geometry, assuming that the magnetic field penetrates uniformly throughout the iron core. These power losses per unit of volume and per period are proportional to the product of the square of the frequency, f^2, and B_{MAX}^2 [115]-[116]. However, the theoretical calculation of eddy-current loss does not agree with measurements of the frequency-dependent losses. The discrepancy has been called excess or anomalous losses [117].

To reproduce the experimentally observed nonlinear frequency dependence of energy losses in transformer iron-cores, composite models based on the losses separation have proven to be valuable for transformer transient simulation [36], [43], [118]-[120].

The total energy losses (hysteresis, eddy, and excess losses) per unit of volume and per period, W_T, are proportional to the involved area by the B–H loop as follows [121]:

$$W_T = \frac{P_T}{f} = \oint H \mathrm{d}B \tag{3.2}$$

where P_T are the total power losses per unit of volume and per period. Then, the total energy losses per unit of volume and per period are given by

$$W_T = W_H + W_{EDDY} + W_{EXCESS} \tag{3.3}$$

where W_H, W_{EDDY} and W_{EXCESS} represent the hysteresis energy losses, the classical eddy-current energy losses, and the excess energy losses, respectively. The hysteresis losses are considered static, while the eddy-current and excess losses are frequency (f) dependent ($W_{EDDY} \propto f$, $W_{EXCESS} \propto f^{1/2}$), so they are referred to as dynamic losses [122]. According to equation (3.2), the losses in terms of power, are frequency dependent as follows: $P_H \propto f$, $P_{EDDY} \propto f^2$ and $P_{EXCESS} \propto f^{3/2}$.

For low frequencies and thin core laminations, H and B can be assumed uniform over the whole cross-section of a lamination. Under these conditions, the losses separation can be translated into their respective magnetic field components, $H_H(t)$, $H_{EDDY}(t)$, and $H_{EXCESS}(t)$, as follows [123]:

$$\begin{aligned} H(t) &= H_H(B) + H_{EDDY}(\mathrm{d}B/\mathrm{d}t) + H_{EXCESS}(B, \mathrm{d}B/\mathrm{d}t) \\ &= H_H(B) + k_{EDDY}\frac{\mathrm{d}B}{\mathrm{d}t} + G(B)\left|\frac{\mathrm{d}B}{\mathrm{d}t}\right|^{0.5} \operatorname{sign}\left(\frac{\mathrm{d}B}{\mathrm{d}t}\right) \end{aligned} \tag{3.4}$$

where k_{EDDY} is a constant parameter which depends on physical aspects of the iron-core, and $G(B)$ is a nonlinear function. In [124]-[128] some functions with different accuracy are proposed. Then, by applying the Ampère's law, the current consumed by a single-phase transformer at no-load conditions can be considered as

$$i(t) = l_e \frac{H(t)}{N} = i_H(t) + i_{EDDY}(t) + i_{EXCESS}(t) \tag{3.5}$$

where N is the number of winding turns through which the current i flows, l_e [m] is the effective length of the iron-core, and i_H(t), i_{EDDY}(t) and $i_{EXCESS}(t)$ are the static hysteresis current, the eddy current, and the excess current, respectively.

The flux ϕ and the uniform B in the transformer iron-core are related, according to Faraday's law, by

$$\phi(t) = B(t) \cdot S_e \tag{3.6}$$

where S_e [m^2] is the cross-sectional area of the core. Then, (3.5) can be rewritten as [123],[125]

$$\begin{aligned} i(t) &= i_{\mathrm{H}}(t) + i_{\mathrm{EDDY}}(t) + i_{\mathrm{EXCESS}}(t) = i_{\mathrm{H}}(\phi) + k_{\mathrm{EDDY}}\frac{\mathrm{d}\phi}{\mathrm{d}t} + G(\phi)\left|\frac{\mathrm{d}\phi}{\mathrm{d}t}\right|^{0.5}\mathrm{sign}\left(\frac{\mathrm{d}\phi}{\mathrm{d}t}\right) \\ &= i_{\mathrm{H}}(\phi) + k_{\mathrm{EDDY}}e + G(\phi)|e|^{0.5}\,\mathrm{sign}(e) \end{aligned} \tag{3.7}$$

where e is the induced voltage at the winding by the flux ϕ.

The previous composite models, describe the frequency dependence by individually modeling each loss component. By combining a static hysteresis model with two dynamic components (eddy-current and excess) to build a dynamic hysteresis model, this type of iron-core models would have the ability to characterize the frequency dependency. The composite models avoid the need to modify the equations of classic static hysteresis models to generalize them into dynamic models (referred to as mathematical dynamic models [129]-[131]).

The three-component dynamic hysteresis models typically include a static hysteresis model implemented as a hysteretic inductor, along with two parallel resistors, one linear and one nonlinear, to replicate classical eddy-current and excess losses, respectively [132]. Fig. 3.7 illustrates the typical shapes of the ϕ–i loops (ϕ–i_{H}, ϕ–i_{EDDY}, and ϕ–i_{EXCESS}) of each component, as well as the dynamic hysteresis loop resulting from the superposition of the static hysteresis loop and the other two loops. The typical shape of the eddy-current loop is a symmetrical ellipse centered at origin. The shape of the excess losses loop differs, exhibiting a wider width near the knee point. Increasing the frequency leads to higher losses per cycle, resulting in a wider dynamic hysteresis loop.

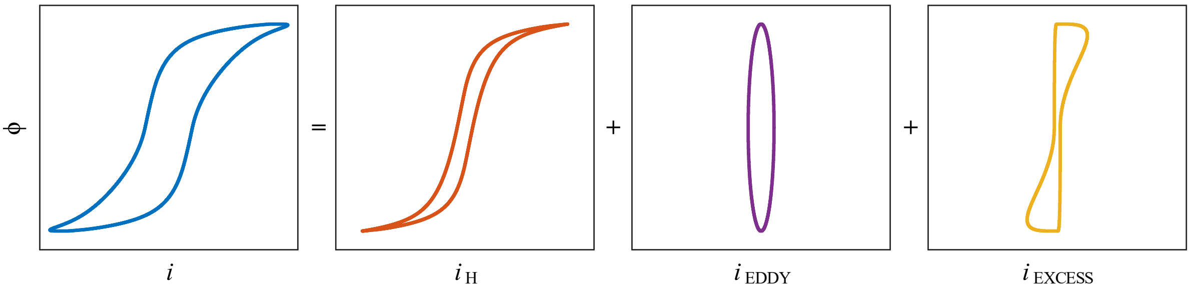

Fig. 3.7. Typical dynamic ϕ–i loop composed by three components: static hysteresis loop plus two dynamic loops.

Fig. 3.8 depicts some composite approaches for the equivalent electric circuit of an iron core. The first circuit in Fig. 3.8(a) is composed by a nonlinear inductor without hysteresis and a parallel linear resistor, which represents all losses grouped into a single component. The inductor represents the anhysteretic magnetization curve (saturation curve) used to characterize the nonlinearity of the iron core. A linear resistor can adequately represent the average losses per period only for a specific operating frequency, but does not accurately reproduce the current waveforms and the hysteresis loops. Moreover, this approach is not suitable for simulating the transformer de-energization and the residual flux.

In the circuit depicted in Fig. 3.8(b), the losses are separated and modeled by three parallel resistors, each one for each type of losses. The static hysteresis loop is determined by a nonhysteretic inductor, and the superposition of the loop generated from a resistor, such that $i_{\mathrm{H}} = i_{\mathrm{m}} + i_{\mathrm{HL}}$, which could be nonlinear for better accuracy. The resistor for excess losses modeling is nonlinear. This second model leads to an improved reproduction of the current waveforms and the hysteresis loops for different operating frequencies, but it is not suitable for simulating transformer de-energization and residual flux since the nonlinear inductor is non-hysteretic.

The last two circuits, depicted in Fig. 3.8(c) and Fig. 3.8(d), are composed by a hysteretic inductor which allows both circuits to adequately simulate the transformer de-energization and the residual flux. Moreover, with the inclusion of nonlinear elements to model the excess losses, they are capable of accurately reproducing the current waveforms and the hysteresis loops for different operating frequencies, up to about 3 kHz [133]. Higher-order losses separation approaches and models suitable for higher frequencies are proposed in [134]-[138]. Formulations for calculating iron core losses during non-sinusoidal excitation are proposed in [139]-[141].

Fig. 3.9(a) illustrates the static hysteresis loops (ϕ–i_H), for different flux levels, of the circuit in Fig. 3.8(b). As the inductor in Fig. 3.8(b) is nonlinear and non-hysteretic, the model is unable to accurately reproduce the initial curve or the minor loops. The static hysteresis loops (major and symmetric minor loops) are the result of an anhysteretic curve plus a width from a resistor. As a result, the tips of all symmetric minor loops are part of the saturation curve. Fig. 3.9(b) illustrates the static hysteresis loops (ϕ–i_H) for the circuits in Fig. 3.8(c) and Fig. 3.8(d) with a hysteretic inductor. In this case, the tips of the minor loops are part of the initial curve, which is different from the saturation curve.

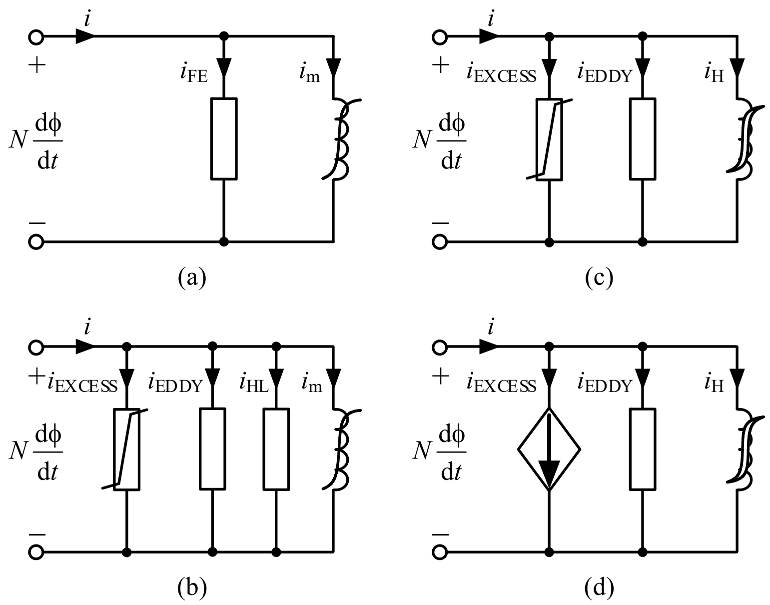

Fig. 3.8. Iron-core composite electric equivalent circuits: (a) classical non-hysteretic model, (b) non-hysteretic composite model, (c) hysteretic composite model, and (c) alternative hysteretic composite model.

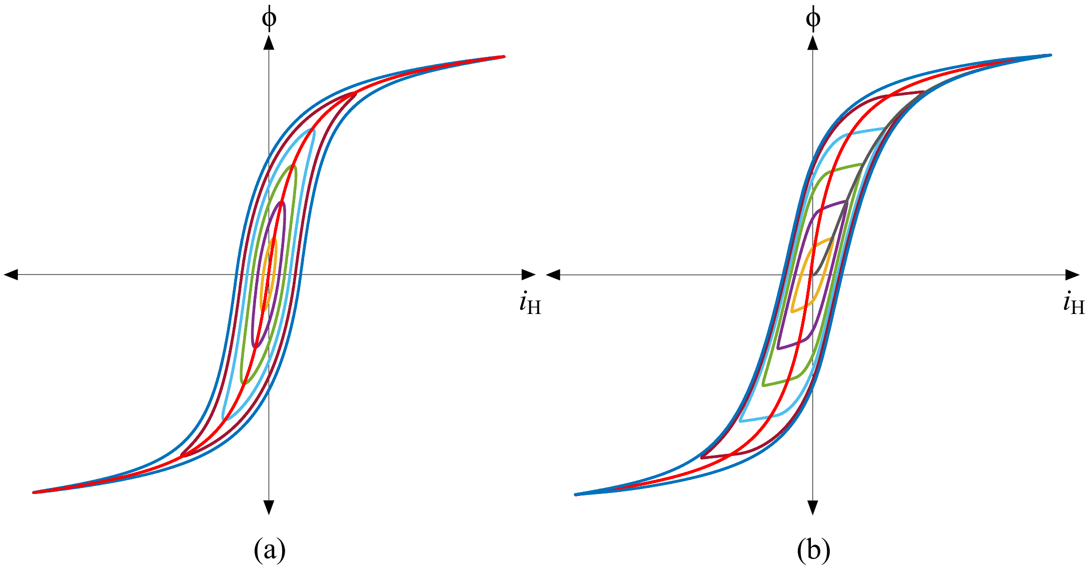

Fig. 3.9. Comparison between static hysteresis loops from (a) the model with a non-hysteretic inductor of Fig. 3.8(b), and (b) the model with a static hysteretic inductor of Fig. 3.8(c) and Fig. 3.8(d).

3.2.3. Hysteretic core models for residual flux prediction

As the classical eddy losses and the excess losses do not influence the residual flux, both components are grouped together as eddy losses from this point onward. Then, the hysteretic core model in this chapter will consists of only hysteresis (subindex H) and eddy (subindex E) components, and the no-load current i_1 is the sum of i_H and i_E, as shown in Fig. 3.10. Commonly, the maximum residual flux value, ϕ_{RM}, is incorrectly marked in many textbooks as the crossings of the dynamic hysteresis loop with the vertical axis, that is, the corresponding flux value when i is null (red point ϕ_0 in Fig. 3.10). This error is usually due to a lack of understanding of the different losses in a core and a confusion between the static and the dynamic hysteresis loops. The residual flux, ϕ_R, only depends on the static hysteresis loop, which cannot be directly measured with a classical no-load test. Therefore, the correct ϕ_{RM} value corresponds to the green point in Fig. 3.10, that is, the corresponding flux value when i_H is null. The green zone in Fig. 3.10 represents the range of the residual flux, which will be explained in next Section 3.3.

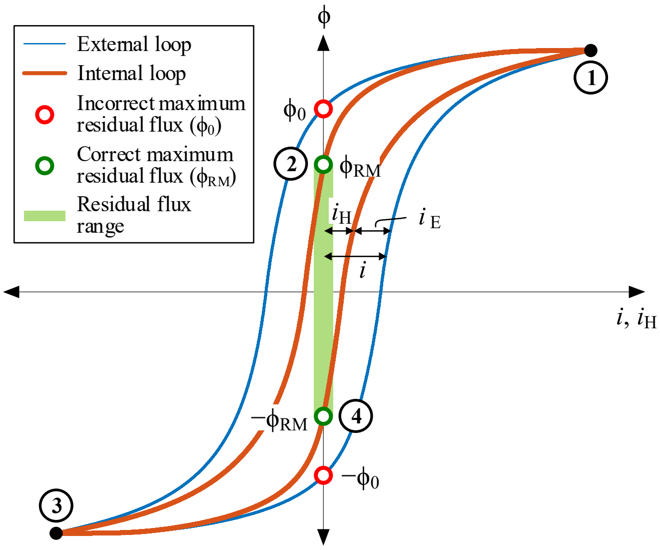

Fig. 3.10. Static loop (internal loop), dynamic loop (external loop) and residual flux range.

Fig. 3.11 depicts four distinct unloaded single-phase transformer models, all sharing the same electrical circuit but featuring different magnetic circuits for different types of core modeling. These differences in core modeling through the magnetic circuit result in different predictions of the residual flux.

The electric circuit includes the winding resistances, R_1 and R_2, the constant leakage inductances, L_{d1} and L_{d2}, and the induced primary voltage, due to the core magnetic flux, ϕ.

The residual flux is physically retained in the iron-core when the transformer is disconnected. Therefore, the modeling must also include a storage function to trap such flux. The magnetic inductance (also called transferance) $\mathfrak{L}_E$ represents the eddy losses, while $\mathfrak{L}_H$ (only present in Type II and Type IV) represents the internal loop hysteresis losses. Note that the hysteresis losses in Type I and Type III are embedded into a hysteretic reluctance $\mathfrak{R}$. The magnetic inductances $\mathfrak{L}_E$ and $\mathfrak{L}_H$ could be placed into the electric circuit as parallel resistances by applying the duality principle [142], as made in most research papers.

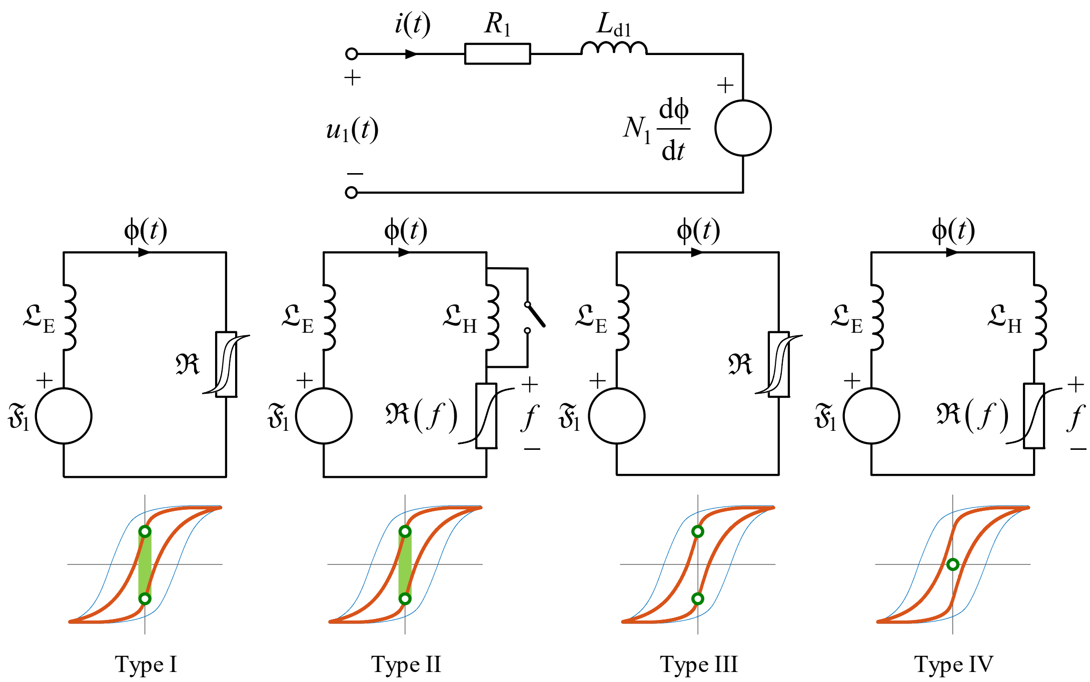

Fig. 3.11. Electric (top) and magnetic circuits (bottom) of an unloaded single-phase transformer, and residual flux ranges for the four models.

The main features of these four types of models are:

- Type I. Reluctance $\mathfrak{R}$ is hysteretic and capable of reproducing major and minor loops, both symmetric and asymmetric ones. Jiles-Atherton and Preisach models, in their classic static versions, are the best examples of this type. This type of models can accurately predict all the residual flux values inside the allowable range.

- Type II. Non-hysteretic reluctance $\mathfrak{R}$ is capable to reproduce major loops when combined with $\mathfrak{L}_H$. The set composed by $\mathfrak{L}_H$ and the magnetic switch provides the memory and storing features to this model. If the magnetic switch is closed due to a transformer de-energization event, the current through $\mathfrak{L}_H$ (representing the residual flux) will continue circulating indefinitely. The magnetic switch is closed when next conditions are met simultaneously: current i_1 is null, and magnetic potential at $\mathfrak{L}_H$ is null. This model predicts the residual flux values inside the allowable range with less accuracy than Type I models.

- Type III. Hysteretic reluctance $\mathfrak{R}$ can only reproduce a unique and rigid major loop [143]. This model only leads to the maximum or minimum residual flux values.

- Type IV. Non-hysteretic reluctance $\mathfrak{R}$. When combined with $\mathfrak{L}_H$, it can reproduce major loops as those in Fig. 3.9(a). This model always leads to a null residual flux value.

Type II model is an original proposal developed expressly for this thesis.

Only Type I (with Jiles-Atherton and Preisach) and Type II models are used in this chapter. Jiles-Atherton and Preisach hysteresis models are detailed in Appendix B.

3.3. De-energization trajectories and range of the residual flux

This section describes the trajectories during the de-energization transient and the resulting range of possible residual fluxes. In the authors' knowledge these trajectories are not sufficiently well explained in the literature, mainly when the residual flux value range is of concern.

Fig. 3.12 illustrates two representative de-energization transient trajectories. Let us now to consider that the circuit breaker aperture starts at the instant marked with a blue circle in Fig. 3.12(a). The flux trajectory follows the major loop illustrated in the figure until the residual flux reaches the value ϕ_{RM}. Note that only the internal hysteresis loop has been taken into account, because the eddy losses do not influence the achieved residual flux.

In the example of Fig. 3.12(b), the circuit breaker aperture initiates at another different instant. In this case, the flux follows the trajectory of an asymmetric minor loop until the residual flux reaches a value ϕ_R, which is smaller than ϕ_{RM}.

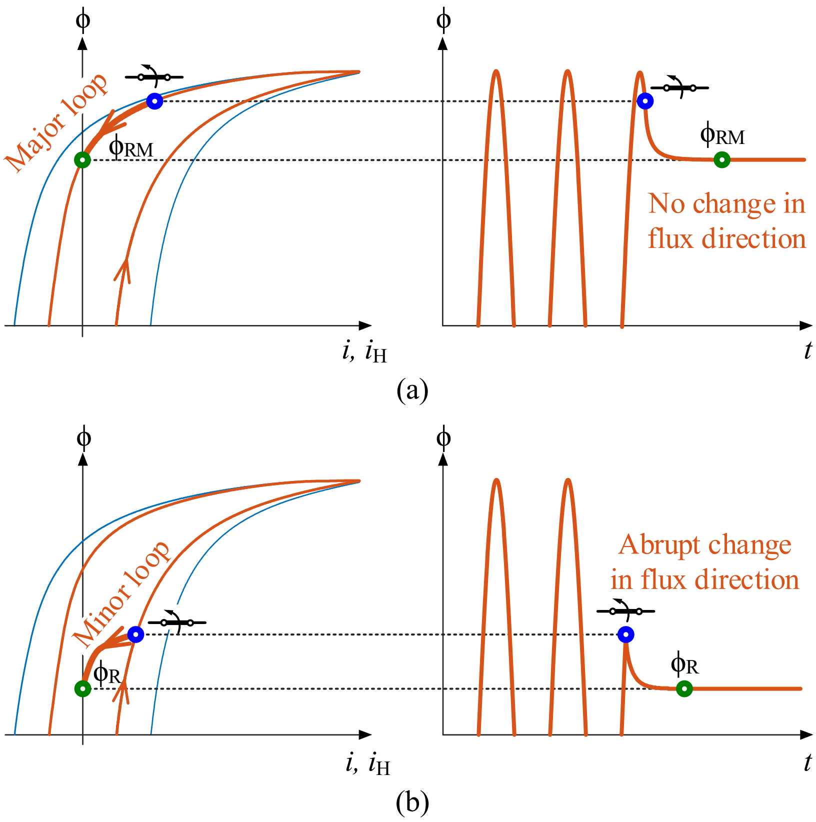

Fig. 3.12. Two representative de-energization transient trajectories and their respective flux waveforms.

The above two examples are representative of all de-energization transients in the hysteresis loop:

- Transients that follow the major loop because the breaker aperture does not provoke a change in flux direction.
- Transients that follow an asymmetric minor loop because the breaker aperture provokes an abrupt change in flux direction.

Based on this, four different regions of the hysteresis loop can be highlighted, which are illustrated in Fig. 3.10. Each zone leads to different well defined residual flux values, because the transient in the hysteresis loop depends only on the instant of breaker aperture initiation. This instant of aperture initiation is best characterized by the corresponding supply voltage point-on-wave (with reference to the maximum of the voltage), and will be called from now on as de-energization point-on-wave, α_D.

If the disconnection starts at a point-on-wave, α_D, between 90° and α_{RM} (between points 1 and 2 in Fig. 3.10), the residual flux will be always ϕ_{RM}. Symmetrically, the residual flux will be always $-\phi_{RM}$ if the switching point-on-wave is between 270° and 270°+α_{RM} (between points 3 and 4). The value of α_{RM} varies for each transformer, and depends on core parameters. Its value can be calculated from some no-load tests, as is detailed in next section.

The possible residual flux values in the remaining two zones are as follows. If α_D is between α_{RM} and 270° (between points 2 and 3), the residual flux can reach a value between ϕ_{RM} and $-\phi_{RM}$ (green zone in Fig. 3.10). However, there is no ambiguity as the specific value will be uniquely defined by the specific minor loop trajectory followed, which will depend only on α_D. The opposite happens for the region between 270°+α_{RM} and 90° (between points 4 and 1), the residual flux values can be within the range $-\phi_{RM}$ to ϕ_{RM}. This dependence on the de-energization point-on-wave is shown in Table 3.1.

Table 3.1. Possible residual flux values.

Points on Fig. 3.10	De-energization point-on-wave α_D			Residual flux range ϕ_R	Trajectory
1 to 2	90°	to	α_{RM}	ϕ_{RM}	Major loop
2 to 3	α_{RM}	to	270°	ϕ_{RM} to $-\phi_{RM}$	Minor loop
3 to 4	270°	to	α_{RM} + 270°	$-\phi_{RM}$	Major loop
4 to 1	270° + α_{RM}	to	90°	$-\phi_{RM}$ to ϕ_{RM}	Minor loop

Fig. 3.13 illustrates two de-energization trajectories at two different circuit breaker interruption speeds. It can be seen that the interruption speed only influences the de-energization trajectory of the external loop and the decaying time of i_1. In contrast, the de-energization trajectory of the internal loop and the decaying time of i_H are uniquely determined by the hysteretic reluctance (e.g., that of Type I model in Fig. 3.11). Thus, the reached residual flux is the same for both breaker speeds. As the residual flux only depends on i_H, the interruption speed and the eddy losses have no influence on the residual flux ϕ_R. This is also stated in [19] as follows: "the residual flux pattern is determined by static characteristics of the core". In summary, it could be said that once the current begins to be interrupted and the flux begins to decay, the value of the future residual flux is already predetermined.

The depicted de-energization trajectories in Fig. 3.12 and Fig. 3.13 contrast with the snailed trajectories shown in some publications [77], which are caused by the inclusion of large external shunt capacitances, mainly due to capacitor banks to compensate reactive power and to model the capacitance of the transmission cables. These capacitances are not included in the models used in this work because they are external to the transformer. The parasitic capacitances are internal to the transformer, but they can be neglected in the modeling due to their low values (usually, in the order of some picofarads, even in large transformers). The laboratory measurements shown in the following sections can be reproduced accurately without the inclusion of any parasitic capacitances into the model.

Lastly, Fig. 3.14 shows an example of the residual flux in function of α_D, obtained by simulation of a single-phase transformer T11 (100 kVA, 15 kV/420 V, short-circuit reactance 0.034 pu) with a Type I model (Jiles-Atherton static hysteresis).

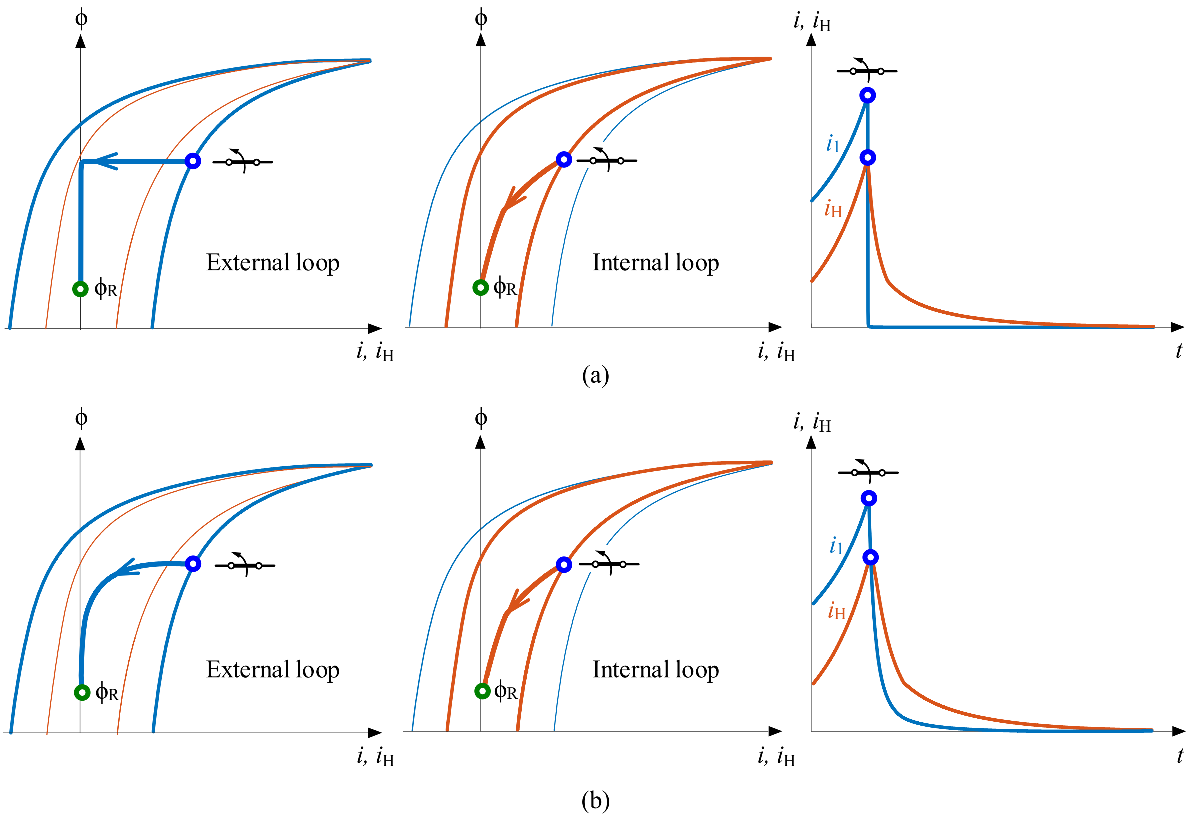

Fig. 3.13. De-energization trajectories and their respective current waveforms (i_1 and i_H) at two different interruption speeds of the circuit breaker.

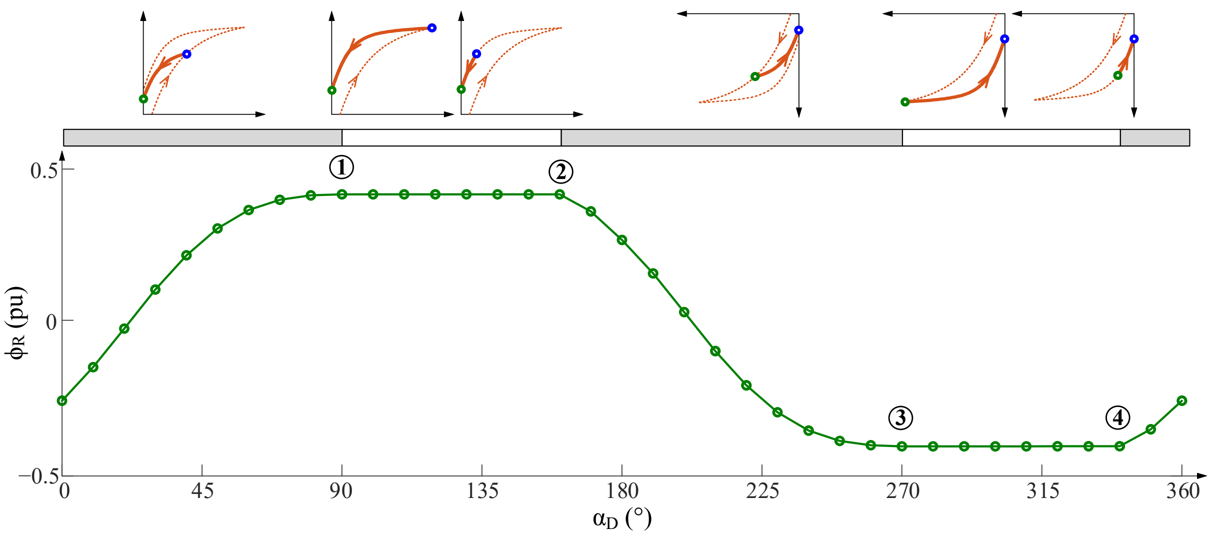

Fig. 3.14. Simulated residual flux values in function of the de-energization point-on-wave (bottom) and its corresponding de-energization trajectories (top) for the transformer T11 (100 kVA).

3.4. Inrush current elimination

3.4.1. Circuit breakers

Current chopping (or simply chopping) in a circuit breaker is the phenomenon in which the current is forcibly interrupted before the natural current zero-crossing. In power systems, the vacuum or SF6 circuit breakers and the unused air blast circuit breakers have chopping capability. In contrast, the old and unused oil circuit breakers do not have chopping capability.

Three different circuit breakers have been used to de-energize and energize the tested transformers:

1. SCR-based breaker: semiconductor breaker composed of two antiparallel silicon-controlled rectifiers. Once the trip signal is sent, the current is not interrupted until its natural zero-crossing, and this happens regardless of the load nature (resistive or inductive). As a consequence, no electric arc is produced. This null chopping capability can be assimilated to that in oil breakers.

2. Electro-mechanical contactor: circuit breaker with chopping capability. If the load is inductive, an electric arc is produced and the interruption will not be instantaneous, but the current will be brought to zero before its natural current zero-crossing. This chopping capability can be assimilated to that in vacuum or SF6 breakers.

3. IGBT-based breaker: semiconductor breaker composed of two IGBTs (each one with an antiparallel diode) connected in series with a common emitter. It has high chopping capability, with a low clearance time at any instant, regardless of the nature of the load. No electric arc is produced. Its high chopping capability cannot be assimilated to any circuit breaker of the power system.

There is a time lapse between the trip signal and the start of the breaker opening (or de-energization point-on-wave). In the SCR breaker, this delay is on the order of hundreds of microseconds. Thus, the trip signal must be sent, at least, around 10° before the desired zero-crossing. In the IGBT breaker, the delay is in the order of microseconds. Then, this delay can be neglected in the IGBT breaker, and trip signal and point-on-wave terms can be used indistinctly. In the contactor, the delay could be on the order of several milliseconds (5 to 10 milliseconds). This delay is undetermined because it depends on the instant at which the trip signal is sent. Thus, the de-energization point-on-wave cannot be controlled in the contactor.

3.4.2. Smart switching to avoid inrush current

At the instant of transformer energization, the flux equals the residual flux. The time evolution of the generated flux depends on the energization point-on-wave. The basic principle to eliminate flux asymmetry and thereby minimize inrush currents is to ensure that the prospective flux at energization matches the residual flux. Thus, the optimal energization point-on-wave occurs when the prospective flux equals the residual flux, as shown in Fig. 3.15. Although there are two optimal energization points-on-wave for each residual flux value, for simplicity, only one of them will be considered.

As the residual flux is only determined by the de-energization trajectory (as shown in previous subsection), which is only influenced by the de-energization point-on-wave, the magnitude of the inrush current can be determined by controlling the de-energization and energization points-on-wave.

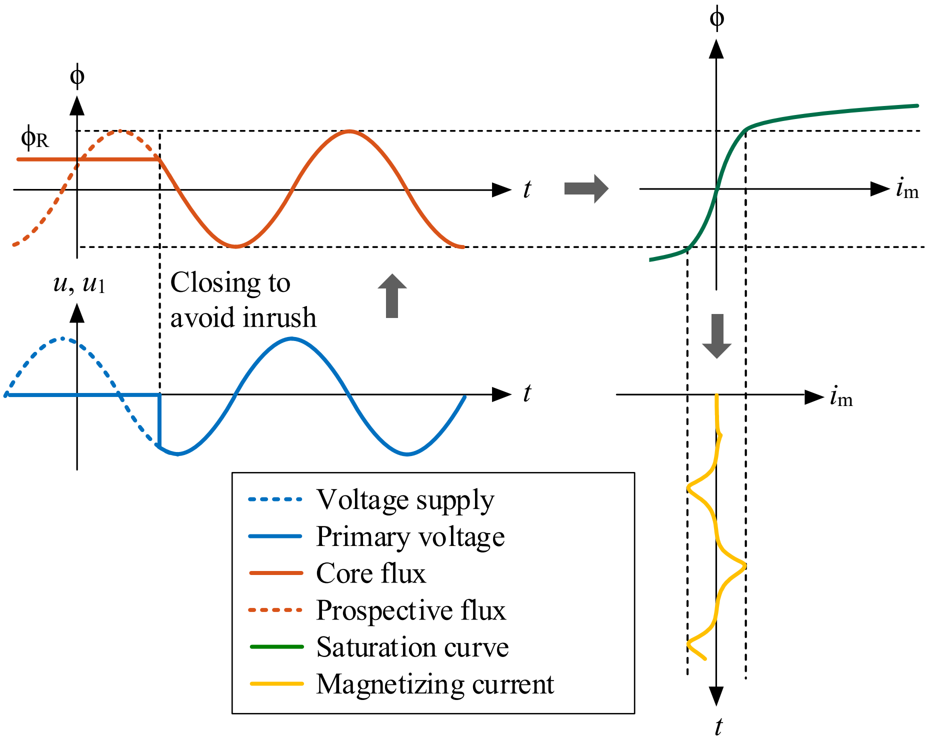

Fig. 3.15. Optimal energization of a single-phase transformer to avoid asymmetrical flux and therefore inrush current.

The proposed strategy comprises two steps:

– Step 1: forcing that the residual flux after de-energization is at its maximum value: ϕ_{RM} or $-\phi_{RM}$. It is proposed to use ϕ_{RM} or $-\phi_{RM}$ because these values can be accurately determined as the crossings of the internal hysteresis loop with the positive vertical axis. For simplicity, only ϕ_{RM} will be considered in this chapter.

– Step 2: energizing the transformer at the optimum energization point-on-wave for ϕ_{RM}.

The next issue is the plotting of the static hysteresis loop ϕ–i_H to accurately estimate ϕ_{RM} from such ϕ–i_H loop. There are two straightforward methods to obtain the ϕ–i_H loop:

– Method 1: this method consists of a no-load test at a very low frequency f (e.g., 2 Hz). To maintain rated flux in the core, the supply voltage must be $U = U_N \cdot (f/f_N)$. This low frequency test provides the quasi static loop as $i_1 \approx i_H$.

– Method 2: this method consists in a no-load test at nominal frequency, and a second test at another frequency. Both tests must be made at rated flux. Then, i_H can be calculated according to

$$i_H = i_1 - i_E = i_1 - \frac{u_1}{R_E} = i_1 - \frac{u_1}{\Delta U / \Delta I} \tag{3.8}$$

where u_1 and i_1 are the primary voltage and current from the nominal frequency test, and $\Delta U / \Delta I$ is the ratio of change of primary voltage and current between both tests.

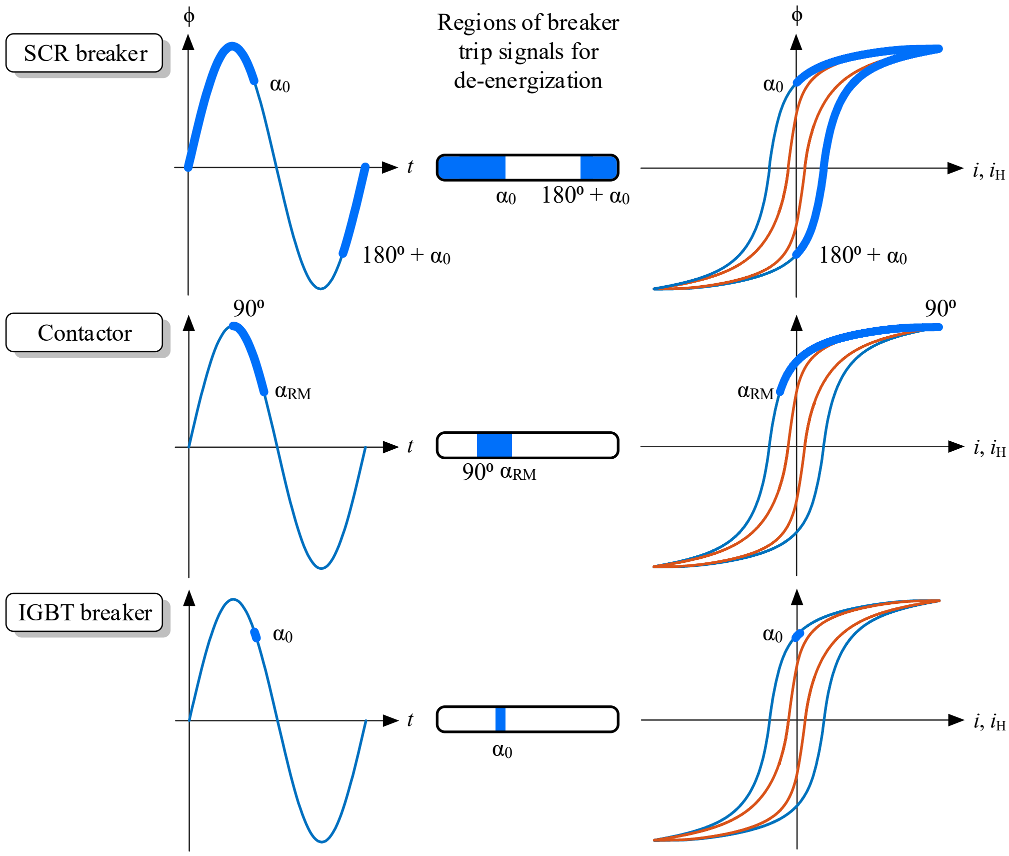

Fig. 3.16. Regions of the hysteresis loop where the trip signal must be sent to each breaker.

To force ϕ_{RM} in the step 1 of the proposed strategy, the de-energization point-on-wave α_D must be between 90° and α_{RM} (Table 3.1). The angle α_{RM} can be obtained as

$$\alpha_{RM} = 180° - \operatorname{asin}\left(\frac{\phi_{RM}}{\phi_{PEAK}}\right) \approx 180° - \operatorname{asin}\left(\frac{\omega\phi_{RM}}{\sqrt{2}U_1}\right) \tag{3.9}$$

The trip signal of the SCR breaker for current interruption in a no-load transformer can be sent at any instant between 90° and α_{RM} because there is only one possible de-energization point-on-wave (see Fig. 3.16). As a consequence, the residual flux ϕ_{RM} will be always achieved.

In the case of the contactor, the current interruption is not abrupt. Thus, no overvoltages are produced and α_D can take any value between 90° and α_{RM} (see Fig. 3.16). In practice, α_D cannot be accurately controlled as previously explained. Anyway, the proposed strategy would be applicable if the contactor were truly controllable. Remember also that the contactor chopping capability can be assimilated to that of vacuum and SF6 power system breakers.

Lastly, the current interruption of a no-load transformer with an IGBT breaker can provoke large overvoltages because the interruption of this breaker is typically abrupt. These overvoltages can damage the transformer isolation. To avoid this, the de-energization trip signal must be sent to the IGBT breaker when the current is near to zero (see Fig. 3.16). This de-energization point-on-wave, α_0, can be calculated as

$$\alpha_0 = 180° - \operatorname{asin}\left(\frac{\phi_0}{\phi_{PEAK}}\right) \approx 180° - \operatorname{asin}\left(\frac{\omega\phi_0}{\sqrt{2}U_1}\right) \tag{3.10}$$

where ϕ_0 is the instantaneous flux when i_1 is null, whose value can be obtained from the plotting of the external loop.

Table 3.2. Smart switching to avoid inrush currents.

Laboratory tested breakers	Equivalent power system breakers	Trip signal for de-energization	De-energization point-on-wave, α_D	Residual flux	Energization point-on-wave, α_E
SCR breaker	Oil breakers	$180° + \alpha_0$ to α_0	α_0	ϕ_{RM}	α_{RM}
Contactor	Vacuum and SF6 breakers	$90°$ to α_{RM}*	$90°$ to α_{RM}	ϕ_{RM}	α_{RM}
IGBT breaker	-	α_0	α_0	ϕ_{RM}	α_{RM}

*Neglecting the delay between the trip signal and α_D.

On the other hand, neglecting the primary winding resistance and the primary leakage inductance, the flux after energization is given by

$$\phi = \phi_R + \frac{\sqrt{2}U_1}{\omega}\left[\sin(\omega t) - \sin(\alpha_E)\right] \tag{3.11}$$

which illustrates that the energization transient flux is affected by the energization point-on wave, α_E, and the residual flux ϕ_R. To avoid the subsequent inrush current, the offset in (3.11) must be null. Then, if ϕ_R is equal to ϕ_{RM}, the optimal α_E is

$$\alpha_E = 180° - \operatorname{asin}\left(\frac{\phi_{RM}}{\phi_{PEAK}}\right) = \alpha_{RM} \tag{3.12}$$

The whole smart switching strategy with different types of breakers to avoid inrush current in single-phase transformers is illustrated in Fig. 3.17 and summarized in Table 3.2.

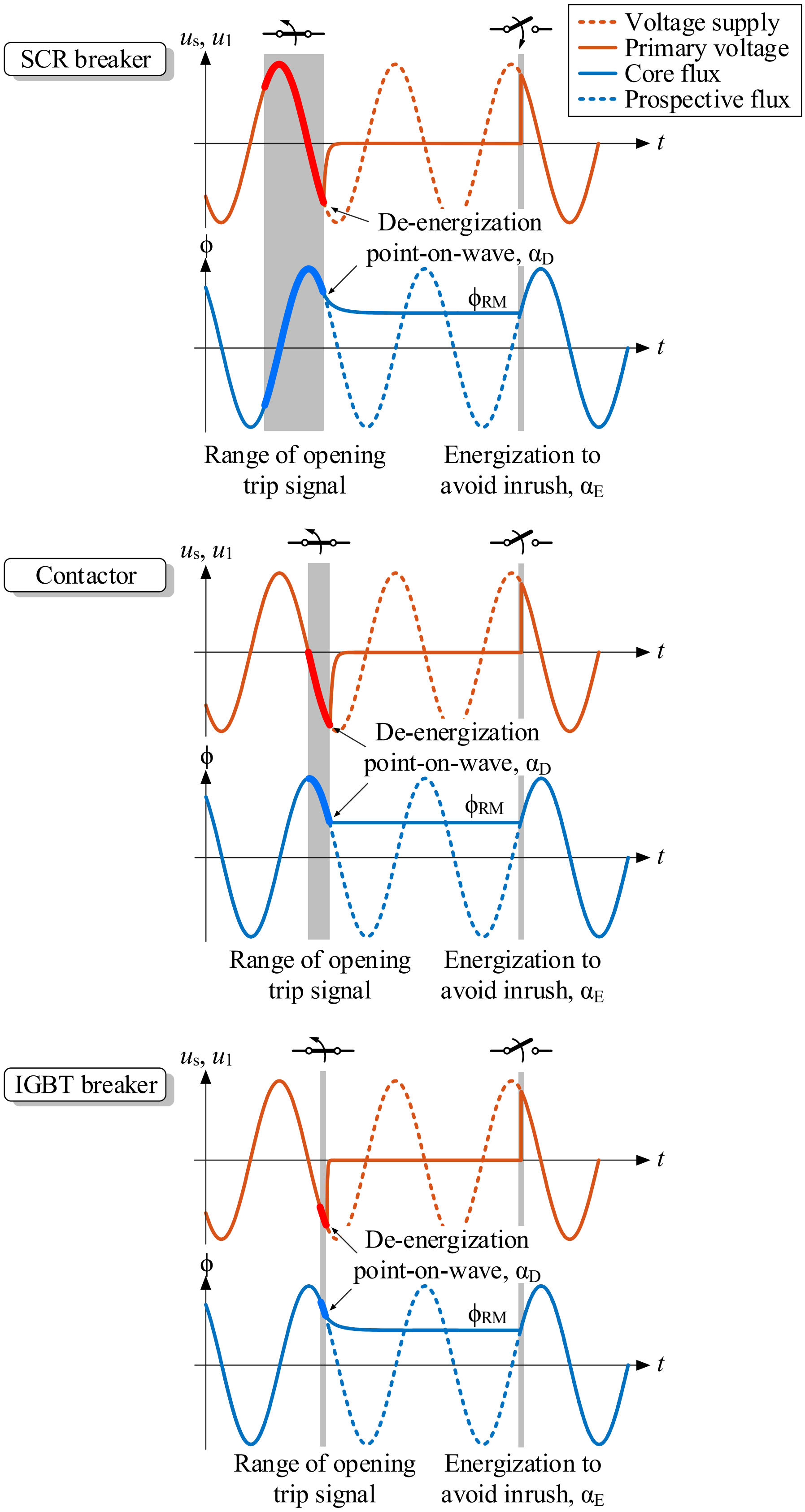

Fig. 3.17. De-energization and energization strategy to avoid inrush current. Opening and closing regions for each breaker.

Finally, if the de-energization cannot be controlled, a compromise solution must be adopted: the recommendation is to energize at a point-on-wave of 0° (when the voltage is at its positive peak). This energization point-on-wave is optimum to avoid inrush current when ϕ_R is null. Thus, the flux peak will be equal or lower than $\phi_{PEAK} = \sqrt{2}\cdot\phi_N + \phi_R$.

3.5. Simulations and experimental results

3.5.1. Residual flux

The analysis of the residual flux and its de-energization trajectories was supported by several experiments conducted on two different single-phase transformers of 320 VA, 120/72 V, short-circuit reactances 0.046 pu and 0.07 pu, respectively, which are denoted as T1 and T3. The laboratory setup for these experiments is depicted in Fig. 3.18.

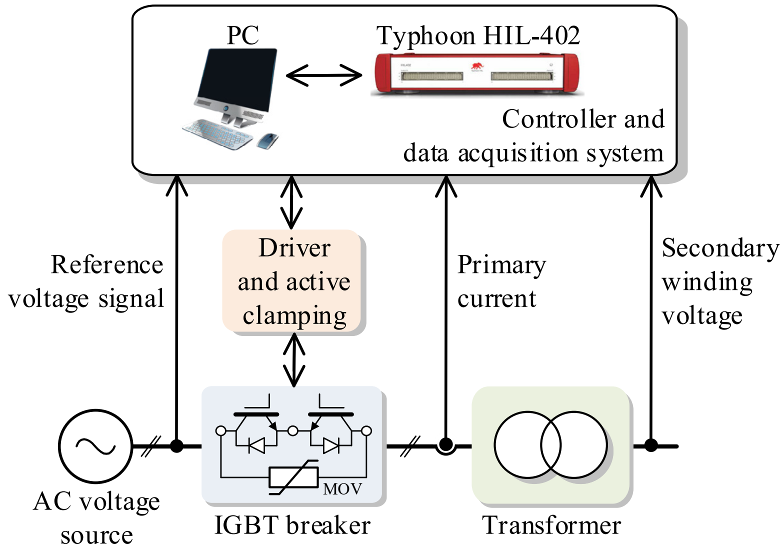

Fig. 3.18. Experimental setup with the IGBT breaker.

Each experiment consists of two stages: (a) transformer de-energization at a desired point-on-wave and (b) transformer energization at upward zero-crossing of the voltage, which results in the most severe positive inrush current when ϕ_R is null. As the residual flux cannot be measured directly, it has been estimated offline using the resultant inrush, as proposed in [144]. The IGBT breaker has been used in both commutations because the absence of electric arc allows a clearer comprehension of the residual flux phenomenon. In each experiment, α_D is varied from 0° to 360° in steps of 10°. The subsequent energizations have been achieved at a constant α_E = 270°, in order to validate the residual flux value. The closing and aperture of the circuit breaker has been controlled with a Typhoon HIL-402, which is a powerful platform for prototyping and real time control. Typhoon HIL-402 has also used for the measured signals acquisition. The obtained results are summarized in Table 3.3 and Fig. 3.19. It can be verified that all results are consistent with the residual flux analysis discussed in Subsection 3.3.

The maximum residual flux values obtained during experiments are ϕ_{RM} = 0.326 pu for T1 and ϕ_{RM} = 0.344 pu for T2. These values fall within the typical range established for small transformers in [77]. The results corroborate that the residual flux only depends on α_D as illustrated in Fig. 3.14.

Table 3.3. Summary of the results of residual flux experiments.

De-energization point-on-wave α_D	Estimated residual flux (pu)		Subsequent energization at α_E = 270° Inrush current peak (pu)	
	T1	T3	T1	T3
0º	−0.125	−0.136	9.83	5.59
10º	−0.026	−0.037	11.32	7.05
20º	0.084	0.071	12.97	8.79
30º	0.179	0.169	14.11	10.10
40º	0.249	0.238	14.76	11.19
50º	0.285	0.285	15.17	11.84
70º	0.306	0.308	15.39	11.81
70º	0.313	0.325	15.50	12.11
80º	0.312	0.326	15.57	12.41
90º	0.313	0.328	15.53	12.38
100º	0.315	0.333	15.34	12.47
110º	0.317	0.333	15.51	12.45
120º	0.319	0.337	15.29	12.57
130º	0.325	0.338	15.66	12.56
140º	0.326	0.344	15.81	12.34
150º	0.324	0.327	15.54	12.59
160º	0.292	0.299	15.26	11.91
170º	0.223	0.224	14.72	11.13
180º	0.130	0.130	13.54	9.81
190º	0.022	0.024	12.03	7.97
200º	−0.087	−0.083	10.91	6.44
210º	−0.181	−0.178	9.56	4.99
220º	−0.246	−0.253	8.30	4.20
230º	−0.282	−0.294	7.87	3.83
240º	−0.298	−0.318	7.73	3.66
250º	−0.304	−0.331	7.34	3.64
260º	−0.305	−0.335	7.42	3.49
270º	−0.305	−0.335	7.49	3.49
280º	−0.307	−0.338	7.50	3.47
290º	−0.309	−0.342	7.42	3.52
300º	−0.313	−0.343	7.51	3.47
310º	−0.317	−0.344	7.51	3.37
320º	−0.320	−0.344	7.33	3.39
330º	−0.313	−0.335	7.53	3.51
340º	−0.283	−0.299	8.19	3.77
350º	−0.217	−0.232	9.20	4.37

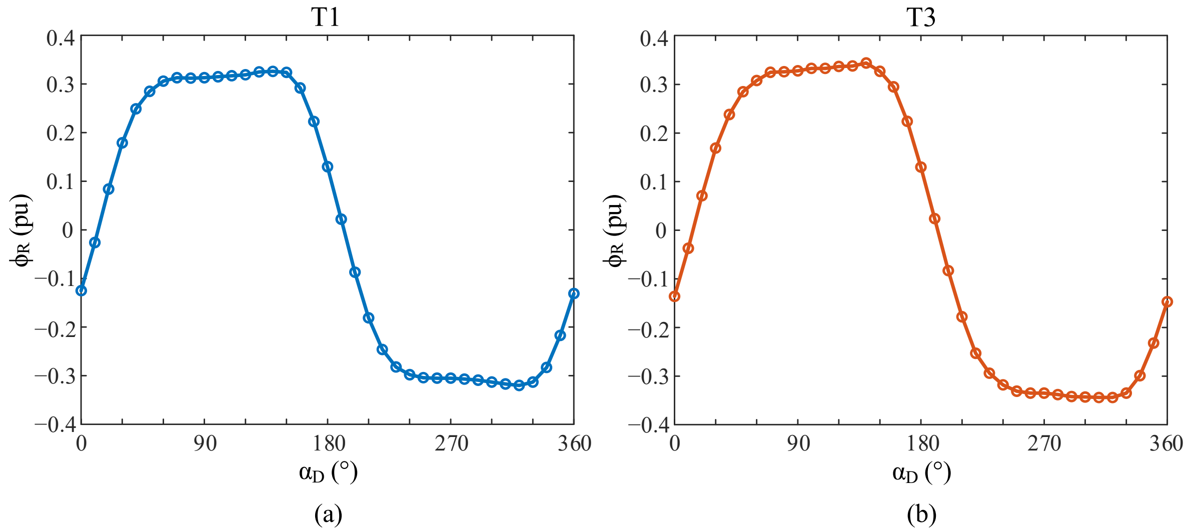

Fig. 3.19. Results of the residual flux experiments.

A second subset of experiments consisted of the de-energization at any point-on-wave with the SCR breaker and the subsequent energization at 0°. The obtained inrush currents in the experiments with the SCR breaker were always of the same amplitude. These results confirm that the de-energization with the SCR breaker always leads to residual fluxes $-\phi_{RM}$ and ϕ_{RM}.

Some dynamic loops and the corresponding external de-energization trajectories obtained during the experiments with the IGBT and SCR breakers are depicted in Fig. 3.20 and Fig. 3.21, respectively.

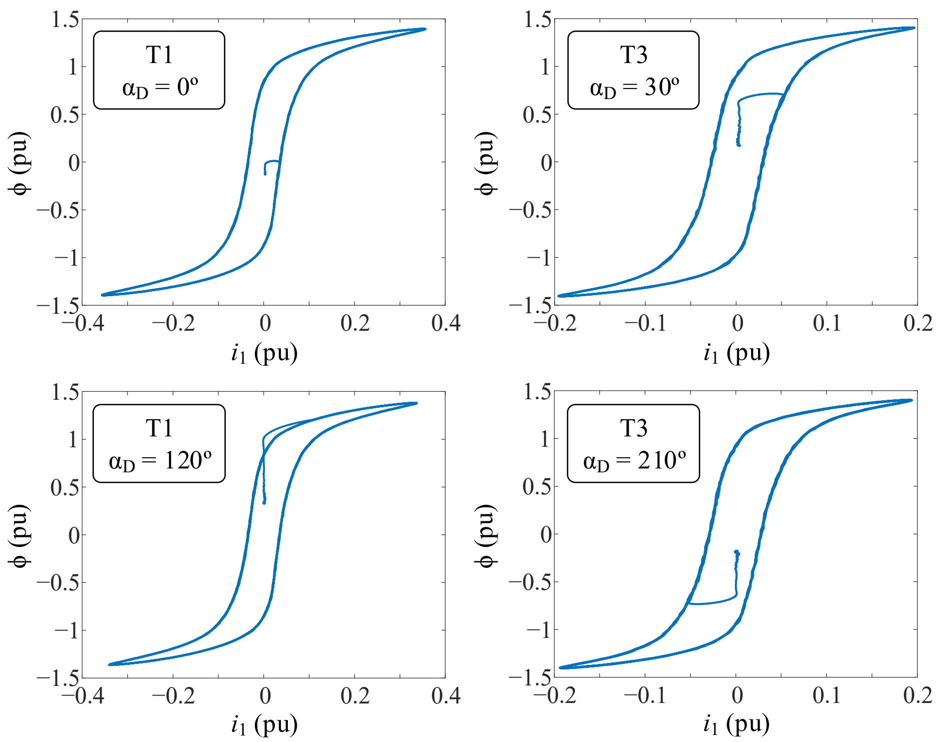

Fig. 3.20. Measured external loops and de-energization trajectories when the IGBT breaker is used.

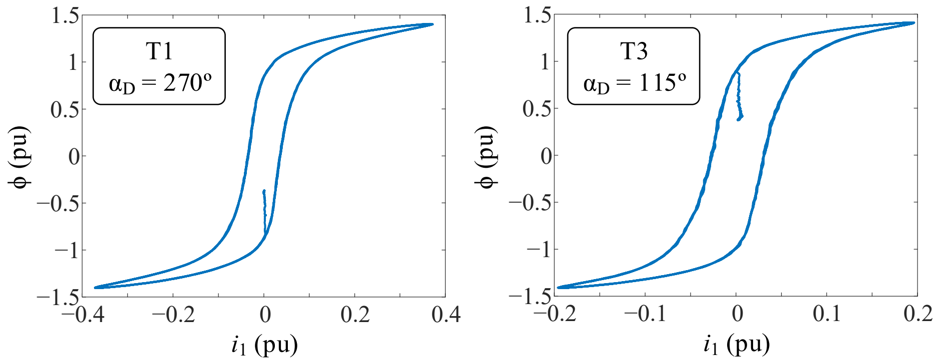

Fig. 3.21. Measured external loops and de-energization trajectories when the SCR breaker is used.

Both transformers T1 and T3 have also been simulated in the Matlab environment to validate the experimentally obtained residual flux values. Each transformer was modeled with two Type I models (Jiles-Atherton and Preisach), as these models are able to accurately represent the residual flux behavior. Both transformers were also simulated using the proposed Type II model.

The value of $\mathfrak{L}_E$ is calculated from the previously mentioned two no-load tests (Subsection 3.4.2) at two different frequencies with the same flux level:

$$\mathfrak{L}_E = \frac{N_1^{\,2}}{R_E} = \frac{N_1^{\,2}}{\Delta U/\Delta I} \tag{3.13}$$

where N_1 is the number of primary winding turns. The value of $\mathfrak{L}_H$ for the Type II model, has been manually adjusted by using the same measurements. The winding parameters, R_1, R_2, L_{d1} and L_{d2}, are estimated with the classical short-circuit test.

The Jiles-Atherton model parameters have been adjusted manually (Table 3.4). The Preisach Distribution Functions (PDFs) of the Preisach models have been calculated with the centered cycles method [51]. This method uses a set of steady-state symmetrical static hysteresis loops at different voltage levels.

Table 3.4. Jiles-Atherton parameters.

Parameter	T1	T3
a_1	1.91×10^4	1.78×10^4
a_2	3.25×10^4	3.21×10^4
a_3	9.90×10^6	9.00×10^6
b	2	2
M_s	22.35×10^6	21.57×10^6
c	0.54	0.492
α	5.00×10^{-7}	1.00×10^{-9}
k_e	500	400
k_{ns}	0.70	0.45
k_s	1.32	2.04
R_E	3 kΩ	2.9 kΩ

In all simulations, the circuit breaker is supposed to be ideal (close to the behavior of the IGBT breaker). Fig. 3.22 depicts a comparison between the measured dynamic loops and those obtained through simulations, as well as a comparison between measured and simulated de-energization trajectories.

Fig. 3.23 shows the residual flux values as a function of α_D, obtained from Jiles-Atherton and Preisach simulations, as well as the values estimated from the experiments. There is a close agreement between the experiments and the simulations, and the results validate the presented analyses of the residual flux and the de-energization trajectories.

The Jiles–Atherton and Preisach hysteresis models have yielded accurate predictions of the residual flux, even when the parameter estimation in both models has been based on limited information (only from no-load tests). The inclusion of additional information from asymmetric minor loops in the parameter estimation process does not result in significant improvements in the prediction of residual fluxes.

The purple line in Fig. 3.23 shows the proposed model (Type II) prediction of the residual flux values in function of α_D. The accuracy in the regions 1 to 2 and 3 to 4 is reasonable, while the errors in the other two regions are larger than in the Type I models. This is because this model is unable to recreate asymmetric minor loops. At any case, this model is a suitable option, better than the type III and IV models. In addition, this proposed model accurately predicts the residual flux for circuit breakers with no chopping capacity, i.e., in breakers where the effective interruption of the current is produced in the natural zero crossing, as the SCR breaker. The antique, but still in use, oil based circuit breakers are other representative breakers of this family.

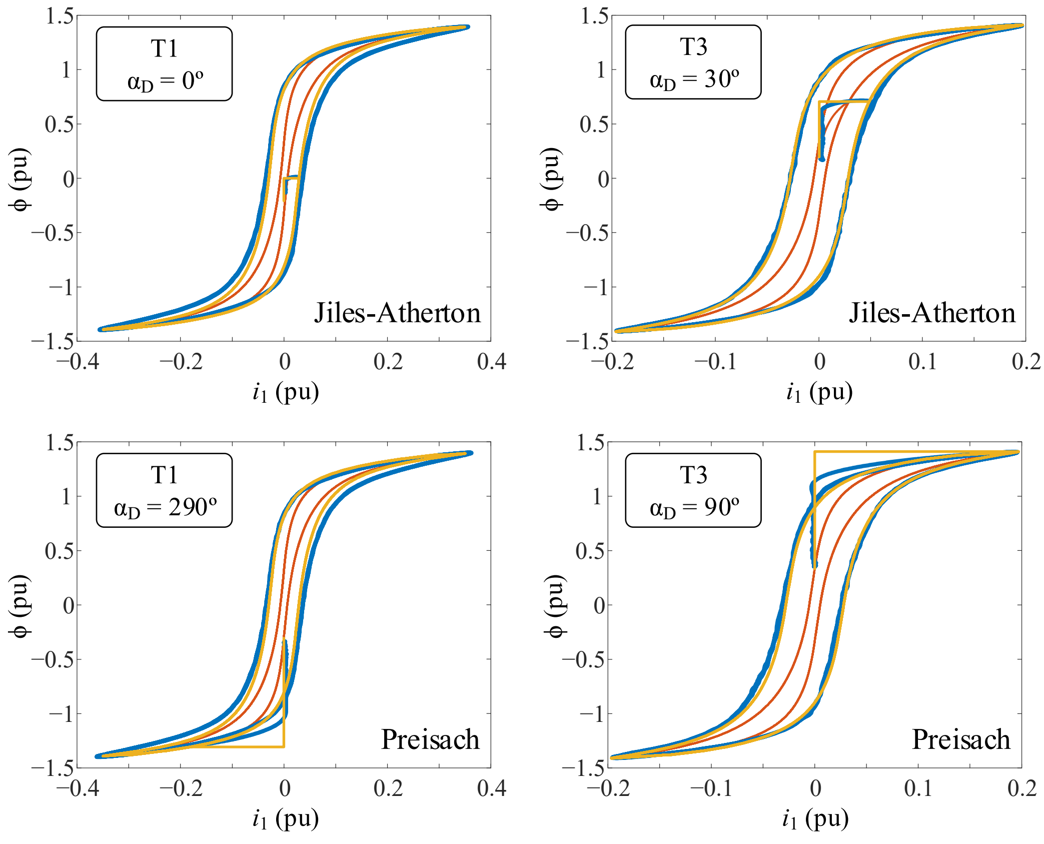

Fig. 3.22. Comparison between measured (blue line) dynamic loops and simulated static and dynamic loops (red and yellow lines, respectively).

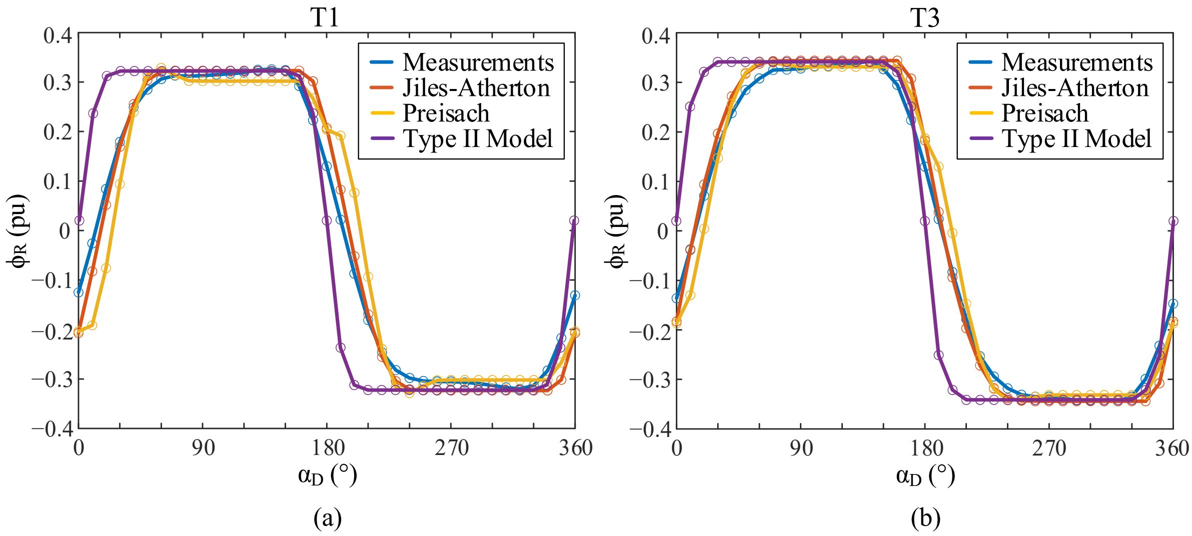

Fig. 3.23. Residual flux values in function of the de-energization point-on-wave: (a) T1, (b) T3.

The measurements and simulations results validate the previous statements about the residual flux:

- The residual flux values are bounded by the internal hysteresis loop, i.e., between $-\phi_{RM}$ and ϕ_{RM}.
- The eddy losses do not influence the residual flux.
- The residual flux values only depend on the de-energization point-on-wave α_D, not on the circuit breaker interruption speed.

3.5.2. Smart switching results

The proposed strategy to avoid large inrush currents was validated for the SCR and the IGBT breakers.

The maximum residual flux value, obtained from the mentioned frequency no-load tests in Subsection 3.4.2 is ϕ_{RM} = 0.326 pu for T1 and ϕ_{RM} = 0.344 pu for T2. Equation (3.9) provides the energization point-on-wave when IGBT breaker is used: α_{RM} = 166.7° for T1 and α_{RM} = 165.9° for T3. The classical no-load test determines the instantaneous flux value when i_1 is null (crossing between the vertical axis and the external loop): ϕ_0 = 1 pu for T1 and ϕ_0 = 0.94 pu for T3. Lastly, (3.10) yields the de-energization point-on-wave: α_0 = 132.5° for T1 and α_0 = 138.4° for T3.

The proposed strategy to avoid large inrush currents was validated for the SCR and the IGBT breakers. Fig. 3.24 shows inrush currents of different severity for transformer T1 with a de-energization point-on-wave α_D = 90°.

Fig. 3.24(a) shows the worst case of inrush current (around 12 pu) for transformer T1 when α_D = 90° and α_E = 270°. In this figure, both switchings have been made with the SCR breaker. It is important to take into account that the maximum residual flux for large transformers is a bit larger (around 0.7 pu) and the resulting inrush currents with this approach could be more severe, despite they are limited by a larger leakage inductance. Fig. 3.24(b) shows the resulting currents with the proposed smart switching using the SCR and the IGBT breakers. As can be seen, there is no overcurrent.

Lastly, Fig. 3.25 depicts the proposed compromise solution (energization point-on-wave $\alpha_E = 0°$) when the de-energization cannot be controlled. The inrush current is less severe, with a first peak of around 1 pu. This demonstrates that good results can be obtained even with uncontrolled de-energization when the energization is adequately controlled.

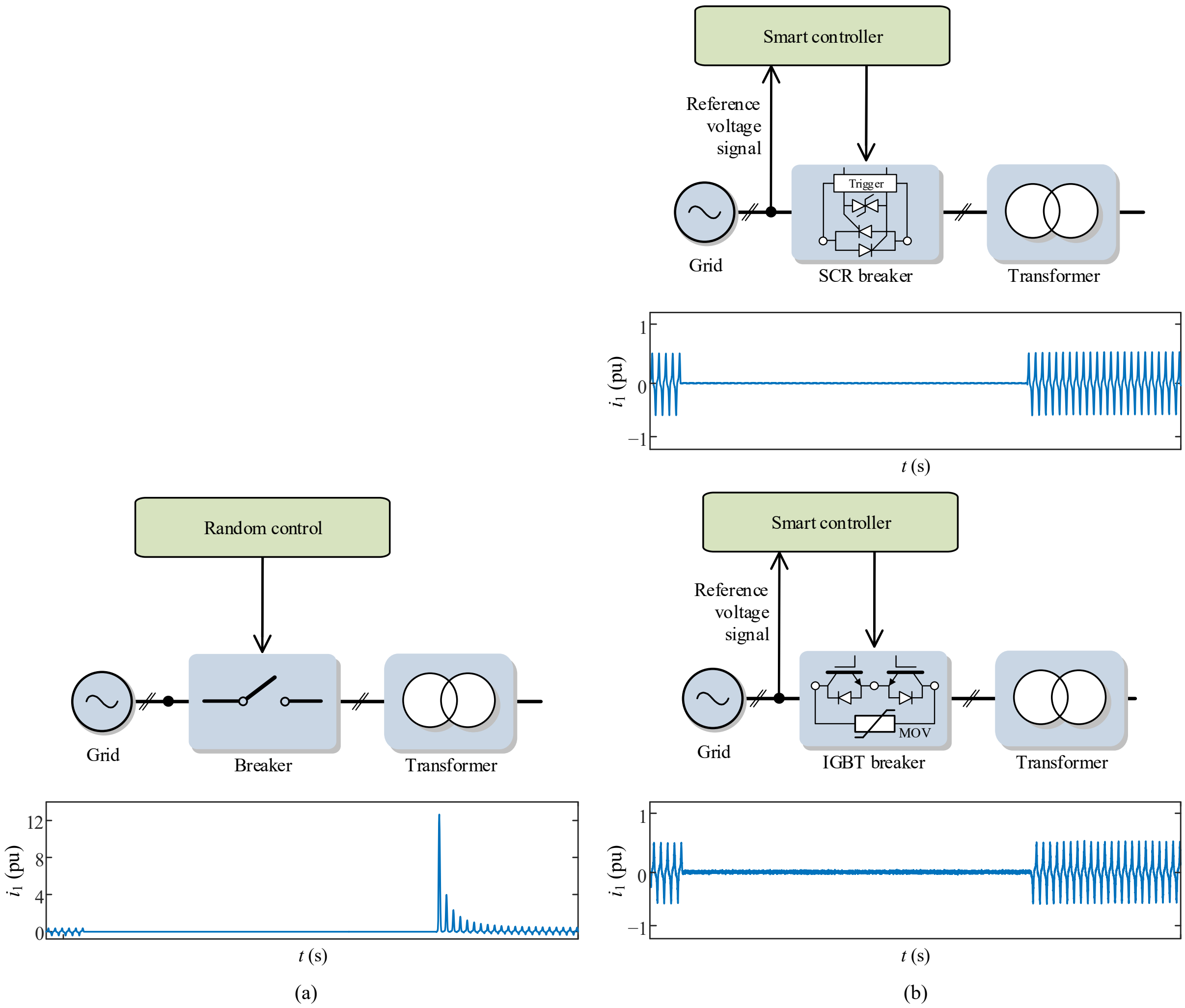

Fig. 3.24. (a) Experimental inrush current resulting from random switching with T1, (b) experimental current resulting from smart switching with T1.

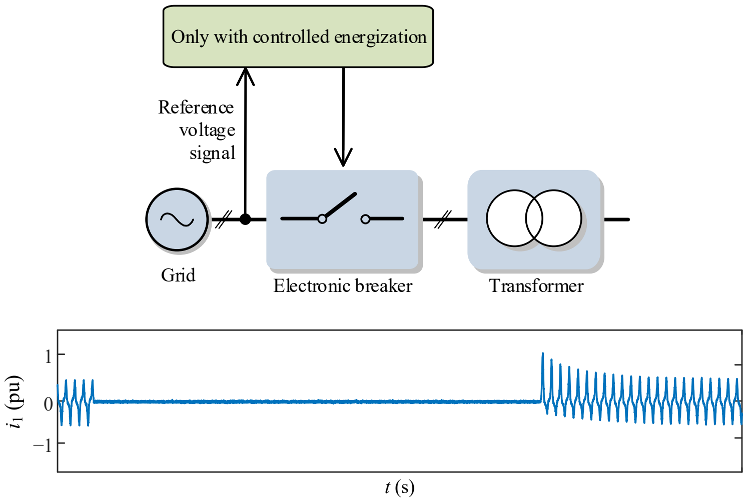

Fig. 3.25. Experimental current with the proposed compromise solution: only controlled energization at $\alpha_E = 0°$, without controlled de-energization or prior residual flux knowledge.

Chapter 4. Saturation Curve Estimation of Single-Phase Transformers using Inrush Currents

4.1. Introduction

This chapter presents a novel methodology for estimating the saturation curve of the single-phase transformer model in Chapter 2.

Some of the existing methodologies for parameters estimation of the nonlinear core models present some problems or limitations. First, standard tests do not drive transformer core into deep saturation and may lead to significant errors in the parameters estimation, affecting the estimation of inrush currents. For example, [145]-[146] propose an algorithm to convert a root mean square (RMS) current-voltage piecewise curve into an instantaneous current-flux piecewise curve. The RMS curve is usually provided by the manufacturer but is limited to light saturation. In [147]-[149], several techniques based on optimization algorithms are presented to estimate the transformer parameters, but all of them consider that the core magnetizing reactance is linear. Thus, they are not suitable for simulating the inrush current. In [150], the saturation characteristic is fitted from current and voltage real-time measurements, but does not match the simulated inrush current.

To diminish these deficiencies, some authors suggest performing inrush tests [144], [151]-[152], being [144] the most remarkable paper. As the inrush current is a transitory phenomenon associated with transformer energization, it is mostly influenced by the residual core flux and the supply voltage phase at the switching instant. The estimation methodologies that perform inrush tests usually have a limitation: it is difficult to adequately measure or compute the residual flux. Reference [144] estimates the residual flux by integration of the registered voltage during the energization transient, assuming that the residual flux is zero to obtain a transient flux and its corresponding transient flux–current loop. Then, the residual flux is the vertical displacement of this transient flux–current loop until it overlaps the flux–current loop from the no-load test. Once the residual flux is obtained, the true transient flux is obtained. Other of the most well-known techniques to compute the residual flux is to record the de-energization voltage waveform to integrate it, but this requires an extra test as in [151]. Finally, [152] proposes an algorithm for determining the saturation curve from measured inrush and steady-state current waveforms, based on the minimization of a specifically defined cost function.

Another method to estimate the flux–current curve of a single-phase transformer is presented in [153], which is based on formulae proposed by Holcomb [20]. They use as data the peak values at each cycle of the worst case of inrush current. The worst case is used to avoid controlling or knowing the switching angle. Moreover, the authors do not propose any new method to measure or estimate the residual flux, and they only suggest that the typical higher value provided by some manufacturers can be used.

W. Sima *et al.*, present in [154] a method to measure deep-saturated magnetizing inductances for single-phase transformers, using an AC source and a DC source.

The main advantages of the proposed methodology in this chapter are:

- It accounts for deep saturation.

- It requires minimal information from only one no-load test and only one inrush test.
- It is not necessary to record voltage and current waveforms.
- In the case of the inrush test, the methodology eliminates the need to know the corresponding residual flux and the energization point-on-wave.
- It is computationally straightforward.

An important contribution of this chapter is the introduction of a signature capable of characterizing all possible inrush currents of a given single-phase transformer.

4.2. Saturation curve

The saturation curve from which the parameters are estimated is that described in Chapter 2. This analytical single-valued function is defined by:

$$\Re(f)^{-1} = \frac{K_1}{\left(1+\left(\frac{|f|}{f_{\mathrm{KNEE}}}\right)^{p}\right)^{1/p}} + K_2 \tag{4.1}$$

where K_1, K_2, p and f_{KNEE}, are experimental parameters that allow this single-valued function to be fitted to the transformer saturation curve (ϕ–f).

Transformers are usually designed to operate at a point lightly below the knee point (f_{KNEE}, ϕ_{KNEE}). Due to this, a fifth parameter is introduced, the degree of saturation k_{SAT}, whose value can typically range from 0.4 to 1. With this parameter in mind, f_{KNEE} is defined as

$$k_{\mathrm{SAT}} = \frac{\sqrt{2}\cdot\phi_{\mathrm{N}}}{K_1 f_{\mathrm{KNEE}}} = \frac{\sqrt{2}\cdot\phi_{\mathrm{N}}}{\phi_{\mathrm{KNEE}}} \tag{4.2}$$

where ϕ_{N} is the RMS value of the nominal magnetic flux and ϕ_{KNEE} is the saturation flux, related to f_{KNEE} by K_1.

4.3. Saturation curve estimation

The general block scheme of the proposed methodology is illustrated in Fig. 4.1. The parameters of the saturation curve are estimated in two stages.

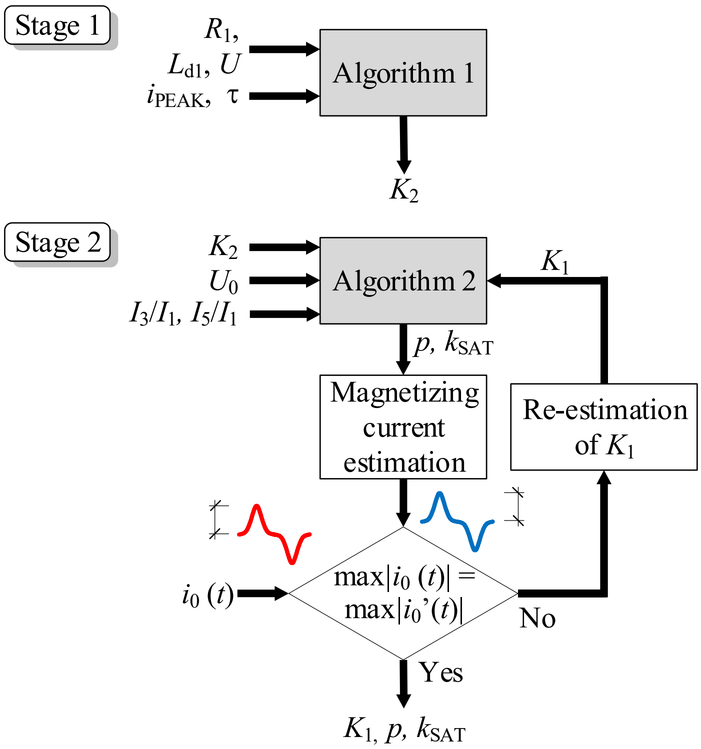

Fig. 4.1. General structure of the proposed estimation methodology.

First, it is necessary to define the decay time, τ, of an inrush current: τ is the elapsed time from the first peak, i_{PEAK}, until the current has dropped to 37% of the difference between i_{PEAK} and the steady-state peak value, i_{STEADY}. For example, in Fig. 4.2, the simulated transformer T11 of 100 kVA has a decay time of $\tau = 0.085$ s.

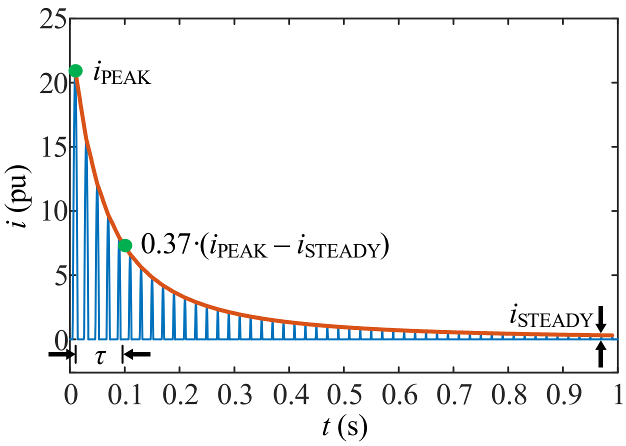

Fig. 4.2. Example of inrush current for the single-phase transformer T11 (100 kVA, R_1 = 0.01 pu and L_{d1} = 0.0173 pu).

During Stage 1, the parameter K_2 is estimated using the absolute value of i_{PEAK} and τ from a unique inrush test. Since i_{STEADY} is significantly lower than i_{PEAK}, it is neglected. Additionally, the RMS pu value of the voltage at which the inrush test was conducted, U, is required, along with the values of R_1 and L_{d1}. These two winding parameters can be reasonably estimated through the classical short-circuit test.

During Stage 2, the third and fifth harmonics ratio of the no-load current, I_3/I_1 and I_5/I_1, are used to estimate the rest of the saturation curve parameters, K_1, p, and k_{SAT}.

4.3.1. Stage 1: K_2 estimation

In order to estimate the slope K_2, the simplified saturation curve of Fig. 2.5(b) is used. This simplified curve only depends on the parameters K_2 and ϕ_{KNEE}.

Next variables and parameters influence the inrush current of a transformer: the residual core flux (ϕ_R), the primary voltage, the energization point-on-wave (α_E), the primary winding impedance (R_1 and L_{d1}), the saturation curve and the impedance of the source (R_S and L_S, which have the same influence as R_1 and L_{d1}). For brevity purposes, R_S and L_S will be omitted from this point, although their values can be added to R_1 and L_{d1} if their influence is significant.

The worst case of inrush current occurs when the core has the maximum residual flux and the switching occurs at the instant of voltage zero-crossing with a polarity that increases the flux in the core. For the same conditions of energization, the inrush current is also more severe for lower R_1 and L_{d1}, higher values of k_{SAT} and lower values of K_2.

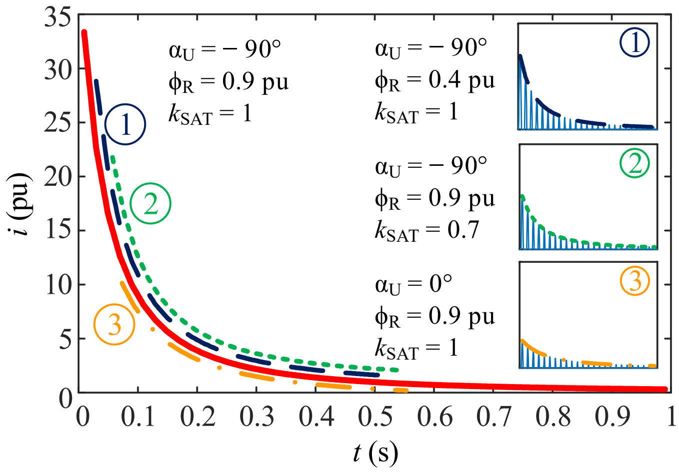

Fig. 4.3. Matching of the main envelope with the envelopes of other different inrush currents for transformer T11.

The envelopes (red line in Fig. 4.2) of all possible inrush currents of a given transformer may appear different, but they are closely interrelated. It has been verified, that all envelopes match with a segment of the worst-case inrush current envelope (referred to as the main envelope), as illustrated in Fig. 4.3. In other words, the envelope of any inrush current of a given transformer can be considered a segment of the main envelope, regardless of the residual flux value and the energization point-on-wave. Assuming an infinite K_1 slope, the inrush current is null during the periods when the transformer is unsaturated. Nonzero current occurs only during saturation intervals, so the core flux, and therefore the inrush current, is damped only during saturation. In conclusion, the inrush current damping in a single-phase transformer is affected only by R_1, L_{d1}, and the K_2 slope. By this reason, the main envelope can be considered as a kind of "signature" of the transformer.

Therefore, if for each transformer exists a main envelope with a unique and general shape, also exists a unique i_{PEAK}–τ curve which can be easily obtained from the main envelope. This i_{PEAK}–τ curve also depends only on R_1, L_{d1} and K_2. Even for different values of k_{SAT}, the curve is exactly the same. The algorithm to estimate K_2 is based on this statement but in a reverse way. It is important to stand out how this highly nonlinear problem affected by some variables can be completely characterized by its main envelope, or by its i_{PEAK}–τ curve.

The previous statements are not true when the nominal flux is greater than ϕ_{KNEE}, that is, when k_{SAT} is greater than 1, which does not correspond to usual transformer designs.

K_2 estimation involves a simulated set of i_{PEAK}–τ curves: a different curve for a different value of K_2 inside a range. For example, Fig. 4.4 shows the set of curves for the transformer T11 of the example. The steps to estimate K_2 are:

1. R_1 and L_{d1} are estimated.
2. A K_2 value is supposed to be known within a common range (e.g., from 0.001 pu to 1 pu).
3. The worst case of inrush current for supposed K_2 is analytically calculated ($k_{SAT} = 1$, $\alpha_E = -90°$, $\phi_R = 0.9$ pu) by using the model equations in Chapter 2. Then, the main envelope (similar to that in Fig. 4.2) is obtained.
4. The i_{PEAK} –τ curve is calculated from the main envelope. To avoid multiple inrush current calculations, which is not feasible, it can be assumed that each point of the main envelope corresponds to a different test, resulting in a different value for i_{PEAK}. Then, τ is calculated for each i_{PEAK} value.
5. The previous steps are repeated for all supposed values of K_2, until a set of i_{PEAK} –τ curves (as those in Fig. 4.4) is obtained. The supposed values of K_2 are varied logarithmically within a range of values chosen according to the rated power of the transformer.
6. The true value of K_2 is estimated from the i_{PEAK}–τ curves for the unique measured pair of values i_{PEAK} and τ.

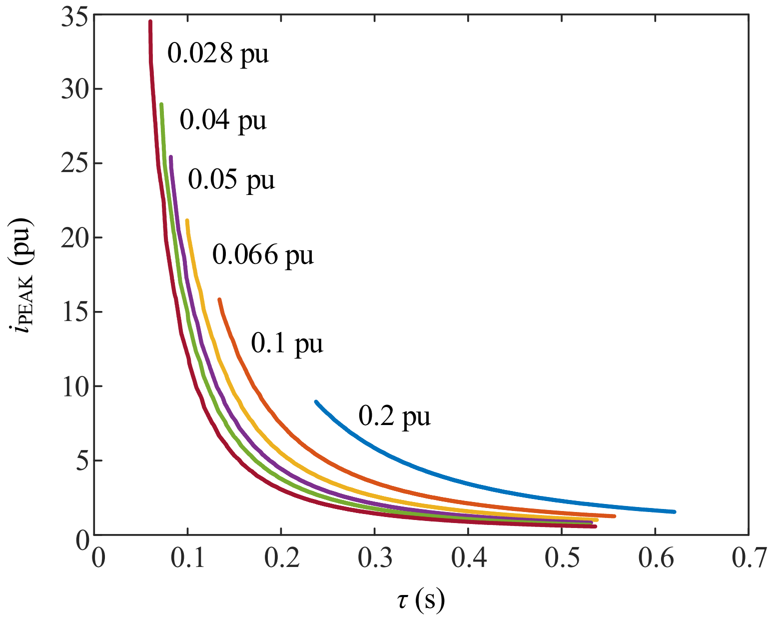

Fig. 4.4. Set of curves i_{PEAK}–τ, for the transformer T11 (100 kVA) for different values of K_2.

Fig. 4.5 shows the flowchart of the algorithm.

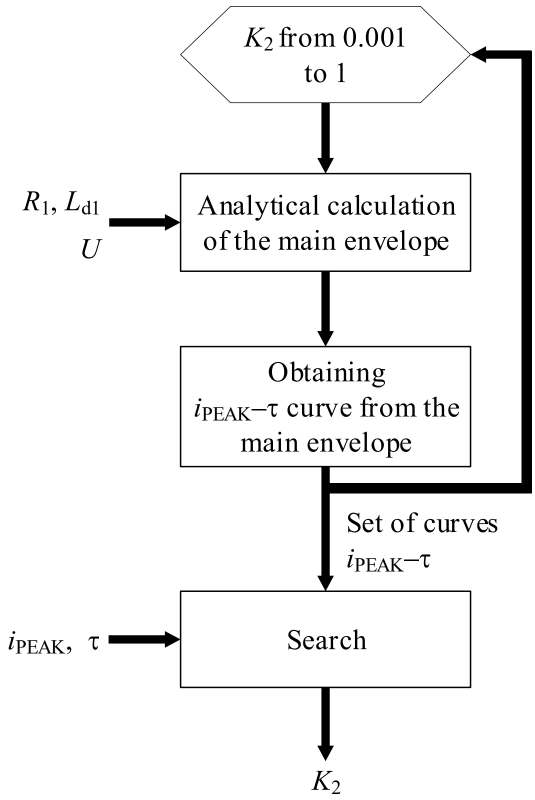

Fig. 4.5. Stage 1: flowchart of Algorithm 1.

4.3.2. Stage 2: K_1, p and k_{SAT} estimation

The magnetizing current of a transformer contains harmonic distortion due to the nonlinear magnetizing characteristic of the core. According to [155], for transformers with CRGO (Cold Rolled Grain Oriented) material, the magnitudes of the third harmonic is between 0.3 and 0.5 pu, and the fifth harmonic is between 0.1 and 0.3 pu, respectively, when the fundamental component is 1 pu.

In the model derived from (4.1), the magnetizing current distortion only depends on p, k_{SAT} and $\mu_r = K_1/K_2$. Assuming μ_r is known, the parameters p and k_{SAT} can be estimated from I_3/I_1 and I_5/I_1 in a reverse way.

The procedure to estimate p, k_{SAT} and K_1 is next described. As K_2 has been previously estimated, an initial value of K_1 is proposed from no-load measurements, as U_0 / I_0 in pu. Then, the parameters p and k_{SAT} are estimated with Algorithm 2, which will be explained later. Using this saturation curve, a steady-state current is calculated or simulated. Then, the peak value of this current is compared with that measured. If both values are not similar, the value of K_1 is modified and all process is repeated. When the values are similar, the estimation process is finished. Note that only the peak values of the no-load currents are compared, instead of the no-load entire waveforms, as the core losses are neglected in the model.

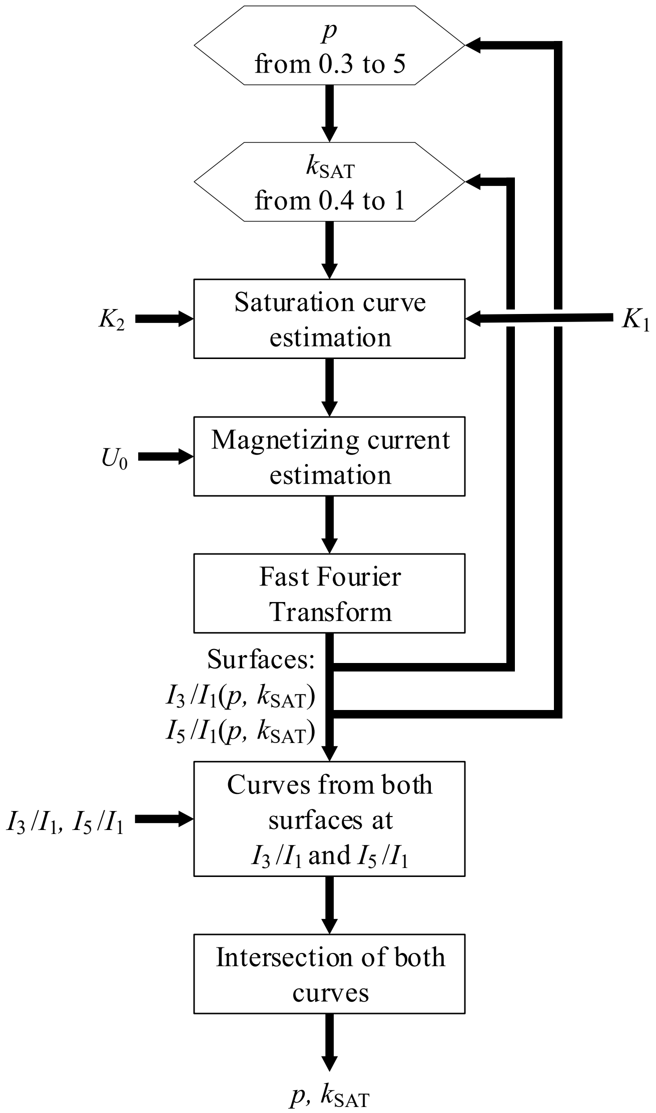

Fig. 4.6. Stage 2: flowchart of Algorithm 2.

Fig. 4.6 depicts the general flowchart of the Algorithm 2 whose steps are:

1. A pair of values for p and k_{SAT} is supposed within ranges from 0.3 to 5 and from 0.4 to 1, respectively.

2. The parameter K_2 is known at this point while p, k_{SAT} and K_1 have been supposed, leading to a saturation curve valid for this iteration. The magnetizing current is simulated assuming a pure sinusoidal flux with a RMS value of 1 pu.

3. The harmonic content of the magnetizing current, I_3/I_1 and I_5/I_1, are calculated by a Fast Fourier Transform (FFT).

4. The previous steps are repeated for all supposed values of p and k_{SAT}. Two surfaces for I_3/I_1 and I_5/I_1 in function of p and k_{SAT} are obtained as illustrated in Fig. 4.7(a). These surfaces are unique for a single-phase transformer when K_1 and K_2 are given.

5. The harmonic content of the laboratory measured no-load current, I_3/I_1 and I_5/I_1, are calculated by a FFT.

6. Each of both surfaces is intersected by a perpendicular plane to the z-axis at the respective harmonic value measured at the laboratory no-load test, resulting in two curves. The intersection point of both curves provides the estimation for p and k_{SAT}, as illustrated in Fig. 4.7(b).

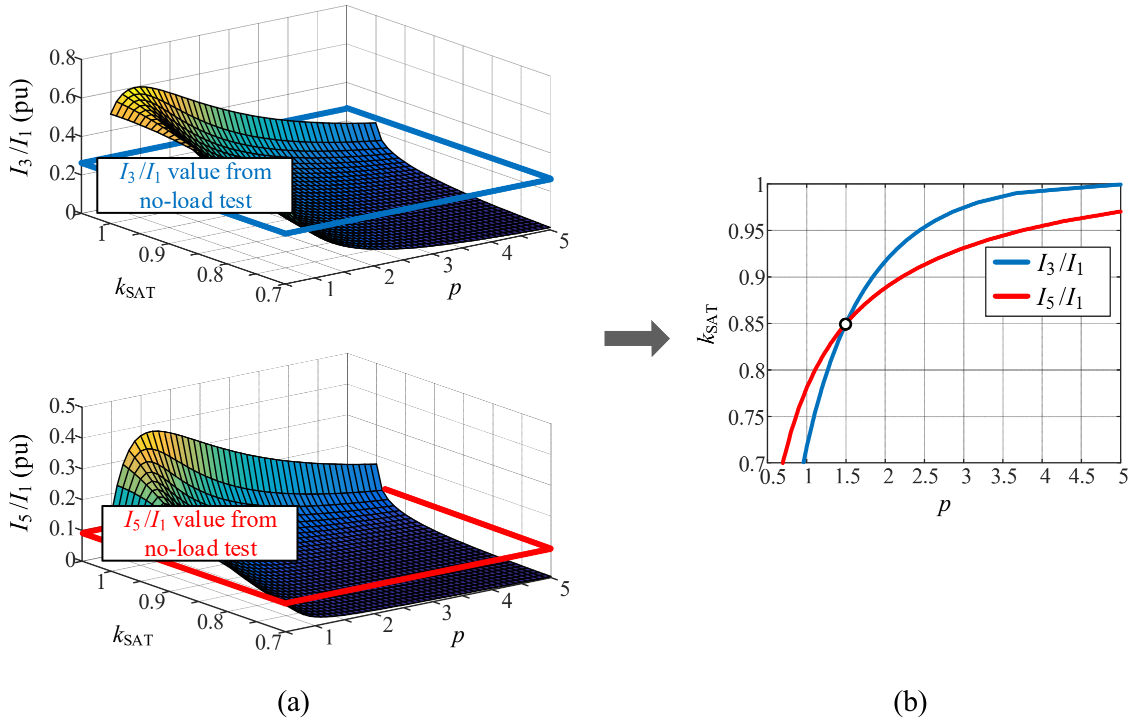

Fig. 4.7. (a) Harmonic surfaces, I_3/I_1 and I_5/I_1, in function of p and k_{SAT}, and (b) resultant curves for p and k_{SAT} estimation.

Typically, the no-load test is performed at nominal voltage. However, this voltage can be insufficient to characterize the knee of the saturation curve. Thus, it is recommended to carry out the no-load test at enough voltage to ensure that the transformer is operating above the knee point during the test. In our experience, this is achieved when the third and fifth harmonics are above 30% and 12%, respectively.

4.4. Experimental validation

In order to validate the proposed methodology, about thirty experimental tests are carried out on different single-phase transformers. Each transformer has different primary winding resistance and short circuit reactance, within the range of (near to) 0 pu to 20 pu, and different no-load current and spectra. All inrush tests are performed without controlling the switching angle, and most of them without controlling the residual flux, they are totally random. A few other tests are performed with previous demagnetization in order to get a null residual flux [156]. Such variety of transformers verifies that the methodology is efficient regardless of their parameters. In this section, twelve tests from three of these transformers are presented. These transformers were not chosen for showing the best estimation results, but to illustrate a rich variety of parameters in true transformers.

The nominal characteristics and parameters of the transformers are shown in Table 4.1. The impedance of the source (autotransformer) used in the tests is $R_S = 1.15\ \Omega$ and $L_S = 2.5$ mH.

Table 4.2 summarizes the results from three inrush tests (without previous demagnetization) for each transformer, as well as the estimated value for K_2 from each test. As can be seen, the values of K_2 from different tests are very close only for transformer T6. Regarding transformer T1, the estimation from test 1.2 deviates from that of tests 1.1 and 1.3 by around a 50%. This deviation is due to the fact that tests 1.2 and 2.3 involve more severe inrush currents than the other tests. Something similar is true for transformer T3. For the three transformers, the K_2 corresponding to the most severe inrush current will be taken as the most accurate value, as in these cases the transformer saturation is deeper.

Table 4.1. Characteristics and parameters of the tested transformers.

	T1	T3	T6
S_N (VA)	320	320	360
U_{N1} (V)	120	120	120
R_1 (pu)	0.0206	0.0172	0.02775
L_{d1} (pu)	0.02335	0.03575	0.04055

Table 4.2. Data from inrush tests and estimated K_2 parameters.

	T1			T3			T6		
Inrush test	1.1	1.2	1.3	3.1	3.2	3.3	6.1	6.2	6.3
U (pu)	1.049	1.049	1.049	1.055	1.055	1.055	1.03	1.03	1.03
i_{PEAK} (pu)	7.44	14.8	9	10.43	8.0	11.6	10.3	11.6	11.3
τ (ms)	34.2	19.6	27.4	28.3	36.2	24.2	30.4	28.4	29.3
K_2 (pu)	0.03	0.015	0.026	0.02	0.02	0.009	0.057	0.048	0.052

Table 4.3 shows the results from the inrush tests with null residual flux, achieved with a previous demagnetization. The estimated values of K_2 using these tests are very similar to the values from less severe previous inrush tests without demagnetization. This is not due to the zero residual flux but to the lower depth of saturation. So, the residual flux does not affect to the estimation.

Table 4.3. Data from inrush tests with null residual flux and estimated K_2 parameters.

Transformer	T1	T3	T6
Inrush test	1.4	2.4	3.4
U (pu)	1.04	1.04	1.04
i_{PEAK} (pu)	7.08	9.09	10.24
τ (ms)	35.4	31.2	30.3
K_2 (pu)	0.031	0.02	0.058

Table 4.4 shows the data from the no-load tests and the rest of estimated parameters (K_1, p and k_{SAT}). T1 and T3 transformers have small p and k_{SAT}, but large K_1 values, which means that the knees of their saturation curves are not very pronounced as both transformers saturate slowly.

Table 4.4. Data from no-load tests and estimated parameters.

	T1	T3	T6
U_0 (pu)	1.18	1.35	1.02
I_0 (pu)	0.38	0.44	0.24
I_3/I_1	0.51	0.51	0.28
I_5/I_1	0.16	0.14	0.15
K_1 (pu)	250	1050	8
p	0.41	0.3	3.0
k_{SAT}	0.6	0.41	1

Finally, the comparison between the measured hysteresis loops (one loop has been obtained from the no-load test and the other loop has been obtained from the inrush test) and the estimated saturation curves are shown in Fig. 4.8. They are very close, with a slight deviation above the knee. Despite this, the close agreement reflects the estimation accuracy.

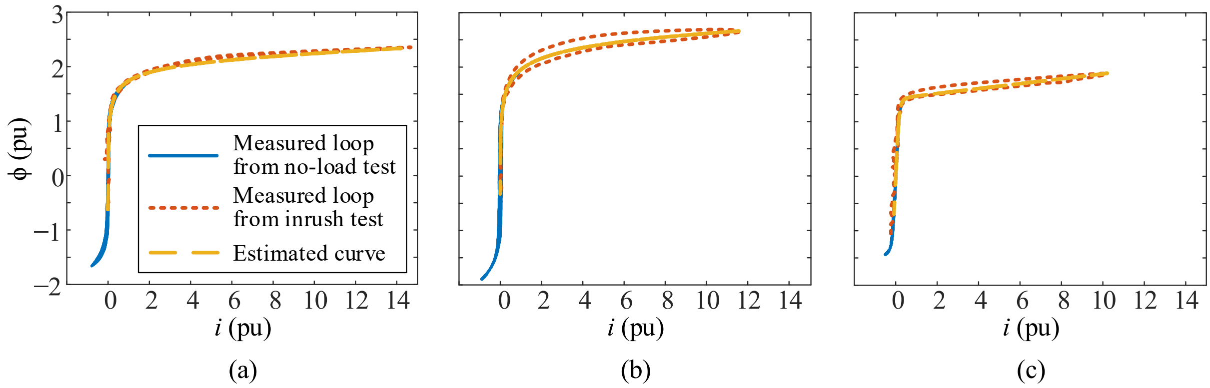

Fig. 4.8. Comparison between measured hysteresis loops and estimated saturation curves of (a) T1, (b) T3 and (c) T6.

4.4.1. Inrush current simulations

To simulate the inrush currents, the transformer model was numerically solved with an ODE solver. To simulate correctly the inrush currents without demagnetization, it is necessary to know the residual fluxes and the switching angles from each test. The switching angles are easily obtained from the recorded voltage waveforms. The residual fluxes could have been estimated as in [144], but the validation of the proposed methodology would be influenced by the residual fluxes estimation accuracy. Thus, it was decided to tie the first peaks of the currents by varying the only unknown variable, the residual flux, and to evaluate and validate the methodology by comparing the values of the subsequent peaks. Table 4.5 summarizes the values for the second and the third peaks of all measured and simulated inrush currents, as well as the errors. The best results are obtained with transformer T3. The good results in all cases show that the saturation parameters have been determined with enough accuracy. Fig. 4.9 shows the comparison between both currents. It can be seen the excellent agreement in all cases.

Table 4.5. Comparison of measured and simulated current peaks of the inrush tests.

Transformer	Test	Number of peak	Measured peak (pu)	Simulated peak (pu)	Absolute error (pu)	Relative error (%)
T1	1.1	2nd	3.45	3.68	0.23	6.66
		3rd	2.37	2.30	0.07	2.95
	1.2	2nd	4.7	5.47	0.77	16.38
		3rd	2.93	3.01	0.08	2.73
	1.3	2nd	3.87	4.12	0.25	6.46
		3rd	2.55	2.5	0.05	1.96
T3	3.1	2nd	4.43	5.06	0.63	14.22
		3rd	2.93	3.15	0.22	7.5
	3.2	2nd	3.92	4.28	0.36	9.18
		3rd	2.69	2.79	0.10	3.72
	3.3	2nd	4.61	5.41	0.9	19.52
		3rd	3.11	3.29	0.18	5.79
T6	6.1	2nd	4.75	4.75	0.0	0.0
		3rd	2.78	2.78	0.0	0.0
	6.2	2nd	5.15	5.12	0.03	0.58
		3rd	2.83	2.92	0.09	3.18
	6.3	2nd	5.13	5.07	0.06	1.17
		3rd	2.83	2.9	0.07	2.47

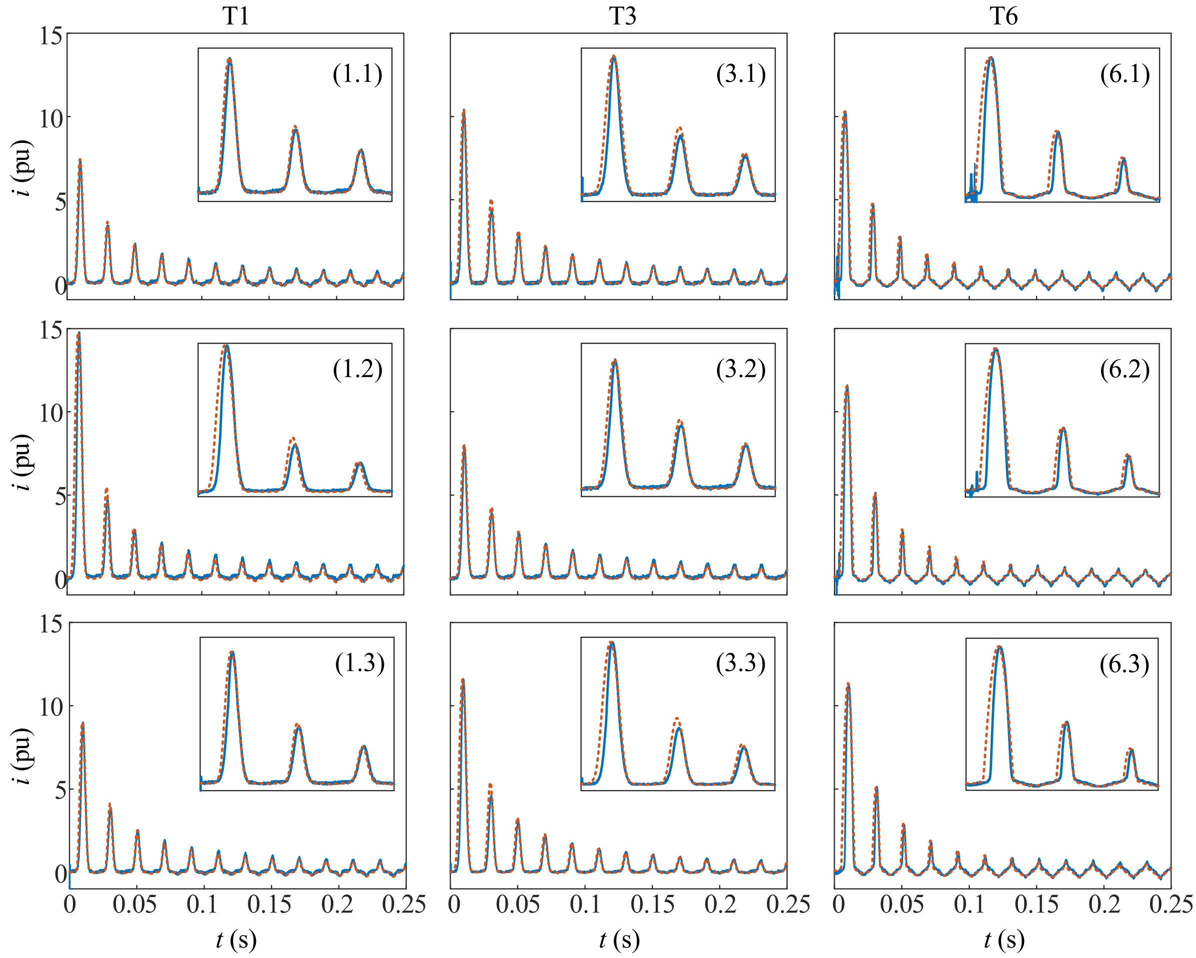

Fig. 4.9. Comparison between recorded inrush currents (full lines) and simulated inrush currents (dotted lines), for the three tested transformers. First column corresponds to T1, second column to T3 and third column to T6.

By other hand, Fig. 4.10 shows the comparison between measured and simulated currents with null residual flux. Table 4.6 summarizes measured and simulated first peak values and the corresponding errors. As can be seen, the relative errors are very small, 2.83% for the worst estimation.

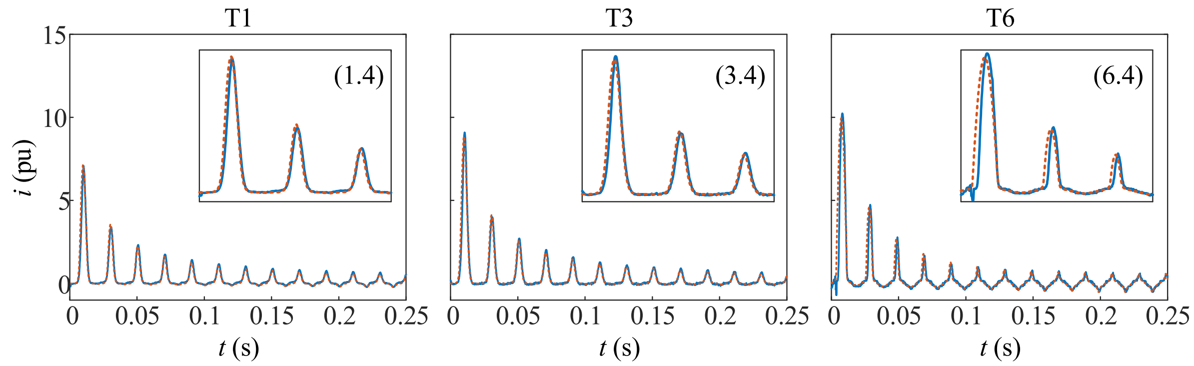

Fig. 4.10. Comparison between recorded inrush currents (solid lines) and simulated inrush currents (dotted lines) with null residual flux, for the three tested transformers. First column corresponds to T1, second column to T3 and third column to T6.

Table 4.6. Comparison of measured and simulated first peak of the inrush test with null residual flux.

Transformer	T1	T3	T6
Inrush test	1.4	2.4	3.4
Measured i_{PEAK} (pu)	7.08	9.09	10.24
Simulated i_{PEAK} (pu)	7.16	8.86	9.95
Absolute error (pu)	0.08	0.23	0.29
Relative error (pu)	1.13	2.53	2.83

4.4.2. Scalability to larger transformers

The proposed methodology can also be applied to larger transformers. This is because the estimation methodology has been tested, by simulation, with realistic power transformers ranging from several tenths of VA to several tenths of MVA, with short-circuit reactances between 0.03 pu and 0.20 pu, with short-circuit reactance to resistance ratio from 1 to 50, with magnetizing reactances between 0.04 pu and 0.004 pu, and with core losses between 0.005 pu and 0.0005 pu. These simulations have been done by using different programming environments such as PSpice, Simscape and PSCAD, each one with a different transformer model. About the knee shape of the simulated saturation curves (p and k_{SAT} parameters), the harmonic distortion of the magnetizing current is inside the usual range in all analyzed cases.

It has been also verified in the laboratory that the method is still valid even with a 320 VA transformer with a 0.04 pu of short-circuit impedance, but only a 0.004 pu of short-circuit reactance (almost all short-circuit impedance is resistive). This is one of the eight transformers previously referenced in the introduction of this section. The results are not included here because it does not represent a realistic grid transformer, despite being a commercial unit.

Table 4.7 contains the characteristics of four of the simulated power transformers, as well as their estimated parameters. T11 has been simulated in PSpice according to the model of Chapter 2, and is the transformer previously used as example in Fig. 4.2, Fig. 4.3, and Fig. 4.4. T12 has been implemented in Simscape, using the Nonlinear Transformer Block (T-model), with the magnetization inductance parameterized by a single saturation point (two straight lines). The last two units have been simulated in PSCAD, T13 with the classical model and T14 with the UMEC (Unified Magnetic Equivalent Circuit) model.

Table 4.7. Data from model power transformers and estimated parameters.

Transformer	T11	T12	T13	T14
S_N (MVA)	0.1	1	50	100
U_{N1} (kV)	15	13.8	47	230
R_1 (pu)	0.01	0.006	0.004	0.0015
L_{d1} (pu)	0.0173	0.0295	0.04	0.065
U_0 (pu)	1	1.1	1	1
I_0 (pu)	0.03	0.18	0.0173	0.0157
I_3/I_1	0.2365	0.86	0.1520	0.3172
I_5/I_1	0.0569	0.77	0.0464	0.0512
K_1 (pu)	72	119	80	390
p	1.49	3.5	2.61	0.7
k_{SAT}	0.85	0.93	0.88	0.69
K_2 (pu)	0.035	0.064	0.068	0.121

Fig. 4.11 compares the model hysteresis loops (from no-load and inrush tests) and the estimated saturation curves. The close agreement confirms the suitability to power transformers. Fig. 4.12 shows the model (given by the PSpice, Simscape or PSCAD models) and the estimated (predicted with the estimated parameters) inrush currents. Table 4.8 shows the model and the estimated first peak values of inrush currents and the corresponding errors. The results are satisfactory in all cases, with a relative error of 2.4% for the worst estimation.

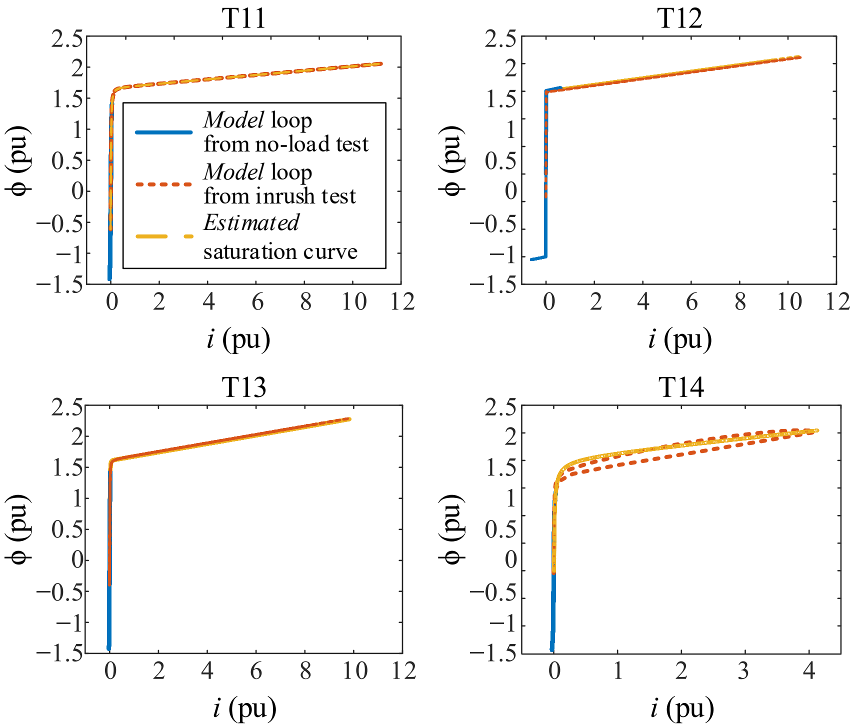

Fig. 4.11. Comparison between the model hysteresis loops and the estimated (predicted with the estimated parameters) saturation curves of power transformers T11 to T14.

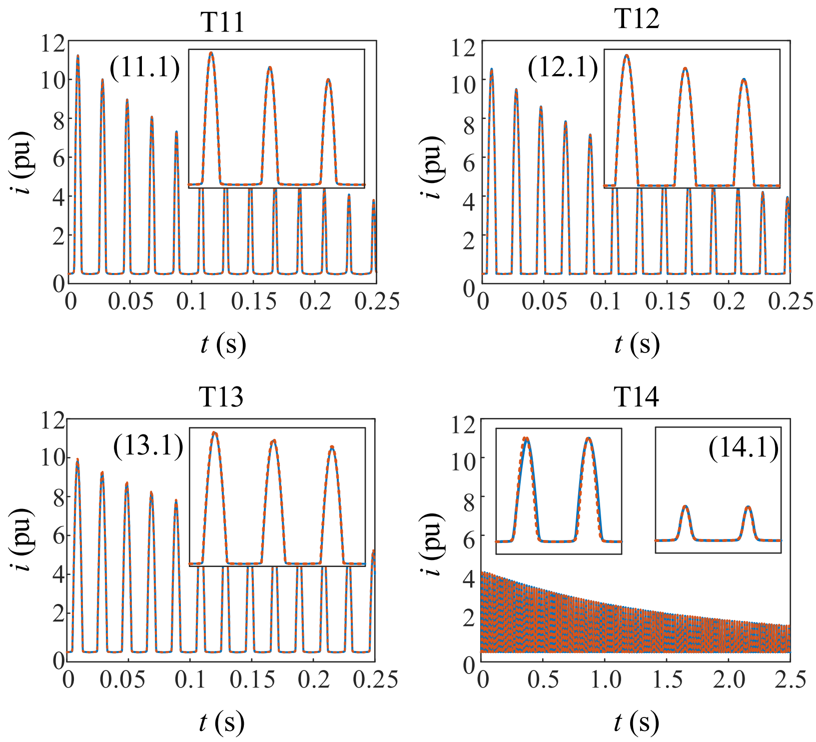

Fig. 4.12. Comparison between the model and the estimated (predicted with the estimated parameters) inrush currents of power transformers T11 to T14. Dotted lines correspond to estimated (predicted) currents.

Table 4.8. Comparison of model and estimated (predicted with the estimated parameters) first peak of the inrush test.

Transformer	T11	T12	T13	T14
Test	11.1	12.1	13.1	14.1
Simulated i_{PEAK} (pu)	11.24	10.55	9.827	4.09
Predicted i_{PEAK} (pu)	11.22	10.52	9.945	4.19
τ (ms)	215.2	243.9	397	2140
Absolute error (pu)	0.02	0.03	0.118	0.10
Relative error (pu)	0.0018	0.0028	0.012	0.024

Chapter 5. Saturation curve estimation of three-phase, three-legged transformers using inrush currents

5.1. Introduction

As explained, power transformer energization may cause large inrush currents when core is saturated. Accurate modeling of the nonlinear magnetizing core of three-phase transformers is an essential subject to efficiently predicts inrush currents. There are different approaches to estimate the saturation curve of three-legged transformers [144], [157]-[175].

The modeling of three-legged transformers is complicated due to the difficulty to obtain all necessary information uniquely from terminal measurements without breaking the winding connection or without using manufacturer data. When a three-legged transformer is energized, the fluxes produced by the phase windings interact with each other. In consequence, the measured currents from a regular three-phase no-load test do not represent the actual magnetizing currents that produce the magnetomotive forces. This phenomenon is known as magnetic coupling or current distortion, because the shape of the currents is distorted, as shown in Fig. 5.1(a), compared with the typical bell shape of the magnetizing current in a single-phase transformer or a three-phase bank, shown in Fig. 5.1(c). Fig. 5.1(b) and Fig. 5.1(d) show the typical ϕ–i loops for three-legged and three-phase bank transformers, respectively. The distortion shows interdependence between the three phases, making the separation of their individual effects a difficult task. To accurately model three-legged transformers, it becomes imperative to consider this magnetic coupling effect.

Some measuring techniques have been proposed in [157]-[165] to disentangle the intertwined currents, enabling a clearer insight into the magnetizing currents. However, these techniques require specific winding connections or different excitations compared to regular operation, making them feasible only in a laboratory. The most notable technique following this approach is the one proposed in [157].

In [166], a methodology is proposed wherein all necessary information can be obtained from measurements taken at the transformer terminals without breaking the winding connections. While this methodology yields good results, it does not consider the deep saturation. The methodology presented in [167] follows a similar approach, but it is very complex since it is based on the finite elements method. Although it considers the deep saturation, the results in this region of the curve are not accurate. The proposal in [168] uses a measured set of inrush currents for the estimation. However, this methodology does not consider magnetic coupling and core asymmetry, limiting its applicability to three-phase banks.

An analytical algorithm is introduced in [144] for both wye and delta connections. It computes the numerical values of the saturation curve by using measurements obtained from single-phase and three-phase inrush and no-load tests. The methodology needs the residual flux value of each inrush test. To estimate it, the proposal requires single-phase tests.

Estimating the saturation curve becomes more difficult with a delta connection in the secondary, as it is necessary to measure the secondary current, which may not be always feasible. Several algorithms that address this issue are proposed in [169]-[171].

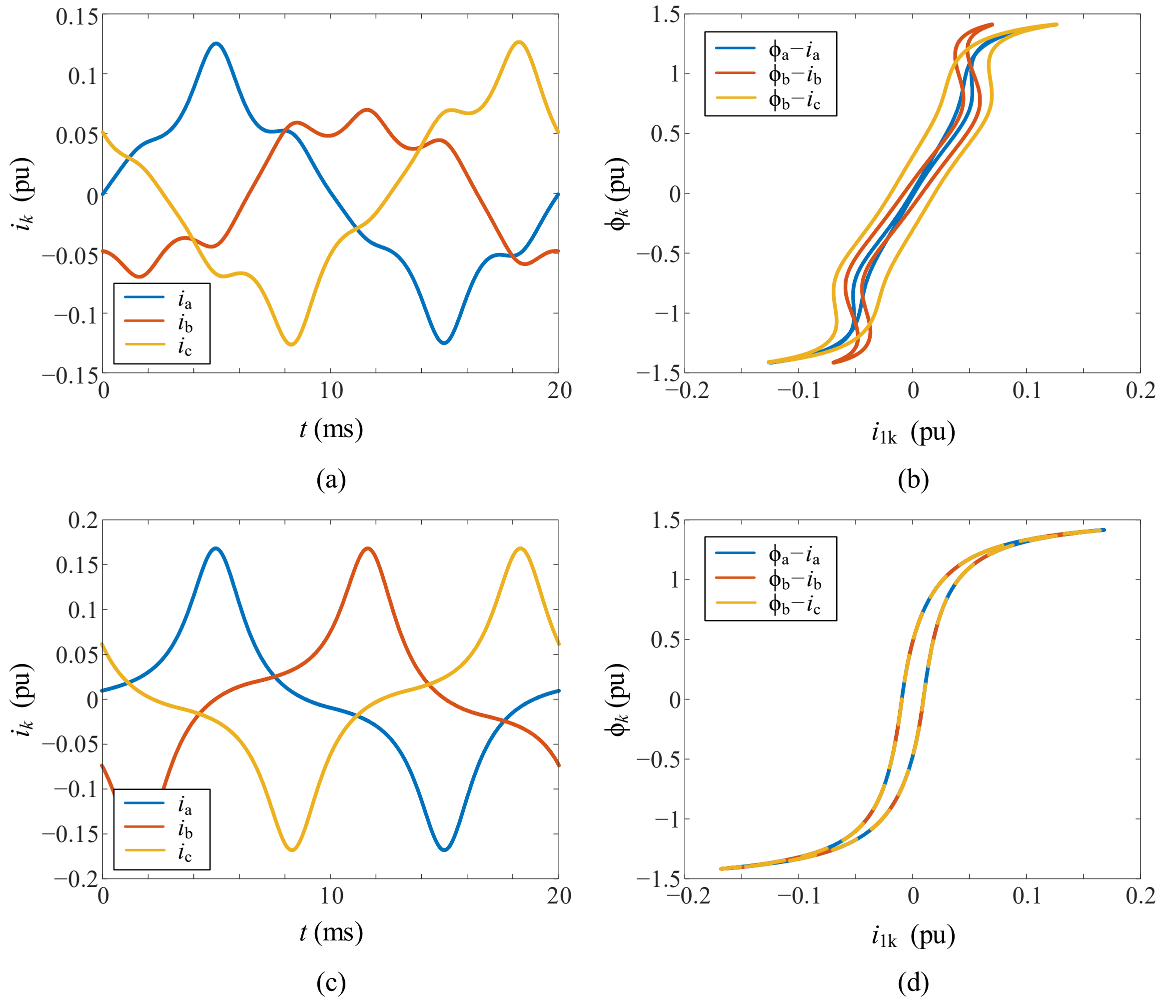

Fig. 5.1. Comparison between typical current waveforms and hysteresis loops during no-load conditions from three-legged transformers and three-phase bank.

They are other approaches based on modern optimization methods (such as Nelder-Mead or PSO) or learning algorithms to estimate the magnetizing characteristics or other parameters of transformers [172]-[175], but most of them are only applicable to single-phase transformers or three-phase banks.

Newer three-legged transformer models have been presented in [176]-[177], as well as several tests to estimate their parameters.

This chapter presents an innovative methodology for the estimation of the saturation curve of three-phase three-legged transformers, including deep saturation and using only one three-phase inrush test and only one three-phase no-load test, both without the need to break the winding connections. This methodology extends the principles outlined in Chapter 4, which were originally developed for single-phase transformers, to the context of three-phase three-legged transformers.

The proposal eliminates the requirement to have knowledge of the residual fluxes, the energization point-on-wave of the used inrush test, and the zero-sequence air path reluctance, as these variables do not affect the methodology. Moreover, there is no requirement to do specific tests. The saturation curve used in previous chapters is also employed in this methodology, which has the usefulness that the involved parameters have a clear physical interpretation. The methodology has been validated with multiple laboratory tests on a small three-phase three-legged transformer and with the inrush measurements during the energization of a 7.5 MVA distribution transformer.

5.2. Transformer model

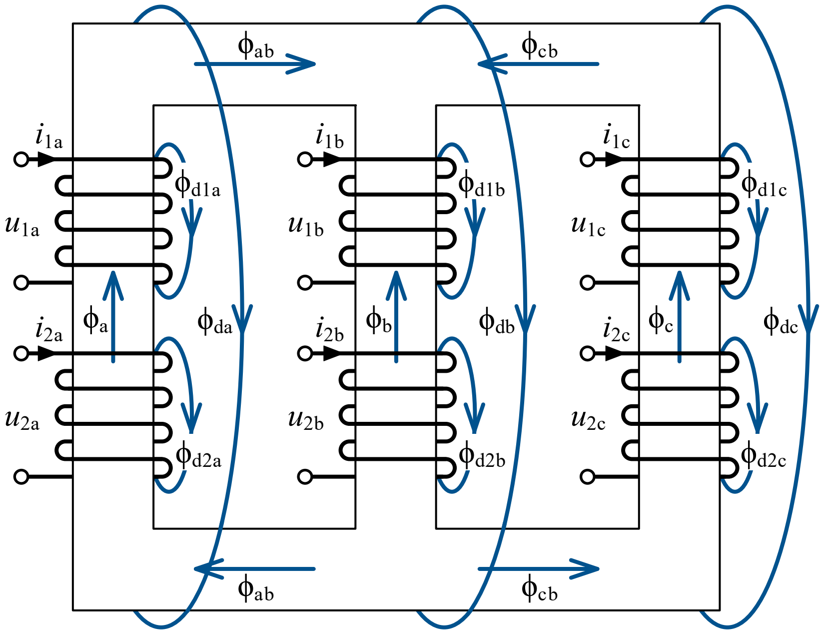

Fig. 5.2. Three-phase, two winding, three-legged transformer.

Fig. 5.2 shows the geometry and the magnetic flux distribution of a three-phase, two-winding, three-legged transformer. In this figure, ϕ_k is the flux at k core leg, ϕ_{d1k} and ϕ_{d2k} are the winding leakage fluxes, ϕ_{ab} and ϕ_{cb}, are the fluxes at the yokes, and ϕ_{da}, ϕ_{db}, and ϕ_{dc} are the fluxes through the air paths.

In this chapter, the transformer is modeled by an electric circuit and a magnetic circuit. This model is simple, but provides accurate results in simulating inrush currents.

5.2.1. Electric circuit

The electric circuit depicted in Fig. 5.3 includes the winding resistances, R_1 and R_2, the linear leakage inductances, L_{d1} and L_{d2}, and the primary and secondary induced voltages, e_{1k} and e_{2k}, induced by the magnetic fluxes across the winding legs, ϕ_k. Iron-core losses, which include eddy and hysteresis losses, are modeled by a constant resistance in parallel with e_{1k}. This resistance is calculated for the nominal frequency.

The electric circuit of the transformer is defined by the following equations

$$
\begin{aligned}
u_{1k} &= R_1 i_{1k} + L_{\mathrm{d}1}\frac{\mathrm{d}i_{1k}}{\mathrm{d}t} + e_{1k}, \qquad e_{1k} = N_1\frac{\mathrm{d}\phi_k}{\mathrm{d}t} \\
u_{2k} &= R_2 i_{2k} + L_{\mathrm{d}2}\frac{\mathrm{d}i_{2\mathrm{k}}}{\mathrm{d}t} + e_{2k}, \qquad e_{2k} = N_2\frac{\mathrm{d}\phi_k}{\mathrm{d}t} \\
i_{1k} &= i_{1\mathrm{m}k} + i_{\mathrm{FE}k} = i_{1\mathrm{m}k} + \frac{N_1}{R_{\mathrm{FE}}'}\frac{\mathrm{d}\phi_k}{\mathrm{d}t}
\end{aligned}
\tag{5.1}
$$

where u_{1k}, u_{2k}, i_{1k}, and i_{2k} represent the voltages and currents of the primary/secondary windings, and N_1 and N_2 denote the number of turns in the primary and secondary windings, respectively, and the currents $i_{\mathrm{FE}k}$ represent the currents through the resistances R_{FE}', which model the core losses.

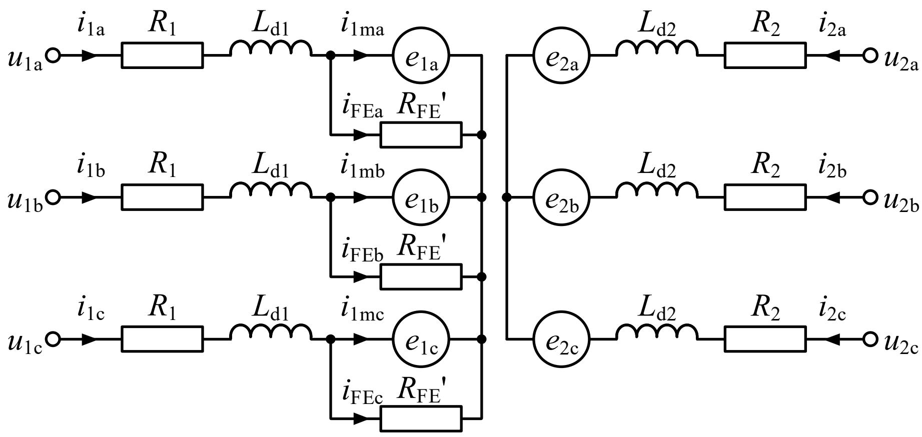

Fig. 5.3. Electric circuit of a Wye-Wye transformer.

5.2.2. Magnetic circuit

Fig. 5.4 depicts the magnetic equivalent circuit of the three-legged iron-core in Fig. 5.2. This magnetic circuit includes the primary and secondary magnetomotive forces, $\mathfrak{F}_{1k}$ and $\mathfrak{F}_{2k}$, which depend on currents $i_{1\mathrm{m}k}$ and i_{2k}. The nonlinear behavior of each core leg is individually represented by a nonlinear reluctance, $\mathfrak{R}_{\mathrm{L}k}$, while the core yokes are characterized by the nonlinear reluctances $\mathfrak{R}_{\mathrm{Yab}}$ and $\mathfrak{R}_{\mathrm{Ycb}}$. The reluctances of the zero-sequence air paths, $\mathfrak{R}_{\mathrm{da}}$, $\mathfrak{R}_{\mathrm{db}}$, and $\mathfrak{R}_{\mathrm{dc}}$, are assumed to be constant. The air paths and fluxes passing through them are different for each leg ($\mathfrak{R}_{\mathrm{d}k}$ and $\phi_{\mathrm{d}k}$). The low values of the yoke reluctances $\mathfrak{R}_{\mathrm{Yab}}$ and $\mathfrak{R}_{\mathrm{Ycb}}$ (when they are not saturated) compared with the high value of $\mathfrak{R}_{\mathrm{da}}$, $\mathfrak{R}_{\mathrm{db}}$ and $\mathfrak{R}_{\mathrm{dc}}$ allows approaching the magnetic circuit in Fig. 5.4 with the simplified magnetic circuit in Fig. 5.5.

In the magnetic equivalent circuit in Fig. 5.5, the nonlinear behavior of each core leg is represented separately from each other by a nonlinear reluctance, $\mathfrak{R}_k$, which depends on its own magnetic potential, f_k. The reluctance of the air path, $\mathfrak{R}_{\mathrm{d}} = \mathfrak{R}_{\mathrm{da}} \| \mathfrak{R}_{\mathrm{db}} \| \mathfrak{R}_{\mathrm{dc}}$, is assumed to be constant. It is assumed that phase b current flows through the winding of the central leg. It is also assumed that the outer core legs (subscripts a and c) length are twice to that of the central leg (subscript b) as the yoke reluctances of Fig. 5.4 have been included into the reluctances of the external legs of Fig. 5.5.

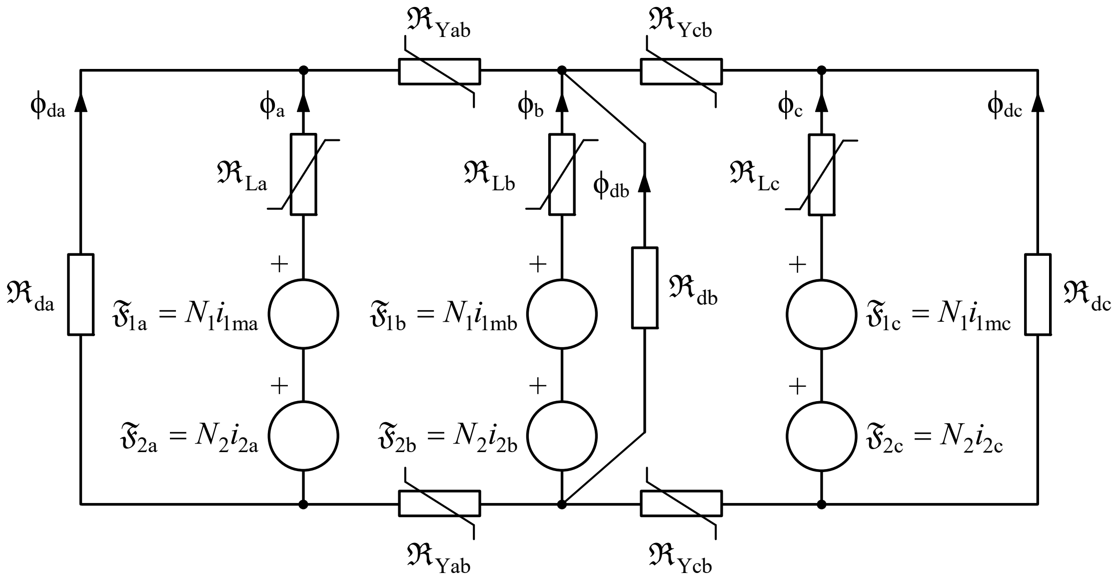

Fig. 5.4. Magnetic equivalent circuit of a three-legged transformer.

The relation between the fluxes and the phase currents given by the simplified magnetic circuit are described by the following equations

$$
\begin{gathered}
N_1 i_{1\mathrm{m}k} + N_2 i_{2k} - f_k + f_{\mathrm{d}} = 0 \\
\phi_k = \frac{f_k}{\mathfrak{R}_k\left(f_k\right)} \\
\phi_{\mathrm{a}} + \phi_{\mathrm{b}} + \phi_{\mathrm{c}} + \phi_{\mathrm{d}} = 0
\end{gathered}
\tag{5.2}
$$

where ϕ_{d} is the flux through the air path and f_{d} is the magnetic potential across the air path.

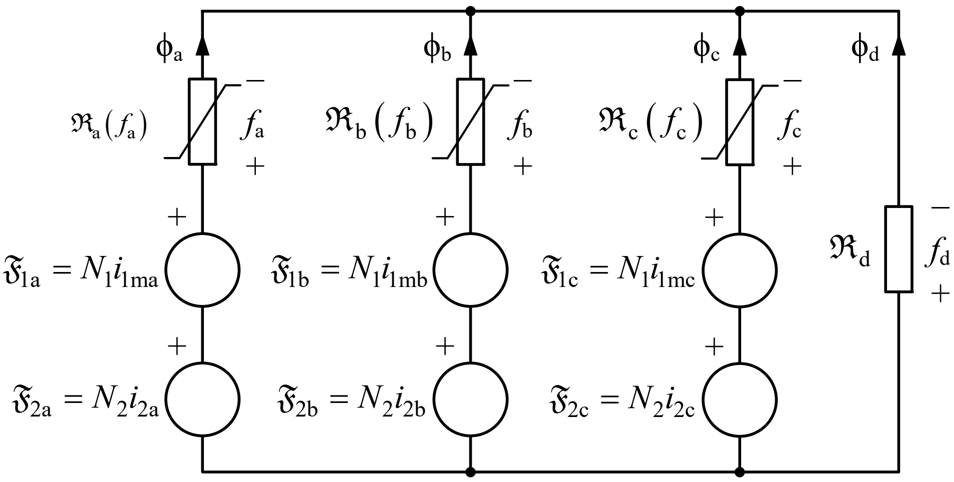

Fig. 5.5. Simplified magnetic equivalent circuit of a three-legged transformer.

5.2.3. Saturation curve

The saturation curve corresponding to the nonlinear reluctances is the same to that used for the single-phase transformer model in Chapter 2. The analytical single-valued function is

$$\Re(f)^{-1} = \frac{K_1}{\left(1+\left(\dfrac{|f|}{f_{\mathrm{KNEE}}}\right)^p\right)^{1/p}} + K_2 \tag{5.3}$$

where K_1, K_2, p and f_{KNEE}, are experimental parameters that allow this single-valued function to be fitted to the transformer saturation curve (ϕ–f).

Transformers are usually designed to operate at a point lightly below the knee point (f_{KNEE}, ϕ_{KNEE}). Due to this, a fifth parameter is introduced, the degree of saturation k_{SAT}, whose value can typically range from 0.4 to 1. With this parameter in mind, f_{KNEE} is defined as

$$k_{\mathrm{SAT}} = \frac{\sqrt{2}\cdot\phi_{\mathrm{N}}}{K_1 f_{\mathrm{KNEE}}} = \frac{\sqrt{2}\cdot\phi_{\mathrm{N}}}{\phi_{\mathrm{KNEE}}} \tag{5.4}$$

where ϕ_{N} is the RMS value of the nominal magnetic flux and ϕ_{KNEE} is the saturation flux, related to f_{KNEE} by K_1.

5.3. Theoretical considerations

5.3.1. Harmonics in the three-phase transformer bank

A three-phase transformer bank consists of a three-phase connection of three single-phase transformers. The main difference with respect to the three-legged transformer is that the magnetic circuits of each phase (of each single-phase transformer) are independent of each other. Consequently, there is no interaction between the three magnetic fluxes. The magnetic circuit of this transformer can be modeled with the equivalent circuit of the three-legged transformer, but considering that the columns a, b, and c are identical, and considering that the reluctance $\Re_{\mathrm{d}}$ is equal to zero, as depicted in Fig. 5.6.

The harmonics in a three-phase transformer bank depend on the winding connections, so the waveform of the no-load currents is not always the same as that of a single-phase transformer.

For a primary grounded wye connection with the secondary windings disconnected (YN connection), if the bank is energized with a symmetrical and balanced voltage system, the resulting fluxes and the secondary voltages are purely sinusoidal, with the same amplitude and shifted 120º among them. In these conditions, the no-load currents are similar to that of a single-phase transformer. The harmonic components of the three currents have the same amplitude and are shifted 120º between the three currents (in a direct- or inverse-sequence), except for the third harmonic. The third harmonics have the same amplitude and are also in phase, meaning they are in zero-sequence. Since the sum of the components in direct- or inverse-sequence is zero, only the sum of the third harmonics circulates through the neutral of the primary connection.

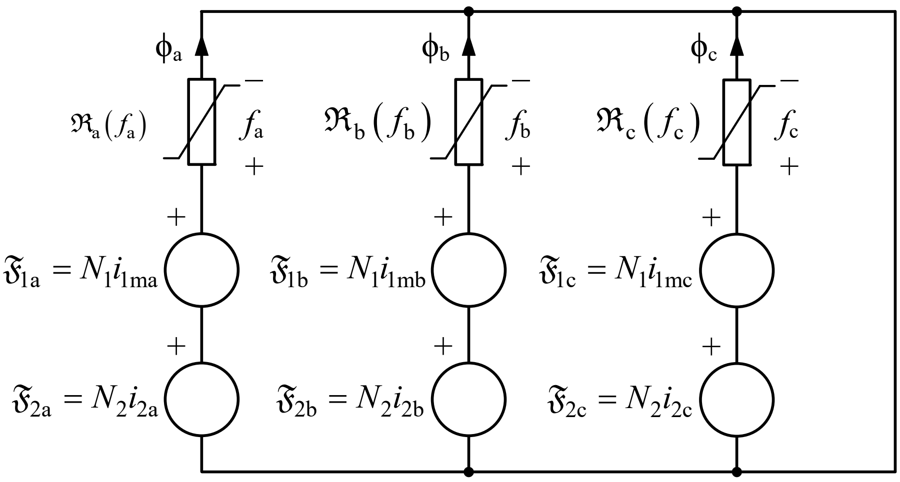

Fig. 5.6. Magnetic equivalent circuit of a three-phase transformer bank.

When the neutral is disconnected from the primary windings (Y connection), the third harmonics cannot circulate through any wire and therefore disappear. In this case, the magnetizing current waveforms do not have the typical bell-shape and the fluxes as well as the primary and secondary voltages become distorted due to the presence of third harmonics. If both windings are ungrounded wye connected (Yy), it is clear that all current, voltage, and flux waveforms remain the same, because again, there is not any possibility for the circulation of the third harmonics. However, it is important to note that the composite secondary voltages are purely sinusoidal in this situation. Conversely, if the wye connected secondary supplies a three-phase load with the neutral connected (transformer connection is then Yyn), the third harmonics can circulate through this neutral wire. However, the three-phase bank with this connection is not commonly used.

When the three-phase bank has a primary grounded connection and a secondary delta connection (YNd) at no-load conditions, the third harmonic circulates by both the primary and the secondary windings. Note that by the secondary winding (delta) only circulates third harmonic. With this type of winding connection, the magnetic potentials are composed by the primary (magnetizing) and the secondary currents, $f_k = N_1 i_{1mk} + N_2 i_{2k}$. Therefore, the primary (magnetizing) currents i_{1mk} have the typical bell-shape waveforms, and the fluxes and voltages are sinusoidal. If the neutral wire is disconnected from the primary windings (Yd connection), the third harmonics disappear from the primary windings, and only circulate by the secondary winding (connected in delta).

Finally, if the primary windings are delta connected and the secondary windings have any connection (Dd, or Dy), it is clear that the third harmonics can circulate through the primary delta winding, without any problem.

5.3.2. No-load currents and harmonics in the three-phase three-legged transformer

The behavior of the three-legged transformer in terms of harmonics is different from that of the three-phase bank.

Firstly, the sum of the fluxes in the three-phase bank may not be zero, while in the three-legged transformer the sum must be zero (assuming an infinite $\Re_d$) or near zero (a large $\Re_d$). Thus, the zero-sequence flux is null or small. For this reason, the behavior of the three-legged transformer with Yy winding connection is different from that of the three-phase bank. The fluxes and voltages with this winding connection are quasi-sinusoidal, and the no-load currents do not contain third harmonics (assuming the three core legs are of equal length). This is because in the three-legged transformers the relationship ϕ_k–i_{1mk} does not match the relationship ϕ_k–f_k (or B–H relationship of the respective leg). In this type of transformers with Yy connection and no-load conditions it follows that

$$\phi_k = \frac{N_1 i_{1mk} + f_d}{\Re\left(i_{1mk},\ f_d\right)} \tag{5.5}$$

where f_d depends on ϕ_a, ϕ_b, and ϕ_c, therefore:

$$\phi_k = \frac{N_1 i_{1mk} + f_d}{\Re\left(i_{1mk},\ \phi_a,\ \phi_b,\ \phi_c\right)} \tag{5.6}$$

that is, each core leg flux depends on the other core leg fluxes, the three core legs interact among them (magnetic cross-coupling). This interaction is responsible for the fact that the no-load current waveforms in a three-legged transformer do not have the typical bell-shape, but are distorted.

However, the core legs in a true three-legged transformer are of different lengths (the outer legs length can be considered around twice to that of the central leg), that is, the core has an asymmetrical design. Due to this, in a true three-legged transformer with Yy winding connection, the third harmonics are not of zero-sequence (the third harmonic of the central leg is shifted 180º with respect to the other third harmonics), which allows the presence of third harmonics in the no-load currents even if the neutral wire is unconnected. Despite this, the fluxes may not be purely sinusoidal as they may have small odd harmonics (depending on $\Re_d$), which, however, can be ignored from a practical point of view. Even if the primary neutral wire is connected (YNy), the third harmonics in the no-load currents are not of zero-sequence due to the core asymmetry. For the secondary windings with a delta connection (YNd or Yd), the current inside de delta wingings also contain odd harmonics besides to the fundamental component.

Finally, when the primary windings are delta connected (Dd or Dy) the no-load currents harmonics can circulate without any limitation, leading to quasi-sinusoidal fluxes.

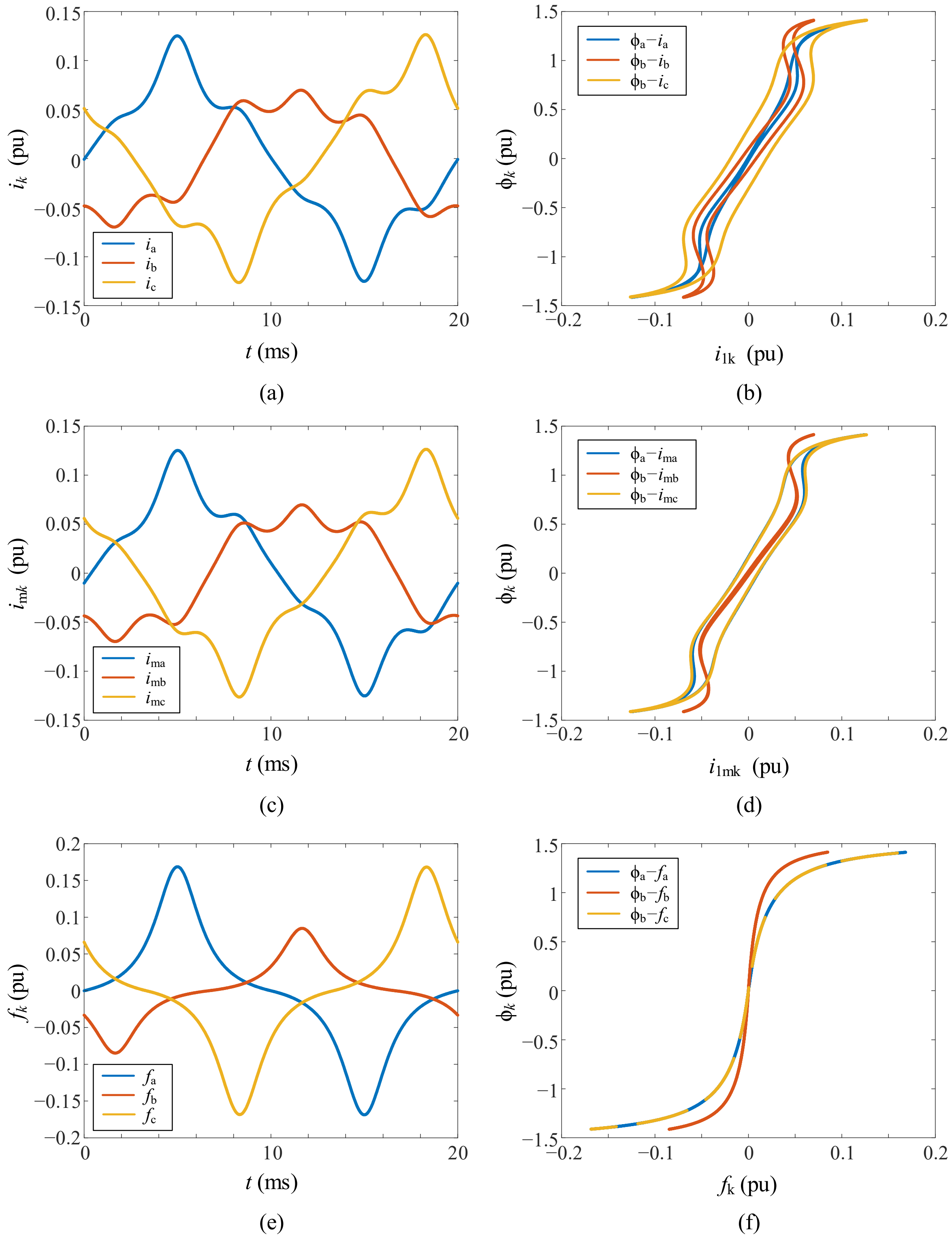

Fig. 5.7. Simulated transformer T31 (100 kVA) with Yy connection.

Fig. 5.7 illustrates the typical waveforms of the currents and loops for a three-legged transformer with Yy connection (they are similar for the YNy connection). Fig. 5.7(a) depicts the no-load currents waveform without the bell-shape (distorted), while the corresponding ϕ_k–i_k loops are depicted in Fig. 5.7(b). It can be seen clearly that the current of the central leg is of lower magnitude, due to the lower length of this core leg. Fig. 5.7(c) and Fig. 5.7(d) illustrate the magnetizing currents and the respective ϕ_k–i_{mk} loops, that is, the no-load currents and the loops without taking into account the core losses. It is important to note that despite the absence of core losses and despite the use of an anhysteretic curve for the core, the loops in Fig. 5.7(d) still have an area, which does not occur in a three-phase bank or a single-phase transformer when the core is also modeled with an anhysteretic curve. This phenomenon is due to the magnetic cross-coupling. Fig. 5.7(e) and Fig. 5.7(f) depict the magnetic potentials and the respective saturation curves. It can be seen that the magnetic potentials are not distorted, and they have the typical bell-shape waveforms.

5.3.3. Inrush currents in the three-phase three-legged transformer

According to (5.6), each core leg flux depend on all the fluxes at every time. Due to this, a phase current during the inrush is always influenced by the other phase currents. For instance, consider the simulation of the transformer T31 (100 kVA), depicted in Fig. 5.8. In this simulation, an infinite K_1 (slope of the linear part of the saturation curve) has been assumed for the three core legs.

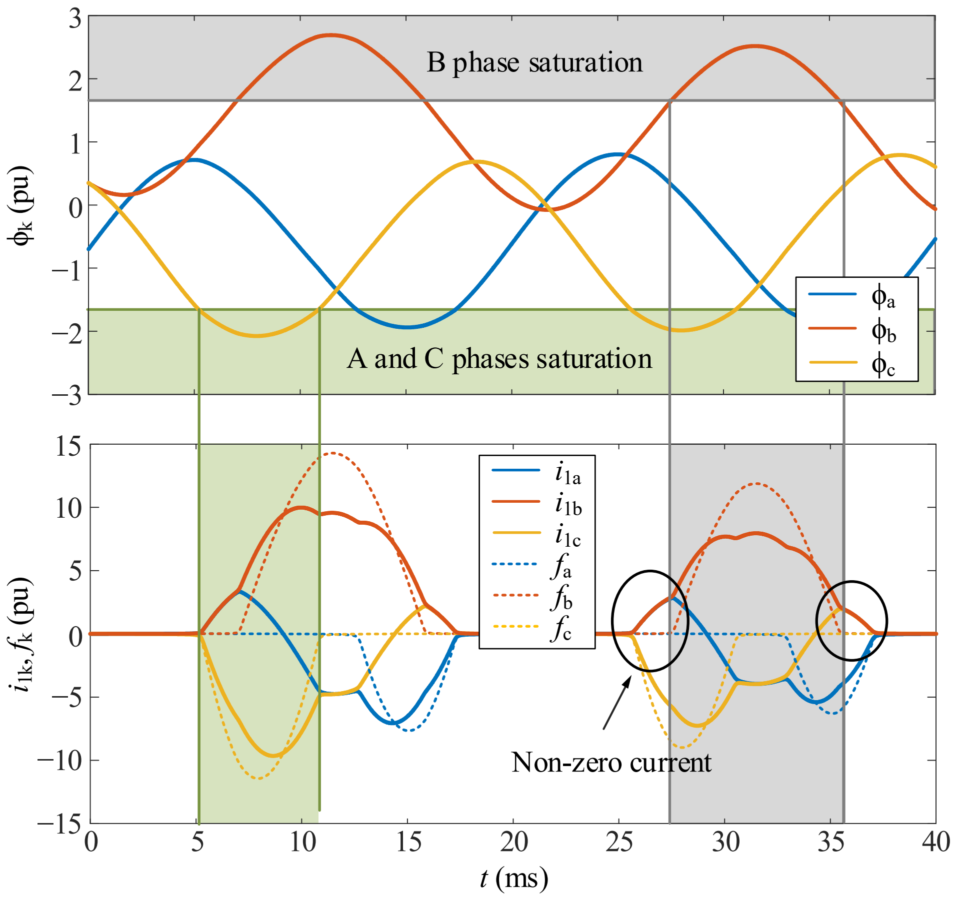

Fig. 5.8. Illustrative fluxes, currents and magnetic potentials during the inrush of the simulated transformer T31 (100 kVA) with Yy connection.

It can be seen that after the transformer energization, all three core legs are unsaturated (each leg corresponds to each phase). After a while, the A phase enters into saturation, causing the respective magnetic potential f_a and the corresponding current i_{1a} to increase. At this moment, the other two phases remain unsaturated, but it can be seen that their respective currents also start to increase, despite their respective magnetic potentials do not increase (they remain null). During these conditions, $f_b = 0$ and $f_c = 0$, therefore, the magnetic circuit of the transformer is equivalent to that depicted in Fig. 5.9 (assuming an infinite K_1 for the three core legs). According to this circuit, the magnetizing currents i_{mb} and i_{mc} must be the same, and the following equation is accomplished:

$$f_d = f_a - N_1 i_{ma} = -N_1 i_{mb} = -N_1 i_{mc} \tag{5.7}$$

This means that the inrush currents during unsaturated conditions of their respective core legs must be very similar (they are not identical because of the core losses). As a consequence, during each cycle, the inrush currents may have one, two or even three peaks, although only one of them is due to the saturation of the corresponding core leg.

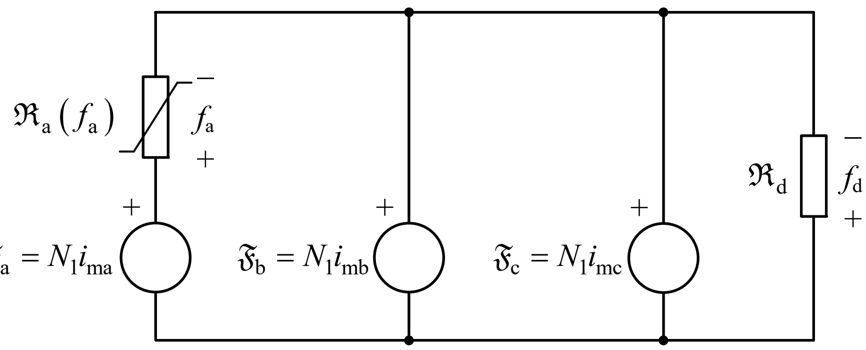

Fig. 5.9. Magnetic circuit during the saturation of the leg corresponding to phase a, while the other legs are unsaturated.

Other important notes on inrush currents in the three-legged transformer are:

- All three phases can never be saturated at the same time (only two of them at most).
- With YNy and Yy winding connections, the magnetic potential of the air branch f_d, is equal to the respective non-saturated current at each moment but with opposite polarity, according to (5.7). This is not true for primary delta connections.
- After an uncontrolled energization, when all three phases are connected at the same time, at least one of the three phases will be saturated.
- Ideally, the three residual fluxes always add up to zero.

Fig. 5.10 shows some inrush currents from the simulated transformer T31 with different winding connections (YNy, YY, YNd and Yd), while Fig. 5.11 depicts the inrush currents for Dy connection. It can be seen that the magnetic potential of the air branch f_d multiplied by -1 for YNy and Yy connections, equals the respective non-saturated current at each time, which is not true for primary delta connections (Fig. 5.11). Also, it can be appreciated that the grounded connections allow a non-zero neutral current.

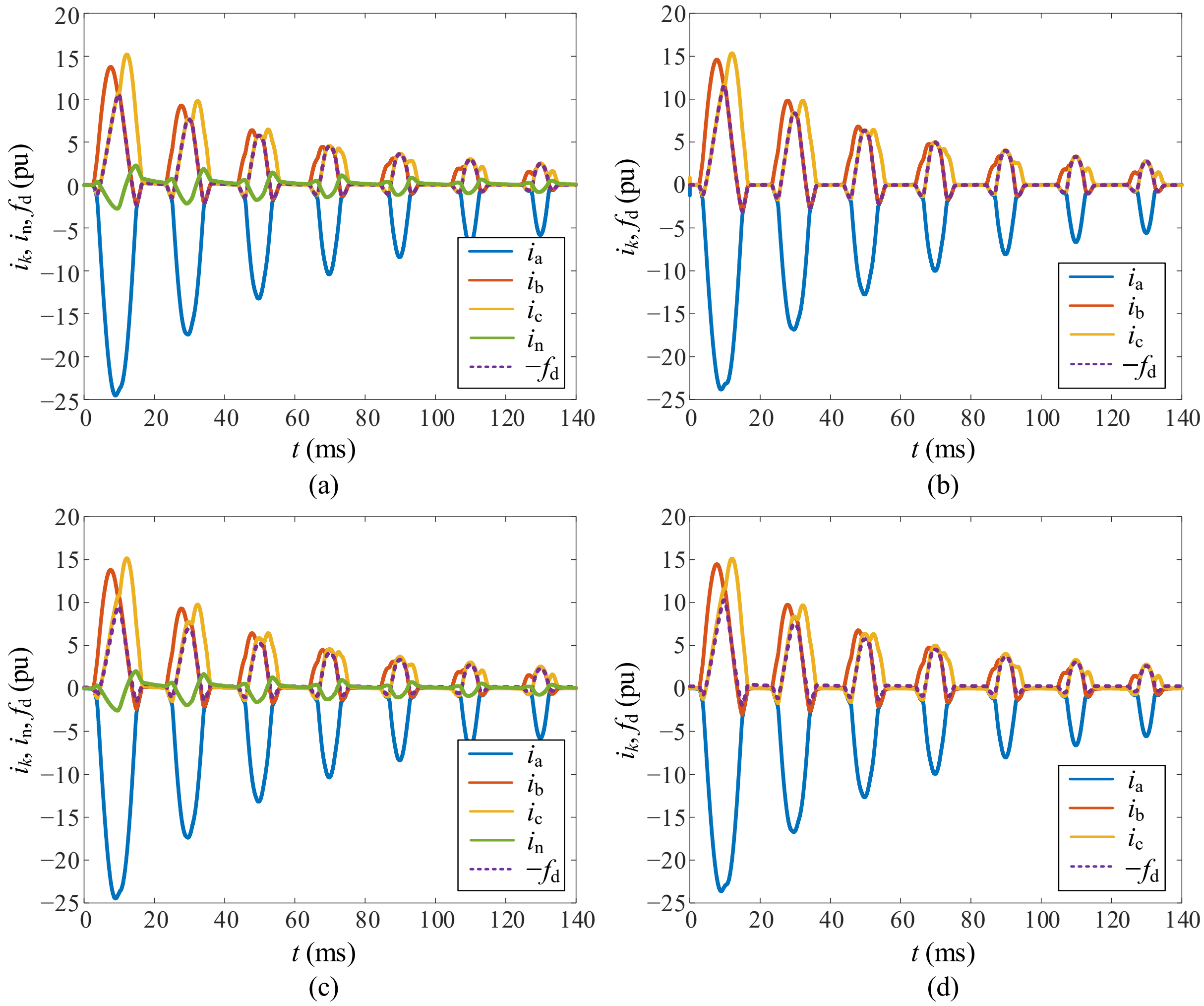

Fig. 5.10. Inrush currents from the simulated transformer T31 (100 kVA) with (a) YNy connection, (b) Yy connection, (c) YNd connection, and (c) Yd connection.

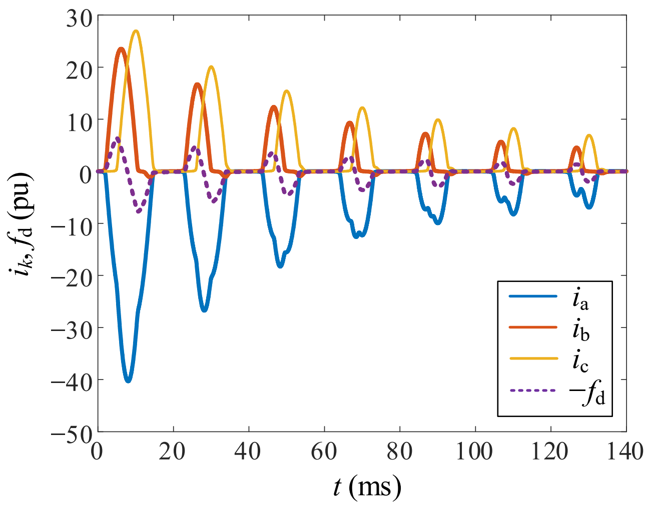

Fig. 5.11. Inrush currents from the simulated transformer T31 (100 kVA) with Dy connection.

5.4. Estimation methodology

In Chapter 4, a methodology was proposed for estimating the saturation curve parameters of single-phase transformers. This chapter extends the methodology to include three-phase three-legged transformers.

The estimation of K_2 was based on the inrush current damping. The envelopes of all possible inrush currents of a given single-phase transformer match a segment of the most severe case's envelope, regardless of the residual flux value and regardless of the energization point-on-wave, α_E. This is true because the inrush current damping in a single-phase transformer is affected only by the winding longitudinal impedance and the K_2 slope (assuming an infinite K_1 slope). The flux, and therefore the inrush current, is damped only during saturation lapses, as the current is null when there is no saturation. Thus, the K_2 value can be directly related to the damping of the inrush current. However, this is not possible for three-legged transformers. As has been explained, a non-zero current continues to circulate through a phase even if the respective core leg is not saturated (as illustrated in Fig. 5.8 for transformer T31), which causes the respective flux to be damped even without saturation, i.e., it is damped all the time until it reaches the steady state. Unlike single-phase transformers, the evolution of a phase inrush current in a three-legged transformer depends on all three phases. This is why the methodology for single-phase transformers in Chapter 4 cannot be directly applied to three-legged transformers. This situation suggests that for K_2 estimation, the three currents should be considered collectively as a single entity at any instant.

Estimating the rest of parameters (K_1, p and k_{SAT}) for single-phase transformers was based on the harmonic distortion of no-load currents, specifically the third and fifth harmonics. This approach cannot be directly applied to three-legged transformers due to interaction between the fluxes of the core legs. As explained in Subsection 5.3.2, the relationship ϕ_k–i_{1mk} does not match the relationship ϕ_k–f_k. In other words, the equivalence between magnetic potential and magnetizing current (which is present on a no-load single-phase transformer) is not fulfilled in three-legged transformers, as shown in first equation of (5.2) and in (5.5). This implies that, to estimate the parameters K_1, p and k_{SAT}, it is necessary the knowledge of the magnetic potentials harmonics instead of the no-load currents harmonics.

The general block scheme of the proposed methodology is depicted in Fig. 5.12, which is divided into two stages. In Stage 1, the parameter K_2 is estimated using as information the recorded current and voltage waveforms from only one inrush test. The values of R_1 and L_{d1} are needed (they are obtained from the classical short-circuit test). In Stage 2, only the waveforms of the three no-load currents at steady state (wye-wye or wye-delta connections) are used to estimate the parameters K_1, p, and k_{SAT}, which can be different for each leg.

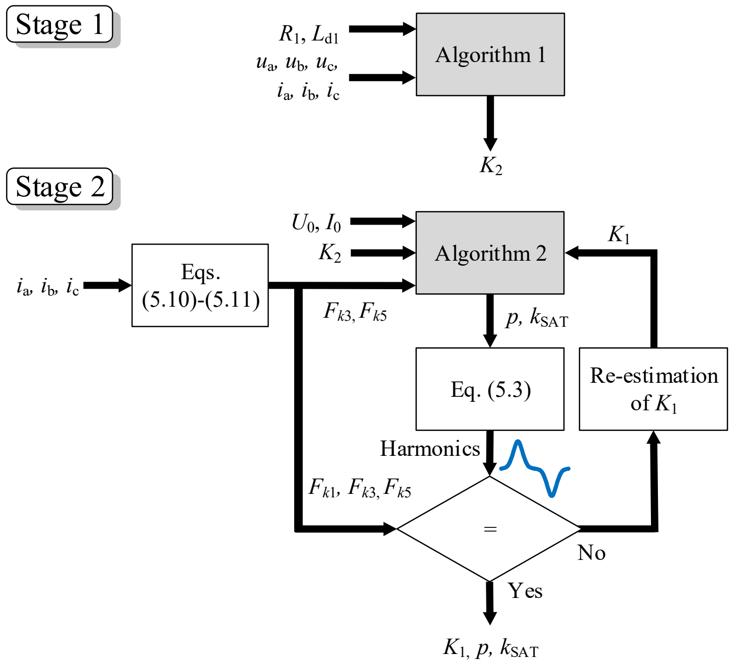

Fig. 5.12. Schematic representation of the saturation curve estimation.

5.4.1. Stage 1: K_2 estimation

The K_2 estimation is inspired on the "p-q theory" in [178], which considers the three-phase systems as a unit, not a superposition or sum of three single-phase circuits.

The algorithm uses a novel equation for the instantaneous reactive power which flows between the grid and the entire three-phase transformer during the inrush, evaluated as

$$q(t) = \frac{1}{\omega}\left(-\omega u_d i_q + \omega u_q i_d + u_0 \frac{di_0}{dt} + u_d \frac{di_d}{dt} + u_q \frac{di_q}{dt}\right) \tag{5.8}$$

where u_d, u_q, u_0, i_d, i_q, and i_0 are the supply voltages and the consumed currents in the dq0 reference frame, and ω is the supply pulsation. Voltages and currents are defined by the Park's transformation as

$$\begin{bmatrix} x_d \\ x_q \\ x_0 \end{bmatrix} = \sqrt{\frac{2}{3}} \begin{bmatrix} \cos(\theta) & \cos\left(\theta - \frac{2\pi}{3}\right) & \cos\left(\theta + \frac{2\pi}{3}\right) \\ -\sin(\theta) & -\sin\left(\theta - \frac{2\pi}{3}\right) & -\sin\left(\theta + \frac{2\pi}{3}\right) \\ \sqrt{\frac{1}{2}} & \sqrt{\frac{1}{2}} & \sqrt{\frac{1}{2}} \end{bmatrix} \begin{bmatrix} x_a \\ x_b \\ x_c \end{bmatrix} \tag{5.9}$$

where x can be either a current i or a voltage u, and θ is the Park's transformation angle: $\theta = \omega t$.

From the instantaneous reactive power, $q(t)$, it is calculated the average value for each period, resulting a new signal, $Q(t)$. Fig. 5.13(a) illustrates $q(t)$ and $Q(t)$ for the simulated transformer T31. The maximum value of $Q(t)$ is called Q_{MAX}, and the elapsed time until $Q(t)$ has decreased to a 37% of

Q_{MAX} value, is called τ. These values are illustrated in Fig. 5.13 (a). By repeating all possible inrush cases to a given transformer, a set of Q_{MAX}-τ points are obtained, as illustrated with the circles of Fig. 5.13 (b). These possible inrush cases are obtained by modifying the residual flux values and/or the energization point-on-wave, α_E.

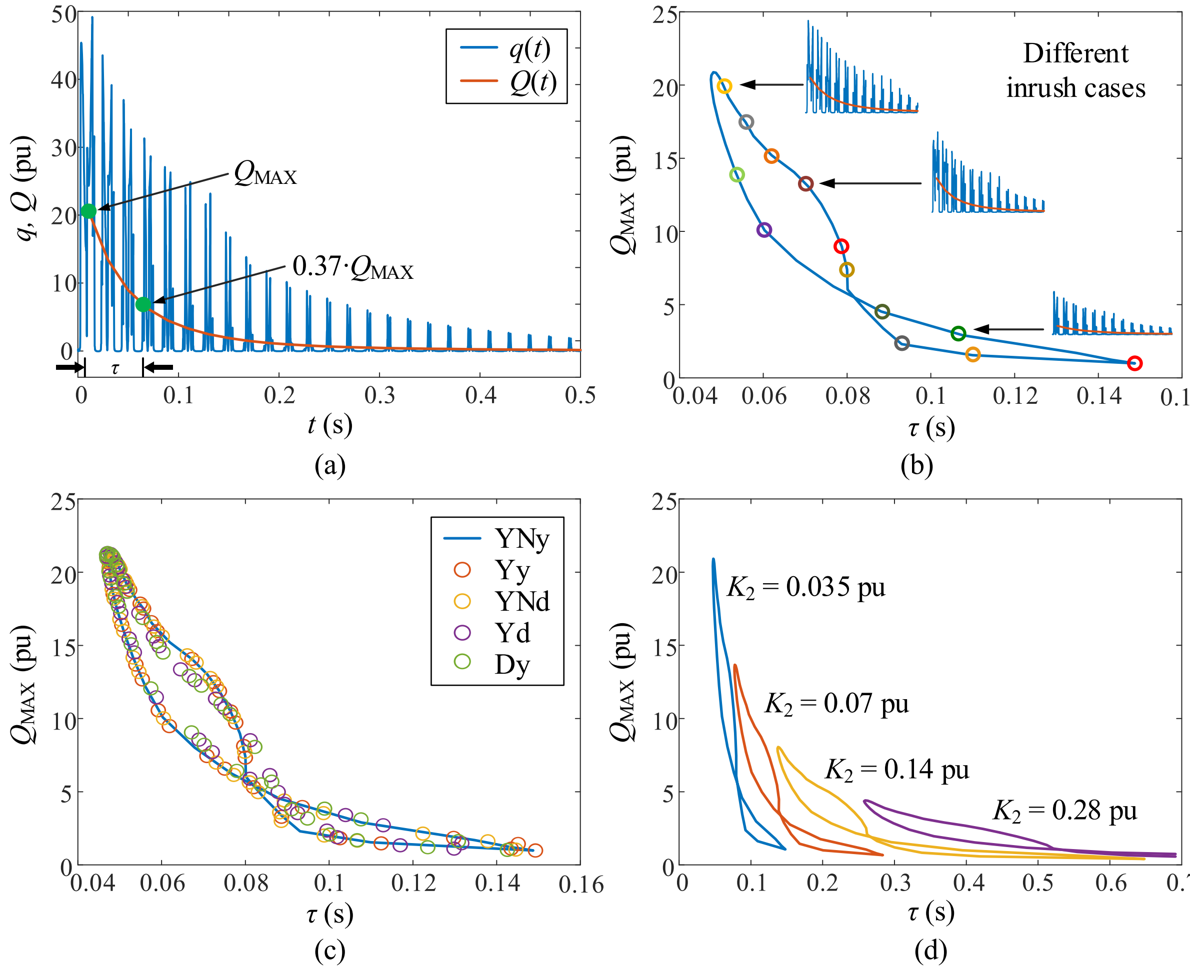

Fig. 5.13. (a) Magnitudes q(t) and Q(t), (b) generation of a Q_{MAX}–τ curve from several inrush cases, (c) Q_{MAX}–τ curves for different winding connections, and (d) Q_{MAX}–τ curves for different K_2 values..

It has been verified by extensive simulations (and by laboratory measurements as shown in next section) that all possible Q_{MAX}-τ points (from all possible inrush cases) approximately fall around a unique Q_{MAX}–τ curve, as illustrated in Fig. 5.13(b). Furthermore, it has also been verified by extensive simulations (and by laboratory measurements) that, for the different winding connections, the Q_{MAX}-τ points approximately fall again around the same Q_{MAX}–τ curve, as illustrated in Fig. 5.13(c). In consequence, this curve can be considered as a "signature" of such three-legged transformer.

Lastly, it has also been verified through extensive simulations that the shape of the Q_{MAX}–τ curve is almost insensitive to the parameters K_1, p k_{SAT}, $\mathfrak{R}_0$, and R_{FE}, and it is only sensitive to R_1, L_{d1}, and K_2. Lastly, Fig. 5.13(d) shows a set of these curves for different K_2 values.

The K_2 estimation procedure requires a simulated set of Q_{MAX}–τ curves: a different curve for a different supposed value of K_2, e.g., the four curves of Fig. 5.13(d).

As was explained, the Q_{MAX}–τ curve shown in Fig. 5.13(b) can be obtained through multiple inrush cases for α_E ranging from 0° to 360°. In our experience, the number of simulations can be reduced to only two distinct inrush cases (α_E = 60° and 120°). These α_E values have been chosen empirically to obtain the best results. From these two inrush cases, the two $Q(t)$ signals and the two Q_{MAX}–τ curves of Fig. 5.14 are obtained. Note that the Q_{MAX}-τ points for each curve are obtained from the same $Q(t)$ signal. The final approach for the Q_{MAX}–τ curve is the average curve of the two preceding ones.

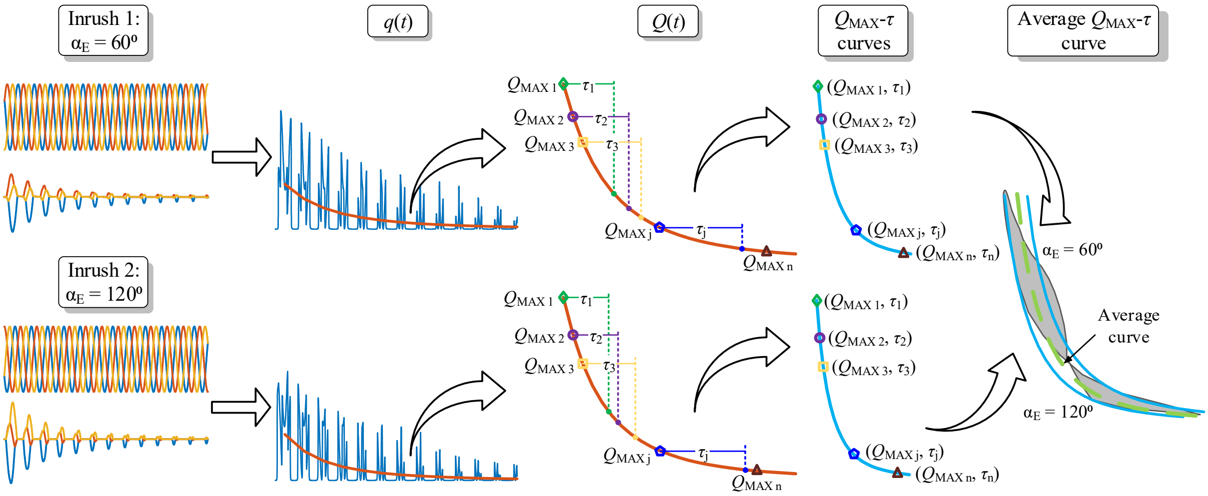

Fig. 5.14. Proposed approach for the Q_{MAX}–τ curve by using only two simulated inrush cases (α_E = 60° and 120°).

The steps of Algorithm 1 (Fig. 5.15) for K_2 estimation are as follows:

1. R_1 and L_{d1} are estimated from the classical short-circuit test.

2. A value for K_2 is assumed within a typical range (according to the rated power of the transformer).

3. The Q_{MAX}–τ approached curve (as that in Fig. 5.14) is calculated for the assumed K_2 value. For these calculations, any winding connection (e.g. YNy) and any residual flux values can be used, but it is more practical to use the following empirical values: $\phi_{R,a}$ = 1.0 pu, $\phi_{R,b}$ = –0.5 pu, $\phi_{R,c}$ = –0.5 pu.

4. The two previous steps are repeated for all assumed K_2 values, to obtain a set of Q_{MAX}–τ curves.

5. Finally, the K_2 parameter is estimated from the calculated set of Q_{MAX}–τ approached curves, using the Q_{MAX} and τ values obtained from the unique measured inrush test, as illustrated in Fig. 5.16.

In summary, the K_2 estimation of the tested transformers in this chapter only required 20 inrush simulations (for 10 different K_2 values and for the 2 commented α_E values) and only one measured inrush test. This illustrates the simplicity of the method.

As mentioned earlier, the Q_{MAX}-τ curve and its approach are only sensitive to K_2 and to the winding leakage impedance. Thus, an error in the winding leakage impedance could lead to an error in K_2 estimation.

During this Stage 1, it is considered a K_2 value for the central leg twice to that of the outer legs.

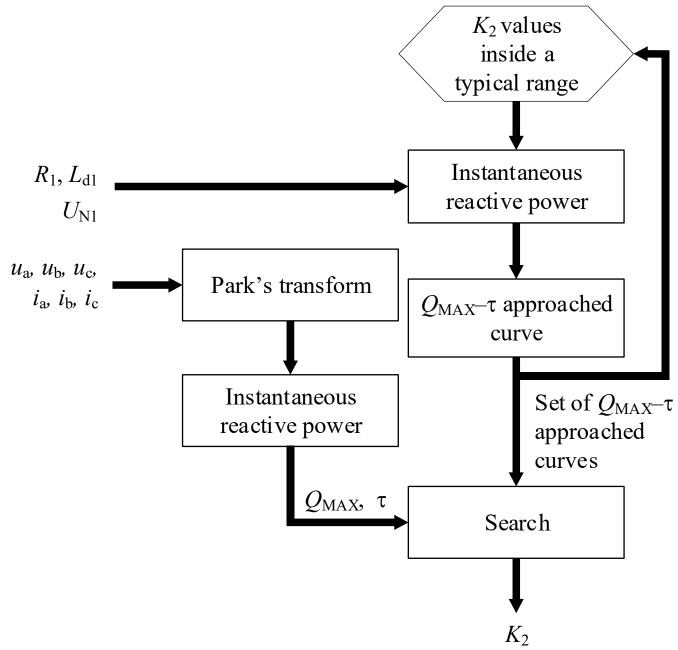

Fig. 5.15. Flowchart of Algorithm 1.

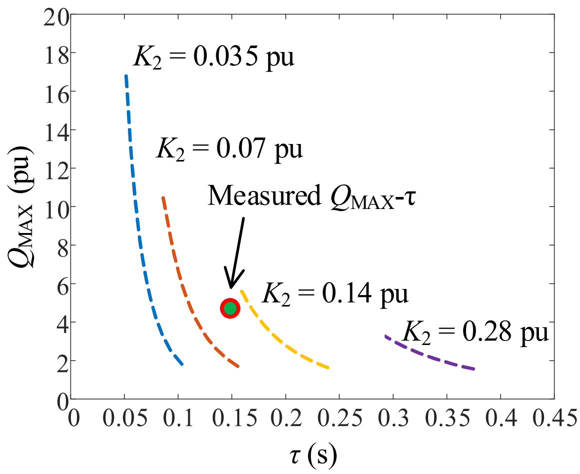

Fig. 5.16. Search of K_2 from the measured inrush test and the Q_{MAX}-τ approached curves.

5.4.2. Stage 2: K_1, p and k_{SAT} estimation

Stage 2 cannot be applicable to Delta-connection in the primary winding by using the line currents; it is necessary to use the phase currents, which cannot be measurable in most practical cases.

In opposite to the single-phase core, the harmonics of the no-load currents of a three-legged transformer are not useful for estimation purposes. It is necessary to obtain the harmonics of the magnetic potentials f_k, which directly depend on $\mu_r = K_1/K_2$, p, and k_{SAT}.

It is assumed that phase *b* current flows through the winding of the central leg. It is also assumed that the outer core legs (subscripts *a* and *c*) length are twice to that of the central leg (subscript *b*). In this case, the third harmonic of f_k can be approached by

$$F_{a3} \approx \left[2N_1\left(i_a - i_b\right)\right]_3 \approx 2 \cdot F_{b3}, \quad F_{c3} \approx \left[2N_1\left(i_c - i_b\right)\right]_3 \tag{5.10}$$

This equation only applies to the third harmonics. It must be noted that, despite the transformer is three-legged, a small quantity of third harmonic component in the line currents is present due to the asymmetric core design.

The fundamental and the fifth harmonic of f_k are considered to be of positive- and negative-sequence, respectively. Both components of f_k can be approached by

$$\begin{aligned} F_{k1} &\approx \left[N_1 i_k - N_1\left(\frac{i_a}{4} + \frac{i_b}{2} + \frac{i_c}{4}\right)\right]_1 \\ F_{k5} &\approx \left[N_1 i_k - N_1\left(\frac{i_a}{4} + \frac{i_b}{2} + \frac{i_c}{4}\right)\right]_5 \end{aligned} \tag{5.11}$$

The procedure to estimate K_1, p, and k_{SAT} for each leg is shown in Fig. 5.12 and described below. As K_2 has been previously estimated, an initial value of K_1 is assumed from no-load measurements, i.e. U_0/I_0 in pu. Then, the parameters p and k_{SAT} are estimated with Algorithm 2, which will be explained below. Using these saturation curve parameters, the steady-state magnetic potential is calculated for any leg as follows: as $f_k = \phi_k \cdot \Re_k(f_k)$ and assuming ϕ_k is sinusoidal with a RMS value of 1 pu, the f_k waveform can be evaluated. Then, the fundamental and the two first odd harmonics of this magnetic potential (F_{k1}, F_{k3}, and F_{k5}) are compared with those previously estimated from measurements. If these values are not similar, the value of K_1 is modified and the whole process is repeated. The estimation process is finished when the values are similar (with an error lower to 10%).

The Algorithm 2 is detailed in Fig. 5.17, and it is composed by the following steps:

1. A pair of values for p and k_{SAT} is assumed to be known, with p ranging from 0.3 to 5 and k_{SAT} ranging from 0.3 to 1.

2. As K_2 has been previously estimated and p, k_{SAT} and K_1 have been assumed, a saturation curve can be constructed for this iteration. Then, a magnetic potential is simulated using (5.3) and assuming a pure sinusoidal flux with a RMS value of 1 pu.

3. The harmonic content of the simulated magnetic potential, F_{k1}, F_{k3} and F_{k5}, is calculated by using the Fast Fourier Transform (FFT).

4. The previous steps are repeated for all assumed combinations of p and k_{SAT}. Then, two surfaces for F_{k3} and F_{k5} depending on p and k_{SAT} are obtained, as those depicted in Fig. 5.18(a).

5. The spectrum of the *k* magnetic potential, F_{k1}, F_{k3} and F_{k5}, are calculated from no-load currents measured at the laboratory, according to (5.10) and (5.11).

6. A perpendicular plane to the z-axis intersects each of the surfaces at the corresponding F_{k3}

and F_{k5} values of the previous step, resulting in the two curves of Fig. 5.18(b). The intersection point between these curves yields the p and k_{SAT} estimation.

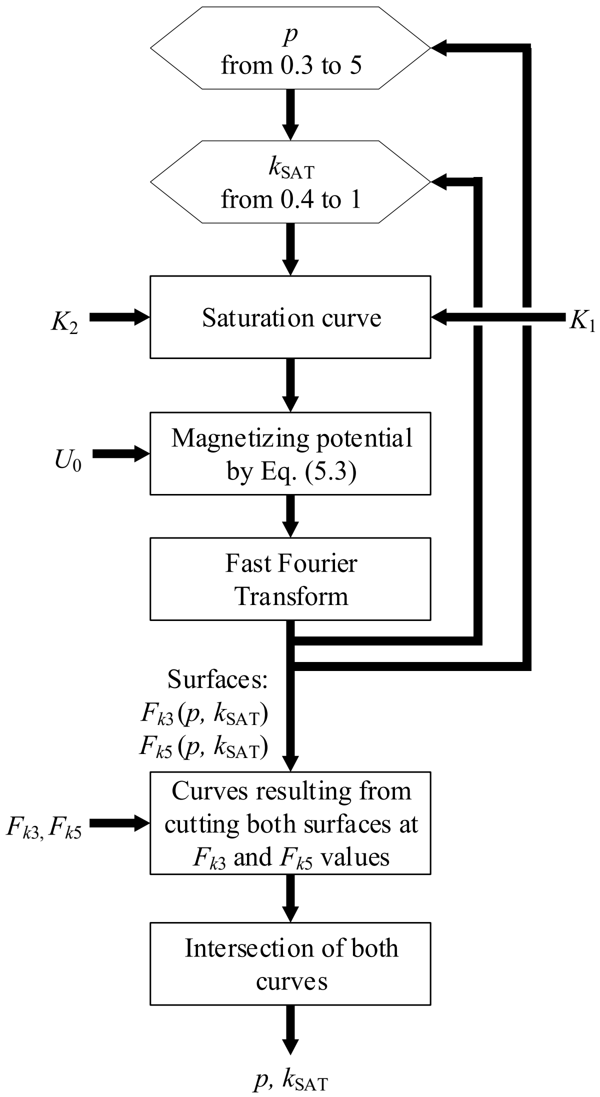

Fig. 5.17. Flowchart of Algorithm 2.

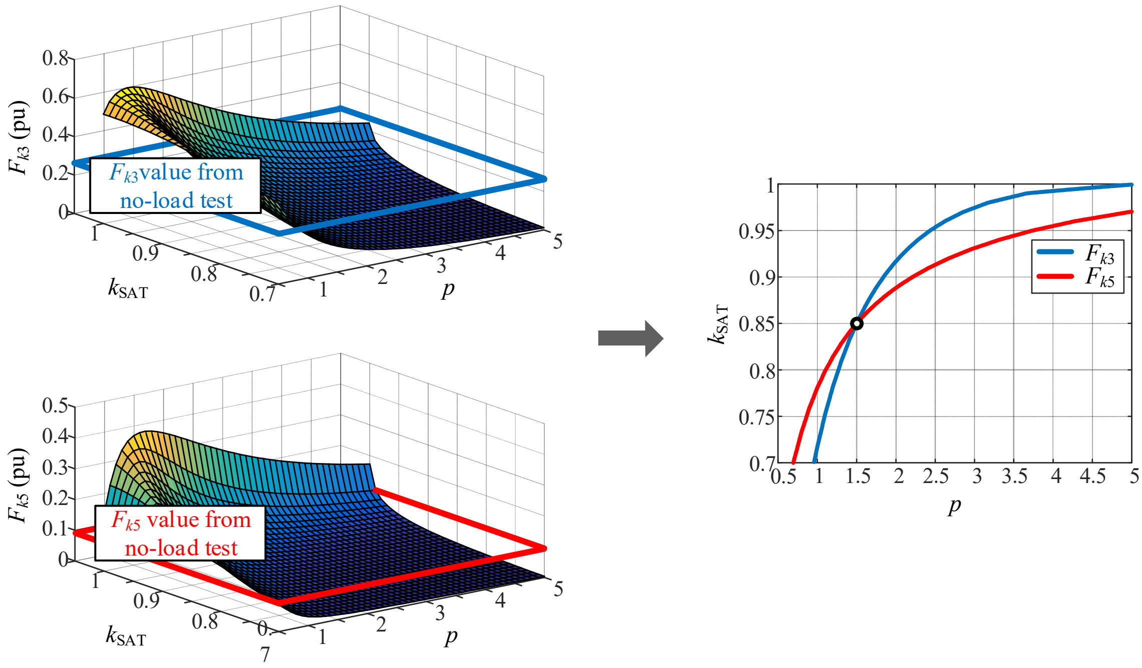

(a) (b)

Fig. 5.18. (a) Harmonic surfaces for the magnetic potential, F_{k3} and F_{k5}, in function of p and k_{SAT}, and (b) resultant curves for p and k_{SAT} estimation.

5.5. Experimental validation and results

The proposed methodology has been validated with multiple experimental tests on a 720 VA, 280/104 V, three-phase, three-legged transformer (namely T21), as well as with the field measurements on a 7.5 MVA, 66/15 kV, U_{cc} = 9% distribution transformer (namely T22) with YNd connection.

The nameplate of transformer T21 is in Table 5.1. Several inrush tests for K_2 estimation were performed to this transformer without controlling the energization point-on-wave or the residual fluxes, resulting in completely random conditions. As the windings of this transformer are available, different inrush tests have been conducted for each winding connection (YNy, Yy, YNd, Yd and Dy). No-load tests at steady-state were also carried out for each winding connection (except Dy) to estimate the rest of the parameters, which are contained in Table 5.1. The reluctance $\mathfrak{R}_0$ of this transformer has been estimated with the zero-sequence no-load test proposed in [157]. This reluctance is used only for validation purposes. The core losses resistance R_{FE}', has been estimated with the classical no-load test. Again, this resistance is used only for validation purposes. The laboratory setup for this transformer includes an autotransformer with impedance R_S = 1.2 Ω and L_S = 2.5 mH.

Table 5.1. Transformer T21: nameplate data and estimated parameters.

	T21		
S_N	720 VA		
U_{N1}/U_{N2}	280/104 V (YNy)		
U_{cc} (%)	12		
r (pu)	0.1197		
x (pu)	0.055		
R_{FE} (pu)	50		
$\Re_d$ (pu)	5.7		
	Phase a	Phase b	Phase c
F_{k1} (pu)	0.1524	0.0798	0.1855
F_{k3} (pu)	0.0625	0.0312	0.1275
F_{k5} (pu)	0.0153	0.0088	0.0211
K_1 (pu)	360	700	350
K_2 (pu)	0.2	0.4	0.2
p	0.467	0.512	0.452
k_{SAT}	0.704	0.757	0.739

Table 5.2 summarizes the results from the inrush tests of T21, as well as the estimated K_2 value from each test. As it can be seen, all the estimated values of K_2 from different tests are very close, with a mean value of 0.200 pu and a standard deviation of 0.065 pu. The estimations with a higher deviation are those with lower Q_{MAX} values or lower τ values. Fig. 5.19 shows the Q_{MAX}-τ points obtained from all inrush tests conducted on T21. As can be seen, all points fall around the same curve, as stated in previous section.

Table 5.2. Transformer T21: data from inrush tests and K_2 estimations.

Connection	YNy				Yy			
Test	1	2	3	4	5	6	7	8
Q_{MAX} (pu)	4.084	4.758	3.184	4.189	2.976	4.283	3.671	3.847
τ (ms)	39.72	35.10	49.68	38.84	49.95	35.28	33.72	48.33
Estimated K_2 (pu)	0.186	0.171	0.242	0.175	0.235	0.166	0.134	0.228
Connection	YNd				Yd			
Test	9	10	11	12	13	14	15	
Q_{MAX} (pu)	2.992	4.118	2.193	3.520	3.836	3.394	4.035	
τ (ms)	49.48	29.28	74.65	45.23	43.05	47.99	41.54	
Estimated K_2 (pu)	0.231	0.114	0.380	0.235	0.220	0.237	0.206	
Connection	Dy							
Test	16	17	18	19				
Q_{MAX} (pu)	2.810	2.201	2.673	1.531				
τ (ms)	42.80	51.15	24.41	59.47				
Estimated K_2 (pu)	0.172	0.200	0.056	0.203				
K_2 mean value (pu)	0.200							
Standard deviation	0.065							

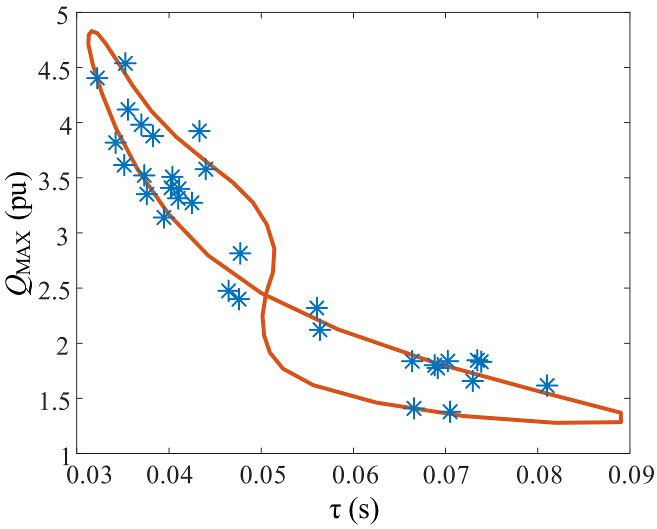

Fig. 5.19. Transformer T21: Q_{MAX}-τ points from experimental inrush tests.

Fig. 5.20 and Fig. 5.21 depict a comparison between the measured and the estimated $\phi - i$ hysteresis loops of T21 for Yy and YNy connections during a no-load test at rated voltage, as well as the comparison between the measured and the estimated no-load currents.

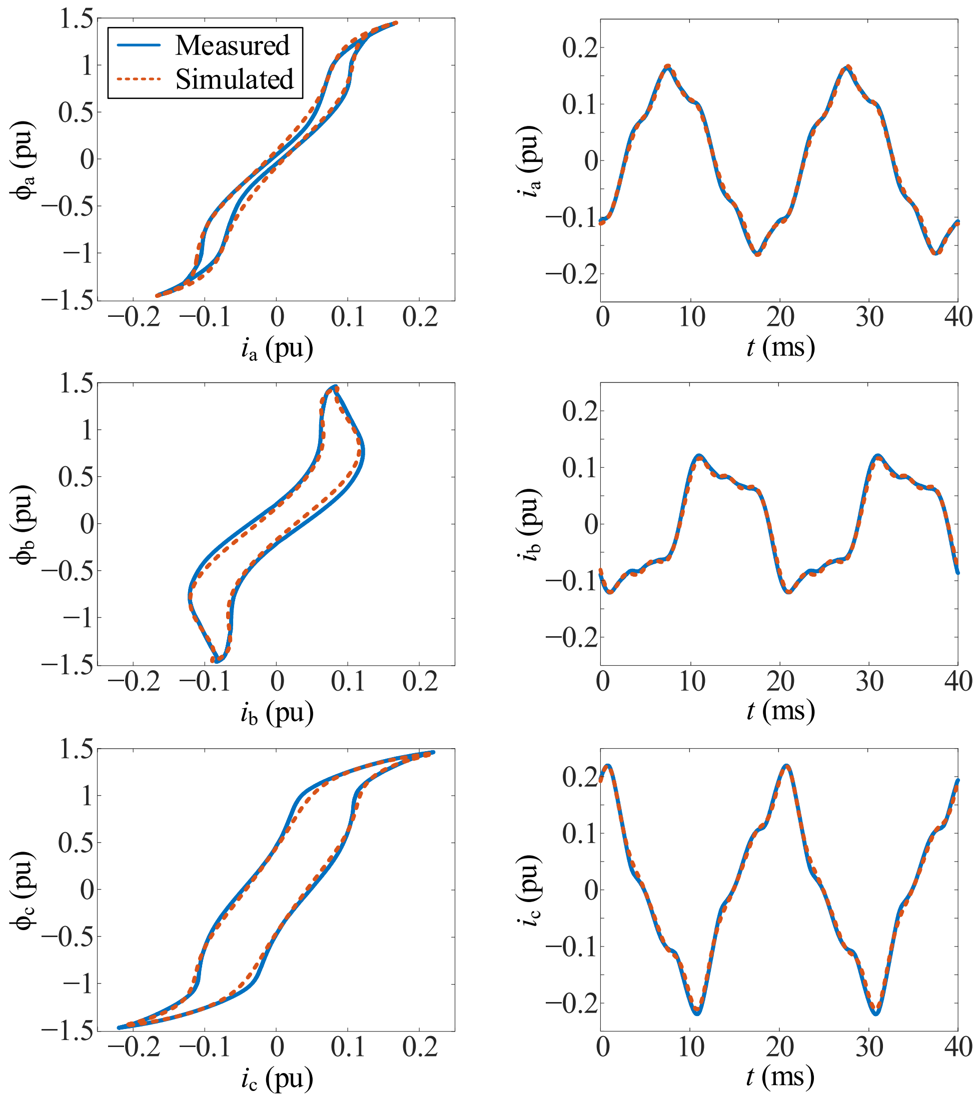

Fig. 5.20. Transformer T21 with connection Yy: three-phase no-load test at rated voltage. Measured (solid lines) and simulated (dotted lines).

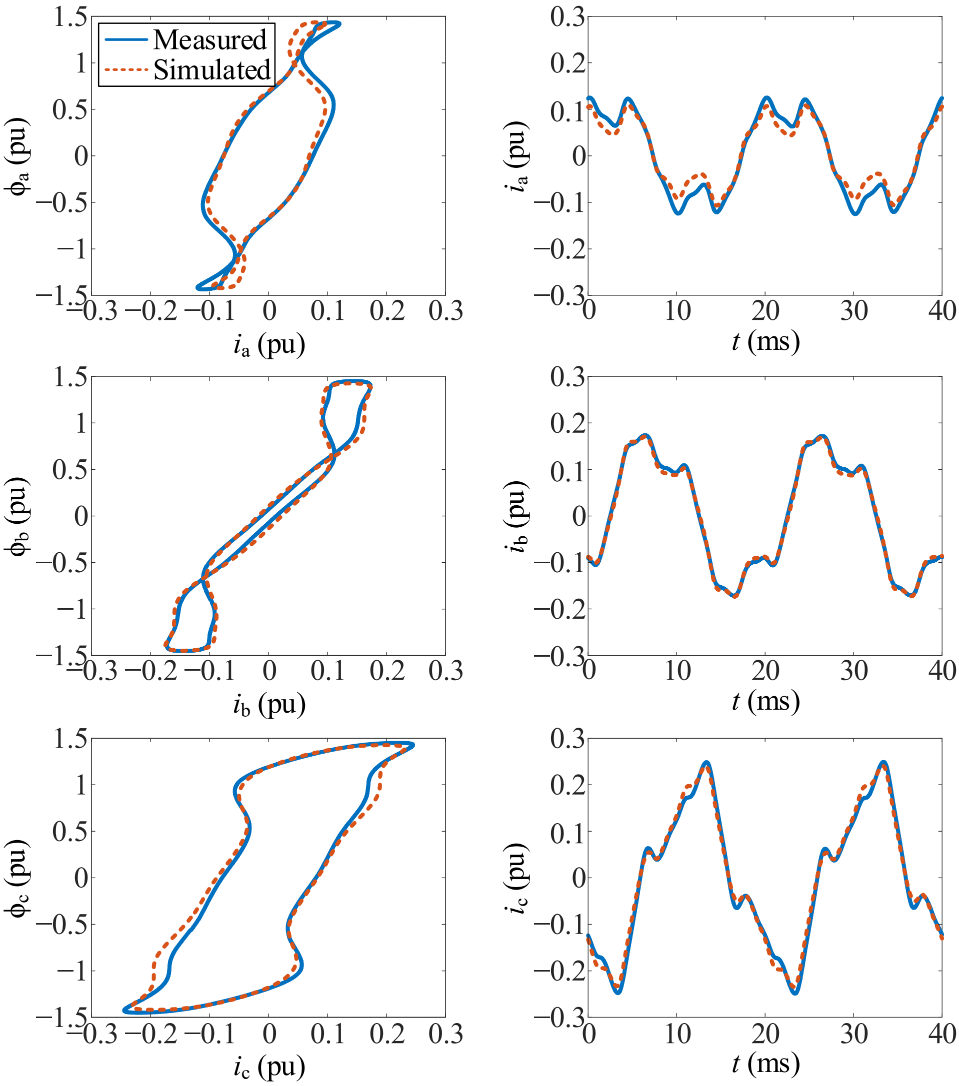

Fig. 5.21. Transformer T21 with connection YNy: three-phase no-load test at rated voltage. Measured (solid lines) and simulated (dotted lines).

To simulate the inrush currents, the transformer model was implemented in Simscape. It is necessary to know the residual fluxes and the energization point-on-wave from each test. The energization points-on-wave can be easily obtained from the recorded voltage waveforms. A comparison between the measured and the simulated inrush currents for the Yy connection of T21 is shown in Fig. 5.22(a). This inrush test was conducted with a prior demagnetization, gradually reducing the supply voltage magnitude before de-energization. Fig. 5.22(b) depicts another comparison of the inrush currents for the Yd connection. In this second inrush test, there was no prior demagnetization and the values of the residual fluxes were roughly estimated to align the first peaks of the inrush currents. The excellent agreement in both cases demonstrates that the saturation parameters have been accurately determined.

Table 5.3 contains the nameplate data of transformer T22 (7.5 MVA, 66 kV/15 kV, 9%), as well as the estimated parameters.

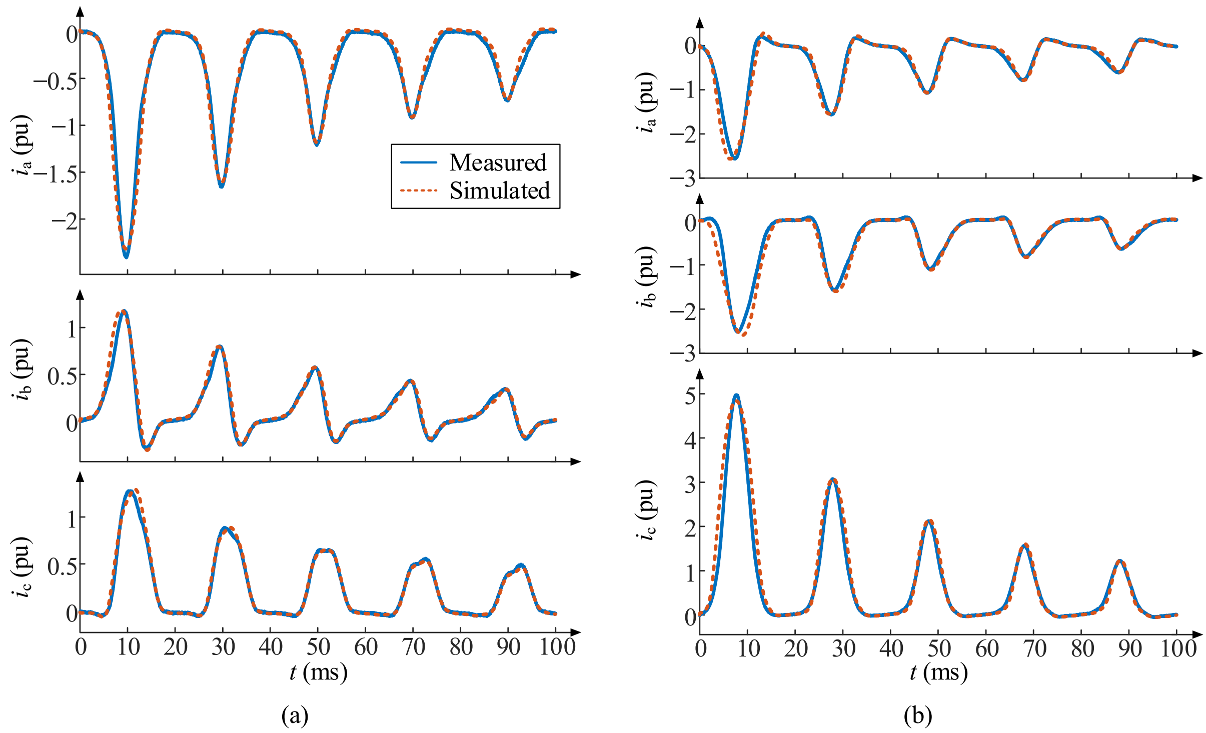

Fig. 5.22. Transformer T21 with (a) Yy connection, and (b) Yd connection: measured (solid lines) and simulated (dotted lines) inrush currents.

Table 5.3. Transformer T22: nameplate data and estimated parameters.

	T22		
S_N	7,5 MVA		
U_{N1}/ U_{N2}	66/15 kV (YNd)		
U_{cc} (%)	9		
r (pu)	0.01189		
x (pu)	0.09		
R_{FE} (pu)	500		
$\mathfrak{R}_d$ (pu)	1000		
	Phase a	Phase b	Phase c
F_{k1} (pu)	0.027	0.0135	0.027
F_{k3} (pu)	0.0051	0.0025	0.0051
F_{k5} (pu)	0.001	0.0005	0.001
K_1 (pu)	100	200	100
K_2 (pu)	0.0085	0.017	0.0085
p	1.5	1.5	1.5
k_{SAT}	0.8	0.8	0.8

Fig. 5.23 shows the measured inrush during the energization of this transformer. The estimated K_2 value is 0.0085 pu, with a Q_{MAX} value of 2.15 pu and a τ value of 0.16 s. Fig. 5.23 also shows the simulated inrush currents for the same event. Since the grid impedance is unknown, the measured primary voltages have been used for the validation procedure. The close agreement reflects the suitability of the methodology for large transformers.

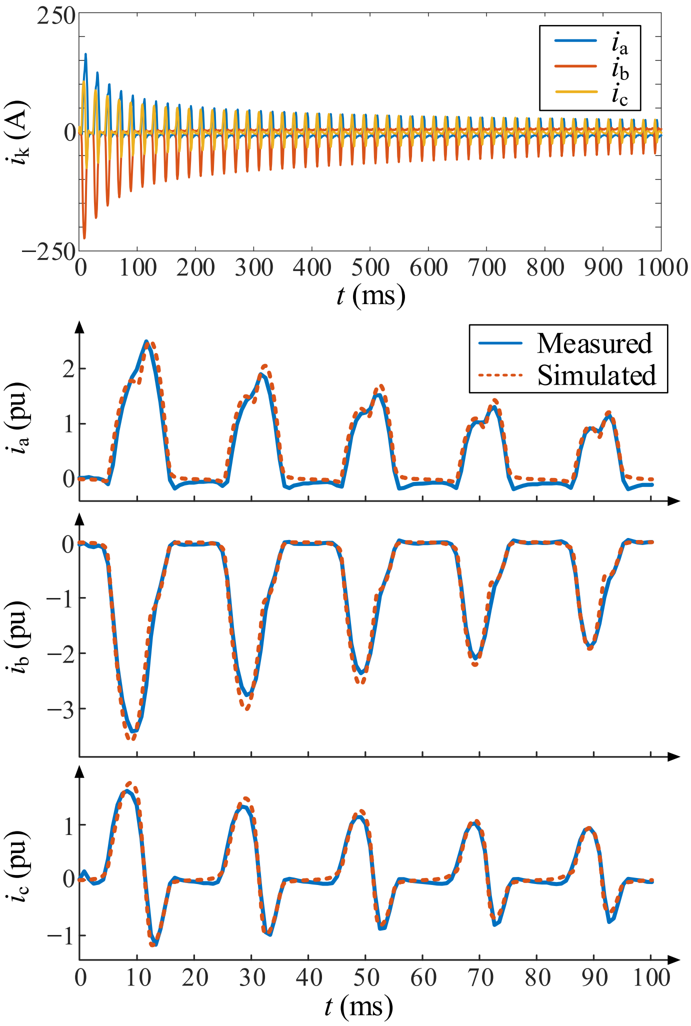

Fig. 5.23. Transformer T22 (7.5 MVA, 66/15 kV, 9%) with YNd connection: measured (solid lines) and simulated (dotted lines) energizing inrush currents.

Chapter 6. Characterization of Protective Current Transformer and Analysis of its Saturation

6.1. Introduction

Current transformers (CTs) are essential instrumentation elements between power systems and measurement devices or protective relays. The main function of a CT is to reduce a large primary current to a lower secondary level that is appropriate for the connected devices. The CT's accurate reproduction of the primary current is a relevant concern. While an ideal CT faithfully reproduces the primary current without any type of error, this is not true for real CTs. In reality, not all of the primary current flows through the secondary circuit due to core consumption, which means that the primary current is not exactly reproduced.

Under certain conditions, the transformation error is abruptly increased by core saturation (due to core nonlinearity), which causes not only an error in the magnitude and phase of the secondary current but also distorts its waveform, affecting the fidelity of primary current reproduction [179].

Classical CTs are classified for metering or protection purposes:

- CTs for metering are accurate between 5% and 125% of rated primary current. Above this level of current, the CT starts to saturate, and the secondary current is clipped to protect the inputs of a connected metering instrument. Metering class accuracy is usually between 0.2% and 1%.

- CTs for protection, in contrast, provide a linear transformation of the primary to secondary current at high overload levels, as they are used for overcurrent protection relays. A relay trip setting is normally 10 to 15 times the maximum load current, and this level should falls on the linear part of the CT saturation curve. Protection class accuracy is usually 1% or 3% at rated primary current and 5% to 10% at 10, 15 or 20 times rated current.

Thus, during overcurrent conditions, the metering CTs must saturate as much as possible to protect the metering instruments, and the error in the secondary current is not a problem but an objective. On the other side, protective CTs must be as linear as possible in case of overcurrents. The error in the secondary current must be relatively small for protection reliability. In order to achieve this objective, the study of the saturation is of great importance in CTs for protection, while it has no importance in CTs for metering. By this reason, this chapter deals with CTs for protection, despite most of the technical characteristics are also valid for metering CTs, starting by the equivalent circuit.

The saturation of CTs for protection can happen mainly in two scenarios [180]: (a) when the primary current is symmetrical but too large, or (b) when it is a transient current with a maintained direct current (DC) component, such as fault currents on networks with a large X/R ratio or inrush currents during energization of large transformers (i.e. with a large time constant). There is a third situation for CT saturation, when the load impedance is not small enough. However, this situation does not occur in practice, as the secondary circuit supplied by the CT is always designed to have a low impedance value.

One of the main concerns in CTs for protection is the discrimination between faults and inrush currents of large transformers. For example, the inrush current is distinguished from an internal fault in the differential protection of a transformer. One of the most common technique is known as the second harmonic restraint method, which consists in the calculation of the rich spectra of the inrush current, and blocking the trip signal of the protection relay when the second harmonic content is larger than a given percentage.

If the secondary current is distorted due to saturation, it is mandatory to compensate such current to substantially mitigate the vulnerability of protective relays to CT saturation and ensure their safe operation. Research efforts are directed toward mitigating saturation effects during transient conditions and improving CT performance in non-sinusoidal or distorted current waveforms. There are several methodologies to recover the primary current from distorted CT secondary current [181]-[191], but almost exclusively for typical fault current waveforms, not for inrush currents. Most of the methodologies are based on advanced signal processing techniques and intelligent algorithms.

Thus, the aims of this chapter are the study of the protection CTs during inrush current, as it has not been sufficiently investigated in the literature, and the characterization of the CTs parameters.

6.2. Current transformer model

Fig. 6.1 shows the equivalent circuit of a CT. It includes an ideal CT with a turns ratio N_1/N_2, the core branch composed by the nonlinear magnetizing inductance referred to the secondary, L_m, and the core losses referred to the secondary, R_{FE}, the primary and secondary winding resistances, R_1 and R_2, the leakage inductances, L_{d1} and L_{d2}, and the burden impedance, Z_B. Note that, despite L_m and R_{FE} are referred to the secondary, the double prime is omitted in this chapter.

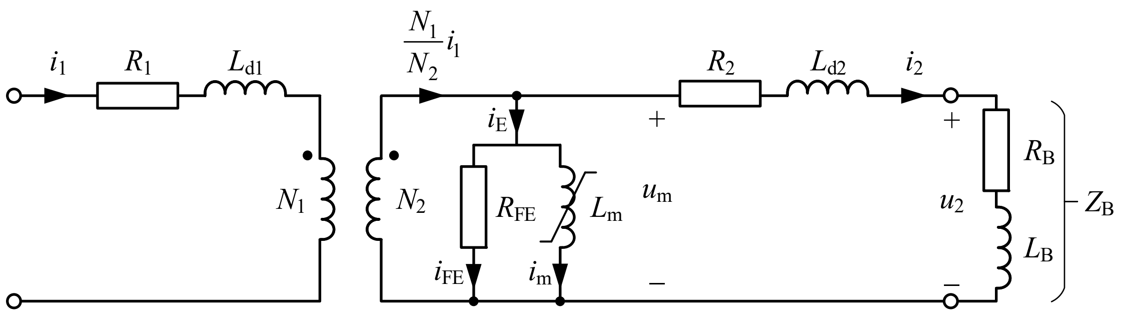

Fig. 6.1. CT equivalent circuit.

6.2.1. On the equivalent circuit for protection current transformers

The accuracy and the dynamic behavior of the CTs for protection are greatly influenced by the summation of the series impedance of the transformer and the burden impedance. Not only the magnitude of these impedances determine the CT transient behavior, but also the character of both impedances has a decisive influence, as will shown later. As the series impedance of the CT depends on its construction, a first classification of conventional CTs can be considered:

- Window CTs, consist of a secondary winding wrapped around a core, with the primary conductor passing through the opening window in the core. The primary series impedance is negligible: $R_1 \approx 0$ and $L_{d1} \approx 0$. Window CTs are manufactured as toroidal or rectangular cores, as shown in Fig. 6.2. This is the most common type of CT, and they are considered in this chapter.

- Wound CTs, feature separate primary and secondary windings wound around a laminated core. The primary series impedance must be considered, as it is not null: $R_1 \neq 0$ and $L_{d1} \neq 0$. These CTs are rarely used in practice, as they are typical of very low ratios. As a result, they are not considered in this chapter.

Another construction characteristic which influences its series impedance is the continuity of the core:

- Continuous core. If the windings in these cores are fully distributed, the leakage reactance is negligibly small and can be considered to be zero, as all the flux circulates by the core. This is illustrated in Fig. 6.2(c). Thus, the series impedance of this transformer is uniquely composed by the secondary resistance.

- Split core: one segment of the core is removable to allow retrofit installation, Fig. 6.2(b), and the segment does not contain its share of the total winding. Thus, the windings are wounded on only a portion of the core. The leakage reactance cannot be neglected because the leakage flux is not null as shown in Fig. 6.2(d).

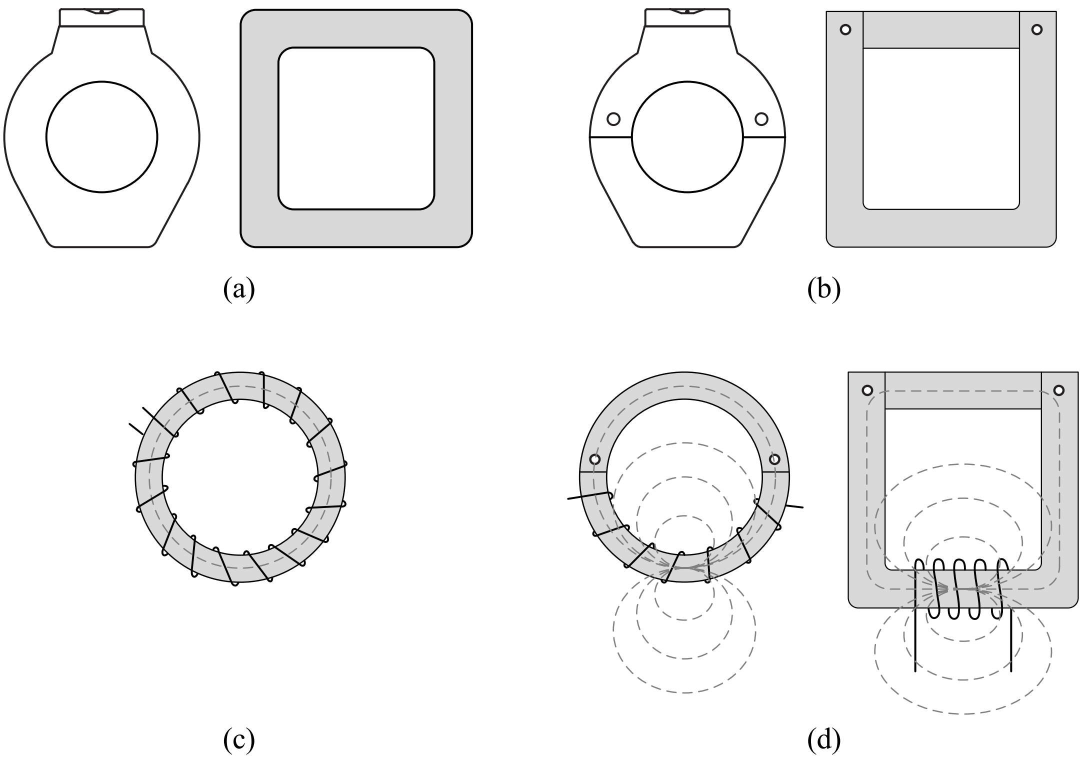

Fig. 6.2. Protection CTs with different construction: (a) continuous core, (b) split core. Detail of the magnetic fluxes in CTs with: (c) toroidal core with fully distributed winding, and (d) split core with winding partially wounded.

Lastly, the IEEE C37.110 defines the following accuracy classes for protection CTs based on the leakage reactances:

- C class (C means calculated): transformers whose leakage reactances are very low, so that the accuracy can be calculated by the secondary excitation characteristic and the equivalent circuit. In general, the continuous core CTs with fully distributed windings could be included into this group. If the CT is multiratio, all windings including turns between taps should be fully distributed around the core periphery.

– T class (T means tested): transformers with a high leakage reactances that cannot be neglected. As this leakage impacts the CT performance, such performance can only be accurately determined by test. In general, this group should include CTs with split core or with non-distributed windings.

As a summary, the most common CTs for protection are window CT, usually toroidal, with a continuous core and a fully distributed secondary winding. Unless otherwise stated, this chapter will deal with this type of CTs, whose model is represented in Fig. 6.2. Remember that the series impedance of this transformer is composed uniquely by the secondary resistance.

In window CTs, the primary impedance (R_1 and L_{d1}) is negligible. When studying the transient behavior of a CT during saturation, the core losses can be neglected. Fig. 6.3 illustrates a simplified model for window CTs, where the ideal transformer has been eliminated.

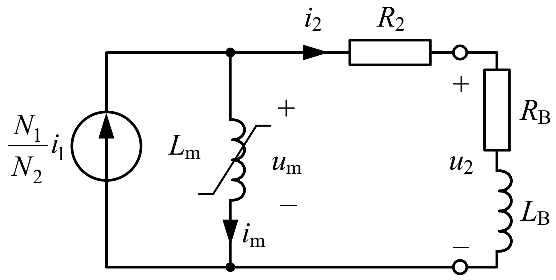

Fig. 6.3. Simplified model of protection CTs for transient conditions.

The nonlinear inductance, L_m, has a high value under normal conditions and a low value (it tends to behave as if it were a short-circuit) when the CT is saturated. The nonlinearity of L_m is characterized by the saturation curve, which relates the magnetizing current, i_m, to the flux ϕ.

In opposite to a voltage transformer, the primary winding of a CT is connected in series with the network or the measured system, which means that the primary current is stiff and completely unaffected by the secondary burden. By this reason, the current $(N_1/N_2)i_1$ in Fig. 6.3 is represented by a current source.

The circuit of Fig. 6.3 can be solved by writing Kirchhoff's voltage law around the secondary (right) loop, as

$$u_m - R_T i_2 - L_T \frac{di_2}{dt} = 0 \tag{6.1}$$

where $R_T = R_2 + R_B$ and $L_T = L_B$.

The magnetizing voltage, u_m, at the magnetizing inductance, L_m, is given by

$$u_m = N_2 \frac{d\phi}{dt} \tag{6.2}$$

The secondary current, i_2,

$$i_2 = \frac{N_1}{N_2} i_1 - i_\mathrm{m} \tag{6.3}$$

where N_1 and N_2 are the primary and secondary winding turns (N_1 is commonly the unity).

Substituting (6.2) in (6.1), the magnetic flux in the core is given by

$$\phi = \frac{1}{N_2}\left(R_\mathrm{T} \int i_2 \mathrm{d}t + L_\mathrm{T} i_2 + \phi_\mathrm{R} \right) \tag{6.4}$$

where ϕ_R is the residual flux in the CT core. Equations (6.3) and (6.4) clearly demonstrate that the behavior of a CT is influenced by the characteristics of the CT itself and the burden to which the CT is connected.

6.3. Steady-state behavior and excitation curves

American manufacturers and industry standards usually illustrate the CT operation by using excitation curves. These curves depict the relationship between the RMS values of the secondary magnetizing voltage (U_m, secondary voltage minus the voltage drop in R_2) and the excitation current (I_E, magnetizing current plus core losses current). Fig. 6.4 displays a typical set of logarithmic-logarithmic excitation curves for a C-class CTs family (multi-ratio CT) of an American manufacturer, whose secondary winding resistances, R_2, are contained in Table 6.1. These curves represent the RMS values of the voltage and current waveforms, unlike in the typical saturation curves, where the instantaneous values of the flux and the current are represented.

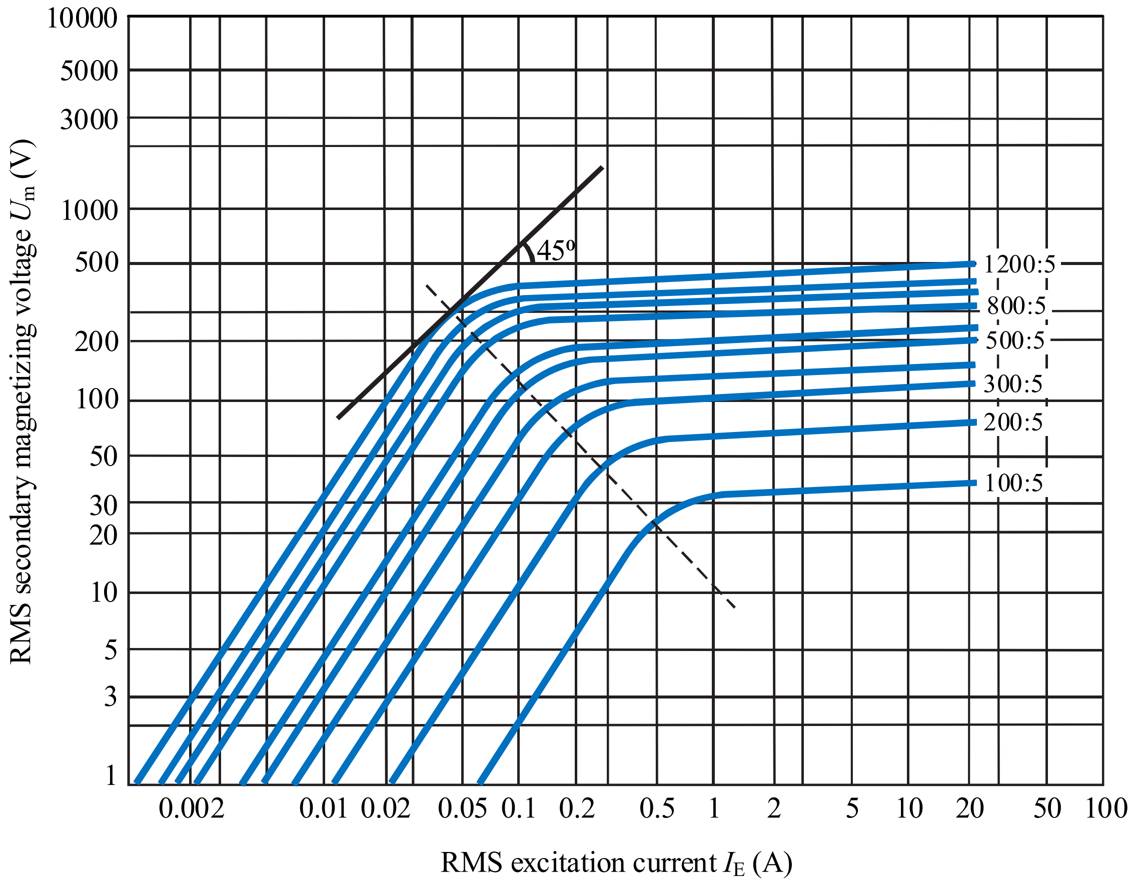

Fig. 6.4. Typical excitation curves for a C-class multi-ratio CT.

Table 6.1. Typical secondary winding resistance, R_2, values for the C-class multi-ratio CT of Fig. 6.4.

Current ratio	Turns ratio	Secondary winding resistance, R_2 (Ω)
100:5	20:1	0.05
200:5	40:1	0.10
300:5	60:1	0.15
400:5	80:1	0.20
500:5	100:1	0.25
600:5	120:1	0.31
800:5	160:1	0.41
900:5	180:1	0.46
1000:5	200:1	0.51
1200:5	240:1	0.61

The steady-state behavior of the CT can be analyzed by using (6.3). It can be seen that i_2 will never be an exact replica of i_1; there will always be an error. The error is defined by the standards in a different way for rated and for highly saturation conditions (i.e., when protection relays must operate).

At rated conditions, the standards limit the ratio error, ε, which is the difference among the RMS primary (referred to the secondary) and secondary currents:

$$\varepsilon = \frac{k_r I_2 - I_1}{I_1} \times 100\% \tag{6.5}$$

where k_r is the nominal transformation ratio, and I_1 and I_2 are the actual primary current and the actual secondary current under measurement conditions, respectively.

When there is a large harmonic content due to CT saturation, it is not possible to use phasors to account for the ratio error. Therefore, at highly saturation conditions, the standards limit the composite error, ε_c, which is the true RMS value of the excitation current:

$$\varepsilon_c = \frac{1}{I_1}\sqrt{\frac{1}{T}\int_0^T i_E{}^2 \mathrm{d}t} \times 100\% = \frac{1}{I_1}\sqrt{\frac{1}{T}\int_0^T \left(k_r i_2 - i_1\right)^2 \mathrm{d}t} \times 100\% \tag{6.6}$$

where T is the frequency period.

6.4. Core saturation

One of the critical considerations in a CT is core saturation. Saturation occurs when the ferromagnetic core is unable to properly handle an increase in its own magnetic flux density. As the voltage across the CT secondary winding increases because either the current or the secondary impedance (secondary winding impedance plus burden) is increased, the flux in the CT core will also increase. This phenomenon leads to an appreciable waveform distortion of the secondary current being measured.

There are two general types of CT saturation: symmetrical and asymmetrical. Symmetrical saturation is due to large symmetrical currents, Fig. 6.5(a). Asymmetrical saturation can be caused by asymmetrical fault currents, Fig. 6.5(b), or by transformer inrush currents, Fig. 6.5(c).

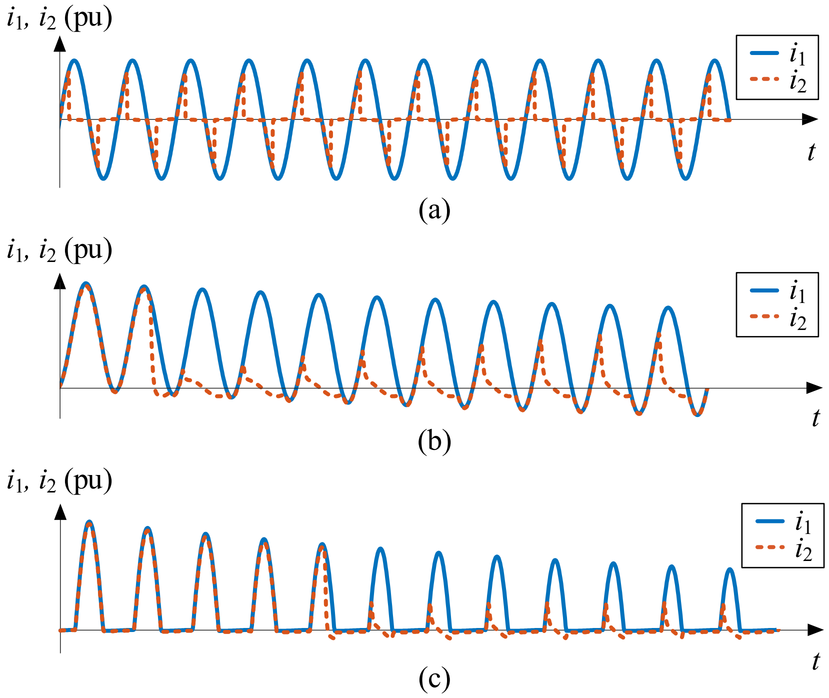

Fig. 6.5. Typical waveforms of different saturated secondary currents due to: (a) large symmetrical primary currents, (b) fault primary currents, and (c) inrush primary currents.

6.4.1. Symmetrical saturation

The symmetrical saturation happens when a symmetrical primary current, without DC offset, is excessively large for the CT core to handle for a given secondary impedance. According to (6.4), a larger secondary impedance results in a larger flux, leading to a more severe saturation. Ideally, if the CT secondary winding is short-circuited and its impedance is zero, it will never reach saturation, despite the magnitude of the primary current (although it is not a realistic situation). The symmetrical saturation can happen when there is a usual secondary impedance and a very large primary current, or when there is a usual primary current and a very large secondary impedance (despite not being realistic this last situation).

Fig. 6.6 illustrates two examples of symmetrical saturation. In the first case depicted in Fig. 6.6, the primary current is excessively high (20 pu) with a purely resistive impedance of 2 pu. In the second case depicted in Fig. 6.6(b), the primary current is smaller (1 pu) but the resistance is of 40 pu. It can be seen that in both cases, the flux increases until it reaches saturation. However, despite the two cases appear equivalent, their dynamic behavior is not identical, and their flux and current waveforms are slightly different.

When the CT is unsaturated, the magnetizing reactance is very high, causing most of the primary current to flow through the secondary winding. Conversely, when the CT saturates, low magnetizing reactance consumes most of the primary current. This provides a definition of saturation in the time domain: the CT saturates during the sections of the waveform where the flux does not change and the secondary current drops to zero.

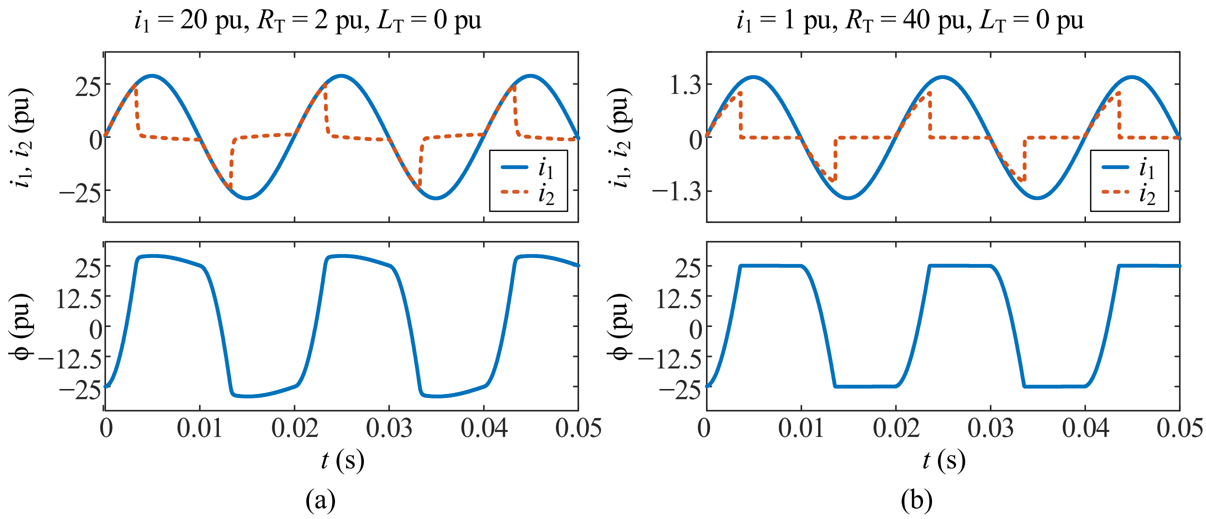

Fig. 6.6. Examples of symmetrical saturation in a protection CT 2000/5 A, C400 (CT4) under different conditions.

In the case of Fig. 6.6(a), where the secondary impedance is small and the current is high, there is a smaller transformation error during unsaturated conditions, because the small total secondary impedance allows most of the current to flow through the secondary winding. When the CT becomes saturated, the flux can grow beyond the saturation point, resulting in a more severe saturation. On the other hand, when there is small current and a very large total secondary impedance, Fig. 6.6(b), the transformation error is greater when CT is unsaturated as the larger total secondary impedance results into a lower secondary current. During saturation, all the current flows through the magnetizing branch, causing in the secondary current an abrupt drop to zero.

It is also important to note that different types of total secondary impedances lead to different saturated current waveforms. Fig. 6.7 illustrates different waveforms for three different types of total secondary impedance: purely resistive, resistive and inductive, and purely inductive.

Note that the purely resistive case of Fig. 6.7(a) is considered to be the base case (R_T = 1 pu), while Fig. 6.7(b) is aimed to analyze the influence of adding inductance to this base case (by this reason, R_T is maintained into 1 pu). In both cases, the secondary current drops to zero during saturation intervals twice during each cycle (once during the positive half-cycle and once during the negative half-cycle). The difference between both waveforms is because the current through an inductive load cannot change instantaneously, so it takes some time to decay. If the total secondary impedance is more resistive, the current drops to zero more abruptly. In summary, it can be concluded that of the addition of the inductance L_T to the secondary changes the waveform of the secondary current.

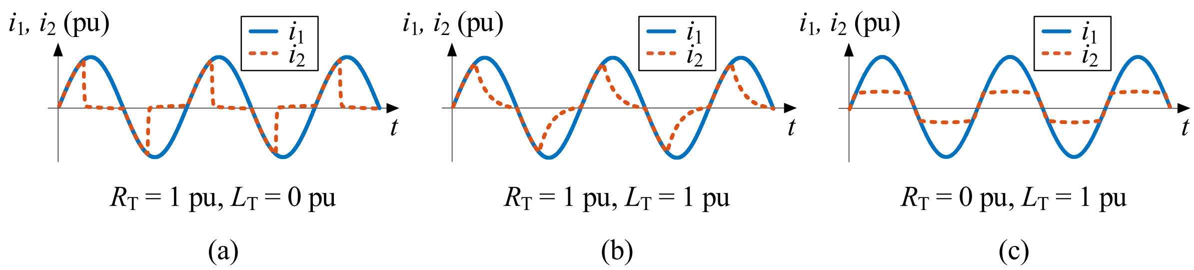

Fig. 6.7. Typical saturated waveforms when the secondary total impedance is of different nature: (a) resistive, (b) resistive and inductive, and (c) purely inductive.

In the pure inductance case, Fig. 6.7(c), the saturated current never drops to zero, but the current peaks are truncated. However, total secondary impedances that are purely inductive for a CT are not common, so this last saturation type can be considered unrealistic.

6.4.2. Asymmetrical saturation

The asymmetrical saturation happens when the applied primary current has high levels of DC offset, as is the case of the inrush currents in power transformers or fault currents in a power system. The DC offset of an asymmetrical current greatly increases the flux in the CT, resulting into a flux waveform radically different from that of the symmetrical case. The main difference between the typical symmetrical and asymmetrical fluxes is illustrated in Fig. 6.8. With the mentioned saturation, the secondary current is saturated only once at each cycle and every during the same half cycle (always positive or negative).

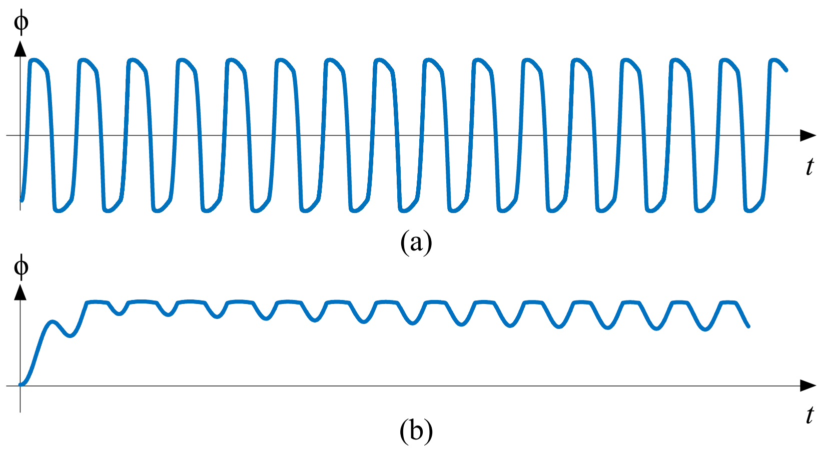

Fig. 6.8. Typical flux waveforms during CT saturation: (a) symmetrical saturation, (b) asymmetrical saturation.

It is important to highlight that even though the asymmetrical saturation is caused mainly by the DC offset, the magnitude current and other factors also influence to its severity. As happens in the symmetrical case, the secondary impedance also determines the shape of the secondary current during the saturation intervals.

Fig. 6.9 and Fig. 6.10 illustrate the effect of the secondary impedance nature (purely resistive, resistive plus inductive, and purely inductive) on the CT transient behavior during fault and inrush currents.

Note again that the purely resistive case in Fig. 6.9(a) and Fig. 6.10(a) is considered to be the base case ($R_T = 1$ pu), while the resistive and inductive case is aimed to analyze the influence of adding inductance to this base case (by this reason, R_T is maintained into 1 pu). A more detailed comparison between these two cases is illustrated in Fig. 6.11 and Fig. 6.12.

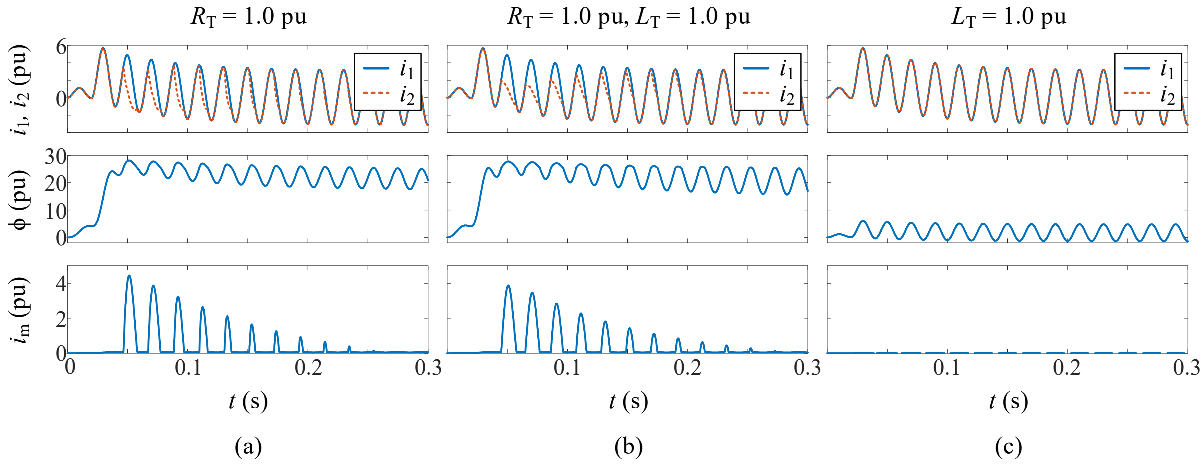

Fig. 6.9. Asymmetrical saturation in CT4 due to a fault current when the total secondary impedance is of different nature: (a) purely resistive, (b) resistive and inductive, and (c) purely inductive.

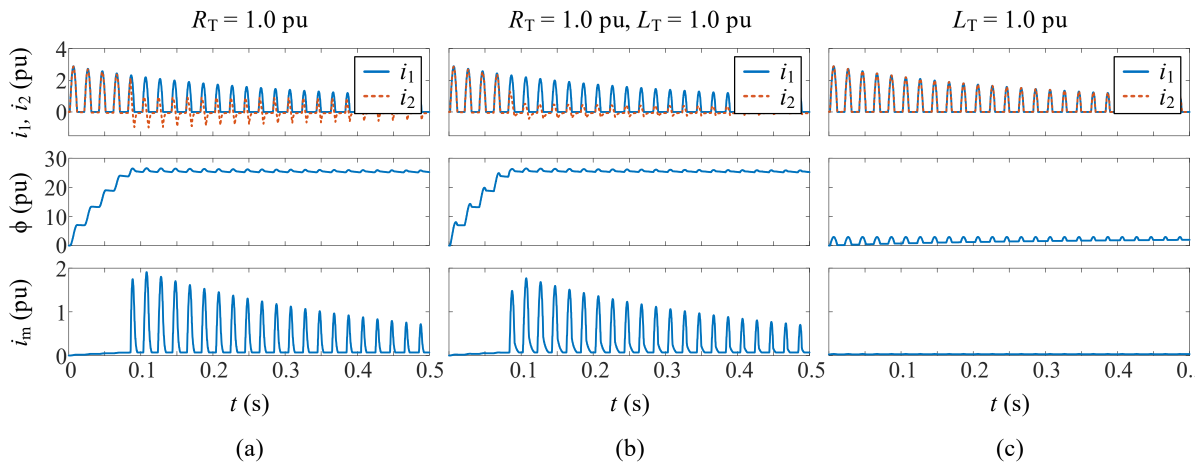

Fig. 6.10. Asymmetrical saturation in CT4 due to an inrush current when the total secondary impedance is of different nature: (a) purely resistive, (b) resistive and inductive, and (c) purely inductive.

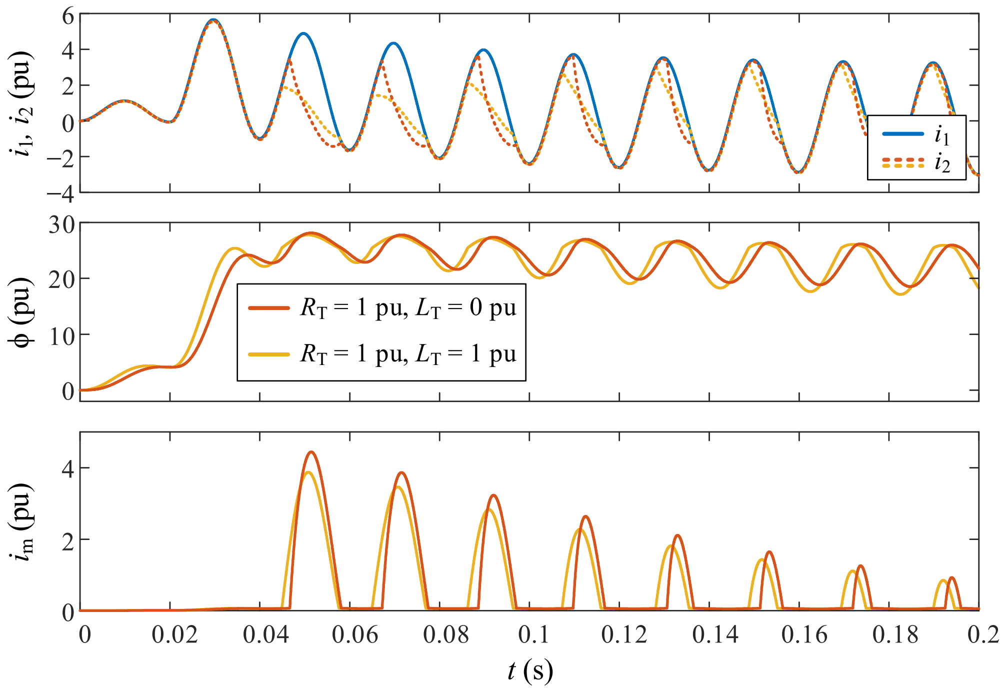

Fig. 6.11. Comparison of asymmetrical saturation in CT4 due to a fault current when the total secondary impedance is of different nature: purely resistive, and resistive and inductive.

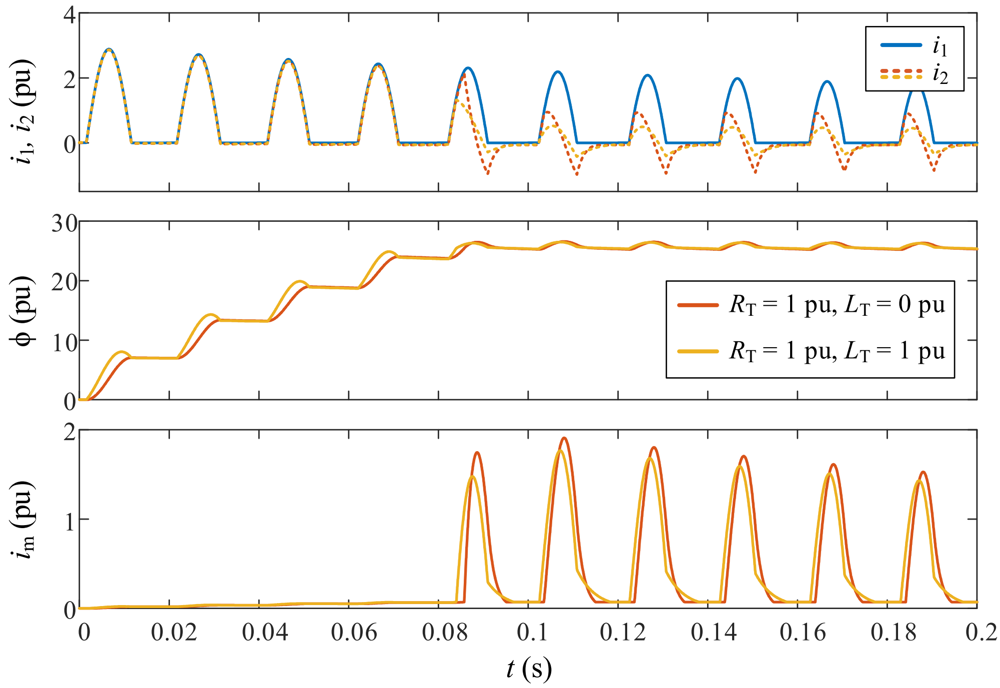

Fig. 6.12. Comparison of asymmetrical saturation in CT4 due to an inrush current when the total secondary impedance is of different nature: purely resistive, and resistive and inductive.

According to (6.4), a component of the flux is proportional to the integral of the secondary current, due to the effect of resistance R_T. Consequently, in the presence of a primary current DC offset, the integration of the current leads to a continuous increase in flux until the saturation level is reached, Fig. 6.9(b) and Fig. 6.10(b). Once the flux reaches saturation, it begins to gradually decrease, first below the saturation level and then to become symmetrical. It is evident from (6.4) that a higher DC offset in the primary current and an increased resistance R_T prompt a more rapid increase in flux, leading to faster saturation.

By other hand, the inductance L_T contributes to a flux component that is directly proportional to the secondary current. However, this flux component due to L_T does not have a large influence on the overall dynamic behavior of the total flux (when compared with the purely resistive case), Fig. 6.9(a) and Fig. 6.10(a). In particular, L_T does not appreciably influence the growth rate of the flux, i.e., the time taken by the CT to reach the saturation for the first time (time-to-saturation) is similar in both cases.

In summary, it can be concluded that the addition of the inductance L_T to the secondary does not have a large influence on the the time-to-saturation nor the damping rate of the flux.

Lastly, when the secondary impedance is purely inductive, the flux is only proportional to the secondary current, meaning there is no integration of DC offset, Fig. 6.9(c) and Fig. 6.10(c). It is important to emphasize that an inductive reactance is not equivalent to a resistance of the same magnitude, as they have different effects.

The time-to-saturation and the damping rate of the flux during transient conditions depend on several factors: the own saturation curve of the CT, the total secondary resistance R_T, the magnitude of the DC offset, the shape of the primary current, the residual flux on the CT core, and the X/R ratio of the measured system. Some of these factors also affect to the amount of time that the CT is saturated at each cycle.

A higher amount of residual flux, a lower saturation flux, a larger total secondary resistance, a larger current magnitude, and more DC offset, result in a shorter time-to-saturation. Regarding the residual flux, the time-to-saturation is lower when there is residual flux with the same polarity of the DC component in the asymmetrical current; and it is larger when the residual flux has the opposite polarity. The effects of the residual flux are illustrated in Fig. 6.13. In this example, the CT is sized to perfectly handle an AC current without DC offset, as shown in Fig. 6.13(a), where there is no residual flux. Fig. 6.13(b) demonstrates how the same current leads to CT saturation when there is a residual flux of 70% of the saturation flux (see Subsection 6.4.4 for definition of the saturation flux, ϕ_{SAT}, in different standards).

Fig. 6.13(c) and Fig. 6.13(d) show how a residual flux with the same polarity than the DC offset of the primary current, aggravates the asymmetric saturation and also leads to an earlier saturation. As it can be seen from these examples, saturation as a result of residual flux is short-lived, lasting about half a cycle. Despite the more severe saturation when there is a residual flux, the saturation ends at about the same time in both cases. The residual flux of non-gapped CTs can be as high as 80% of the saturation flux.

The amount of time the CT is saturated is less at each cycle as the DC component decays, which is ruled by the X/R ratio of the power system at the point of the fault in the case of a fault current, or by the power transformer in the case of an inrush current. When the DC offset is at its maximum level in a fault current, the CT flux can potentially increase to $1 + X/R$. The inrush current magnitude is usually lower than fault current magnitude.

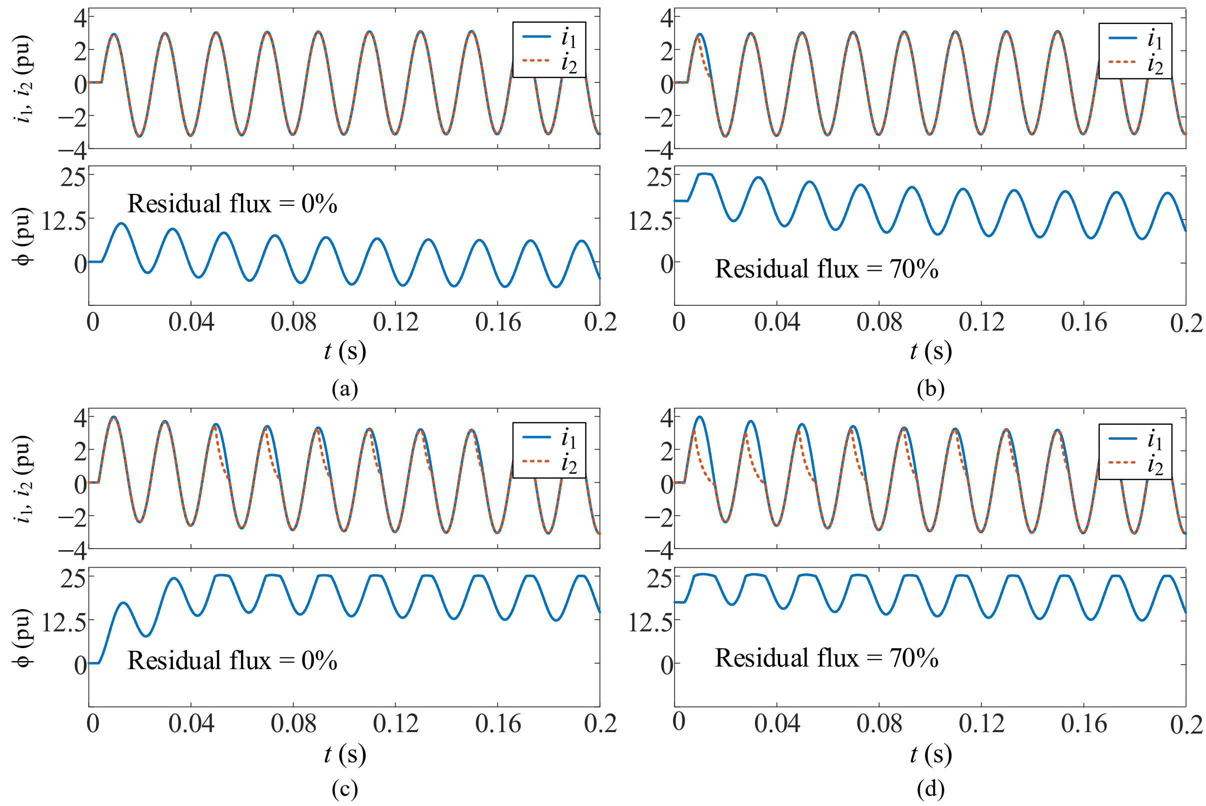

Fig. 6.13. Influence of the residual flux on CT saturation of CT4: (a) symmetrical primary current with null residual flux and (b) with no null residual flux, and (c) fault primary current with null residual flux and (d) with no null residual flux.

Not all saturated waveforms are obvious at first sight as those of the last figures, which have sharp edges and large portions missing. When saturation is low, it is difficult to detect if the waveforms are or not saturated. Appendix F proposes an FPGA-based smart sensor to detect CT saturation, specifically developed for inrush current.

6.4.3. Residual flux

Similarly to power transformers, CTs also experience the phenomenon of residual flux. Likewise, the de-energization trajectories and all aspects related to residual flux, as explained in Chapter 3, are applicable to CTs. The maximum residual flux in CTs (green point) is usually referred to the saturation flux (see Subsection 6.4.4 for definition of the saturation flux, ϕ_{SAT}, in different standards).

When a breaker operates, the current is usually interrupted at a zero crossing. For both symmetrical and asymmetrical currents, there is a positive or negative flux in the core when a current zero crossing occurs. This flux can be significant during high-magnitude asymmetrical current (when a DC component is present). This flux remains in the CT after the breaker opens and affects their behavior the next time it is energized.

As explained before, the residual flux can either help or hinder a CT's performance, depending on whether the residual flux has the same or opposite polarity to that of the measured current. It takes more time for the CT to saturate if the residual flux has the opposite polarity to the measured current and less time if it has the same polarity.

The only way to eliminate the residual flux is by CT demagnetization. It can be done by applying primary rated current and a variable burden to the CT secondary. Initially, the burden must have a high resistance to cause the CT to saturate in both positive and negative directions. Then, the CT is brought out of saturation by gradually decreasing the burden, and consequently the secondary voltage, to zero. This demagnetization procedure is typically only feasible in laboratories or during system maintenance, but it is almost never done in practice.

The saturation as a direct result of the residual flux is of short duration, lasting about half a cycle. Because of this short saturation time, the residual flux has little effect on standard protection algorithms and it is normally neglected in CT saturation calculations. Despite this, negative effects for certain protection functions due to residual flux can be avoided by application of gapped CT cores. With gapped cores and reasonable core sizes, the residual flux is significantly reduced. It also increases the magnetizing current, but this increase in magnetizing current due to a small gap will have no significant effect on the protection accuracy rating of the CT.

The maximum residual flux of non-gapped cores is typically in the range of 60% to 95% of the saturation flux, and it depends on the magnetic core material.

Another option to reduce the residual flux is to use different grades of steel for the core. Cold-rolled, grain-oriented, silicon steel is the core material used for almost all protective CTs. This material can have a residual flux as high as 80%. While hot-rolled silicon steel does not have as high permeability or as low losses as cold-rolled steel, its maximum residual flux is about half that of cold-rolled steel.

Biased-core CTs have been also proposed to reduce the maximum residual flux [192]. These CTs consist of a core made of two equal sections. Through a suitable arrangement of bias windings and a DC power supply, one core section is magnetically biased to approximately 75% of the maximum flux density in the positive direction, while the other core section is magnetically biased in the negative direction. The transformer operates as a conventional transformer, except for the flux-resetting action of the bias windings, which prevents any residual flux from being retained in the core.

Table 6.2 shows the results of a survey on the residual flux values of 141 CTs for a 230 kV system.

Table 6.2. Residual flux survey on a 230 kV system [193].

Residual flux as a percentage of the saturation flux	Percentage of CTs
0-20	39
21-40	18
41-60	16
61-80	27

6.4.4. Definitions of the knee-point voltage, the saturation voltage and the saturation flux according to IEEE and IEC standards

In addition to defining saturation in the time domain, it is also important to define saturation in terms of RMS quantities so that the equivalent circuit of the CT and the excitation curve can be worked out. IEEE and IEC standards give different definitions for the knee-point voltage, U_{KNEE}, for the saturation voltage, U_{SAT}, and for the saturation flux, ϕ_{SAT}, resulting in different numerical values for the same CT. To further complicate the situation, some definitions have recently changed in sucesive versions of the same standard.

According to the IEEE standards [193]-[194], the knee-point voltage, U_{KNEE}, of a CT with a non-gapped core is the point of maximum permeability on the excitation curve, plotted on logarithmic–logarithmic axes with square decades, where the tangent to the curve makes a 45° angle with the abscissa. This is exemplified in Fig. 6.14, and results in a knee-point of about 300 V for a 1200:5 CT. When the CT has a gapped core, the knee-point voltage is the point where the tangent to the curve makes an angle of 30° with the abscissa.

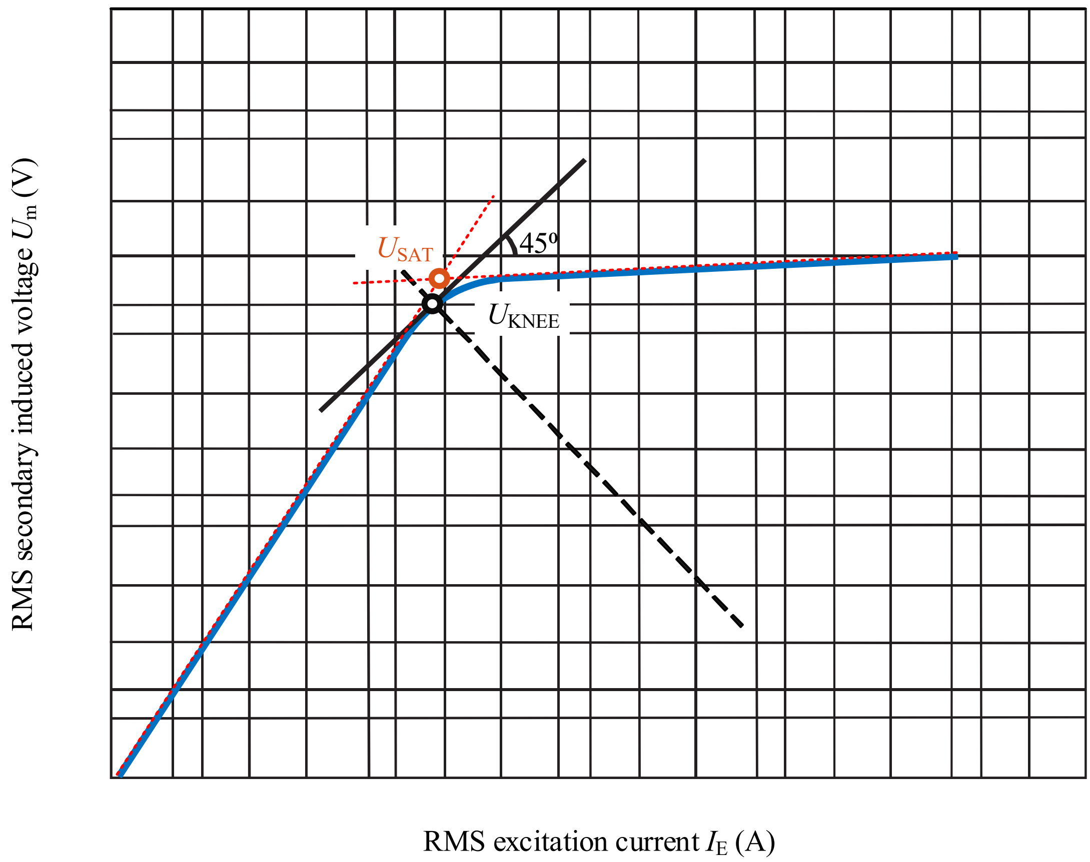

Fig. 6.14. IEEE definitions of knee-point voltage and saturation voltage.

The IEC [195]-[196] gives a different definition of the knee-point voltage. They locate it at a point on the excitation curve where an increase in the secondary voltage of 10% causes an increase in current of 50%. It is important to note that the IEEE and the IEC definitions yield to different knee-points for the same CT. On a square log–log excitation curve, a tangent straight line through this point will have a slope as log(1+0.1) / log(1+0.5) = 0.235. The tangent line ascends by 1 vertical decade across 4.25 horizontal decades, creating an angle of 13° with the abscissa. The voltage at this point is approximately 20% to 25% higher than the knee-point voltage given by the IEEE definition.

Regarding the saturation voltage, U_{SAT}, the newest IEEE C37.110 standard version redefines it as the RMS value of the symmetrical voltage across the secondary winding of the CT for which the peak induction just exceeds the saturation flux density. It can be found graphically by locating the intersection of the straight portions of the excitation curve on log–log axes (red point in Fig. 6.14). The IEEE saturation flux, ϕ_{SAT}, is calculated from U_{SAT} as

$$\phi_{SAT} = \frac{1}{N_2}\frac{\sqrt{2}U_{SAT}}{2\pi f} \tag{6.7}$$

where f is the voltage frequency.

Originally, the IEC defined the saturation flux as the peak value of the flux which would exist in a core in the transition from the non-saturated to the fully saturated condition and deemed to be that point on the saturation curve at which a 10 % increase in the excitation current causes flux to be increased by 50 %, see Fig. 6.15. This definition gained no acceptance because the saturation value was too low, and led to misunderstandings and contradictions.

The IEC has redefined the saturation flux as the maximum value of the flux enclosed by the secondary winding in a CT, corresponding to the magnetic saturation of the core material. According to IEC, a sinusoidal voltage must be applied to the secondary winding with the primary winding open-circuited, at a very low frequency to minimize eddy losses (known as DC saturation test), and the waveforms of both the applied voltage and the excitation current must be recorded. When integrating the voltage, a saturation curve must be result, where the saturation flux will correspond to the flux value at which the curve becomes practically horizontal.

Fig. 6.15 shows the static hysteresis loop of the CT, obtained by a DC saturation test. The old and new definitions of the saturation flux, according to the IEC, has also been marked in the figure.

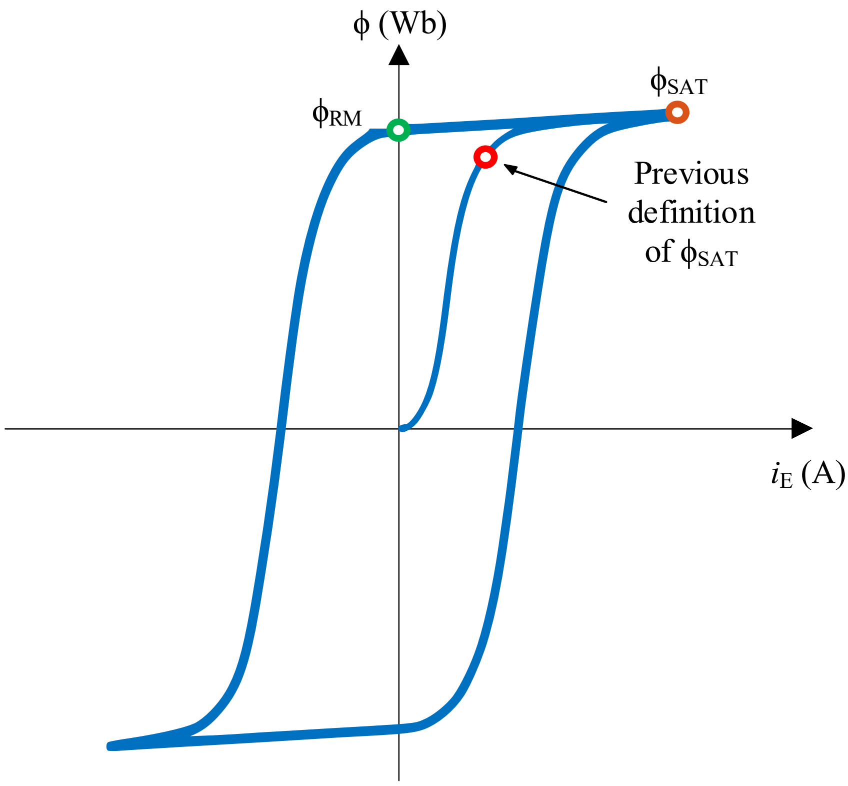

Fig. 6.15. IEC definitions of the saturation flux. The static hysteresis loop allows the maximum residual flux acquisition.

Then, the IEC saturation voltage is calculated from the saturation flux as

$$U_{\text{SAT}} = \frac{N_2 \cdot 2\pi f}{\sqrt{2}} \phi_{\text{SAT}} \tag{6.8}$$

This subsection finishes with another definition of the saturation voltage: the point where the CT error starts to exceed the 10% of 20 times the rated current. That is, the saturation voltage is the voltage U_m for a composite error $\varepsilon_c = 10\%$, i.e., for I_E equal to 10% of 20 times the rated current. This definition is related with the IEEE C-rating: secondary voltage U_2 ($U_2 = U_m - R_2 \cdot 20 I_{N2}$) for a composite error $\varepsilon_c = 10\%$, i.e., for I_E equal to 10% of 20 times the rated current. Related to this last definition of saturation voltage, a popular rule of thumb to avoid saturation is to assure that the IEEE C-rating is twice the secondary voltage induced by the maximum fault current [197]. This ensures operation near the knee-point for the maximum symmetrical fault current, as that the knee-point voltage can be typically considered the 46% of the last defined saturation voltage.

6.5. Saturation curve estimation

The dynamic study of the CT requires the knowledge of the instantaneous ϕ-i saturation curve. This curve can be obtained from the U_m–I_E excitation curve in RMS values by using the Dommel-Neves algorithm [146]. The excitation curves of the protection CT4 used in the most examples of this chapter are shown in Fig. 6.16(a) in log-log scale, and in Fig. 6.16(b) in linear scale. The point values of the excitation curve for the 2000/5 ratio are given in Table 6.3 [197].

The remaining characteristics of CT4 are:

- Multi-ratio CT 2000/5 A, C400.
- Secondary winding resistance: $R_2 = 1.02\ \Omega$.
- Ratio error $\varepsilon = 3\%$ at rated current, and composite error $\varepsilon_c = 10\%$ at 20 times the rated current.
- Rated burden B-4.0 at 60 Hz (see Table 6.4): $Z_B = 4\ \Omega$, $R_B = 2\ \Omega$, $L_B = 9.2$ mH, $PF_B = 0.5$, $S_B = 100$ VA.
- IEC equivalence (see Table 6.5): 100 VA, 5P20, with a ratio error $\varepsilon = 1\%$ at rated current, and a composite error $\varepsilon_c = 5\%$ at 20 times the rated current. Rated burden $Z_B = 4\ \Omega$, $PF_B = 1$, $S_B = 100$ VA.

Table 6.3. Excitation curve values of the protection CT 2000/5 A, C400 (CT4).

I_E (A)	U_m (V)
0.001	3.0
0.002	7.5
0.003	12.5
0.004	18
0.010	60
0.020	150
0.025	200
0.030	235
0.040	276
0.050	300
0.080	356
0.100	372
0.200	400
1.000	447
4.000	466
6.000	472
10.00	486

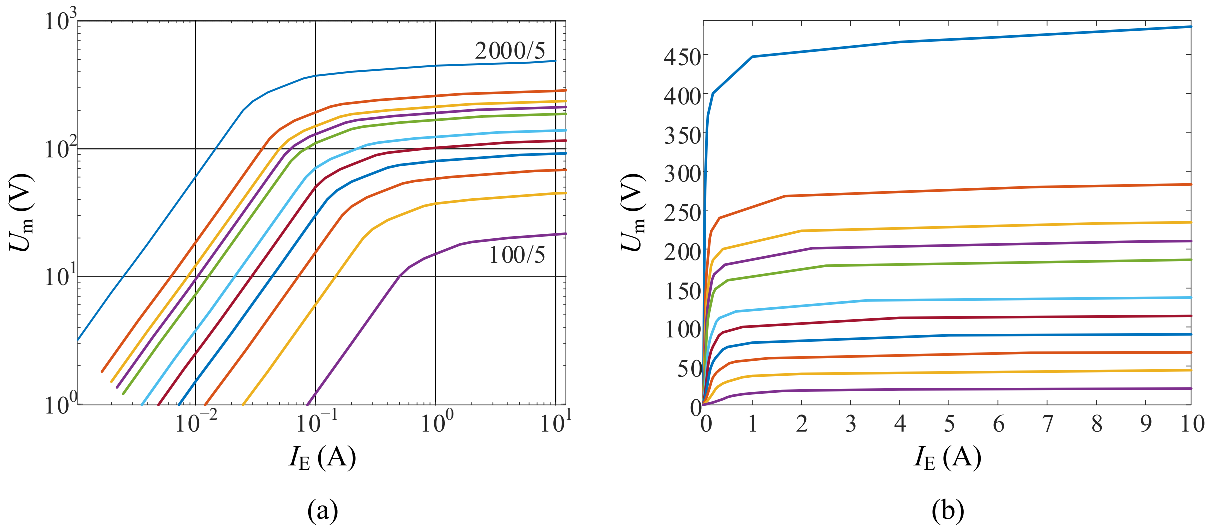

Fig. 6.16. Excitation curves of the protection multi-ratio CT 2000/5 A, C400 (CT4): (a) log-log scale, and (b) linear scale.

Given the data of any curve in Fig. 6.16, the data of another curve can be easily extracted by taking into account that the secondary magnetizing voltages are proportional to the ratio while the excitation currents are inversely proportional to the ratio. For example, the points of the 100/5 A curve can be obtained from the points of the 2000/5 A curve by dividing the voltages by (2000/5)/(100/5) = 20, while the currents are multiplied by 20. Regarding the secondary winding resistances, they are proportional to the ratio, e.g., the resistance of the 100/5 winding is 20 times smaller than the resistance of the 2000/5 winding.

Table 6.4. Standard relaying burdens for CTs with 5 A secondary windings according to IEEE.

Burden designation	Resistance (Ω)	Inductance (mH)	Impedance (Ω)	Total power at 5 A (VA)	Power factor	Secondary terminal voltage (V)
B-0.1	0.09	0.116	0.1	2.5	0.9	10
B-0.2	0.18	0.232	0.2	5.0	0.9	20
B-0.5	0.45	0.580	0.5	12.5	0.9	50
B-1.0	0.50	2.300	1.0	25.0	0.5	100
B-2.0	1.00	4.600	2.0	50.0	0.5	200
B-4.0	2.00	9.200	4.0	100.0	0.5	400
B-8.0	4.00	18.400	8.0	200.0	0.5	800

Table 6.5. Equivalence between IEEE and IEC protective accuracy classes for 5 A CTs.

Secondary terminal voltage (V)	Secondary burden designation	Impedance (Ω)	IEEE protective accuracy	Equivalent IEC protective accuracy
10	B-0.1	0.1	C10	2.5VA-5P20
20	B-0.2	0.2	C20	5.0VA-5P20
50	B-0.5	0.5	C50	12.5VA-5P20
100	B-1.0	1.0	C100	25VA-5P20
200	B-2.0	2.0	C200	50VA-5P20
400	B-4.0	4.0	C400	100VA-5P20
800	B-8.0	8.0	C800	200VA-5P20

The instantaneous ϕ-i curves of CT4 obtained with the Dommel-Neves algorithm are shown in Fig. 6.17(a). Next, the CT4 curves of Fig. 6.17(a) have been adjusted to the saturation curve of (2.7), and the estimated parameters are shown in Table 6.6. Fig. 6.17(b) plots the predicted curves with the estimated parameters. Lastly, Fig. 6.18 compares three of the original curves in Fig. 6.17(a) with the estimated curves in Fig. 6.17(b). It is apparent the goodness of the estimation as the curves are very similar, specially by taking into account that original data of Fig. 6.16(a) was given in logarithmic scale.

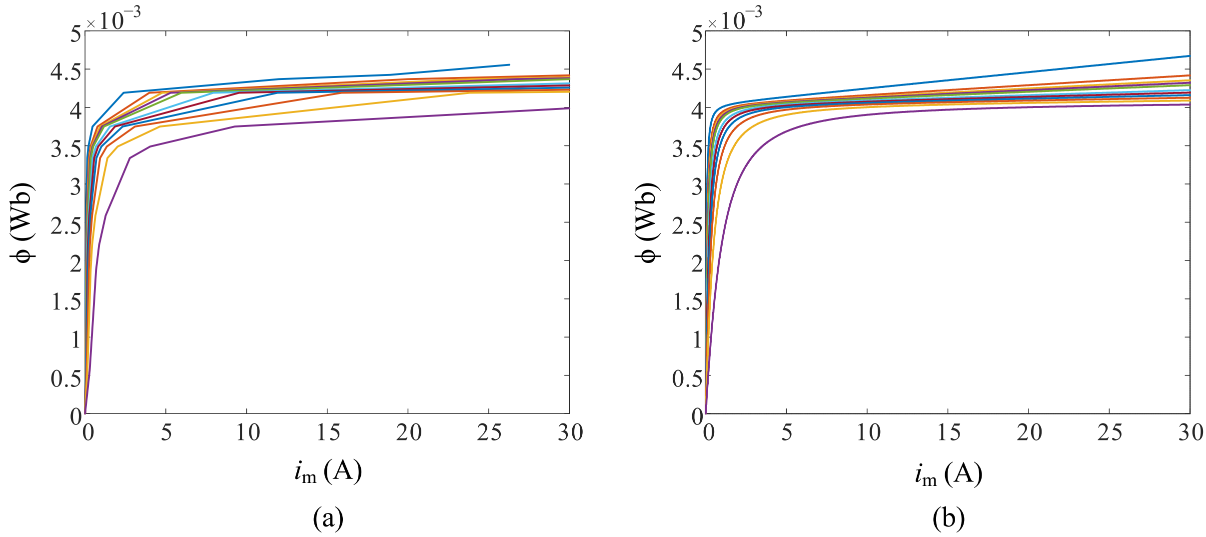

Fig. 6.17. Saturation curves of CT4: (a) direct conversion from points in excitation curve, and (b) saturation curve from estimated parameters.

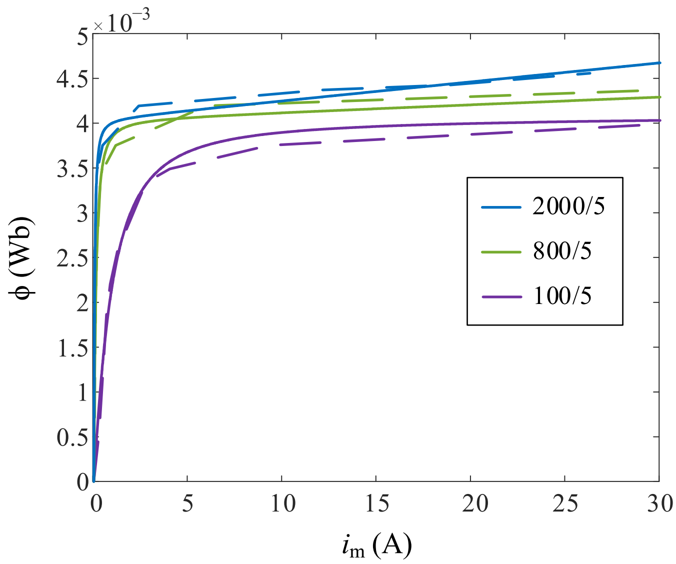

Fig. 6.18. Comparison between three of the original saturation curves of CT4 in Fig. 6.17(a) (dotted line) with those predicted by the estimated parameters in Fig. 6.17(b) (solid line).

Table 6.6. Estimated saturation curve parameters of the protection multi-ratio CT 2000/5 A, C400 (CT4).

Ratio	K_1 (Wb/A·t)	K_2 (Wb/A·t)	p	k_{SAT}
2000/5	0.0670	$21.2\cdot10^{-6}$	1.393	0.0466
1200/5	0.0402	$12.7\cdot10^{-6}$	1.393	0.0467
1000/5	0.0335	$10.6\cdot10^{-6}$	1.393	0.0468
900/5	0.0302	$9.5\cdot10^{-6}$	1.393	0.0469
800/5	0.0268	$8.5\cdot10^{-6}$	1.393	0.0470
600/5	0.0201	$6.4\cdot10^{-6}$	1.393	0.0471
500/5	0.0167	$5.3\cdot10^{-6}$	1.393	0.0472
400/5	0.0134	$4.2\cdot10^{-6}$	1.393	0.0473
300/5	0.0101	$3.2\cdot10^{-6}$	1.393	0.0474
200/5	0.0067	$2.1\cdot10^{-6}$	1.393	0.0475
100/5	0.0034	$1.1\cdot10^{-6}$	1.393	0.0476

6.6. Experimental results

Three CTs have been tested in the laboratory. CT1 is a protection transformer of 100/5 A, 5 VA, with no other data available. CT2 is a protection transformer of 1000/5 A, 20 VA, 5P10 (i.e., the ratio error at rated current is $\varepsilon = 1\%$, and the composite error at 20 times the rated current is $\varepsilon_c = 5\%$). CT3 is a metering transformer of 800/5 A, 15 VA, class 0.5 (i.e., the ratio error at 0.05 times the rated current is $\varepsilon = 1.5\%$, and the ratio error at rated current is $\varepsilon = 0.5\%$).

Different excitation tests were made at eight different secondary voltages and rated frequency, and the instantaneous waveforms of secondary voltage and current were registered. The results are shown in Fig. 6.19(a), Fig. 6.20(a) and Fig. 6.21(a). It can be observed that the no test was made at a depth saturation voltage. The instantaneous ϕ-i curve was obtained from the excitation tests, and the results are shown in Fig. 6.19(b), Fig. 6.20(b) and Fig. 6.21(b).

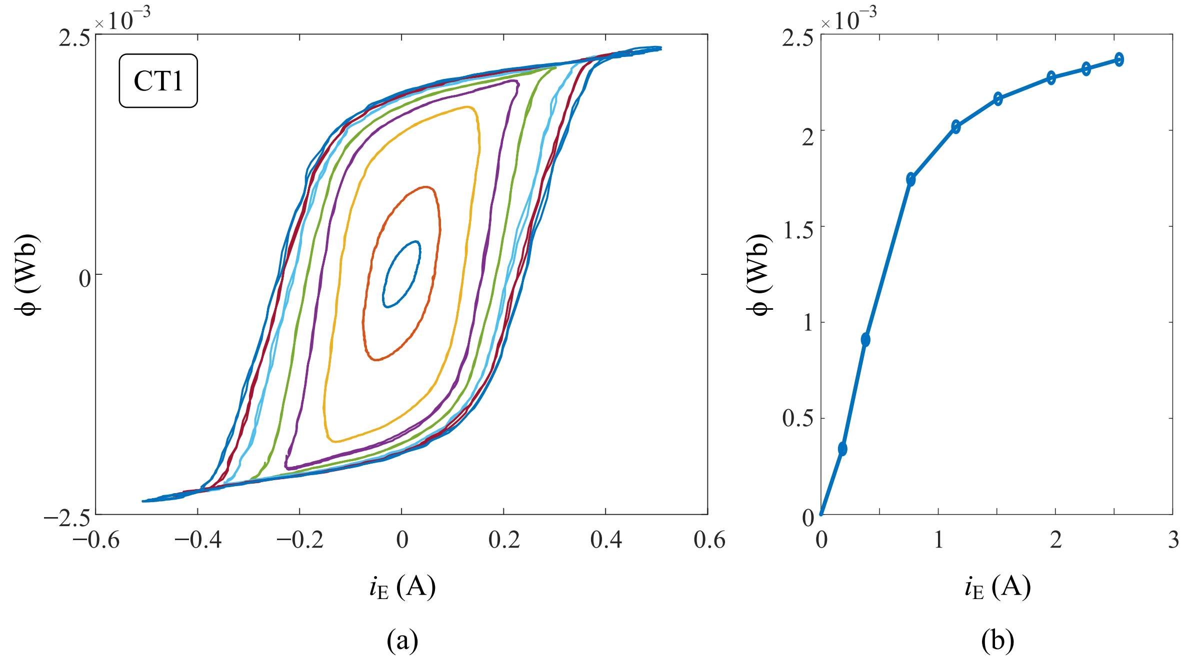

Fig. 6.19. Protection CT 100/5 A, 5 VA (CT1): (a) Excitation tests at different levels of current, and (b) obtained saturation curve.

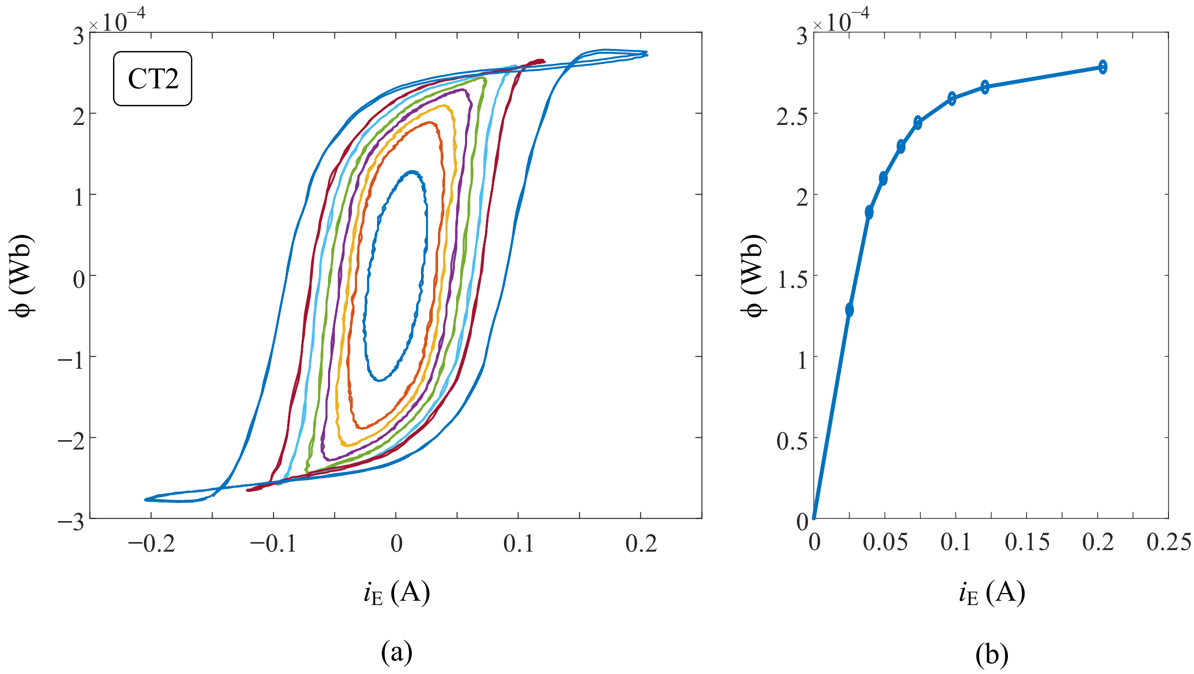

Fig. 6.20. Protection CT 1000/5 A, 20 VA, 5P10 (CT2): (a) Excitation tests at different levels of current, and (b) obtained saturation curve.

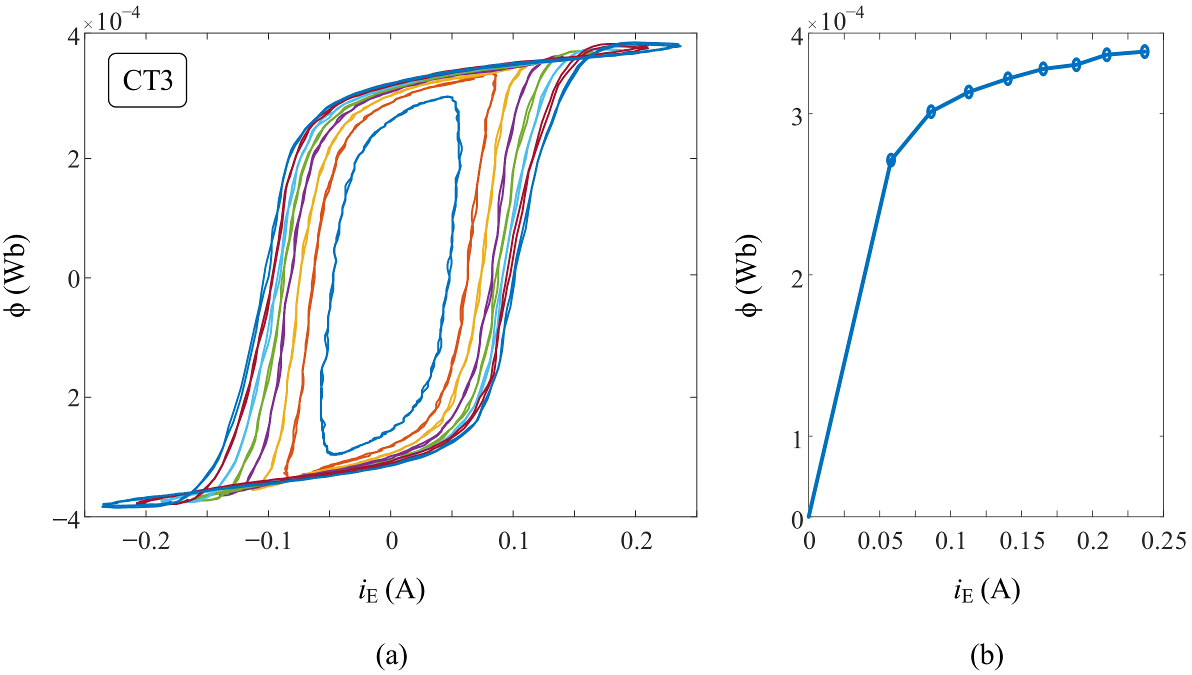

Fig. 6.21. Metering CT 800/5 A, 15 VA (CT3): (a) Excitation tests at different levels of current, and (b) obtained saturation curve.

For comparison purposes, the U_m-I_E excitation curves in RMS values and in log-log scale for the three CTs are illustrated in Fig. 6.22. It is clear from this figure that the achieved saturation was no severe in all cases.

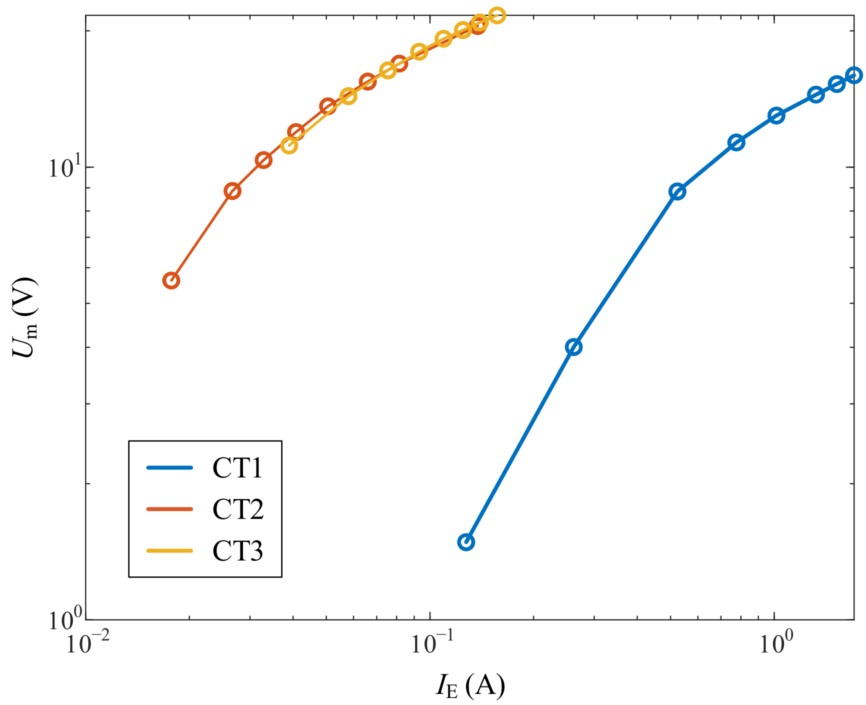

Fig. 6.22. Experimental excitation curves for CT1, CT2, and CT3.

Chapter 7. Conclusions and further work

7.1. Main contributions and conclusions

The main contributions of this thesis and their respective conclusions can be summarized as follows:

Single-phase power transformer

1. An analysis of the inrush current phenomenon and all the variables and parameters affecting its severity has been carried out.

2. The residual flux phenomenon and the de-energization trajectories have been thoroughly examined in order to predict the residual flux value in a very simple manner.

3. A straightforward strategy (smart switching) has been proposed to avoid inrush current, without the need to measure or estimate at any time the residual flux, either during de-energization or before energization.

4. Using a simple transformer model, a novel and simple methodology has been developed to estimate the saturation curve (including the slope of the saturation zone), employing minimum information from straightforward measurements (no-load test and inrush current).

The transient de-energization trajectories of the single-phase transformer have been analyzed in this paper for three main purposes: (1) understanding its behavior, (2) predicting residual flux values, and (3) to propose a methodology to avoid inrush currents in single-phase transformers, more simple than the literature methodologies. It has been demonstrated that: (a) the range of residual flux values is determined by the static hysteresis loop, while eddy losses have no influence, (b) the residual flux value is independent of the circuit breaker interruption speed and (c) only depends on the de-energization point-on-wave. The proposed smart switching only requires two pieces of data (obtained from only two simple no-load tests): ϕ_{RM} and ϕ_{i0}, or the corresponding voltage points-on-wave α_{RM} and α_{i0}, along with understanding of the used breaker technology. In opposite to the literature methodologies, the proposed smart switching does not require to estimate the residual flux or to preset a known value previous to each energization, avoiding complex measurement setups and continuous signal acquisition during each de-energization. It can be applied to any power transformer installed on the grid or in industrial facilities, extending beyond transformers in laboratories. Although the proposed methodology is applicable to SCR and IGBT breakers with equal results, the SCR breaker is a more cost-effective solution suitable for large power systems.

By other hand, among the hundreds of papers in the literature using an inrush test to, e.g., validate their proposed models, only a few papers use an inrush test to estimate the transformer parameters. In contrast to such literature methods, the one described in this paper: (a) does not need the knowledge of the residual flux or the knowledge of the energization point-on-wave, and (b) no values for these two variables are assumed. Strictly speaking, it is not required all the inrush current waveform as only the i_{PEAK} and τ values are the unique inputs for the estimation procedure of the saturation slope K_2. Even, these two pieces of information (i_{PEAK} and τ) could be visually obtained from a simple scope, but also from manufacturer data tables or from the protective relays programming experience. The results show that a more severe inrush test leads to a more accurate K_2 estimation. The saturation curve obtained from a given test characterizes with a good accuracy all possible equally or less severe inrush tests.

The results demonstrate that a saturation curve model with only two slopes is accurate enough to predict inrush currents.

An important contribution is that the nonlinear transformer core can be fully characterized by its signature (main envelope of the inrush current peaks in the worst case) plus the harmonic content of the no-load current.

Three-phase three-legged power transformer

1. An innovative methodology to estimate the saturation curve, including deep saturation. Unlike other methodologies, the proposal only requires terminal measurements (only one three-phase inrush test and only one three-phase no-load test) without breaking the winding connections and without knowledge of the residual flux. No special tests with specific winding connections are necessary.

The proposal is applicable to all transformers, regardless of their winding connections. In contrast to other methodologies described in the literature, the approach presented in this paper does not need the knowledge of the residual flux or the knowledge of the energization point-on-wave, in such a way that an inrush test with controlled switching is not necessary. Moreover, there is no requirement to determine the air path reluctance or assume any value prior to the saturation curve estimation. These remarkable features allow the methodology to be applied to any transformer installed on the grid or in industrial facilities, extending its practicality beyond laboratory transformers. Consequently, it is a more practical alternative compared to other methodologies described in the literature.

An important contribution lies in the characterization of the nonlinear transformer core and the magnetic interaction between its core legs through its signature: the instantaneous reactive power.

Current transformer

1. A comprehensive analysis of the current transformer saturation has been carried out.

2. An approach has been proposed to characterize the magnetizing characteristics of the current transformer solely based on the nameplate and the class information provided in the IEEE and IEC standards.

3. An FPGA-based smart sensor has been developed to detect current transformer saturation, particularly during inrush current measurements.

It has been observed that the time-to-saturation mainly depends on the total secondary resistance, whereas the total secondary inductance does not exert significant influence. Saturation during inrush currents (which has not been extensively studied in the literature) is more likely to occur with a higher inrush current decay constant, a condition found in large transformers.

The points of the saturation curve (instantaneous values) of a CT have been obtained from the points of the excitation curve (RMS values). Using these points of the saturation curve, the parameters of a simple model of saturation curve can be adjusted.

Finally, it has been proposed a new methodology to detect the CT saturation mainly during inrush conditions, as well as its implementation into an FPGA-based smart sensor. This represents an important initial step towards secondary current compensation.

7.2. Further work

The possible lines of research opened up by the present work are the following:

1. Extension to three-phase transformers of the methodology to avoid inrush currents, without the need to measure and/or estimate residual fluxes.

2. Extension of the methodology from Chapter 6 to estimate the saturation curve of five-legged transformers.

3. Analysis of the phenomenon of sympathetic currents that occur when multiple transformers operate in parallel.

4. Development of models for three-winding transformers.

5. Proposal of typical values for the parameters of the saturation curve of protection CTs. This is especially interesting for CTs based on IEC standards, as the excitation curve is not provided by the manufacturer, in contrast to the CTs based on IEEE standards.

6. Furthermore, the compensation of the saturated current needs to be implemented based on the knowledge developed in this thesis.

References

[1] D. Povh and W. Schultz, “Analysis of Overvoltages Caused by Transformer Magnetizing Inrush Current,” *IEEE Trans. Power Appar. Syst.*, vol. PAS-97, no. 4, pp. 1355-1365, July 1978.

[2] J. F. Witte, F. P. DeCesaro and S. R. Mendis, “Damaging long-term overvoltages on industrial capacitor banks due to transformer energization inrush currents,” *IEEE Tran. Ind. Appl.*, vol. 30, no. 4, pp. 1107-1115, July-Aug. 1994.

[3] M. Steurer and K. Frohlich, “The impact of inrush currents on the mechanical stress of high voltage power transformer coils,” *IEEE Trans. Power Del.*, vol. 17, no. 1, pp. 155-160, Jan. 2002.

[4] R. A. Turner and K. S. Smith, “Resonance excited by transformer inrush current in inter-connected offshore power systems,” in Proc. IEEE Industry Applications Society Annual Meeting IAS ’08, Oct. 5–9, 2008, pp. 1–7.

[5] H. C. Seo and C. H. Kim, “The analysis of power quality effects from the transformer inrush current: A case study of the Jeju power system, Korea,” 2008 IEEE Power and Energy Society General Meeting - Conversion and Delivery of Electrical Energy in the 21st Century, Pittsburgh, PA, USA, 2008, pp. 1-6.

[6] N. W. Priambodo, B. B. S. D. A. Harsono, K. G. Hadith Mangunkusumo and B. Sofiarto Munir, “A Case Study of Transformer Inrush Current Analysis in Java-Bali Power System,” 2019 5th International Conference on Science and Technology (ICST), Yogyakarta, Indonesia, 2019.

[7] M. -C. Nițu, “Effects of Inrush Current on Operating Transformers when the Series Resonance Condition is Met,” 2023 Power Quality and Electromagnetic Compatibility at Low Frequency (PQEMC-LF), Craiova, Romania, 2023, pp. 25-28.

[8] M. Nagpal, T. G. Martinich, A. Moshref, K. Morison and P. Kundur, “Assessing and limiting impact of transformer inrush current on power quality,” *IEEE Trans. Power Del.*, vol. 21, no. 2, pp. 890-896, Apr. 2006.

[9] M. Khederzadeh, “Power quality enhancement by TCSC application to mitigate the impact of transformer inrush current,” 2008 IEEE/PES Transmission and Distribution Conference and Exposition, Chicago, IL, USA, 2008, pp. 1-5.

[10] S. Whaite, B. Grainger, and A. Kwasinski, “Power Quality in DC Power Distribution Systems and Microgrids,” *Energies*, vol. 8, no. 5, pp. 4378–4399, May 2015.

[11] A. Guzman, S. Zocholl, G. Benmouyal, and H. J. Altuve, “A current based solution for transformer differential protection - Part I: Problem statement,” *IEEE Trans. Power Del.*, vol. 16, no. 4, pp. 485–491, Oct. 2001.

[12] C. Mo, T.Y. Ji, L.L. Zhang and Q.H. Wu, "Equivalent statistics based inrush identification method for differential protection of power transformer,"" Electric Power Systems Research, vol. 203, p. 107664, Feb. 2022.

[13] P. Mishra, A. Swain, A. K. Pradhan and P. Bajpai, “Sequence Current based Inrush Detection in High Permeability Core Transformers,” *IEEE Trans. Instrum. Meas.*, 2023.

[14] T. R. Specht, “Transformer magnetizing inrush current,” *AIEE Trans.*, vol. 70, no.4, pp. 323–328, Apr. 1951.

[15] W. K. Sonneman, C. L. Wagner, and G. D. Rockefeller, “Magnetizing inrush phenomena in transformer banks,” *IEEE Trans. Power App. Syst.*, vol. PAS-77, no. 3, pp. 884–892, Oct. 1958.

[16] G. Bertagnolli, Short-Circuit Duty of Power Transformers, Second Revised Edition. ABB, 1996.

[17] Y. Wang, S. G. Abdulsalam, and W. Xu, “Analytical formula to estimate the maximum inrush current,” *IEEE Trans. Power Del.*, vol. 23, no. 2, pp. 1266–1268, Apr. 2008.

[18] S. Jazebi, F. de León and N. Wu, “Enhanced Analytical Method for the Calculation of the Maximum Inrush Currents of Single-Phase Power Transformers,” *IEEE Trans. Power Del.*, vol. 30, no. 6, pp. 2590-2599, Dec. 2015.

[19] S. E. Zirka, Y. I. Moroz, C. M. Arturi, N. Chiesa and H. K. Hoidalen, "Topology-Correct Reversible Transformer Model," *IEEE Trans. Power Del.*, vol. 27, no. 4, pp. 2037-2045, Oct. 2012.
[20] J. F. Holcomb, "Distribution transformer magnetizing inrush current," *Trans. Amer. Inst. Electr. Eng., Part III (Power Appar. Syst.)*, vol. 80, no. 3, pp. 697–702, Apr. 1961.
[21] R. Yacamini and A. Abu-Nasser, "Numerical calculation of inrush current in single-phase transformers," *Proc. Inst. Elect. Eng.*, vol. 128, no.6, pt. B, pp. 327–334, Nov. 1981.
[22] A. Moradi, and S. M. Madani, "Technique for inrush current modelling of power transformers based on core saturation analysis," *IET Gener. Transm. Distrib.*, vol. 12, no. 10, pp. 2317-2324, May 2018.
[23] G. Komarzyniec, "Calculating the Inrush Current of Superconducting Transformers," *Energies*, vol. 14, no. 20, p. 6714, Oct. 2021.
[24] M. Basu and K. P. Basu, "Computerised evaluation of the magnetising inrush current in transformers," *Electr. Power Syst. Res.*, vol. 2, no. 3, pp. 179-182, Nov. 1979.
[25] C. E. Lin, C. -L. Cheng, C. -L. Huang and J. -C. Yeh, "Investigation of magnetizing inrush current in transformers. I. Numerical simulation," *IEEE Trans. Power Del.*, vol. 8, no. 1, pp. 246-254, Jan. 1993.
[26] J. J. Rico, E. Acha and M. Madrigal, "The study of inrush current phenomenon using operational matrices," *IEEE Trans. Power Del.*, vol. 16, no. 2, pp. 231-237, April 2001.
[27] M. G. Vanti, S. L. Bertoli, S. H. L. Cabral, A. G. Gerent and P. Kuo-Peng, "Semianalytic Solution for a Simple Model of Inrush Currents in Transformers," *IEEE Trans. Magn.*, vol. 44, no. 6, pp. 1270-1273, June 2008.
[28] R. A. Naghizadeh, B. Vahidi, and S. H. Hosseinian, "Modeling of inrush current in transformers using inverse Jiles-Atherton hysteresis model with a neuro-shuffled frog-leaping algorithm approach," *IET Elect. Power Appl.*, vol. 6, no. 9, pp. 727–734, Nov. 2012.
[29] E. Sorrentino, "Approximate method to compute the maximum rms current in a distribution feeder due to simultaneous inrush currents in downstream transformers," *Electr. Power Syst. Res.*, vol. 145, pp. 89-98, Apr. 2017.
[30] Ł. Majka, B. Baron, and P. Zydroń, "Measurement-Based Stiff Equation Methodology for Single Phase Transformer Inrush Current Computations," *Energies*, vol. 15, no. 20, p. 7651, Oct. 2022.
[31] R. S. Girgis and E. G. teNyenhuis, "Characteristics of inrush current of present designs of power transformers," in Proc. IEEE Power Eng, Soc. Gen. Meeting, Jun. 2007, pp. 1–6.
[32] R. Hamilton, "Analysis of Transformer Inrush Current and Comparison of Harmonic Restraint Methods in Transformer Protection," *IEEE Trans. Ind. Appl.*, vol. 49, no. 4, pp. 1890-1899, July-Aug. 2013.
[33] X. Lin, J. Huang, L. Zeng and Z. Q. Bo, "Analysis of Electromagnetic Transient and Adaptability of Second-Harmonic Restraint Based Differential Protection of UHV Power Transformer," I*EEE Trans. Power Del.*, vol. 25, no. 4, pp. 2299-2307, Oct. 2010,.
[34] Z. Ruhan, N. N. B. Mansor, and H. A. Illias, "Identification of Inrush Current Using a GSA-BP Network," Energies, vol. 16, no. 5, p. 2340, Feb. 2023.
[35] P. C. Y. Ling and A. Basak, "Investigation of magnetizing inrush current in a single-phase transformer," *IEEE Trans. Magn.*, vol. 24, no. 6, pp. 3217-3222, Nov. 1988.
[36] W. Chandrasena, P. G. McLaren, U. D. Annakkage and R. P. Jayasinghe, "An improved low-frequency transformer model for use in GIC studies," *IEEE Trans. Power Del.*, vol. 19, no. 2, pp. 643-651, Apr. 2004.
[37] Shin-Der Chen, R. -L. Lin and Chih-Kun Cheng, "Magnetizing inrush model of transformers based on structure parameters," *IEEE Trans. Power Del.*, vol. 20, no. 3, pp. 1947-1954, July 2005.
[38] J. Faiz and S. Saffari, "Inrush Current Modeling in a Single-Phase Transformer," *IEEE Trans. Magn.*, vol. 46, no. 2, pp. 578-581, Feb. 2010.

[39] A. Tokić, I. Uglešić and G. Štumberger, “Simulations of Transformer Inrush Current by Using BDF-Based Numerical Methods,” *Math. Probl. Eng.*, vol. 2013, p. 10(s), Jul. 2013.

[40] E. Cardelli, A. Faba and F. Tissi, “Prediction and Control of Transformer Inrush Currents,” *IEEE Trans. Magn.*, vol. 51, no. 3, pp. 1-4, March 2015.

[41] S. Jazebi, F. de León, A. Farazmand and D. Deswal, “Dual Reversible Transformer Model for the Calculation of Low-Frequency Transients,” *IEEE Trans. Power Del.*, vol. 28, no. 4, pp. 2509-2517, Oct. 2013.

[42] J. A. Corea-Araujo, J. A. Martinez-Velasco, F. González-Molina, J. A. Barrado-Rodrigo, L. Guasch-Pesquer and F. Castro-Aranda, “Validation of single-phase transformer model for ferroresonance analysis,” *Electr. Eng.*, vol. 100, pp. 1339–1349 Sept. 2018.

[43] W. Sima, D. Peng, M. Yang, Y. Liu, P. Duan, J. Deng and H. Qian, “Low-frequency model for single-phase transformers based on the three-component Preisach model considering deep saturation,” *Int. J. Electr. Power Energy Syst.*, vol. 110, pp. 107-117, Sept. 2019.

[44] H. Altun, S. Sünter and Ö. Aydoğmuş, “Modeling and analysis of a single-phase core-type transformer under inrush current and nonlinear load conditions,” *Electr. Eng.*, vol. 103, pp. 2961–2972, Dec. 2021.

[45] J. Pedra, L. Sainz, F. Córcoles, R. López, and M. Salichs, “PSPICE computer model of a nonlinear three-phase three-legged transformer,” *IEEE Trans. Power Del.*, vol. 19, no. 1, pp. 200–207, Jan. 2004.

[46] U. Rudez and R. Mihalic, “Sympathetic inrush current phenomenon with loaded transformers,” *Electr. Power Syst. Res.*, vol. 138, pp. 3-10, Sept. 2016.

[47] W. Xu, S. G. Abdulsalam, Yu Cui and Xian Liu, “A sequential phase energization technique for transformer inrush current reduction - Part II: theoretical analysis and design guide,” *IEEE Trans. Power Del.*, vol. 20, no. 2, pp. 950-957, Apr. 2005.

[48] H. -C. Seo, C. -H. Kim, S. -B. Rhee, J. -C. Kim and O. -B. Hyun, "Superconducting Fault Current Limiter Application for Reduction of the Transformer Inrush Current: A Decision Scheme of the Optimal Insertion Resistance,” *IEEE Trans. Appl. Supercond.*, vol. 20, no. 4, pp. 2255-2264, Aug. 2010.

[49] S. M. Madani, M. Rostami, G. B. Gharehpetian, and R.H. Maram, “Improved bridge type inrush current limiter for primary grounded transformers,” *Electr. Power Syst. Res.*, vol. 95, pp. 1-8, Feb. 2013.

[50] Tseng, H.T.; Chen, J.F. “Bidirectional impedance-type transformer inrush current limiter,” *Electr. Power Syst. Res.*, vol. 104, pp. 193-206, Nov. 2013.

[51] A. A. Ahmed and H. A. Abdelsalam, “Mitigation of transformer-energizing inrush current using grid-connected photovoltaic system,” *Int. J. Electr. Power Energy Syst.*, vol. 79, pp. 312-321, July 2016.

[52] Y. Guo, Z. Zheng, Q. Xie and J. Zhao, “Study of Resistive Type SFCL for Limiting Inrush Current of LCC-HVDC Converter Transformer,” *IEEE Trans. Appl. Supercond.*, vol. 31, no. 8, pp. 1-4, Nov. 2021.

[53] Y. Wang, X. Yin, J. Qiao, L. Tan and W. Xu, “Inrush current suppression technology for floating nuclear power plants based on connecting Pre-T in series,” *Int. J. Electr. Power Energy Syst.*, vol. 135, 107508, Feb. 2022.

[54] V. Molcrette, J. -L. Kotny, J. -P. Swan and J. -F. Brudny, “Reduction of inrush current in single-phase transformer using virtual air gap technique,” *IEEE Trans. Magn.*, vol. 34, no. 4, pp. 1192-1194, July 1998.

[55] C. K. Cheng, J. F. Chen, T. J. Liang, and S. D. Chen, “Transformer design with consideration of restrained inrush current,” *Int. J. Electr. Power Energy Syst.*, vol. 28, pp. 102-108, Feb. 2006.

[56] M. M. Islam, K. M. Muttaqi and D. Sutanto, “A Saturated Amorphous Alloy Core-Based Inrush Current Limiter to Eliminate Inrush Currents and Restrain Harmonics during Transformer Energization,” *IEEE Trans. Ind. Appl.*, vol. 57, no. 6, pp. 6634-6645, Nov.-Dec.

[57] R. Dogan, S. Jazebi and F. de León, “Investigation of Transformer-Based Solutions for the Reduction of Inrush and Phase-Hop Currents,” *IEEE Trans. Power Electron.*, vol. 31, no. 5, pp. 3506-3516, May 2016.
[58] B. Kovan, F. de Leon, D. Czarkowski, Z. Zabar and L. Birenbaum, “Mitigation of Inrush Currents in Network Transformers by Reducing the Residual Flux With an Ultra-Low-Frequency Power Source,” *IEEE Trans. Power Del.*, vol. 26, no. 3, pp. 1563-1570, July 2011.
[59] F. de León, A. Farazmand, S. Jazebi, D. Deswal and R. Levi, “Elimination of Residual Flux in Transformers by the Application of an Alternating Polarity DC Voltage Source,” *IEEE Trans. Power Del.*, vol. 30, no. 4, pp. 1727-1734, Aug. 2015.
[60] S. Sanati and Y. Alinejad-Beromi, “Fast and Complete Mitigation of Residual Flux in Current Transformers Suitable for Auto-Reclosing Schemes Using Jiles-Atherton Modeling,” *IEEE Trans. Power Del.*, vol. 37, no. 2, pp. 765-774, April 2022.
[61] E. Hajipour, M. Salehizadeh, M. Vakilian and M. Sanaye-Pasand, “Residual Flux Mitigation of Protective Current Transformers Used in an Autoreclosing Scheme,” *IEEE Trans. Power Del.*, vol. 31, no. 4, pp. 1636-1644, Aug. 2016.
[62] S. Zhang et al., “Improved Flux-Controlled VFCV Strategy for Eliminating and Measuring the Residual Flux of Three-Phase Transformers,” *IEEE Trans. Power Del.*, vol. 35, no. 3, pp. 1237-1248, June 2020.
[63] L. Prikler, G. Banfai, G. Ban, and P. Becker, “Reducing the magnetizing inrush current by means of controlled energization and de-energization of large power transformers,” *Electr. Power Syst. Res.*, vol. 76, no. 8, pp. 642-649, May 2006.
[64] N. Chiesa and H. K. Høidalen, “Novel Approach for Reducing Transformer Inrush Currents: Laboratory Measurements, Analytical Interpretation and Simulation Studies,” *IEEE Trans. Power Del.*, vol. 25, no. 4, pp. 2609-2616, Oct. 2010.
[65] U. Parikh and B. R. Bhalja, “Mitigation of magnetic inrush current during controlled energization of coupled un-loaded power transformers in presence of residual flux without load side voltage measurements,” *Int. J. Electrical Power Energy Syst.*, vol. 76, pp. 156-164, Mar. 2016.
[66] R. Cano-González, A. Bachiller-Soler, J. A. Rosendo-Macías, and G. Álvarez-Cordero, “Controlled switching strategies for trans-former inrush current reduction: A comparative study,” *Electr. Power Syst. Res.*, vol. 145, pp. 12-18, Apr. 2017.
[67] D. Bejmert, M. Kereit and K. Boehme, “Controlled energization procedures of power transformers,” *Int. J. Electr. Power Energy Syst.*, vol. 135, pp. 107555, Feb. 2022.
[68] D. Cavallera, V. Oiring, J. -L. Coulomb, O. Chadebec, B. Caillault and F. Zgainski, “A New Method to Evaluate Residual Flux Thanks to Leakage Flux, Application to a Transformer,” *IEEE Trans. Magn.*, vol. 50, no. 2, pp. 1005-1008, Feb. 2014.
[69] C. Wei, X. Li, M. Yang, Z. Ma, and H. Hou, “Novel Remanence Determination for Power Transformers Based on Magnetizing Inductance Measurements,” *Energies*, vol. 12, no. 24, p. 4616, Dec. 2019.
[70] C. Huo, S. Wu, Y. Yang, C. Liu and Y. Wang, “Residual Flux Density Measurement Method of Single-Phase Transformer Core Based on Time Constant,” *IEEE Access*, vol. 8, pp. 171479-171488, 2020.
[71] C. Huo, Y. Wang, Z. Zhao and C. Liu, “Residual Flux Measurement of the Single-Phase Transformer Based on Transient Current Method,” *IEEE Trans. Appl. Supercond.*, vol. 30, no. 4, pp. 1-5, June 2020.
[72] S. Wu, Y. Ren, Y. Wang, C. Huo and C. Liu, “Residual Flux Measurement of Power Transformer Based on Transient Current Difference,” *IEEE Trans. Magn.*, vol. 58, no. 2, pp. 1-5, Feb. 2022.
[73] C. Huo, Y. Wang, S. Wu, Y. Yang and Z. Zhao, “Residual Flux Density Measurement Method for Transformer Core Considering Relative Differential Permeability,” *IEEE Trans. Magn.*, vol. 57, no. 2, pp. 1-4, Feb. 2021.

[74] H. Zhang et al., "A New Method to Measure the Residual Flux by Magnetic Sensors and a Finite-Element Model," *IEEE Trans. Instrum. Meas.*, vol. 72, pp. 1-10, 2023.
[75] D. Vulin, K. Milicevic, I. Biondic and G. Petrovic, "Determining the Residual Magnetic Flux Value of a Single-Phase Transformer Using a Minor Hysteresis Loop," *IEEE Trans. Power Del.*, vol. 36, no. 4, pp. 2066-2074, Aug. 2021.
[76] D. I. Taylor, J. D. Law, B. K. Johnson and N. Fischer, "Single-Phase Transformer Inrush Current Reduction Using Prefluxing," *IEEE Trans. Power Del.*, vol. 27, no. 1, pp. 245-252, Jan. 2012.
[77] N. Chiesa, A. Avendaño, H. K. Høidalen, B. A. Mork, D. Ishchenko and A. P. Kunze, "On the ringdown transient of transformers," in International Conference on Power Systems Transients (IPST'07) in Lyon, France, June 4-7, 2007, pp. 1–6.
[78] D. C. Jiles and D. Atherton, "Ferromagnetic hysteresis," *IEEE Trans. Magn.*, vol. 19, no. 5, pp. 2183-2185, Sep. 1983.
[79] E. Cardelli, E. Della Torre, V. Esposito and A. Faba, "Theoretical Considerations of Magnetic Hysteresis and Transformer Inrush Current," *IEEE Trans. Magn.*, vol. 45, no. 11, pp. 5247-5250, Nov. 2009.
[80] D.S. Schmool and D. Markó, "Magnetism in Solids: Hysteresis," in Reference Module in Materials Science and Materials Engineering, Elsevier, 2018.
[81] E. Cardelli, "Chapter 4 - Advances in Magnetic Hysteresis Modeling," in Handbook of Magnetic Materials, vol. 24, K.H.J. Buschow, Elsevier, 2015, pp. 323-409.
[82] D. C. Jiles, "Theory of ferromagnetic hysteresis," *J. Appl. Phys.*, vol. 55, no. 6, pp. 2115–2120, Mar. 1984.
[83] D. C. Jiles and D. L. Atherton, "Theory of ferromagnetic hysteresis," *J. Magn. Magn. Mater.*, vol. 61, no. 1-2, pp. 48–60, Sep. 1986.
[84] F. Preisach, "Uber die magnetische nachwrikung," *Zeitschrift fur Physik*, vol. B 94, pp. 277–302, May 1935.
[85] E. C. Stoner and E. P. Wohlfarth, "A mechanism of magnetic hysteresis in heterogeneous alloys," *Phil. Trans. Roy. Soc.*, vol. 240A, pp. 599–642, May 1948.
[86] A. Globus, "Universal hysteresis loop for soft ferrimagnetic polycrystals," Physica B+C, vol. 86-88, pp. 943-944, Jan.-Mar. 1977.
[87] F. Liorzou, B. Phelps and D. L. Atherton, "Macroscopic models of magnetization," *IEEE Trans. Magn.*, vol. 36, no. 2, pp. 418-428, March 2000.
[88] E. Della Torre, "Effect of interaction on the magnetization of single-domain particles," *IEEE Trans. Audio Electroacoust.*, vol. 14, no. 2, pp. 86-92, June 1966.
[89] D. Atherton, B. Szpunar and J. Szpunar, "A new approach to Preisach diagrams," *IEEE Trans. Magn.*, vol. 23, no. 3, pp. 1856-1865, May 1987.
[90] I. D. Mayergoyz and G. Friedman, "Generalized Preisach model of hysteresis," *IEEE Trans. Magn.*, vol. 24, no. 1, pp. 212-217, Jan. 1988.
[91] D. L. Atherton and J. R. Beattie, "A mean field Stoner–Wohlfarth hysteresis model," *IEEE Trans. Magn.*, vol. 26, pp. 3059–3061, Nov. 1990.
[92] D. C. Jiles, "Frequency dependence of hysteresis curves in conducting magnetic materials," *J. Appl. Phys.*, vol. 76, no. 10, pp. 5849–5855, Nov. 1994.
[93] D. A. Philips, L. R. Dupre and J. A. A. Melkebeek, "Magneto-dynamic field computation using a rate-dependent Preisach model," *IEEE Trans. Magn.*, vol. 30, no. 6, pp. 4377-4379, Nov. 1994.
[94] K. Chwastek, "Modelling offset minor hysteresis loops with the modified Jiles–Atherton description," *J. Phys. D: Appl. Phys.*, vol. 42, p. 165002, July 2009.
[95] N. Sadowski, N. J. Batistela, J. P. A. Bastos and M. Lajoie-Mazenc, "An inverse Jiles-Atherton model to take into account hysteresis in time-stepping finite-element calculations," *IEEE Trans. Magn.*, vol. 38, no. 2, pp. 797-800, March 2002.
[96] A. Sutor, S. J. Rupitsch and R. Lerch, "A Preisach-based hysteresis model for magnetic and ferroelectric hysteresis," *Appl. Phys. A*, vol. 100, pp. 425–430, July 2010.

[97] Z. Szabó and J. Füzi, "Implementation and identification of Preisach type hysteresis models with Everett Function in closed form," *J. Magn. Magn. Mater.*, vol. 406, pp. 251-258, May 2016.
[98] W. Xu, N. Duan, S. Wang, Y. Guo and J. Zhu, "A Stress-Dependent Magnetic Hysteresis Model for Soft Magnetic Composite Materials," *IEEE Trans. Appl. Supercond.*, vol. 26, no. 7, pp. 1-5, Oct. 2016.
[99] D. C. Jiles and W. Kiarie, "An Integrated Model of Magnetic Hysteresis, the Magnetomechanical Effect, and the Barkhausen Effect," *IEEE Trans. Magn.*, vol. 57, no. 2, pp. 1-11, Feb. 2021.
[100] G. Amanoloaei, A. Stancu and L. Stoleriu, "Dynamic Stoner–Wohlfarth Model for Time-Dependent Magnetization Analysis," *IEEE Trans. Magn.*, vol. 12, no. 6103105, pp. 1-5, Sep. 2021.
[101] Y. Ma, E. Wang, H. Yang and S. Yao, "Reconsideration of Nonphysical Solution in Jiles–Atherton Model for Real-Time Hysteresis Estimation," *IEEE Trans. Magn.*, vol. 58, no. 6, pp. 1-9, June 2022.
[102] S. Tumanski, Handbook of Magnetic Measurements. 1st Edition. CRC Press, 2011.
[103] I. Mayergoyz, "Mathematical models of hysteresis," *IEEE Trans. Magn.*, vol. 22, no. 5, pp. 603-608, Sep. 1986.
[104] R. G. Harrison, "Positive-Feedback Theory of Hysteretic Recoil Loops in Hard Ferromagnetic Materials," *IEEE Trans. Magn.*, vol. 47, no. 1, pp. 175-191, Jan. 2011.
[105] F. De Leon and A. Semlyen, "A simple representation of dynamic hysteresis losses in power transformers," *IEEE Trans. Power Del.*, vol. 10, no. 1, pp. 315–321, Jan. 1995.
[106] J. A. Barker, D. E. Schreiber, B. G. Huth and D. H. Everett, "Magnetic hysteresis and minor loops: models and experiments," Proc. R. Soc. Lond. A, vol. 386, pp. 251-261, April 1983.
[107] S. N. Talukdar and J. R. Bailey, "Hysteresis models for system studies," *IEEE Trans. Power Appar. Syst.*, vol. 95, no. 4, pp. 1429-1434, July 1976.
[108] E. P. Dick and W. Watson, "Transformer Models for Transient Studies Based on Field Measurements," *IEEE Trans. Power Appar. Syst.*, vol. PAS-100, no. 1, pp. 409-419, Jan. 1981.
[109] G. Bertotti, "General properties of power losses in soft ferromagnetic materials," *IEEE Trans. Magn.*, vol. 24, no. 1, pp. 621-630, Jan. 1988.
[110] G. W. Swift, "Power Transformer Core Behavior Under Transient Conditions," *IEEE Trans. Power Appar. Syst.*, vol. PAS-90, no. 5, pp. 2206-2210, Sept. 1971.
[111] S. E. Zirka, Y. I. Moroz, R.G. Harrison and K. Chwastek, "On physical aspects of the Jiles-Atherton hysteresis models," *J. Appl. Phys.*, vol. 112, no. 14, pp. 043916, Aug. 2012.
[112] F. Brailsford, "Domain-wall energy and hysteresis loss in ferromagnetic material," *Proc. Inst. Electr. Eng.*, vol. 117, no. 5, pp. 1052-1055, May 1970.
[113] J. B. Goodenough, "Summary of losses in magnetic materials," *IEEE Trans. Magn.*, vol. 38, no. 5, pp. 3398-3408, Sept. 2002.
[114] F. Dong Tan, J. L. Vollin and S. M. Cuk, "A practical approach for magnetic core-loss characterization," *IEEE Trans. Power Electron.*, vol. 10, no. 2, pp. 124-130, March 1995.
[115] D. C. Jiles, "Modelling the effects of eddy current losses on frequency dependent hysteresis in electrically conducting media," *IEEE Trans. Magn.*, vol. 30, no. 6, pp. 4326-4328, Nov. 1994.
[116] D. C. Jiles "Frequency dependence of hysteresis curves in conducting magnetic materials," *J. Appl. Phys.*, vol. 76, no. 10 pp. 5849–5855, Nov. 1994.
[117] F. Brailsford, and R. Fogg, "Anomalous iron losses in cold-reduced grain-oriented transformer steel," *Proc. Inst. Electr. Eng.*, vol. 111, no. 8, pp. 1463-1467, Aug. 1964.
[118] A. V. Radun, "Development of Dynamic Magnetic Circuit Models Including Iron Saturation and Losses," *IEEE Trans. Magn.*, vol. 50, no. 5, pp. 1-10, May 2014.
[119] W. Sima, M. Zou, M. Yang, D. Peng and Y. Liu, "Saturable reactor hysteresis model based on Jiles–Atherton formulation for ferroresonance studies," *Int. J. Electr. Power Energy Syst.*, vol. 101, pp. 482-490, Oct. 2018.

[120] A. Gaudreau, P. Picher, L. Bolduc and A. Coutu, “No-load losses in transformer under overexcitation/inrush-current conditions: tests and a new model,” *IEEE Trans. Power Del.*, vol. 17, no. 4, pp. 1009-1017, Oct. 2002.
[121] J. R. González-Teodoro, E. Romero-Cadaval and R. Asensi, “Per-Unit Hysteresis and Eddy Loss Method Based on 3D Finite Elements for Non-Symmetric Toroidal Magnetic,” *IEEE Access*, vol. 8, pp. 34919-34928, 2020.
[122] A. Lotfi, H. K. Høidalen, E. Agheb and A. Nysveen, “Characterization of Magnetic Losses in the Transformer Tank Steel,” *IEEE Trans. Magn.*, vol. 52, no. 5, pp. 1-4, May 2016.
[123] M. Elleuch and M. Poloujadoff, “Analytical model of iron losses in power transformers,” *IEEE Trans. Magn.*, vol. 39, no. 2, pp. 973-980, March 2003.
[124] M. Popescu, D. M. Ionel, A. Boglietti, A. Cavagnino, C. Cossar and M. I. McGilp, "”A General Model for Estimating the Laminated Steel Losses Under PWM Voltage Supply,” *IEEE Trans. Ind. Appl.*, vol. 46, no. 4, pp. 1389-1396, July-Aug. 2010.
[125] S. E. Zirka, Y. I. Moroz, P. Marketos, A. J. Moses, D. C. Jiles and T. Matsuo, “Generalization of the Classical Method for Calculating Dynamic Hysteresis Loops in Grain-Oriented Electrical Steels,” *IEEE Trans. Magn.*, vol. 44, no. 9, pp. 2113-2126, Sept. 2008.
[126] S. E. Zirka, Y. I. Moroz, N. Chiesa, R. G. Harrison and H. K. Høidalen, “Implementation of Inverse Hysteresis Model Into EMTP—Part II: Dynamic Model,” *IEEE Trans. Power Del.*, vol. 30, no. 5, pp. 2233-2241, Oct. 2015.
[127] Z. He, J. -S. Kim and C. -S. Koh, “An Improved Model for Anomalous Loss Utilizing Loss Separation and Comparison With ANN Model in Electrical Steel Sheet,” *IEEE Trans. Magn.*, vol. 58, no. 9, pp. 1-5, Sept. 2022.
[128] Y. Li, J. Zhu, Y. Li, and L. Zhu, “A hybrid Jiles–Atherton and Preisach model of dynamic magnetic hysteresis based on backpropagation neural networks,” *J. Magnetism Magn. Mater.*, vol. 544, p. 168655, Feb. 2022
[129] A. Salvini, F. R. Fulginei and G. Pucacco, “Generalization of the static Preisach model for dynamic hysteresis by a genetic approach,” *IEEE Trans. Magn.*, vol. 39, no. 3, pp. 1353-1356, May 2003.
[130] Y. Wang and Z. Liu, “Estimation Model of Core Loss Under DC Bias,” *IEEE Trans. Appl. Supercond.*, vol. 26, no. 7, pp. 1-5, Oct. 2016.
[131] I. Podbereznaya and A. Pavlenko, “Accounting for dynamic losses in the Jiles-Atherton model of magnetic hysteresis,” *J. Magn. Magn. Mater.*, vol. 513, pp. 167070, Nov. 2020.
[132] T. Sato and Y. Sakaki, “Physical meaning of equivalent loss resistance of magnetic cores,” *IEEE Trans. Magn.*, vol. 26, no. 5, pp. 2894-2897, Sept. 1990.
[133] E. J. Tarasiewicz, A. S. Morched, A. Narang, and E. P. Dick, “Frequency dependent eddy current models for nonlinear iron cores,” *IEEE Trans. Power Syst.*, vol. 8, no. 2, pp. 588–597, May 1993.
[134] H. Li, L. Wang, J. Li and J. Zhang, “An Improved Loss-Separation Method for Transformer Core Loss Calculation and Its Experimental Verification,” *IEEE Access*, vol. 8, pp. 204847-204854, 2020.
[135] X. Liu, L. Zhao, C. Ma, Q. Ge, and Y. Li, ‘‘Optimization simulation analysis of leakage magnetic field and loss characteristics of high frequency nanocrystalline transformer,’’ in Proc. 25th Int. Conf. Electr. Mach. Syst. (ICEMS), Chiang Mai, Thailand, Nov. 2022, pp. 1–6.
[136] H. Cui and K. D. T. Ngo, ‘‘Transient core-loss simulation for ferrites with nonuniform field in SPICE,’’ *IEEE Trans. Power Electron.*, vol. 34, no. 1, pp. 659–667, Jan. 2019.
[137] L. Wang, H. Zhang, Z. Cai, T. Chen, H. Yang and J. Zhang, “A Higher-Order Loss-Separation Model for Fast Estimation of Core Loss in High-Frequency Transformers,” *IEEE Access*, vol. 11, pp. 91009-91015, 2023.
[138] L. Bu, S. Han, J. Feng and Y. Pan, “Unified magnetic equivalent circuit-based model of two-core Sen transformer for low-frequency electromagnetic transients and its numerical calculation,” *Int. J. Electr. Power Energy Syst.*, vol. 141, pp. 108184, Oct. 2022.

[139] S. Yue, Y. Li, Q. Yang, X. Yu and C. Zhang, "Comparative Analysis of Core Loss Calculation Methods for Magnetic Materials Under Nonsinusoidal Excitations," *IEEE Trans. Magn.*, vol. 54, no. 11, pp. 1-5, Nov. 2018.
[140] Z. Yan, C. Qimi and Z. Junbo, "Predicting Core Losses Under the DC Bias Based on the Separation Model," *IEEE J. Emerg. Sel. Top. Power Electron.*, vol. 5, no. 2, pp. 833-840, June 2017.
[141] S. Barg, K. Ammous, H. Mejbri and A. Ammous, "An Improved Empirical Formulation for Magnetic Core Losses Estimation Under Nonsinusoidal Induction," *IEEE Trans. Power Electron.*, vol. 32, no. 3, pp. 2146-2154, March 2017.
[142] E. R. Laithwaite "Magnetic equivalent circuits for electrical machines," *Proc. Inst. Elect. Eng.*, vol.114, no. 11, pp. 1805-1809, Nov. 1967.
[143] O. Justus, "Dynamisches Verhalten elektrischer Maschinen," Vieweg, 1991, 10-30.
[144] S. G. Abdulsalam, Wilsun Xu, W. L. A. Neves and Xian Liu, "Estimation of transformer saturation characteristics from inrush current waveforms," *IEEE Trans. Power Del.*, vol. 21, no. 1, pp. 170-177, Jan. 2006.
[145] S. Prusty and M. Rao, "A direct piecewise linearized approach to convert rms saturation characteristic to instantaneous saturation curve," *IEEE Trans. Magn.*, vol. 16, no. 1, pp. 156-160, Jan. 1980.
[146] W. L. A. Neves and H. W. Dommel, "On modelling iron core nonlinearities," *IEEE Trans. Power Syst.*, vol. 8, no. 2, pp. 417-425, May 1993.
[147] M. I. Mossad, M. Azab and A. Abu-Siada, "Transformer parameters estimation from nameplate data using evolutionary programming techniques," *IEEE Trans. Power Del.*, vol. 29, no. 5, pp. 2118-2123, Oct. 2014.
[148] M. I. Abdelwanis, A. Abaza, R. A. El-Sehiemy, M. N. Ibrahim and H. Rezk, "Parameter estimation of electric power transformers using Coyote optimization algorithm with experimental verification," *IEEE Access*, vol. 8, pp. 50036-50044, Mar. 2020.
[149] M. P. Ćalasan, A. Jovanović, V. Rubežić, D. Mujičić and A. Deriszadeh, "Notes on parameter estimation for single-phase transformer," *IEEE Trans. Ind. Appl.*, vol. 56, no. 4, pp. 3710-3718, Jul.-Aug. 2020.
[150] H. Dirik, C. Gezegin and M. Özdemir, "A novel parameter identification method for single-phase transformers by using real-time data," *IEEE Trans. Power Del.*, vol. 29, no. 3, pp. 1074-1082, Jun. 2014.
[151] A. Ketabi and M. Naseh, "Single-phase transformer modeling for inrush currents simulation using differential evolution," *Euro. Trans. Electr. Power*, vol. 22, no. 3, pp. 402-411, Apr. 2012.
[152] A. Tokić, M. Kasumović, M. Pejić, V. Milardić and T. C. Akinci, "Determination of single-phase transformer saturation characteristic by using Nelder–Mead optimization method," *Electr. Eng.*, vol. 101, no. 1, Jan. 2021.
[153] R. Oyanagi, T. Noda and M. Ichikawa, "A Method for Estimating the Current–Flux Curve of a Single-Phase Transformer for Electromagnetic Transient Simulations of Inrush Currents," *Electr. Eng. Japan*, vol. 204, no. 2, pp. 181-192, Feb. 2018.
[154] W. Sima, B. Zou, M. Yang and F. De León, "New method to measure deep-saturated magnetizing inductances for dual reversible models of single-phase two-winding transformers," *IEEE Trans. Power Del.*, vol. 36, no. 1, Feb. 2021.
[155] S. V. Kulkarni and S. A. Khaparde, "Magnetic characteristics," in *Transformer engineering*, CRC Press, 2004.
[156] M. Yang, R. Kazemi, S. Jazebi, D. Deswal and F. De Leon, "Retrofitting the BCTRAN transformer model with non-linear magnetizing branches for the accurate study of low-frequency deep saturating transients", *IEEE Trans. Power Del.*, vol. 33, no. 5, pp. 2344-2353, Oct. 2018.
[157] E. F. Fuchs and Y. You, "Measurement of λ–i characteristics of asymmetric three-phase transformers and their applications," *IEEE Trans. Power Del.*, vol. 17, no. 4, pp. 983-990, Oct. 2002.

[158] B. A. Mork, F. Gonzalez, D. Ishchenko, D. L. Stuehm and J. Mitra, "Hybrid Transformer Model for Transient Simulation—Part II: Laboratory Measurements and Benchmarking," *IEEE Trans. Power Del.*, vol. 22, no. 1, pp. 256-262, Jan. 2007.
[159] M. A. S. Masoum, P. S. Moses and A. S. Masoum, "Derating of Asymmetric Three-Phase Transformers Serving Unbalanced Nonlinear Loads," *IEEE Trans. Power Del.*, vol. 23, no. 4, pp. 2033-2041, Oct. 2008.
[160] X. Li, X. Wen, P. N. Markham and Y. Liu, "Analysis of Nonlinear Characteristics for a Three-Phase, Five-Limb Transformer Under DC Bias," *IEEE Trans. Power Del.*, vol. 25, no. 4, pp. 2504-2510, Oct. 2010.
[161] Q. Wu, S. Jazebi, and F. de León, "Parameter estimation of three-phase transformer models for low-frequency transient studies from terminal measurements," *IEEE Trans. Magn.*, vol. 53, no. 7, Jul. 2017.
[162] M. Dolinar, D. Dolinar, G. Stumberger, B. Polajzer, and J. Ritonja, "A three-phase core-type transformer iron core model with included magnetic cross saturation," *IEEE Trans. Magn.*, vol. 42, no. 10, pp. 2849–2851, Oct. 2006.
[163] A. Shintemirov, W. H. Tang and Q. H. Wu, "Transformer Core Parameter Identification Using Frequency Response Analysis," *IEEE Trans. Magn.*, vol. 46, no. 1, pp. 141-149, Jan. 2010.
[164] E. P. Dick and W. Watson, "Transformer Models for Transient Studies Based on Field Measurements," *IEEE Trans. Power App. Syst.*, vol. PAS-100, no. 1, pp. 409-419, Jan. 1981.
[165] S. Calabro, F. Coppadoro and S. Crepaz, "The Measurement of the Magnetization Characteristics of Large Power Transformers and Reactors through D.C. Excitation," *IEEE Trans. Power Del.*, vol. 1, no. 4, pp. 224-234, Oct. 1986.
[166] Q. Wu, T. Hong, S. Jazebi and F. de León, "Experimentally Validated Method to Measure the λ–i Characteristics of Asymmetric Three-Phase Transformers," *IEEE Trans. Magn.*, vol. 55, no. 4, pp. 1-9, April 2019.
[167] Y. Wang, Y. Shangguan and J. Yuan, "Determination Approach for the Parameters of Equivalent Circuit Model of Deep Saturated Three-Phase Integrative Transformers," *IEEE Trans. Magn.*, vol. 54, no. 11, pp. 1-5, Nov. 2018.
[168] T. Canal, F. X. Zgainski and V. L. Renouard, "Determination of the saturation curve of power transformers by processing transient measurements," *Elect. Power Syst. Res.*, vol. 195, pp. 107153, June 2021.
[169] C. G. A. Koreman, "Determination of the magnetizing characteristic of three-phase transformers in field tests," *IEEE Trans. Power Del.*, vol. 4, no. 3, pp. 1779-1785, Jul. 1989.
[170] W. L. A. Neves and H. W. Dommel, "Saturation curves of delta-connected transformers from measurements," *IEEE Trans. Power Del.*, vol. 10, no. 3, pp. 1432-1437, Jul. 1995.
[171] N. Chiesa and H. K. Hoidalen, "Analytical Algorithm for the Calculation of Magnetization and Loss Curves of Delta-Connected Transformers," *IEEE Trans. Power Del.*, vol. 25, no. 3, pp. 1620-1628, Jul. 2010.
[172] M. Valii, M. Bigdeli, F. Hojjatiparast, "Transient model parameters identification of transformer based on PSO algorithm," in Proceedings of the 3rd International Conference on Electric Power and Energy Conversion Systems (EPECS), pp. 1–5, 2013.
[173] R. Aghmasheh, V. Rashtchi and E. Rahimpour, "Gray Box Modeling of Power Transformer Windings Based on Design Geometry and Particle Swarm Optimization Algorithm," *IEEE Trans. Power Del.*, vol. 33, no. 5, pp. 2384-2393, Oct. 2018.
[174] M. I. Abdelwanis, A. Abaza, R. A. El-Sehiemy, M. N. Ibrahim and H. Rezk, "Parameter Estimation of Electric Power Transformers Using Coyote Optimization Algorithm With Experimental Verification," *IEEE Access*, vol. 8, pp. 50036-50044, Mar. 2020.
[175] V. Milardić, A. Tokić, I. Uglešić and A. Xemard, "Extraction of transformer saturation curve from ferroresonance measurements based on Nelder− Mead optimization method," *Elect. Power Syst. Res.*, vol. 223, pp. 109604, Oct.2023.
[176] J. Zhao et al., "Topological Transient Models of Three-Phase, Three-Legged Transformer," *IEEE Access*, vol. 7, pp. 102519-102529, Jul. 2019.

[177] A. Rezaei-Zare, M. Mostafaei, H. Gras, M. Martinez-Duro and J. Mahseredjian, "A Reversible Three-Phase Transformer Model for Energization Transients Based on Topological Remnant Flux Calculation," 2023 IEEE Kansas Power and Energy Conference (KPEC), Manhattan, KS, USA, 2023, pp. 1-5.
[178] H. Akagi, S. Ogasawara and H. Kim, "The Theory of Instantaneous Power in Three-Phase Four-Wire Systems: A Comprehensive Approach," in Conference Records of the IEEE–IAS Annual Meeting, 1999, pp. 431–439.
[179] L. J. Powell, "Current Transformer Burden and Saturation," *IEEE Trans. Ind. Appl.*, vol. IA-15, no. 3, pp. 294–303, May 1979.
[180] A. Hargrave, M. J. Thompson and B. Heilman, "Beyond the knee point: A practical guide to CT saturation," in Proceedings of the 71st Annual Conference for Protective Relay Engineers (CPRE), College Station, TX, USA, 26–29 March 2018.
[181] Y. C. Kang, J. K. Park, S. H. Kang, A. T. Johns and R. K. Aggarwal, "An algorithm for compensating secondary currents of current transformers," *IEEE Trans. Power Del.*, vol. 12, no. 1, pp. 116-124, Jan. 1997.
[182] H. Khorashadi-Zadeh and M. Sanaye-Pasand, "Correction of saturated current transformers secondary current using ANNs," IEEE Trans. Power Del., vol. 21, no. 1, pp. 73-79, Jan. 2006.
[183] A. Wiszniewski, W. Rebizant and L. Schiel, "Correction of Current Transformer Transient Performance," *IEEE Trans. Power Del.*, vol. 23, no. 2, pp. 624-632, April 2008.
[184] Z. Lu, J. S. Smith and Q. H. Wu, "Morphological Lifting Scheme for Current Transformer Saturation Detection and Compensation," *IEEE Trans. Circuits Syst. I: Regul. Pap.*, vol. 55, no. 10, pp. 3349-3357, Nov. 2008.
[185] F. B. Ajaei, M. Sanaye-Pasand, M. Davarpanah, A. Rezaei-Zare and R. Iravani, "Compensation of the Current-Transformer Saturation Effects for Digital Relays," *IEEE Trans. Power Del.*, vol. 26, no. 4, pp. 2531-2540, Oct. 2011.
[186] A. Hooshyar and M. Sanaye-Pasand, "Accurate Measurement of Fault Currents Contaminated With Decaying DC Offset and CT Saturation," *IEEE Trans. Power Del.*, vol. 27, no. 2, pp. 773-783, April 2012.
[187] E. Hajipour, M. Vakilian and M. Sanaye-Pasand, "Current-Transformer Saturation Compensation for Transformer Differential Relays," *IEEE Trans. Power Del.*, vol. 30, no. 5, pp. 2293-2302, Oct. 2015.
[188] F. Naseri, Z. Kazemi, E. Farjah and T. Ghanbari, "Fast Detection and Compensation of Current Transformer Saturation Using Extended Kalman Filter," *IEEE Trans. Power Del.*, vol. 34, no. 3, pp. 1087-1097, June 2019.
[189] A. Ameli, M. Ghafouri, H. H. Zeineldin, M. M. A. Salama and E. F. El-Saadany, "Accurate Fault Diagnosis in Transformers Using an Auxiliary Current-Compensation-Based Framework for Differential Relays," *IEEE Trans. Instrum. Meas.*, vol. 70, pp. 1-14, 2021
[190] S. Yang, Y. Zhang, Z. Hao, Z. Lin and B. Zhang, "CT Saturation Detection and Compensation: A Hybrid Physical Model- and Data-Driven Method," *IEEE Trans. Power Del.*, vol. 37, no. 5, pp. 3928-3938, Oct. 2022.
[191] Y. Wu, C. Tian, Z. Zhang, B. Chen, S. Liu and Y. Chen, "A Novel Current Transformer Based on Virtual Air Gap and its Basic Measuring Characteristics," *IEEE Trans. Power Del.*, vol. 38, no. 1, pp. 13-25, Feb. 2023.
[192] T. Specht, "Biased-core-current-transformer design method," *Electr. Eng.*, vol. 64, no. 9, pp. 635-639, Sept. 1945.
[193] "IEEE Guide for the Application of Current Transformers Used for Protective Relaying Purposes," in IEEE Std C37.110-2023, pp.1-89, May 2023.
[194] "IEEE Standard Requirements for Instrument Transformers," in IEEE Std C57.13-2016 (Revision of IEEE Std C57.13-2008), pp.1-96, June 2016.
[195] "Instrument Transformers—Part 1: General requirements," in IEC 61869-1, 2023.
[196] "Instrument Transformers—Part 2: Additional requirements for current transformers," in IEC 61869-2, 2012.

[197] S. E. Zocholl and D. W. Smaha, "Current Transformer Concepts," proceedings of the 46th Annual Georgia Tech Protective Relaying Conference, Atlanta, GA, April 1992.
[198] *Power Transformers - Part 5: Ability to Withstand Short Circuit,* IEC 60076-5, 2006.
[199] J. J. Grainger and W. D. Stevenson, Power system analysis (McGraw-Hill series in electrical and computer engineering Power and energy). New York: McGraw-Hill, 1994.
[200] A. Greenwood, Electrical transients in power systems, 2nd ed. New York, NY, USA: Wiley, 1991, ch. 13, pp. 422-462.
[201] J. Machowski, J. W. Bialek and J. R. Bumby, "The Power System in the Steady State," in Power System Dynamics: Stability and Control, New York, NY, USA: Wiley, 20008, pp. 65-122.
[202] Grupo EPM, ET-TD-ME06-01 Especificación Técnica Transformador de Distribución Sumergido en Aceite, 2017.
[203] C. P. J. Jansen, J. G. Slootweg and R. A. C. T. de Groot, "Calculation of Transformer Inrush Currents occurring during the Energizing of the Public Grid after a major Black Out," 2005 IEEE Russia Power Tech, St. Petersburg, Russia, 2005, pp. 1-7.
[204] Siemens AG. (2017). Power Engineering Guide, Edition 8.0. [Online]. Available: https://new.siemens.com/global/en/products/energy/topics/powerengineering-guide.html
[205] M. Lambert, M. Martínez-Duró, J. Mahseredjian, F. de León and F. Sirois, "Transformer Leakage Flux Models for Electromagnetic Transients: Critical Review and Validation of a New Model," *IEEE Trans. Power Del.*, vol. 29, no. 5, pp. 2180-2188, Oct. 2014.
[206] ABB Electric Systems Technology, Institute, "Power Transformers and Reactors" in Electrical Transmission and Distribution Reference Book, 5th ed. Raleigh, NC: ABB Electric Systems Technology Institute, 1997, pp. 96-144.
[207] F. de León, S. Jazebi and A. Farazmand, "Accurate Measurement of the Air-Core Inductance of Iron-Core Transformers With a Non-Ideal Low-Power Rectifier," *IEEE Trans. Power Del.*, vol. 29, no. 1, pp. 294-296, Feb. 2014.
[208] L. K. Ell and M. E. Council, "Distribution transformer excitation harmonics," *Electr. Power Syst. Res.*, vol. 17, no. 1, pp. 13-19 July, 1989.
[209] "IEEE Guide for Liquid-Immersed Transformers Through-Fault-Current Duration," in IEEE Std C57.109-2018 (Revision of IEEE Std C57.109-1993), vol., no., pp.1-24, 5 Oct. 2018, doi: 10.1109/IEEESTD.2018.8486931.
[210] I. Zamora, G. Buigues, A. J. Mazón and P. Eguía, "Coordination and Selection of Expulsion and Current-Limiting Fuses in Pad-Mounted Transformer Primary Protection," 9th Spanish-Portuguese Congress on Electrical Engineering, Marbella, Spain, 2005.
[211] R. Apolonio, J. C. Oliveira, A. B. de Vasconcellos and R. Szczypior, "Experimental and computational analysis of effects caused by voltage variations on ground return single-phase distribution systems: zero sequence harmonics and impacts," 2004 IEEE/PES Transmision and Distribution Conference and Exposition: Latin America (IEEE Cat. No. 04EX956), Sao Paulo, Brazil, 2004, pp. 511-516.
[212] G. Rockefeller, J. Boyle, L. Lawhead, J. Horak, "Transformer Protection Application Guide," Basler Electric Company, 2007.
[213] R. Nylen, "Power Transformer Protection. Application Guide," ABB Relays, 1988.
[214] R. Capella, "Publicación Técnica Schneider: PT-071. Protecciones eléctricas en MT," Centro de Formación Schneider, 2003.
[215] R. Capella, "Publicación Técnica Schneider: PT-004. Centros de Transformación MT/BT," Centro de Formación Schneider, 2003.
[216] L. F. Blume, G. Camilli, S. B. Farnham and H. A. Peterson, "Transformer magnetizing inrush currents and influence on system operation," *Electr.Eng.*, vol. 63, no. 6, pp. 366-374, June 1944.
[217] H. S. Bronzeado, P. B. Brogan and R. Yacamini, "Harmonic analysis of transient currents during sympathetic interaction," *IEEE Trans. Power Syst.*, vol. 11, no. 4, pp. 2051-2056, Nov. 1996.

[218] E. Colombo and G. Santagostino, “Results of the inquiries on actual network conditions when switching magnetizing and small inductive and on transformer and shunt reactor saturation characteristics,” *Electra*, vol. 94, pp. 35–53, May 1984.
[219] Y. Bernard, E. Mendes and Z. Ren, “Determination of the distribution function of Preisach’s model using centred cycles,” *Compel Int. J. Comput. Math. Electr.*, vol. 19. no. 4, pp. 997-1006, Dec. 2000.
[220] J. M. Mendel, “Tutorial on higher-order statistics (spectra) in signal processing and system theory: theoretical results and some applications,” *Pro. IEEE*, vol. 79, no. 3, pp. 278-305, March 1991.

Appendix A. Elimination of the Number of Winding Turns in Transformer Model Equations

The experimental determination of the reluctance in the magnetic circuit of the transformer models has a significant drawback. Typically, it is not possible to measure or estimate the true values of its parameters, since the exact numbers of winding turns in the transformer windings is often unknown. This, in turn, also complicates the measurement or estimation of the flux based on voltage measurements. Therefore, it is recommended to exclude the numbers of winding turns in the transformer equations.

This drawback can be addressed in two different ways: by reducing all the equations to per unit (pu) or by reducing only the magnetic circuit variables with a reduction to the primary side.

A.1. Per unit reduction

The base values for the per unit reduction of a single-phase transformer are as follows:

$$\begin{gathered}
S_{\mathrm{B}} = S_{\mathrm{N}},\ \omega_{\mathrm{B}} \\
\begin{aligned}
U_{\mathrm{B1}} &= U_{\mathrm{N1}} & U_{\mathrm{B2}} &= U_{\mathrm{N2}} \\
I_{\mathrm{B1}} &= \frac{S_{\mathrm{B}}}{U_{\mathrm{B1}}} & I_{\mathrm{B2}} &= \frac{S_{\mathrm{B}}}{U_{\mathrm{B2}}} \\
Z_{\mathrm{B1}} &= \frac{\left(U_{\mathrm{B1}}\right)^2}{S_{\mathrm{B}}} & Z_{\mathrm{B2}} &= \frac{\left(U_{\mathrm{B2}}\right)^2}{S_{\mathrm{B}}} \\
L_{\mathrm{B1}} &= \frac{Z_{\mathrm{b1}}}{\omega_{\mathrm{B}}} & L_{\mathrm{B2}} &= \frac{Z_{\mathrm{B2}}}{\omega_{\mathrm{B}}} \\
\lambda_{\mathrm{B1}} &= \frac{U_{\mathrm{B1}}}{\omega_{\mathrm{B}}} & \lambda_{\mathrm{B2}} &= \frac{U_{\mathrm{B2}}}{\omega_{\mathrm{B}}}
\end{aligned} \\
\phi_{\mathrm{B}} = \frac{\lambda_{\mathrm{B1}}}{N_1} = \frac{\lambda_{\mathrm{B2}}}{N_2} \\
\Re_{\mathrm{B}} = \frac{\omega_{\mathrm{B}} N_1^{\ 2}}{Z_{\mathrm{B1}}} = \frac{\omega_{\mathrm{B}} N_2^{\ 2}}{Z_{\mathrm{B2}}} \\
\mathfrak{F}_{\mathrm{b}} = N_1 I_{\mathrm{B1}} = N_2 I_{\mathrm{B2}}
\end{gathered} \tag{A.1}$$

where ω_{B} can be either $\omega_{\mathrm{B}} = 1$ rad/s or $\omega_{\mathrm{B}} = \omega_{\mathrm{N}} = 2\pi f_{\mathrm{N}}$ rad/s. The second option offers the advantage that the RMS value of the reduced flux is equal to 1 pu, while the reduced reluctances and the reduced inductances are equal.

The reduced equations of the single-phase transformer model in Chapter 1 are the following

$$u_1^{\mathrm{pu}} = r_1 i_1^{\mathrm{pu}} + \frac{l_{\mathrm{d1}}}{\omega_{\mathrm{B}}}\frac{\mathrm{d}i_1^{\mathrm{pu}}}{\mathrm{d}t} + \frac{1}{\omega_{\mathrm{B}}}\frac{\mathrm{d}\phi^{\mathrm{pu}}}{\mathrm{d}t}, \qquad u_2^{\mathrm{pu}} = r_2 i_2^{\mathrm{pu}} + \frac{l_{\mathrm{d2}}}{\omega_{\mathrm{B}}}\frac{\mathrm{d}i_2^{\mathrm{pu}}}{\mathrm{d}t} + \frac{1}{\omega_{\mathrm{B}}}\frac{\mathrm{d}\phi^{\mathrm{pu}}}{\mathrm{d}t}$$

$$i_{\mathrm{1m}}^{\mathrm{pu}} = i_1^{\mathrm{pu}} - \frac{1}{r_{\mathrm{FE}}\omega_{\mathrm{B}}}\frac{\mathrm{d}\phi^{\mathrm{pu}}}{\mathrm{d}t} \tag{A.2}$$

$$i_{\mathrm{m}}^{\mathrm{pu}} + i_2^{\mathrm{pu}} - f^{\mathrm{pu}} = 0, \qquad f^{\mathrm{pu}} = \mathfrak{R}^{\mathrm{pu}}\left(f^{\mathrm{pu}}\right)\cdot\phi^{\mathrm{pu}}$$

where the reduced signals and reduced reluctance are indicated with the superscript “pu”, while the reduced linear parameters are denoted by lowercase letters, calculated as

$$r_1 = \frac{R_1}{Z_{\mathrm{B1}}}, \qquad l_{\mathrm{d1}} = \frac{L_{\mathrm{d1}}}{L_{\mathrm{B1}}}, \qquad r_2 = \frac{R_2}{Z_{\mathrm{B2}}}, \qquad l_{\mathrm{d2}} = \frac{L_{\mathrm{d2}}}{L_{\mathrm{B2}}}, \qquad r_{\mathrm{FE}} = \frac{R_{\mathrm{FE}}}{Z_{\mathrm{B1}}} \tag{A.3}$$

It can be seen that the writing of the reduced equations is identical to the equation system presented in Chapter 2, but eliminating the numbers of winding turns and pre-multiplying the derivative operator by $1/\omega_b$.

The reduced expression of the saturation curve is given by

$$\mathfrak{R}^{\mathrm{pu}}\left(f^{\mathrm{pu}}\right)^{-1} = \mathfrak{R}_{\mathrm{B}}\mathfrak{R}\left(\frac{f}{\mathfrak{F}_{\mathrm{B}}}\right)^{-1} = \frac{K_1^{\mathrm{pu}}}{\left(1+\left(\frac{\left|f^{\mathrm{pu}}\right|}{f_{\mathrm{KNEE}}^{\mathrm{pu}}}\right)^{p}\right)^{1/p}} + K_2^{\mathrm{pu}} \tag{A.4}$$

where the reduced parameters are calculated as

$$K_1^{\mathrm{pu}} = K_1\mathfrak{R}_{\mathrm{B}} = \frac{K_1\omega_{\mathrm{B}}N_1^{\,2}}{Z_{\mathrm{B1}}} = \frac{K_1\omega_{\mathrm{B}}N_2^{\,2}}{Z_{\mathrm{B2}}}, \qquad K_2^{\mathrm{pu}} = K_2\mathfrak{R}_{\mathrm{B}}\frac{K_2\omega_{\mathrm{B}}N_1^{\,2}}{Z_{\mathrm{B1}}} = \frac{K_2\omega_{\mathrm{B}}N_2^{\,2}}{Z_{\mathrm{B2}}},$$

$$f_{\mathrm{KNEE}}^{\mathrm{pu}} = \frac{f_{\mathrm{KNEE}}}{\mathfrak{F}_{\mathrm{B}}} = \frac{f_{\mathrm{KNEE}}}{N_1 I_{\mathrm{B1}}} = \frac{f_{\mathrm{KNEE}}}{N_2 I_{\mathrm{B2}}} \tag{A.5}$$

The reduced equations for the three-phase transformer model from Chapter 4, can be calculated in the same way, with the base voltages being the nominal voltages of the windings (not the phase voltages) as following

$$S_{\mathrm{B}} = \frac{S_{\mathrm{N}}}{3}$$

$$U_{\mathrm{B1}} = \begin{cases} U_{\mathrm{N1}}/\sqrt{3} & \text{Wye-connected} \\ U_{\mathrm{N1}} & \text{Delta-connected} \end{cases} \qquad U_{\mathrm{B2}} = \begin{cases} U_{\mathrm{N2}}/\sqrt{3} & \text{Wye-connected} \\ U_{\mathrm{N2}} & \text{Delta-connected} \end{cases} \tag{A.6}$$

The reduced equation system results in

$$u_{1k}^{pu} = r_1 i_{1k}^{pu} + \frac{l_{d1}}{\omega_b}\frac{di_{1k}^{pu}}{dt} + \frac{1}{\omega_b}\frac{d\phi_k^{pu}}{dt}, \qquad u_{2k}^{pu} = r_2 i_{2k}^{pu} + \frac{l_{d2}}{\omega_b}\frac{di_{2k}^{pu}}{dt} + \frac{1}{\omega_b}\frac{d\phi_k^{pu}}{dt}$$
$$i_{mk}^{pu} = i_{1k}^{pu} - \frac{1}{r_{FE}\omega_b}\frac{d\phi_k^{pu}}{dt}, \qquad i_{mk}^{pu} + i_{2k}^{pu} - f_k^{pu} + f_d^{pu} = 0, \qquad f_k^{pu} = \Re_k^{pu}\left(f_k^{pu}\right)\cdot\phi_k^{pu} \tag{A.7}$$
$$\phi_a^{pu} + \phi_b^{pu} + \phi_c^{pu} + \phi_d^{pu} = 0, \qquad f_d^{pu} = \Re_d^{pu}\phi_d^{pu}$$

A.2. Reduction to the primary of magnetic variables

This second option for eliminating the number of winding turns in transformer model equations has the advantage that the external variables from both windings, i.e., the variables from the electric circuit (voltages and currents), are represented in true values, while only the variables from the magnetic circuit are modified.

The base values for the reduction to the primary of a single-phase transformer are as follows:

$$\begin{gathered}
S_B = 1,\ \omega_B \\
U_{B1} = 1 \qquad U_{B2} = \frac{1}{r_{tr}} \\
I_{B1} = 1 \qquad I_{B2} = r_{tr} \\
Z_{B1} = 1 \qquad Z_{B2} = \frac{1}{r_{tr}^2} \\
L_{B1} = \frac{1}{\omega_B} \qquad L_{B2} = \frac{1}{r_{tr}^2\omega_B} \\
\lambda_{B1} = \frac{1}{\omega_B} \qquad \lambda_{B2} = \frac{1}{r_{tr}\omega_B} \\
\phi_B = \frac{1}{\omega_B N_1} = \frac{1}{r_{tr}\omega_B N_2} \\
\Re_B = \omega_B N_1^2 = \omega_B N_2^2 r_{tr}^2 \\
\mathfrak{F}_B = N_1 = N_2 r_{tr}
\end{gathered} \tag{A.8}$$

The equations reduced to the primary of the single-phase transformer model in Chapter 2, introducing new magnetic variables, are the following

$$u_1 = R_1 i_1 + L_{d1}\frac{di_1}{dt} + \frac{d\lambda_1}{dt}, \qquad u_2 = R_2 i_2 + L_{d2}\frac{di_2}{dt} + \frac{1}{r_{tr}}\frac{d\lambda_1}{dt}$$
$$i_{1m} = i_1 - \frac{1}{R_{FE}^{'}}\frac{d\lambda_1}{dt} \tag{A.9}$$
$$i_{1m} + \frac{i_2}{r_{tr}} - f^{'} = 0, \qquad f^{'} = \Re^{'}\left(f^{'}\right)\cdot\lambda_1$$

where the total flux linked by the primary winding is $\lambda_1 = N_1\phi_1$, $r_{tr} = N_1/N_2$ is the ratio between the numbers of winding turns, and the new magnetic variables are

$$f^{'} == \frac{f}{N_1}, \qquad \Re^{'} = \frac{\Re}{N_1^{\,2}} \tag{A.10}$$

These new magnetic variables are indicated with a prime superscript, and have been calculated using $\omega_B = 1$. The ratio between the numbers of winding turns can be determined experimentally, or approached as the transformation ratio, $r_t = U_{N1}/U_{n2}$.

The saturation curve reduced to the primary is given by

$$\Re'\left(f^{'}\right)^{-1} = \frac{K_1^{'}}{\left(1+\left(\dfrac{\left|f^{'}\right|}{f_{\mathrm{KNEE}}^{'}}\right)^{p}\right)^{1/p}} + K_2^{'} \tag{A.11}$$

where

$$K_1^{'} = K_1 N_1^{\,2}, \qquad K_2^{'} = K_2 N_1^{\,2}, \qquad f_{\mathrm{KNEE}}^{'} = \frac{f_{\mathrm{KNEE}}}{N_1} \tag{A.12}$$

It is important to note that the original equation system in Chapter 2 is identical to the equation system reduced to the primary, when the following modifications to the original system are taken into account:

$$\begin{gathered} N_1 \to 1, \qquad N_2 \to \frac{1}{r_{tr}}, \qquad \phi \to \lambda_1, \qquad f \to f^{'} \\ \Re \to \Re^{'}, \qquad K_1, K_2, f_{\mathrm{KNEE}} \to K_1^{'}, K_2^{'}, f_{\mathrm{KNEE}}^{'} \end{gathered} \tag{A.13}$$

The reduced equations for the three-phase transformer model from Chapter 5, with the base voltages being the nominal voltages of the windings (not the phase voltages), are given by

$$\begin{gathered} u_{1\mathrm{k}} = R_1 i_{1\mathrm{k}} + L_{\mathrm{d}1}\frac{\mathrm{d}i_{1\mathrm{k}}}{\mathrm{d}t} + \frac{\mathrm{d}\lambda_{1\mathrm{k}}}{\mathrm{d}t}, \qquad u_{2\mathrm{k}} = R_2 i_{2\mathrm{k}} + L_{\mathrm{d}2}\frac{\mathrm{d}i_{2\mathrm{k}}}{\mathrm{d}t} + \frac{1}{r_{\mathrm{tr}}}\frac{\mathrm{d}\lambda_{1\mathrm{k}}}{\mathrm{d}t} \\ i_{\mathrm{mk}} = i_{1\mathrm{k}} - \frac{1}{R_{\mathrm{FE}}^{'}}\frac{\mathrm{d}\lambda_{1\mathrm{k}}}{\mathrm{d}t}, \qquad i_{\mathrm{mk}} + \frac{i_{2\mathrm{k}}}{r_{\mathrm{tr}}} - f_{\mathrm{k}}^{'} + f_{\mathrm{d}}^{'} = 0, \qquad f_{\mathrm{k}}^{'} = \Re_{\mathrm{k}}^{'}\left(f_{\mathrm{k}}^{'}\right)\cdot\lambda_{1\mathrm{k}} \\ \lambda_{1\mathrm{a}} + \lambda_{1\mathrm{b}} + \lambda_{1\mathrm{c}} + \lambda_{1\mathrm{d}} = 0, \qquad f_{\mathrm{d}}^{'} = \Re_{\mathrm{d}}^{'}\lambda_{1\mathrm{d}} \end{gathered} \tag{A.14}$$

where, again, the value of r_{tr} can be determined experimentally or obtained from the transformation ratio, $r_t = U_{N1}/U_{n2}$, and both winding connections.

An important consideration to take into account is that although the two reductions presented fulfill the objective of eliminating the numbers of winding turns from the equations, both numbers are still required for performing the reductions (to calculate the base values), which seems contradictory to the objective. In reality, for both reductions, any values of N_1 and N_2 can be assumed, as long as the r_{tr} ratio is satisfied, and the reduced values will always be the same. Without performing the reduction, the variables and parameters of the magnetic circuit would be indeterminate since different values of N_1 and N_2, even if they satisfy the r_{tr} ratio, would result in different magnetic circuits.

Appendix B. Transformer tests to determine linear parameters

To determine the linear parameters of a transformer, two classical tests can be performed: the no-load test and the short-circuit test. To perform the tests, it is necessary to know the nominal power, S_N, the nominal voltages, U_{N1} and U_{N2}, and from these values the nominal currents, I_{N1} and I_{N2}.

The two tests are valid for both single-phase and three-phase transformers, with the exception that when referring to real powers in a three-phase transformer, these are three-phase, and when referring to real voltages and currents, these are line values.

B.1. No-load test

In this test, one winding of the transformer (typically the low-voltage winding, although it can also be done through the high-voltage winding) is energized at its nominal voltage, while the other winding is left open (no-load). This test measures the supplied voltage (U_0), consumed current (I_0), and consumed power (W_0). The no-load current during the test is much smaller than the nominal current ($I_0 << I_{N2}$).

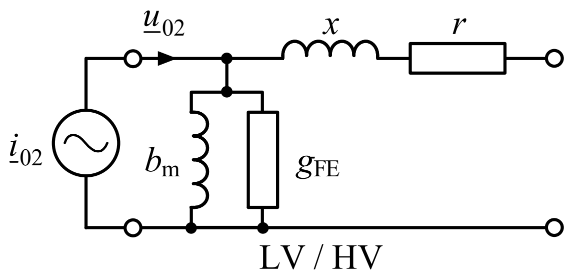

Fig. B.1. Reduced scheme of the no-load test, with the transformer energized by the low-voltage winding.

With the per unit reduced scheme depicted in Fig. B.1, it is satisfied that

$$u_0 = u_{01} = u_{02}, \qquad i_0 = i_{01} = i_{02} \tag{B.1}$$

The parameters b_m and g_{FE} can be calculated as follows

$$\begin{gathered} \underline{z}_0 \approx \frac{1}{g_{FE} + jb_m} \\ g_{FE} = \frac{w_0}{(u_0)^2} = \frac{w_0}{1} = w_0, \qquad y_0 = \frac{i_0}{(u_0)^2} = \frac{i_0}{1} = i_0 \\ b_m = \sqrt{(i_0)^2 - (w_0)^2} \end{gathered} \tag{B.2}$$

considering that u_0 = 1 pu.

B.2. Short-circuit test

In this test, one winding of the transformer (typically the high-voltage winding, although it can also be done through the low-voltage winding) is energized until the consumed current reaches the nominal current (the voltage is gradually increased from 0 V), while the other winding is short-circuited. This test measures the supplied voltage (U_{sc}), consumed current (I_{sc}), and consumed power (W_{sc}). The short-circuit voltage during the test is much smaller than the nominal voltage ($U_{sc} << U_{N1}$).

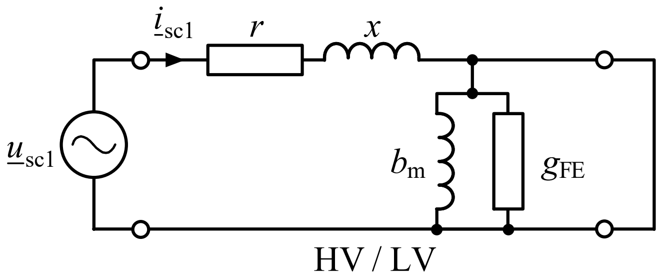

Fig. B.2. Reduced scheme of the short-circuit test, with the transformer energized by the high-voltage winding.

With the per unit reduced scheme depicted in Fig. B.2, it is satisfied that

$$u_{sc} = u_{sc1} = u_{sc2}, \qquad i_{sc} = i_{sc1} = i_{sc2} \tag{B.3}$$

The parameters r and x can be calculated as follows

$$\begin{gathered} \underline{z}_{sc} \approx r + jx \\ r = \frac{w_{sc}}{\left(i_{sc}\right)^2} = \frac{w_{sc}}{1} = w_{sc}, \qquad z_{sc} = \frac{u_{sc}}{i_{sc}} = \frac{u_{sc}}{1} = u_{sc} \\ x = \sqrt{\left(i_0\right)^2 - \left(w_0\right)^2} \end{gathered} \tag{B.4}$$

considering that $i_{sc} = 1$ pu.

Appendix C. Summary of typical and measured values in the literature for power transformer parameters and currents

In this appendix, several tables are provided with typical and/or measured values of various transformer parameters that can be found in the literature. Data from inrush currents and no-load currents are also presented.

C.1. Typical parameters

Table C.1. Minimum short-circuit impedance that power transformers must have according to standard IEC 60076-5 [198].

S_N (kVA)	Minimum z_{cc} (pu)
<= 630	0.04
631-1250	0.05
1251-2500	0.06
2501-6300	0.07
6301-25000	0.08
25001-40000	0.10
40001-63000	0.11
63001-100000	0.125
> 100000	> 0.125

Table C.2. Typical ranges of leakage reactance as a function of voltage for transformers 25 MVA and larger [199].

U_{N1} (kV)	x_{sc} (pu)	
	Forced-air-cooled	Forced-oil-cooled
34.5	0.05-0.08	0.09-0.14
69	0.06-0.10	0.10-0.16
115	0.06-0.11	0.10-0.20
138	0.06-0.13	0.10-0.22
161	0.06-0.14	0.11-0.25
230	0.07-0.16	0.12-0.27
345	0.08-0.17	0.13-0.28
500	0.10-0.20	0.16-0.34
700	0.11-0.21	0-19-0.35

Table C.3. Typical values of short-circuit resistances for oil-immersed three-phase transformers [200].

	r_{sc} (pu)					
S_N (MVA) / U_{N1} (kV)	15	69	138	230	500	765
2	0.0073	0.0081	0.01	-	-	-
4	0.0063	0.0066	0.008	-	-	-
10	0.0052	0.0054	0.006	0.0067	-	-
20	0.0044	0.0045	0.0049	0.0052	-	-
40	0.0035	0.0036	0.0039	0.0042	-	-
100	-	0.0026	0.0028	0.0030	-	-
255	-	-	-	-	-	0.0095
750	-	-	-	-	0.00176	-

Table C.4. Typical values of power transformer parameters in pu [201].

S_N (MVA)	U_{sc} (pu)	$w$sc (pu)	i_0 (pu)	w_0 (pu)
150	0.11	0.0031	0.003	0.001
240	0.15	0.0030	0.0025	0.0006
426	0.145	0.0029	0.002	0.0006
630	0.143	0.0028	0.004	0.0007

Table C.5. Maximum allowable values of no-load current, no-load losses, short-circuit losses at 85°C and short-circuit voltage at 85°C for single-phase transformers with primary voltages of 13.2 kV, 11.4 kV, 7.62 kV and 4.16 kV [202].

S_N (kVA)	i_0 (pu)	W_0 (W)	W_{sc} (W)	u_{sc} (pu)
3	0.025	21	70	0.03
5	0.025	30	90	0.03
10	0.025	50	140	0.03
15	0.024	70	195	0.03
25	0.02	100	290	0.03
37.5	0.02	135	405	0.03
50	0.019	160	510	0.03
75	0.017	210	710	0.03

Table C.6. Maximum allowable values of no-load current, no-load losses, short-circuit losses at 85°C and short-circuit voltage at 85°C for single-phase transformers with primary voltage of 34.5 kV [202].

S_N (kVA)	i_0 (pu)	W_0 (W)	W_{sc} (W)	u_{sc} (pu)
25	0.024	185	360	0.04
37.5	0.02	230	490	0.04
50	0.02	265	605	0.04
75	0.019	330	820	0.04

Table C.7. Maximum allowable values of no-load current, no-load losses, short-circuit losses at 85°C and short-circuit voltage at 85°C for three-phase transformers with primary voltages of 4.16 kV, 11.4 kV and 13.2 kV [202].

S_N (kVA)	i_0 (pu)	W_0 (W)	W_{sc} (W)	u_{sc} (pu)
30	0.036	135	515	0.03
45	0.035	180	710	0.03
75	0.035	265	1090	0.035
112.5	0.026	365	1540	0.035
150	0.024	450	1960	0.04
225	0.021	615	2890	0.04
300	0.020	765	3575	0.045
400	0.019	930	4730	0.045
500	0.017	1090	5780	0.05
630	0.016	1285	7140	0.05

Table C.8. Maximum allowable values of no-load current (I_0), no-load losses (W_0), short-circuit losses (W_{sc}) at 85°C and short-circuit voltage at 85°C (u_{sc}) for three-phase transformers with primary voltage of 34.5 kV [202].

S_N (kVA)	i_0 (pu)	W_0 (W)	W_{sc} (W)	u_{sc} (pu)
75	0.035	390	1370	0.06
112.5	0.026	500	1890	0.06
150	0.025	610	2400	0.06
225	0.025	790	3330	0.06
300	0.020	950	4210	0.06
400	0.020	1150	5320	0.06
500	0.017	1330	6370	0.06
630	0.017	1540	7690	0.06

Table C.9. Three-phase transformer parameters provided by manufacturers [203].

Parameters	Transformers		
S_N (MVA)	20	50	160
U_{N1} (kV)	66	70.5	220
U_{N2} (kV)	10.6	10.5	66
u_{sc} (pu)	0.147	0.11	0.178
W_{sc} (kW)	87.6	116	459
W_0 (kW)	10.3	31.3	71.4
i_0 (pu)	0.00077	0.0023	0.00104

Table C.10. Liquid-immersed three-phase distribution transformers with Dyn winding connection [204].

S_N (kVA)	U_{N1} (kV)	U_{N2} (V)	Max. W_0 (W)	Max. W_{sc} (kW)	u_{sc} (pu)
100	10	400	145	1.75	0.04
100	20	400	145	1.75	0.04
160	10	400	210	2.35	0.04
160	20	400	210	2.35	0.04
250	10	400	300	3.25	0.04
250	20	400	300	3.25	0.04
400	10	400	430	4.6	0.04
400	20	400	430	4.6	0.04
630	10	400	600	6.5	0.04
630	20	400	600	6.5	0.04
800	10	400	650	8.4	0.06
800	20	400	650	8.4	0.06
1000	10	400	770	10.5	0.06
1000	20	400	770	1.5	0.06
2000	10	400	1450	18	0.06
2000	20	400	1450	18	0.06
2500	10	400	1750	22	0.06
2500	20	400	1750	22	0.06

Table C.11. Measured short-circuit reactances for two different transformers [205].

Type	S_N (MVA)	U_{N1} (kV)	U_{N2} (kV)	Windings	x_{sc} (pu)
Single-phase	360	230	24	-	0.1454
Three-phase	96	400	6.8	1 and 2	0.23
four-winding			6.8	1 and 3	0.232
			6.8	1 and 4	0.24

Table C.12. Typical values of short-circuit reactances and impedances in single-phase transformers [206].

S_N (kVA)	U_{N1} (kV)							
	2.5		15		25		69	
	x_{sc} (pu)	z_{sc} (pu)	x_{sc} (pu)	z_{sc} (pu)	x_{sc} (pu)	z_{sc} (pu)	x_{sc} (pu)	z_{sc} (pu)
3	0.011	0.022	0.008	0.028	-	-	-	-
10	0.015	0.022	0.013	0.024	0.044	0.052	-	-
25	0.020	0.025	0.017	0.023	0.048	0.052	-	-
50	0.021	0.024	0.021	0.025	0.049	0.052	0.063	0.065
100	0.031	0.033	0.029	0.032	0.050	0.052	0.063	0.065
500	0.047	0.048	0.049	0.050	0.051	0.052	0.064	0.065

Table C.13. Comparison of measurements and finite-elemnt simulations of air-core inductance for different single-phase transformers [207].

S_N (kVA)	Core type	Winding	Measured L_{AIR} (μH)	FEM L_{AIR} (μH)
1	Shell	1	640	645
		2	894	850
		3	973	1069
		4	1267	1300
1	Toroidal	1	314	316
		2	374	383
4	Toroidal	1	81	75.2
		2	118	119.6
25	Toroidal	1	50	51.7

C.2. No-load and inrush currents

Table C.14. Typical magnetizing current values [200].

S_N (MVA) / U_{N2} (kV)	i_m (pu)			
	350	650	900	1300
20	0.0080	0.0090	0.0010	0.012
40	0.0065	0.0074	0.0082	0.0094
60	0.0058	0.0065	0.0073	0.0084
80	0.0054	0.0061	0.0068	0.0077
100	0.0051	0.0059	0.0065	0.0073
150	0.0047	0.0053	0.0061	0.0067
200	-	0.0051	0.0058	0.0064
300	-	0.0049	0.0055	0.0061
500	-	0.0047	0.0053	0.0059

Table C.15. Typical no-load current values of three-phase transformers [206].

S_N (kVA) / U_{N1} (kV)	i_0 (pu)					
	2.5	15	25	69	138	161
500/3	0.037	0.037	0.038	0.049	-	-
1000/3	0.033	0.033	0.036	0.043	-	-
2500/3	-	0.031	0.032	0.038	-	-
5000/3	-	-	0.028	0.031	0.025	0.041
10000/3	-	-	0.030	0.031	0.024	0.036
25000/3	-	-	0.022	0.024	0.031	0.039
50000/3	-	-	-	-	0.031	0.039

Table C.16. No-load currents of different 25 kVA single-phase transformers excited by the secondary winding [208].

S_N (kVA)	U_{N1} (kV)	U_{N2} (V)	U_2 = 1 pu		U_2 = 1.1 pu	
			i_0 (pu)	THD (%)	i_0 (pu)	THD (%)
25	7.62	240	0.0055	42.3	0.0092	61.1
25	8.00	240	0.0103	84.1	-	-
25	8.00	240	0.0072	53.5	0.0156	78.2
25	8.00	240	0.0074	55.1	0.0189	79.6
25	13.80	240	0.0052	74.5	0.0233	98.2
25	13.80	240	0.0060	58.2	0.0162	88.8
25	13.80	240	0.0091	82.8	0.0365	94.2
25	14.40	240	0.0066	62.6	0.0202	91.0
25	19.92	240	0.0100	94.9	0.0400	98.9
25	19.92	240	0.0079	85.0	0.0300	102.0
25	19.92	240	0.0103	104.0	0.0457	100.0

Table C.17. No-load currents of different 50 kVA single-phase transformers excited by the secondary winding [208].

S_N (kVA)	U_{N1} (kV)	U_{N2} (V)	U_2 = 1 pu		U_2 = 1.1 pu	
			i_0 (pu)	THD (%)	i_0 (pu)	THD (%)
50	8000	240	0.0030	44.8	0.0044	61.1
50	8000	240	0.0103	64.4	0.0284	77.9
50	8000	240	0.0028	41.7	0.0040	61.0
50	8000	240	0.0100	71.4	0.0292	83.0
50	8000	240	0.0053	47.6	0.0096	66.2
50	8000	240	0.0058	58.4	0.0134	81.8
50	8000	240	0.0154	58.1	0.0286	60.5

Table C.18. No-load current harmonics of three different single-phase transformers (8000/254 V, 60 Hz) excited by the secondary winding [211].

S_N (kVA)	5		15		25	
Harmonic	i_0 (pu)	(%)	i_0 (pu)	(%)	I_0 (pu)	(%)
$I_{(1)}$	0.0370	100	0.0131	100	0.0254	100
$I_{(3)}$	0.0185	50.00	0.0077	58.72	0.0116	46.00
$I_{(5)}$	0.0068	18.45	0.0040	30.28	0.0029	11.50
$I_{(7)}$	0.0020	5.34	0.0019	14.68	0.0004	1.50
$I_{(9)}$	0.0009	2.43	0.0008	6.42	0.00036	1.40
THD (%)	-	53.60	-	2.75	-	47.30

Table C.19. No-load current harmonics of three different single-phase transformers (8000/254 V, 60 Hz) excited at 115% of nominal secondary voltage [211].

S_N (kVA)	5		15		25	
Harmonic	i_0 (pu)	(%)	i_0 (pu)	(%)	i_0 (pu)	(%)
$I_{(1)}$	0.1322	100	0.0910	100	0.0790	100
$I_{(3)}$	0.0890	67.39	0.0695	76.32	0.0480	60.80
$I_{(5)}$	0.0496	37.50	0.0431	47.37	0.0216	27.40
$I_{(7)}$	0.0244	18.61	0.0215	23.68	0.0096	12.20
$I_{(9)}$	0.0115	8.83	0.0084	9.21	0.0043	5.40
THD (%)	-	79.78	-	93.35	-	68.66

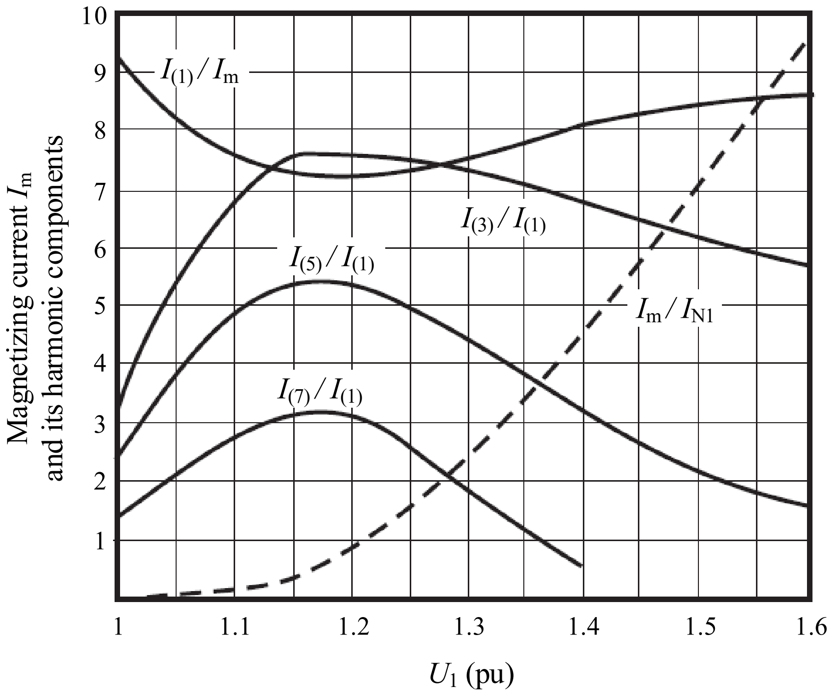

Fig. C.1. Magnetizing current and its harmonic components for different excitation voltages [212].

Table C.20. Typical values of decay time as a function of the nominal power [204].

S_N (MVA)	Time constant, τ(s)
0.5-1.0	0.16-0.2
1.0-10	0.2-1.2
>10	1.2-720

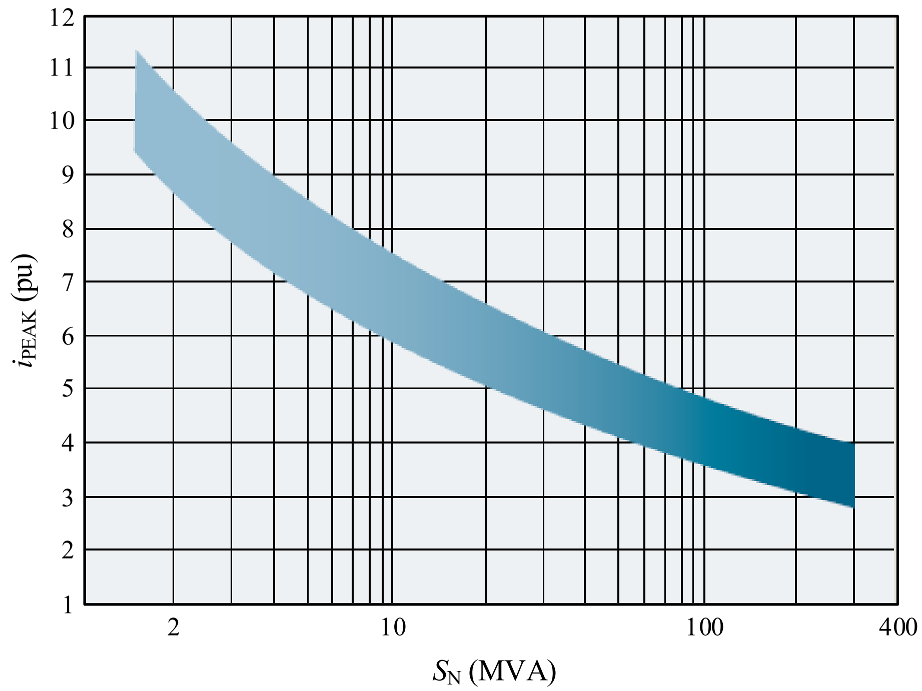

Fig. C.2. Maximum inrush current peak as a function of the nominal power [204].

Table C.21. Typical short-time thermal load capability of oil-inmersed transformers [210].

Time (s)	Times nominal current
2	25
10	11.3
30	6.3
60	4.75
300	3
1800	2

Table C.22. Recommended setting for unrestrained operation for the transformer differential relay [213].

Connection	S_N (MVA)	Recommended setting x I_{N1} when energizing from the	
		High voltage winding	Low voltage winding
-	<10	20	20
Yy	10-100	13	13
Yy	>100	8	8
Yd	-	13	13
Dy	<100	13	20
Dy	>100	8	13

Table C.23. Maximum inrush current peaks for various transformer winding connections [216].

Connection		i_{PEAK} (pu)			
		Three single-phase transformers		Three-phase three-legged transformer	
Primary	Secondary	Simultaneous switching	Sequential switching	Simultaneous switching	Sequential switching
YN	y	26	26	13	14.5
YN	d	26	29	13	14.5
Y	y	20	20	11	11
Y	d	20	20	11	11
D	Y	20	30	15.5	15.5
D	d	20	30	15.5	15.5

Table C.24. Maximum peak inrush current on the medium voltage side for liquid insulated medium and low voltage transformers [214].

S_N (kVA)	i_{PEAK} (pu)	τ (s)
100	14	0.15
160	12	0.20
250	12	0.22
315	12	0.24
400	12	0.25
500	12	0.27
630	11	0.30
800	10	0.30
1000	10	0.35
1250	9	0.35
1600	9	0.40
2000	8	0.45
2500	8	0.5

Table C.25. Maximum peak inrush current on the medium voltage side for dry insulated medium and low voltage transformers [214].

S_N (kVA)	i_{PEAK} (pu)	τ (s)
160	10.5	0.13
250	10.5	0.18
400	10	0.25
630	10	0.26
800	10	0.30
1000	10	0.30
1250	10	0.35
1600	10	0.40
2000	9.5	0.40

Table C.26. Maximum inrush current peaks of different three-phase transformers referred to the high voltage nominal current [213].

Connection	S_N (kVA)	i_{PEAK} (pu)	
		u_{sc} = 0.04 pu	u_{sc} = 0.06 pu
Yz and Yy	50	23	17
	100	22	16
	200	21	15
Yy	250	21	16.5
	630	19.5	15
	1600	18	13.5
Dy	250	14	11
	630	13	10
	1600	12	9

Table C.27. Typical maximum inrush current peaks of single-phase transformers energized by the high voltage winding [206].

S_N (kVA)	i_{PEAK} (pu)	
	Core type	Shell type
2000	7-11	-
10000	5-10	3.5-7
20000	-	2.5-6

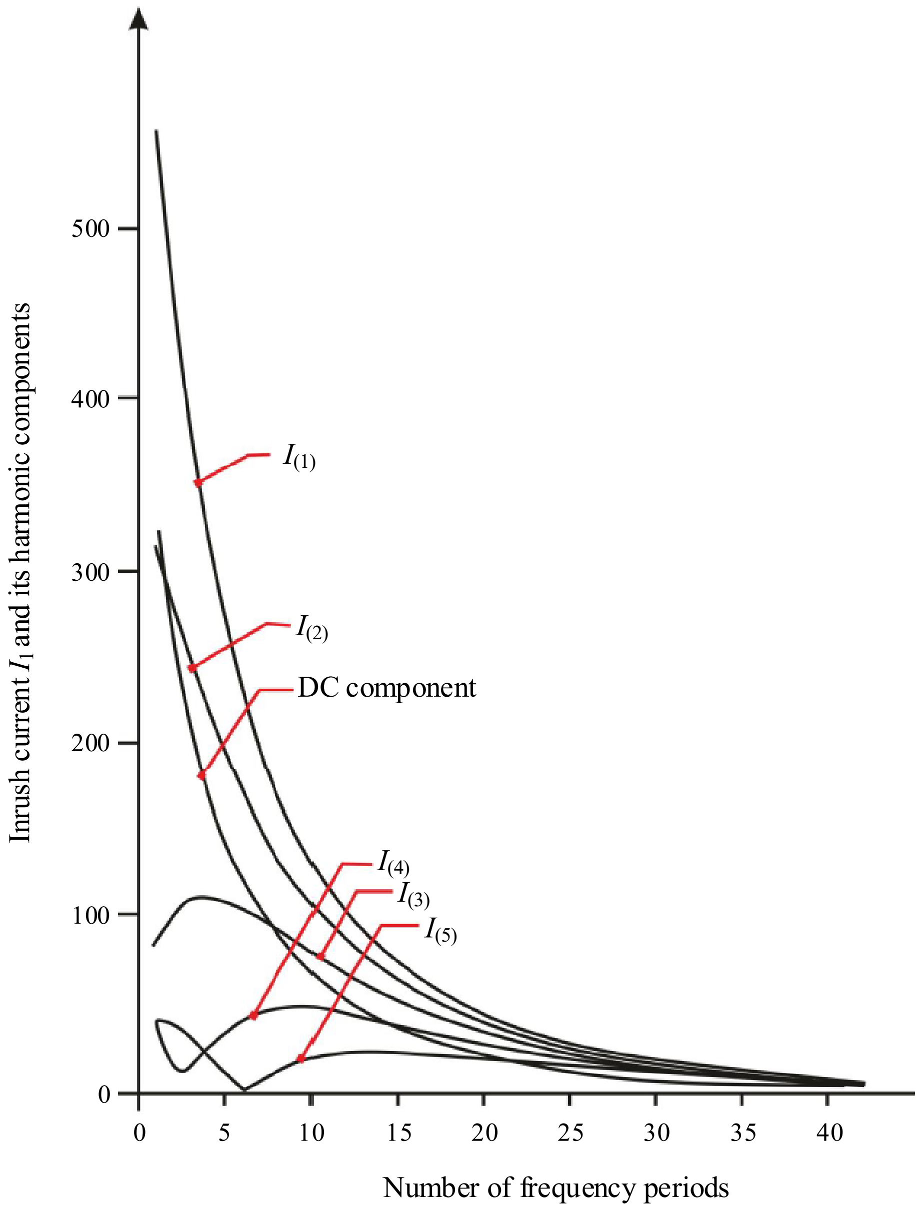

Fig. C.3. Example of harmonic components evolution in an inrush current [217].

C.3. Residual flux

Table C.28. Maximum possible residual flux values for two different power transformers (60 Hz) [218].

Type	S_N (MVA)	U_{N1} (kV)	U_{N2} (kV)	U_{N3} (kV)	ϕ_R(pu)
Single-phase three-winding	330/330/50	500	275	73.5	$0.75\sqrt{2}$
Three-phase three-legged	30	138	36.1	-	$0.9\sqrt{2}$

Appendix D. Static Hysteresis Models

D.1. Static Jiles-Atherton model

The original JA theory is based on the decomposition of the magnetization M between a reversible and an irreversible component [78]:

$$M = M_{\mathrm{rev}} + M_{\mathrm{irr}} \tag{D.1}$$

and they are linked with the magnetic field intensity, H, by the anhysteretic magnetization.

The JA model describes the relation between M and H by using an anhysteretic curve M_{an}-H_{eff} (anhysteretic magnetization in function of the effective field strength). The original JA model uses a modified Langevin function for this anhysteretic curve. This work uses the function proposed in [19] for a better fit of the hysteresis loop because depends on more parameters than the modified Langevin function:

$$M_{\mathrm{an}} = \mathrm{sgn}\left(H_{\mathrm{eff}}\right)\left[\frac{a_1\left|H_{\mathrm{eff}}\right| + \left|H_{\mathrm{eff}}\right|^b}{a_3 + a_2\left|H_{\mathrm{eff}}\right| + \left|H_{\mathrm{eff}}\right|^b}\right]M_{\mathrm{s}} \tag{D.2}$$

where

$$H_{\mathrm{eff}} = H + \alpha M \tag{D.3}$$

and α is a constant parameter known as the interdomain coupling coefficient, M_{s} is the saturation magnetization, and a_1, a_2, a_3 and b, are positive constants without a physical meaning. They have to meet the next two constraints: $a_2 \geq a_1$ and b must be a positive integer (with a common value of 2).

The Jiles-Atherton model is defined by the following differential equation [82], [83], [92], [99]:

$$\frac{\mathrm{d}M}{\mathrm{d}H} = \frac{c\dfrac{\mathrm{d}M_{\mathrm{an}}}{\mathrm{d}H_{\mathrm{eff}}} + \dfrac{\delta_{\mathrm{M}}\left(M_{\mathrm{an}} - M\right)}{\dfrac{\delta k}{\mu_0} - \dfrac{\alpha\left(M_{\mathrm{an}} - M\right)}{1-c}}}{1 - \alpha c\dfrac{\mathrm{d}M_{\mathrm{an}}}{\mathrm{d}H_{\mathrm{eff}}}} \tag{D.4}$$

where c and k are parameters. The former dictates how much of the behavior is defined by M_{an} and how much by M_{irr}, while k is referred to as the bulk coupling coefficient. δ_{M} and δ are calculated as follows [99], [119], [131]:

$$\delta_M = \begin{cases} 0 & \text{if } H < 0 \quad \text{and} \quad M_{an} - M \geq 0 \\ 0 & \text{if } H \geq 0 \quad \text{and} \quad M_{an} - M \leq 0 \\ 1 & \text{otherwise} \end{cases}$$
$$\delta = \begin{cases} 1 & \text{if } H \geq 0 \\ -1 & \text{otherwise} \end{cases} \tag{D.5}$$

To achieve a better fit of the hysteresis loop, k is considered variable in this work as a function of M according to

$$k = k_e \left(k_{ns} + k_s \frac{|M|}{M_s} \right) \tag{D.6}$$

where k_e, k_{ns} and k_s are new constant parameters.

D.2. Static Preisach model

The main idea of the Preisach model is that the magnetic field in a ferromagnetic material can be considered as a set of elementary hysteresis loops called hysterons, which only have two states: +1 and −1. They are illustrated in Fig. D.1(a). A switching field couple, which can be expressed by the plane (α, β), characterizes a hysteron. Representing the saturation flux density and saturation magnetic field intensity as B_{SAT} and H_{SAT}, respectively, when $H = H_{SAT}$ all hysterons are positive and the flux density will be $B = B_{SAT}$. At the other tip of the loop, if $H = -H_{SAT}$ all hysterons will be negative and $B = -B_{SAT}$. This means that α and β are bounded to the range $[-H_{SAT}, H_{SAT}]$ [84], [89], [90]. As the hysteresis is an energetically dissipative phenomenon, next constraint must be accomplished: α ≥ β. These conditions lead to define a triangle in the plane (α , β), known as Preisach triangle, depicted in Fig. D.1(b).

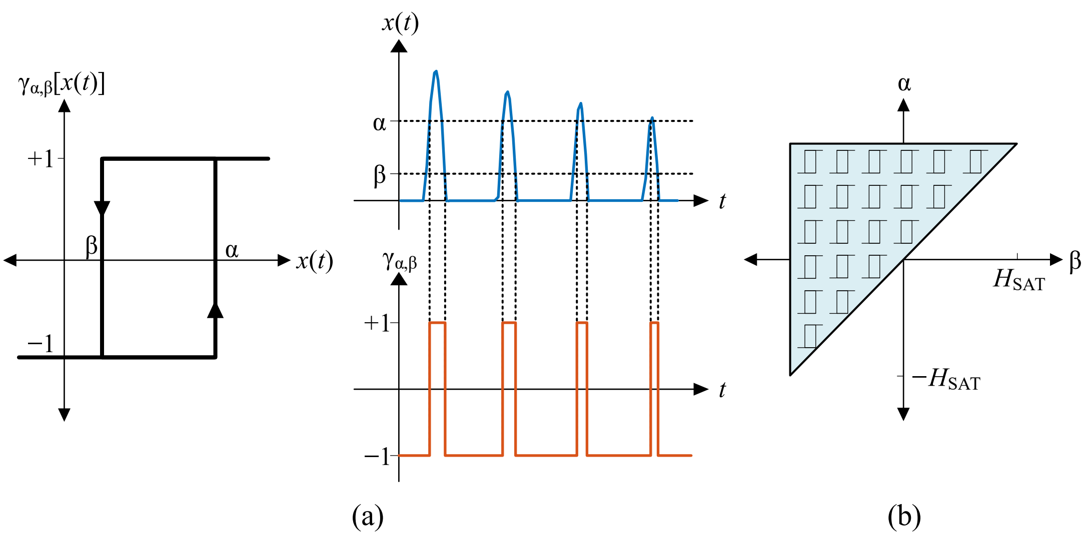

Fig. D.1. (a) Generic diagram and functionality of a hysteresis operator and (b) the Preisach triangle.

The static Preisach model can be defined mathematically by a surface integral as follows [84], [89], [90]:

$$B = \iint_{\alpha \geq \beta} \mu(\alpha,\beta)\gamma_{\alpha,\beta}(H)\,\mathrm{d}\alpha\,\mathrm{d}\beta \tag{D.7}$$

where γα,β( ), is the operator associated with each hysteron and μ(α,β) is the Preisach Distribution Function (PDF) which depends on the core and determines the weight of each hysteron. The value of γα,β depends on the actual input, $H(t)$, and the previous state, and it is defined as [43], [90]

$$\gamma_{\alpha,\beta}(H) = \begin{cases} +1 & H > \alpha \\ \text{previous output} & \beta < H < \alpha \\ -1 & H < \beta \end{cases} \tag{D.8}$$

In Fig. D.2 it is demonstrated how the hysterons switch their value according to a specific input function $H(t)$. In the beginning half of all hysterons are set to −1, while the other half are set to 1. For a rising slope of $H(t)$, the hysterons with the property $\alpha < h(t)$ are set to 1. For a falling slope of $H(t)$, the hysterons with the $\beta > h(t)$ are reset to −1. This divides the Preisach plane into one part with activated hysterons and another part containing deactivated hysterons. Therefore, the Preisach triangle will always be divided between two different regions, one where the value of all hysteresis operators is equal to 1, and another where all are equal to −1. The evaluation of the integral in (D.7) results in the static hysteresis loop.

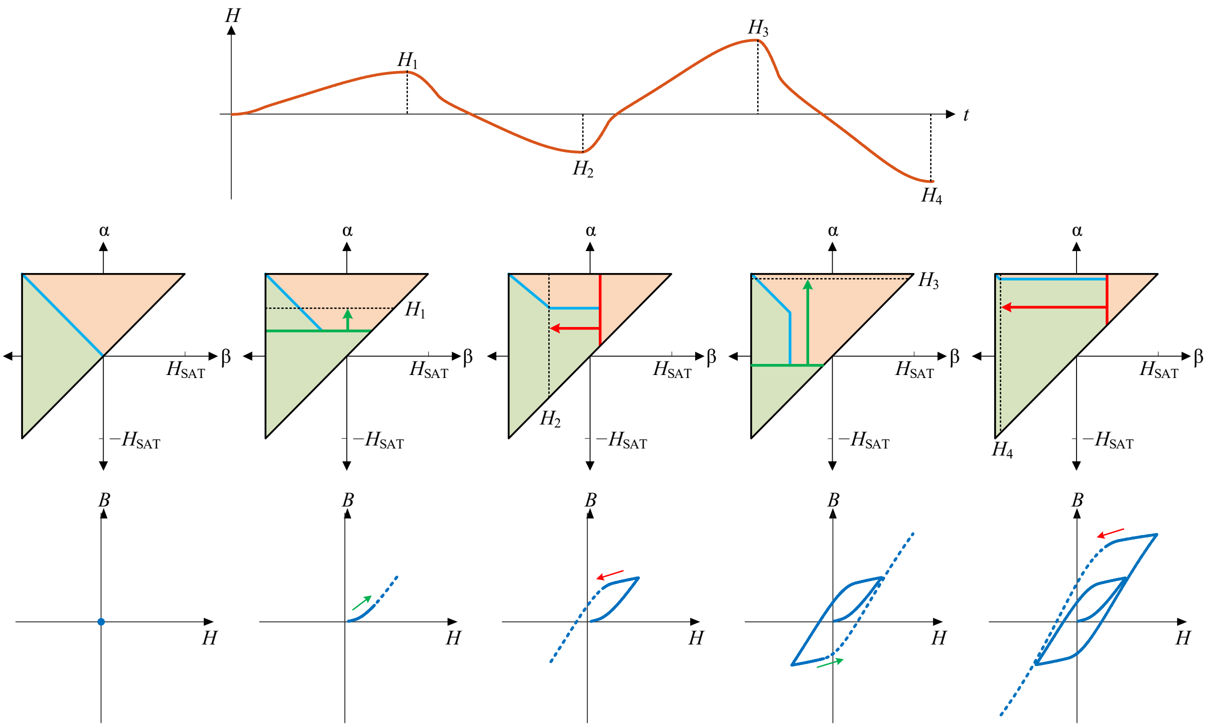

Fig. D.2. Graphical representation of Preisach model behavior.

On the other hand, it has been stated that the Preisach model is a static hysteresis model, meaning it is independent of the input rate, as illustrated in Fig. D.3. It can be observed that for different inputs with varying rates but the same maximum and minimum values, the resulting output is exactly equal for both inputs.

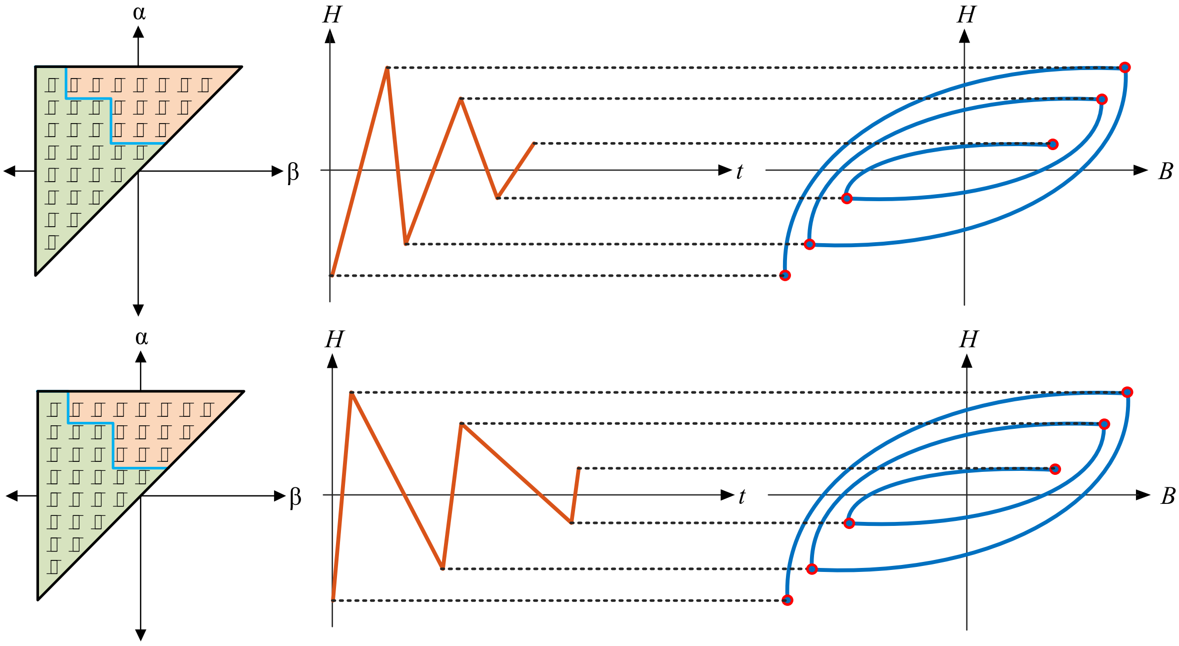

Fig. D.3. Comparison between two different inputs (with identical maximum and minimum values but different rates of change) for the static Preisach model that result in the same description of hysteresis loops.

The main problem of the Preisach model is to determine the PDF. In this work has been used the centered cycles method [219], which determines numerically the PDF from no-load measurements in steady state and does not make any assumption concerning the material type.

Appendix E. Measurements

E.1. Single-phase transformers

Six different single-phase transformers have been tested on laboratory (T1 to T6), whose nominal values are shown in Table E.1.

The summarized results of the no-load and the short-circuit tests are given in Table E.2 and Table E.3, respectively. The waveforms (voltages, currents, fluxes and ϕ–i loops) from these tests are depicted from Fig. E.1 to Fig. E.12. Fig. E.13 show the harmonic content of the no-load currents, while Fig. E.14 shows the resultant ϕ–i loops from no-load tests conducted at different voltage levels. Finally, some inrush currents from transformers T2, T4 and T5 (transformers whose inrush currents were not included in Chapter 4) are depicted in Fig. E.15.

Table E.1. Nominal values of single-phase transformers T1 to T6.

Parameter	T1	T2	T3	T4	T5	T6
S_N (VA)	320	320	320	320	320	360
U_{N1} (V)	120	120	120	120	120	120
r (pu)	0.0412	0.0368	0.0344	0.0373	0.0387	0.0554
x (pu)	0.0266	0.0557	0.0850	0.0554	0.0785	0.0811

Table E.2. Summarized results from the no-load tests.

	T1	T2	T3	T4	T5	T6
Measures	High-voltage winding					
I_0 (A)	0.480	0.255	0.729	0.226	0.273	0.263
i_0 (pu)	0.180	0.096	0.243	0.085	0.103	0.099
U_0 (V)	120.998	121.177	122.276	121.527	120.008	120.939
u_0 (pu)	1.008	1.010	1.019	1.013	1.000	1.008
W_0 (W)	10.829	8.321	5.128	7.566	8.425	8.535
w_0 (pu)	0.035	0.026	0.014	0.024	0.026	0.027
	Low-voltage winding					
I_0 (A)	0.730	0.384	-	0.362	0.388	0.374
i_0 (pu)	0.160	0.084	-	0.079	0.085	0.082
U_0 (V)	71.318	70.994	-	70.788	70.431	70.220
u_0 (pu)	1.019	1.014	-	1.011	1.006	1.003
W_0 (W)	10.485	7.916	-	7.854	8.084	7.980
w_0 (pu)	0.033	0.025	-	0.025	0.025	0.025

Table E.3. Summarized results from the short-circuit tests.

Measures	T1	T2	T3	T4	T5	T6
			High-voltage winding			
I_{sc} (A)	2.662	2.720	2.922	2.795	2.711	2.750
i_{sc} (pu)	0.998	1.020	0.974	1.048	1.017	1.031
U_{sc} (V)	7.438	9.674	11.584	8.368	10.635	11.866
u_{sc} (pu)	0.062	0.081	0.096	0.070	0.089	0.099
W_{sc} (W)	13.101	11.453	18.686	13.002	12.740	13.402
w_{sc} (pu)	0.041	0.036	0.052	0.041	0.040	0.042
			Low-voltage winding			
I_{sc} (A)	-	4.752	-	4.535	4.635	4.774
i_{sc} (pu)	-	1.040	-	0.992	1.014	1.044
U_{sc} (V)	-	6.149	-	4.891	6.836	7.687
u_{sc} (pu)	-	0.088	-	0.070	0.098	0.110
W_{sc} (W)	-	13.203	-	12.456	16.114	17.319
w_{sc} (pu)	-	0.041	-	0.039	0.050	0.054

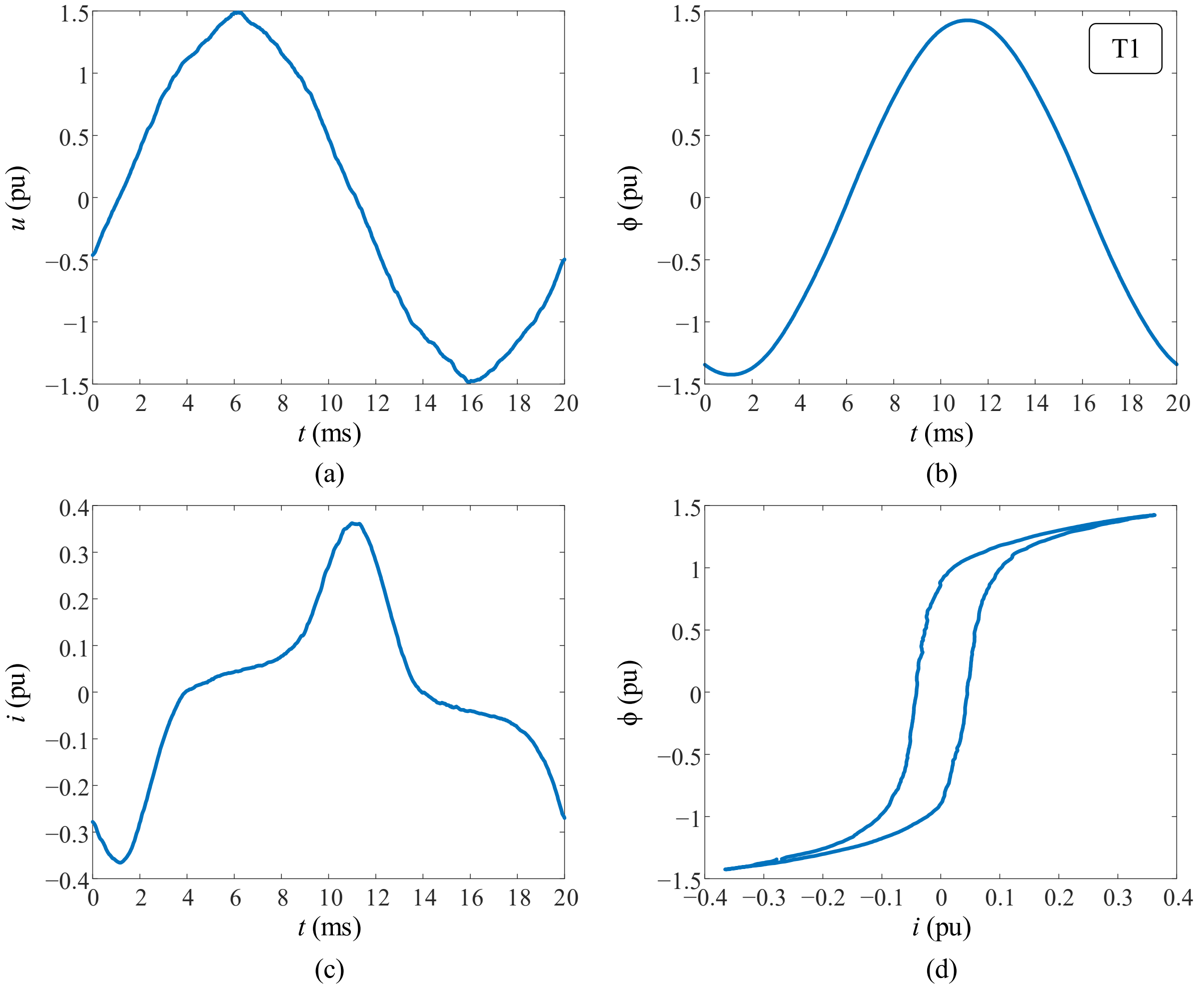

Fig. E.1. No-load test of T1 performed by the high-voltage winding: (a) primary voltage, (b) flux, (c) no-load current and (d) ϕ–i loop.

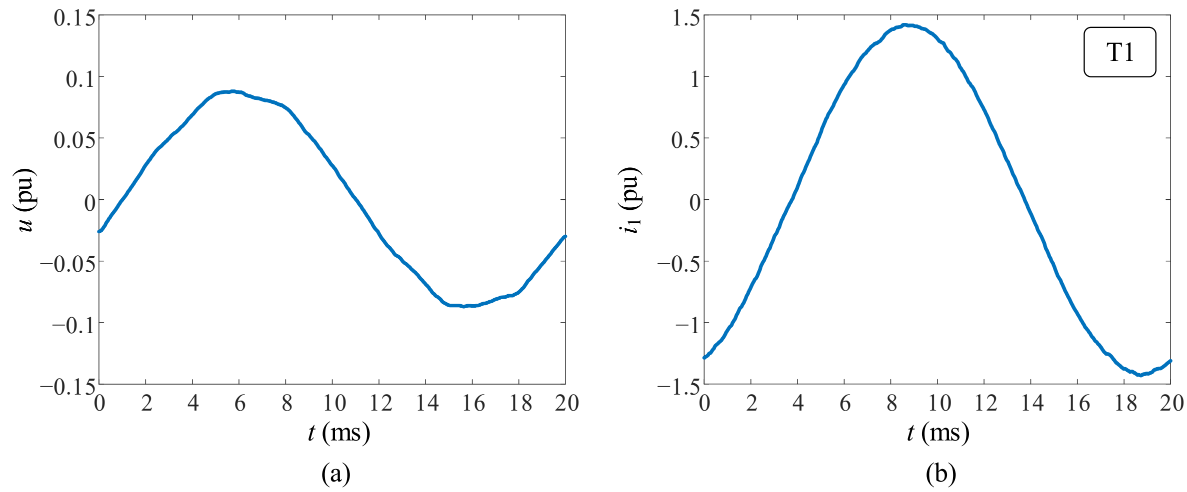

Fig. E.2. Short-circuit test of T1 performed by the high-voltage winding: (a) primary voltage, (b) flux, (c) no-load current and (d) ϕ–i loop.

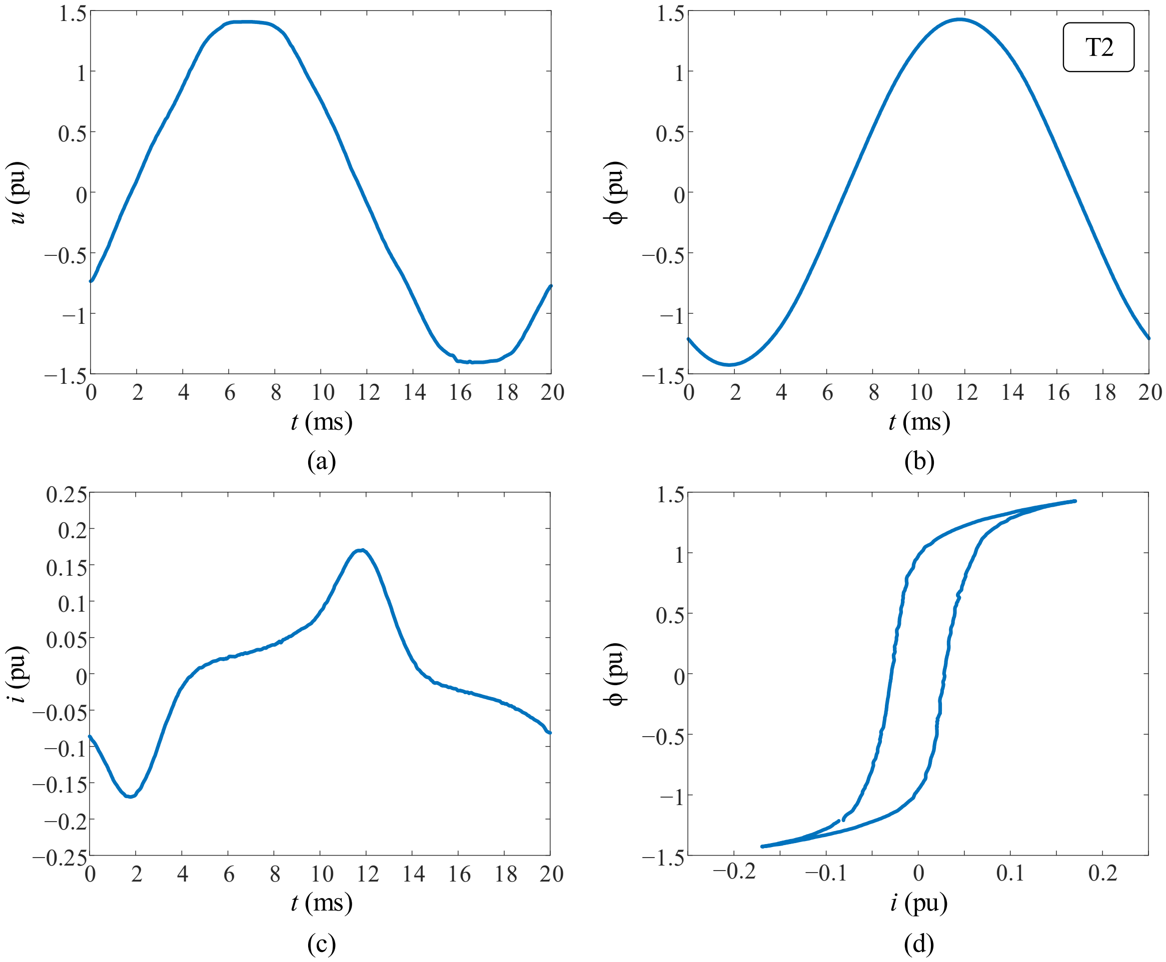

Fig. E.3. No-load test of T2 performed by the high-voltage winding: (a) primary voltage, (b) flux, (c) no-load current and (d) ϕ–i loop.

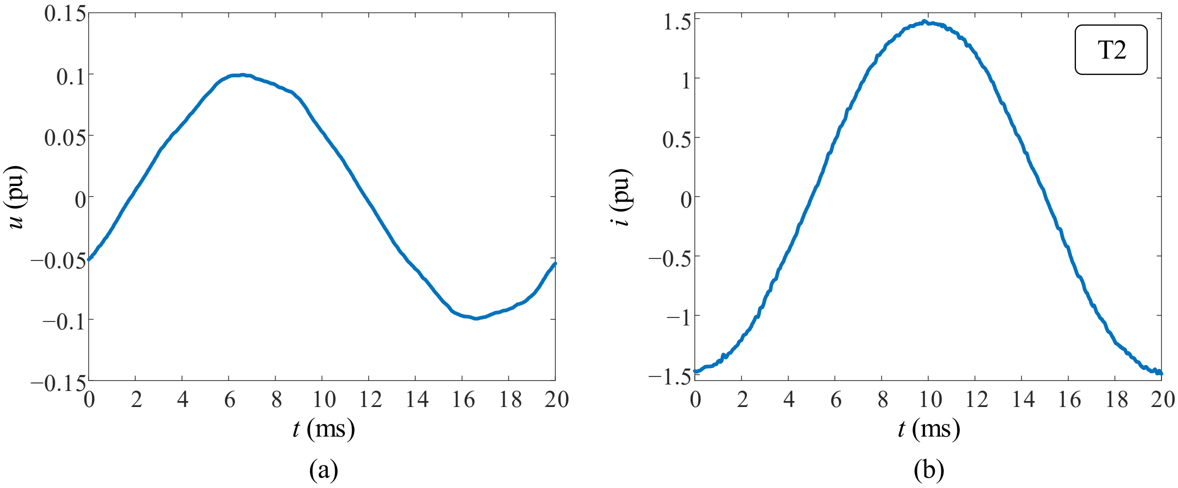

Fig. E.4. Short-circuit test of T2 performed by the high-voltage winding: (a) primary voltage, (b) flux, (c) no-load current and (d) ϕ–i loop.

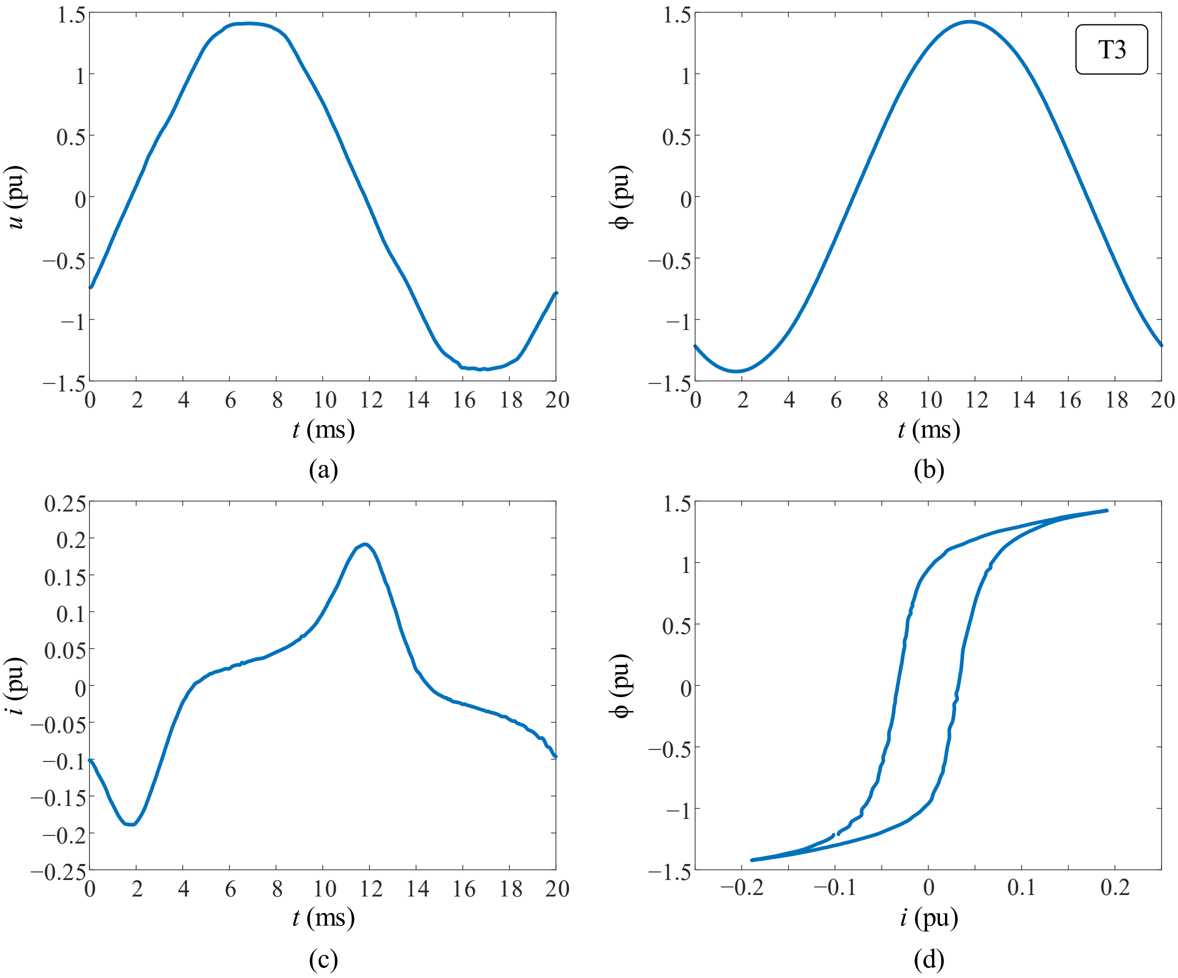

Fig. E.5. No-load test of T3 performed by the high-voltage winding: (a) primary voltage, (b) flux, (c) no-load current and (d) ϕ–i loop.

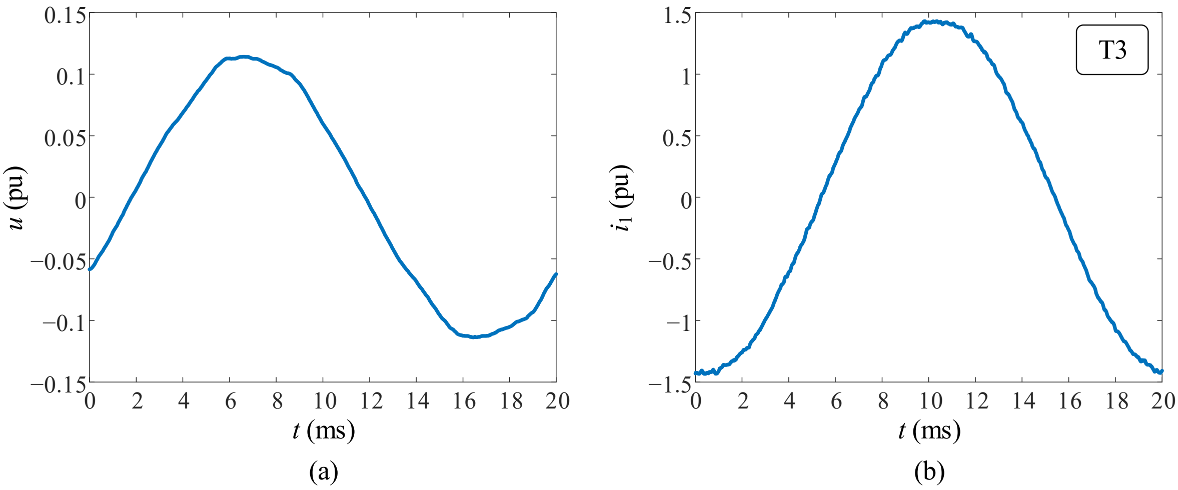

Fig. E.6. Short-circuit test of T3 performed by the high-voltage winding: (a) primary voltage, (b) flux, (c) no-load current and (d) ϕ–i loop.

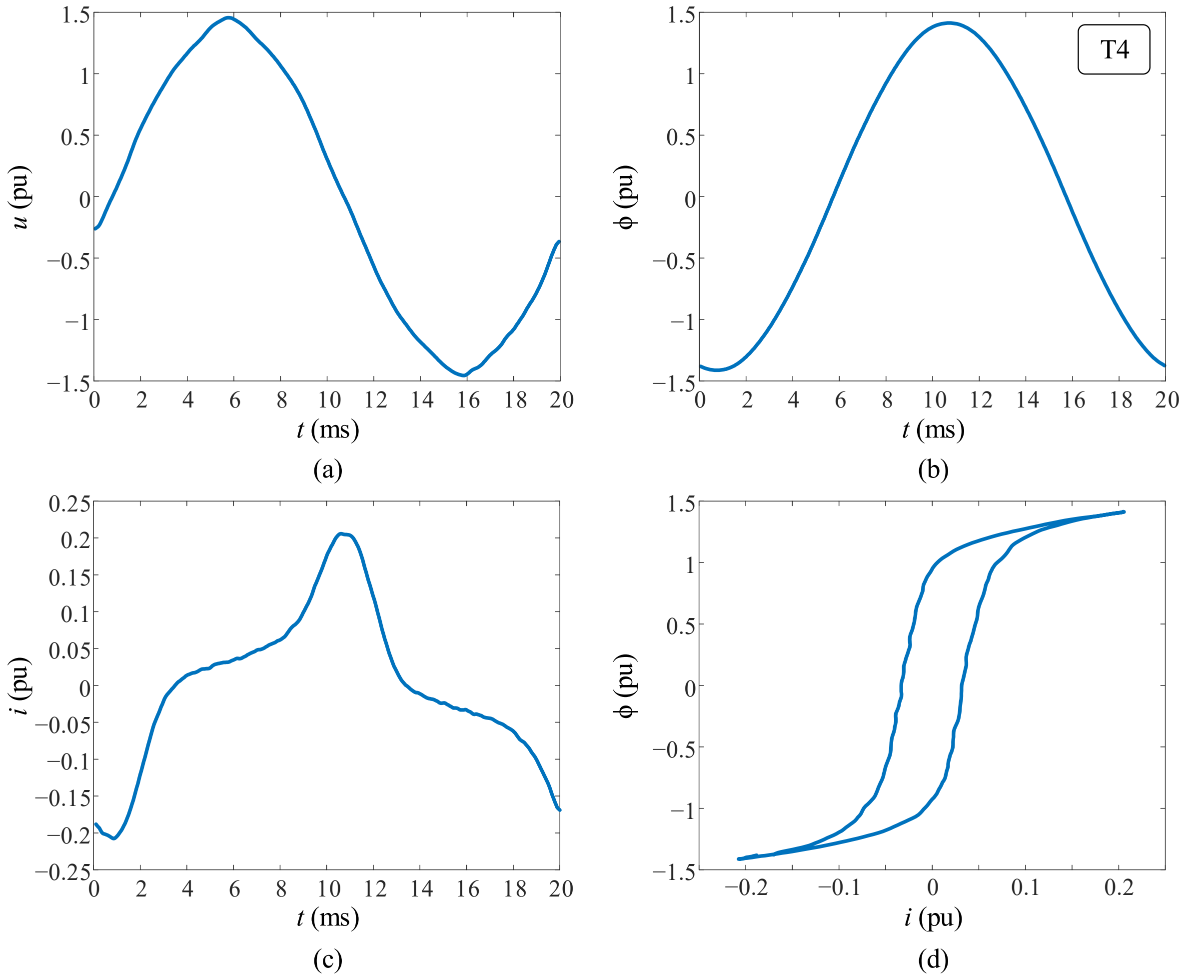

Fig. E.7. No-load test of T4 performed by the high-voltage winding: (a) primary voltage, (b) flux, (c) no-load current and (d) ϕ–i loop.

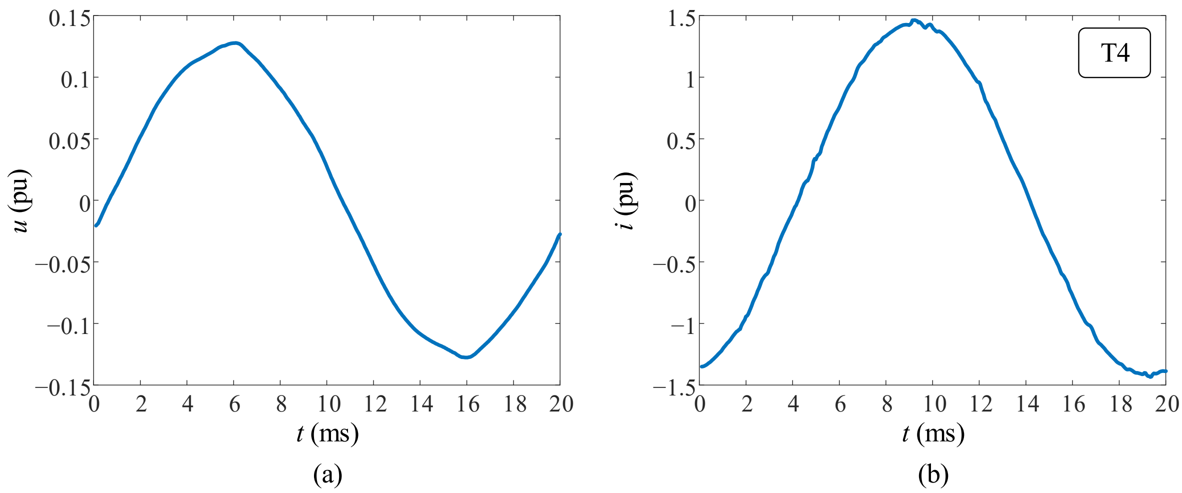

Fig. E.8. Short-circuit test of T4 performed by the high-voltage winding: (a) primary voltage, (b) flux, (c) no-load current and (d) ϕ–i loop.

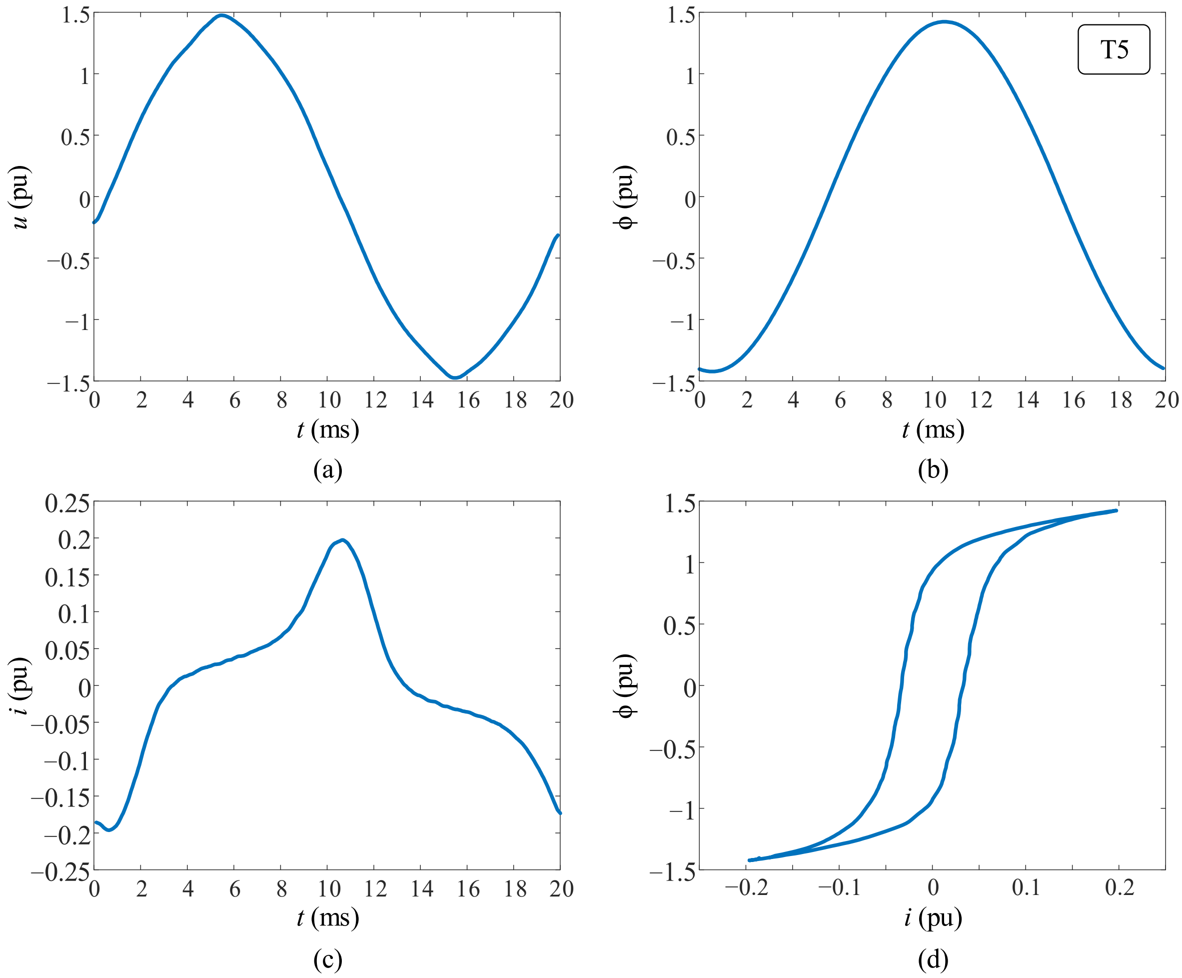

Fig. E.9. No-load test of T5 performed by the high-voltage winding: (a) primary voltage, (b) flux, (c) no-load current and (d) ϕ–i loop.

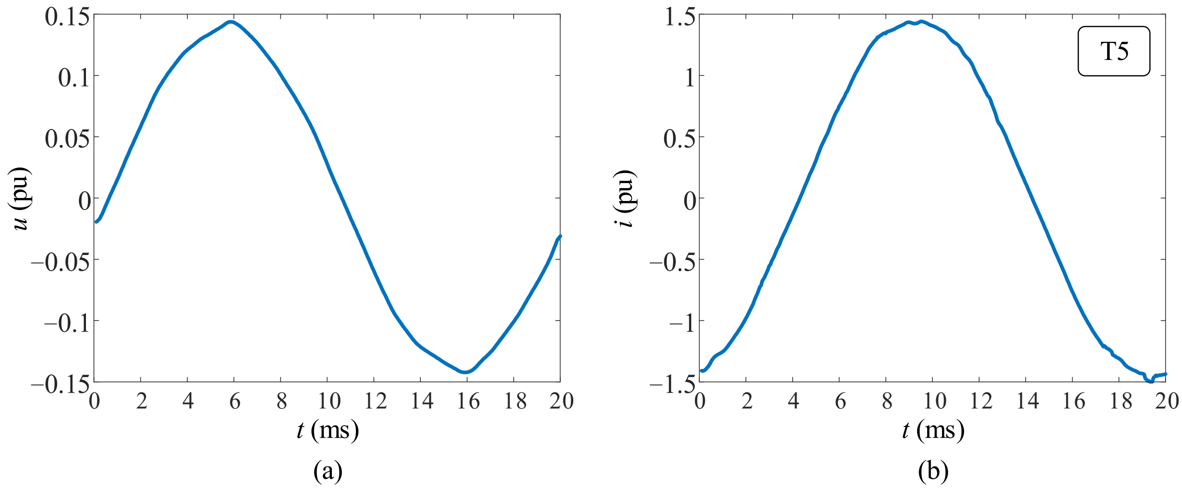

Fig. E.10. Short-circuit test of T5 performed by the high-voltage winding: (a) primary voltage, (b) flux, (c) no-load current and (d) ϕ–i loop.

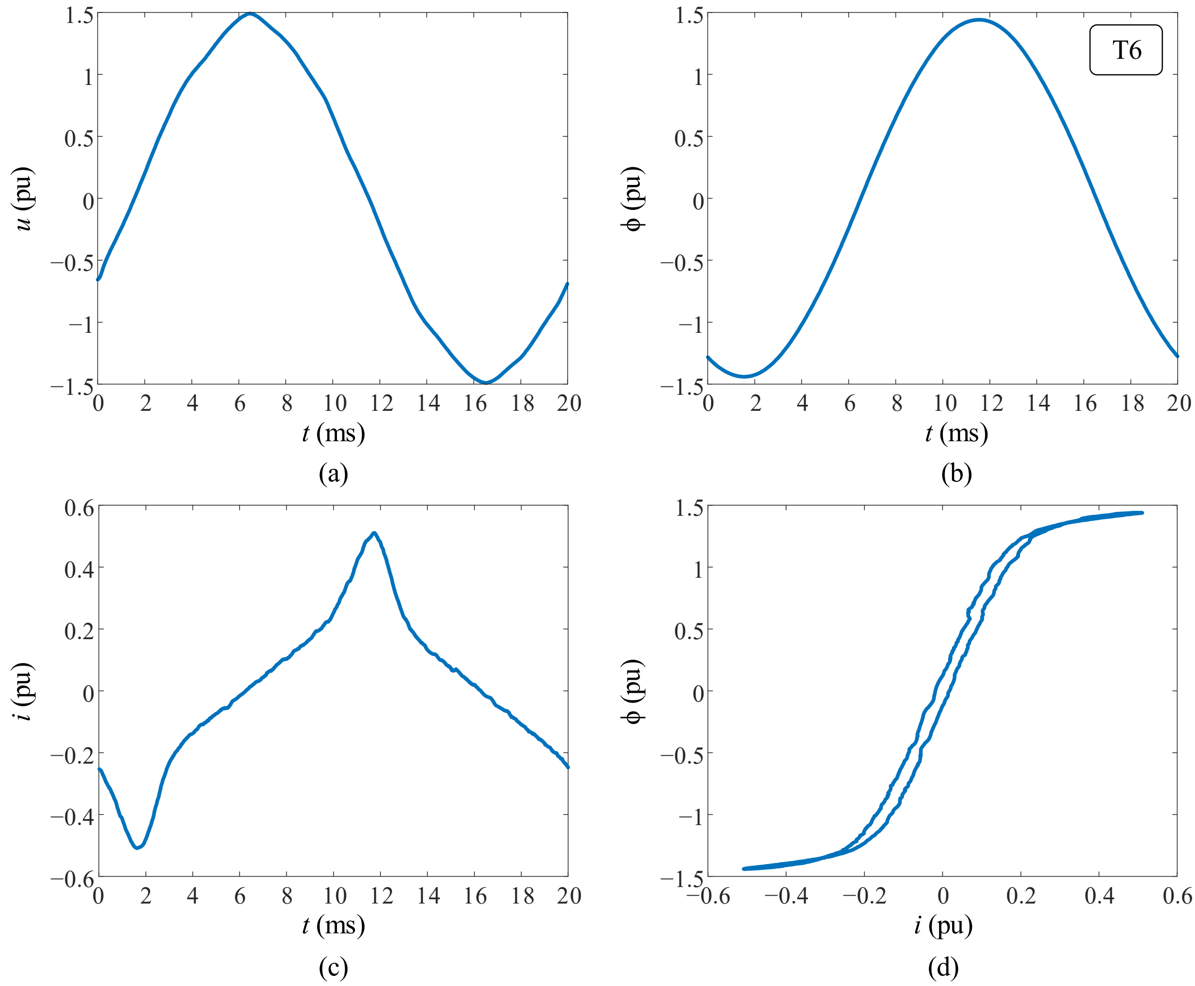

Fig. E.11. No-load test of T6 performed by the high-voltage winding: (a) primary voltage, (b) flux, (c) no-load current and (d) ϕ–i loop.

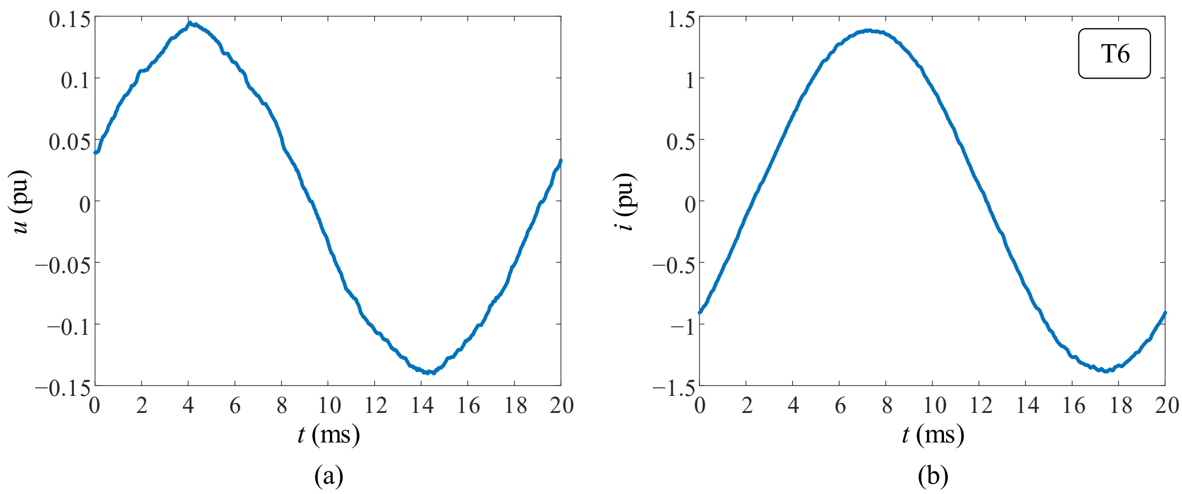

Fig. E.12. Short-circuit test of T6 performed by the high-voltage winding: (a) primary voltage, (b) flux, (c) no-load current and (d) ϕ–i loop.

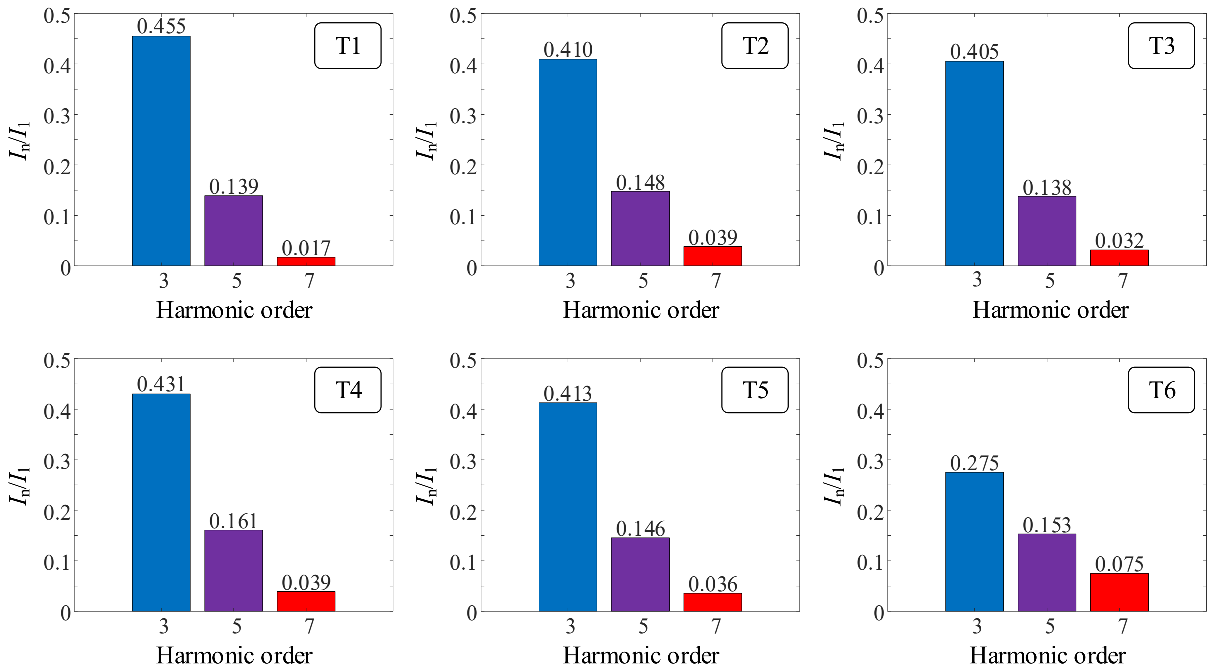

Fig. E.13. Harmonic content of the no-load currents of T1-T6.

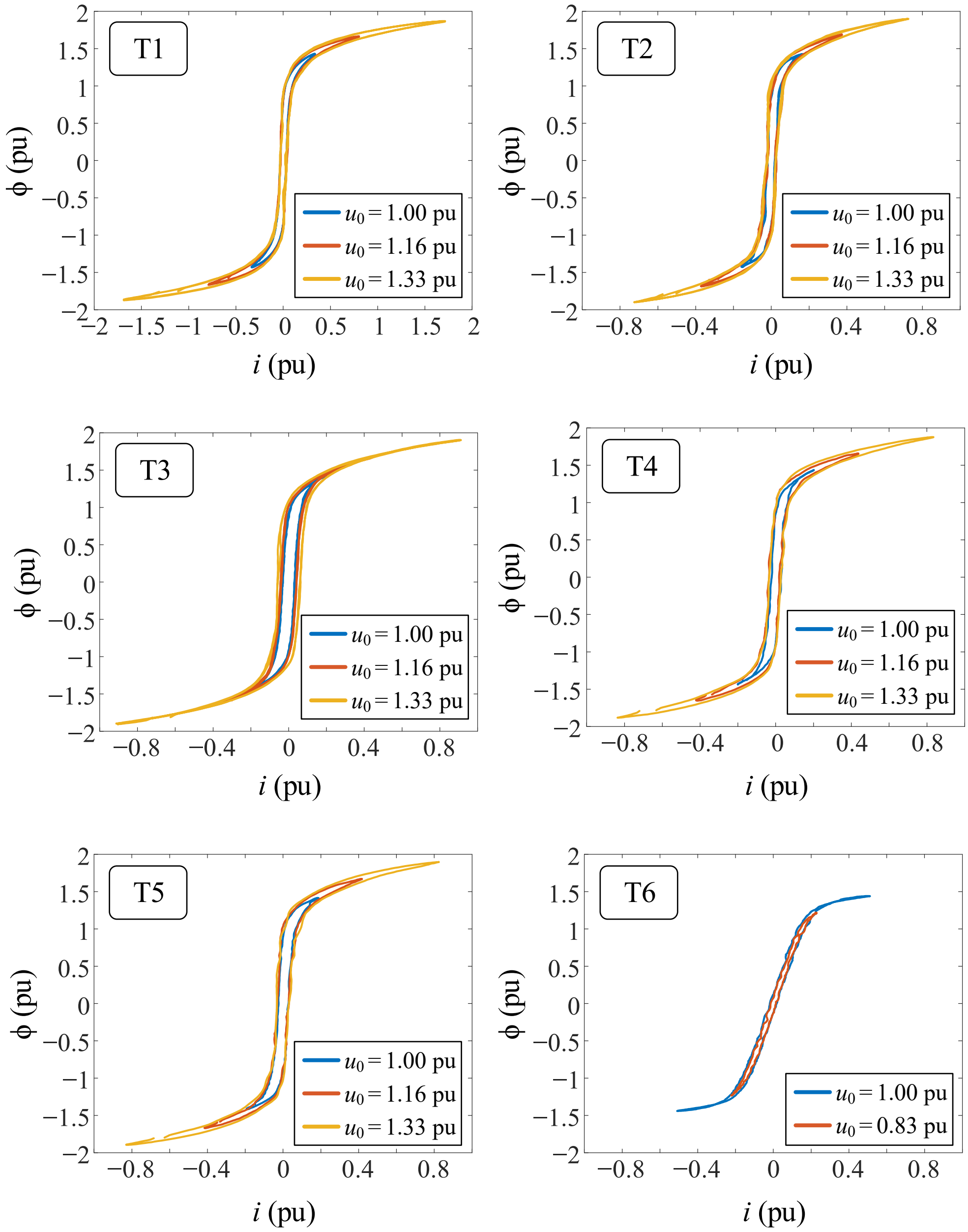

Fig. E.14. ϕ–i loops of T1-T6 obtained from no-load tests performed at different voltage levels.

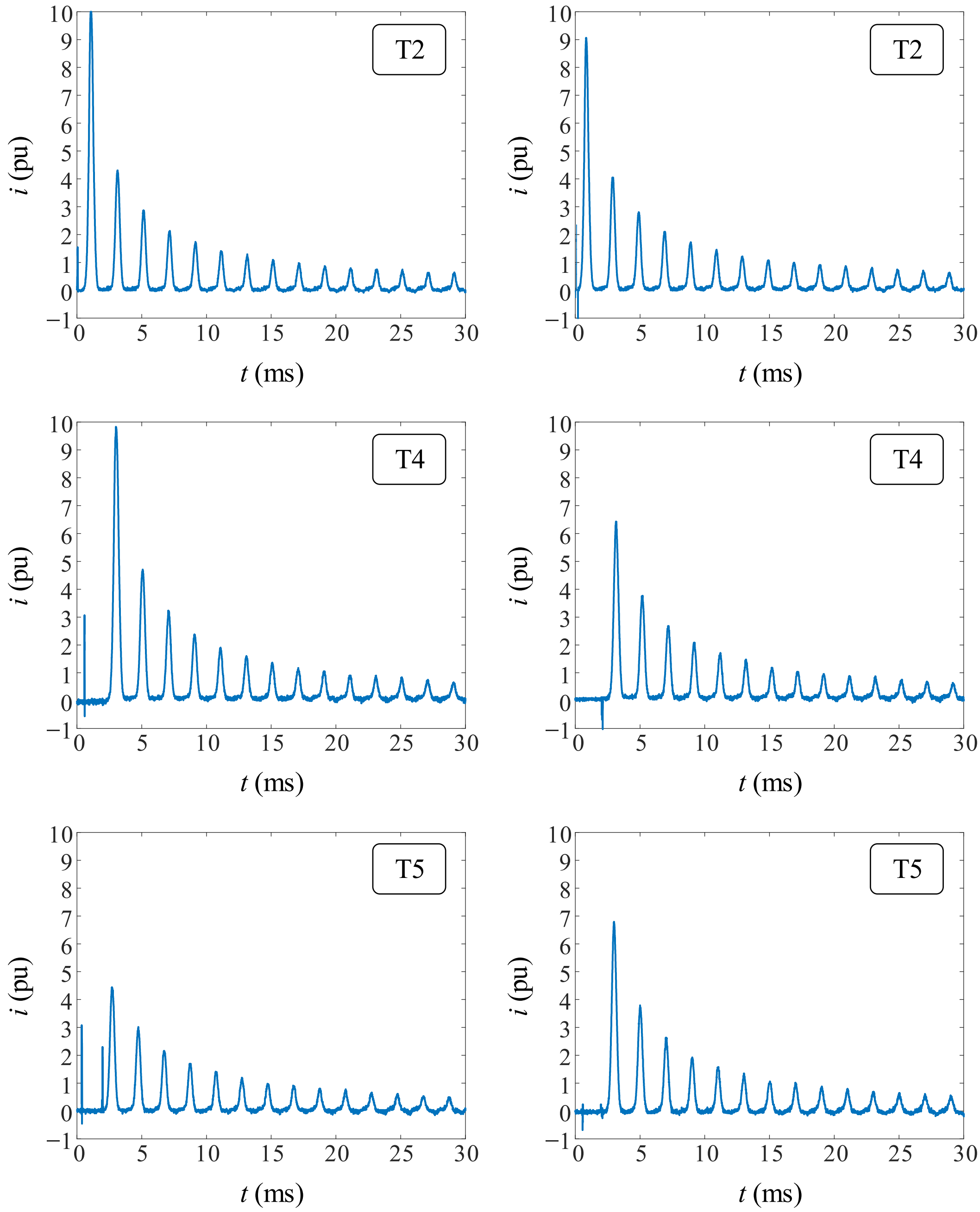

Fig. E.15. Measured inrush currents from transformers T2, T4 and T5.

E.2. Three-phase three-legged transformers

The measurements from the three-phase no-load tests of transformer T21, which were not presented in Chapter 5, corresponding to YNd and Yd connections, are depicted in Fig. E.16 and Fig. E.17, respectively. Additionally, Fig. E.18 and Fig. E.19 show the resultant ϕ–i loops from the Fuchs tests [157] (single-phase tests) conducted in transformer T21.

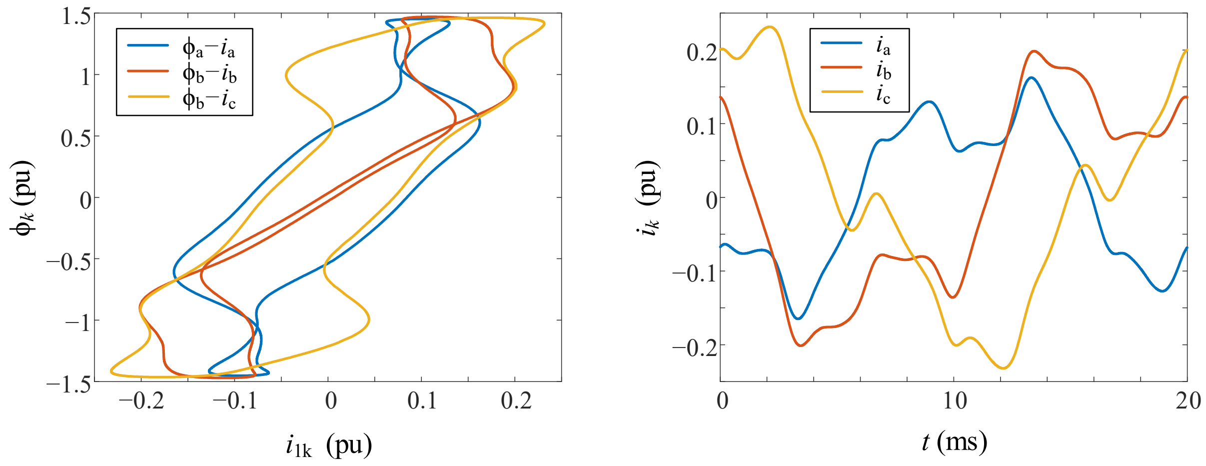

(a) (b)

Fig. E.16. Three-phase no-load test at rated voltage of transformer T21 with connection YNd: (a) ϕ–i loops, and (b) no-load currents.

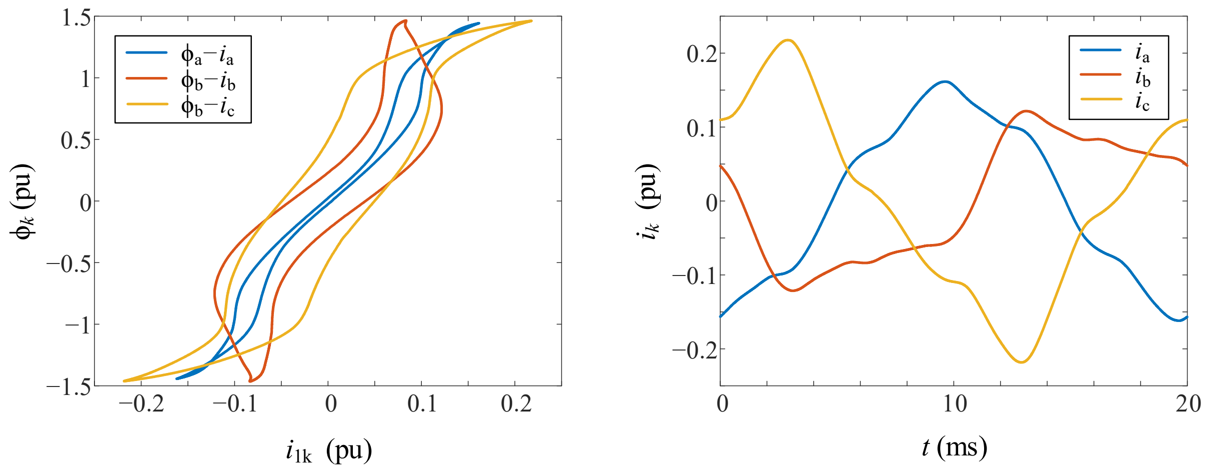

(a) (b)

Fig. E.17. Three-phase no-load test at rated voltage of transformer T21 with connection Yd: (a) ϕ–i loops, and (b) no-load currents.

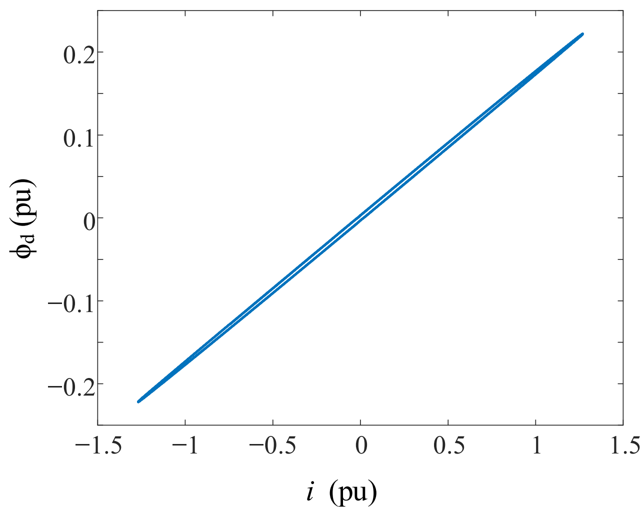

Fig. E.18. Zero-sequence test [157] of transformer T21.

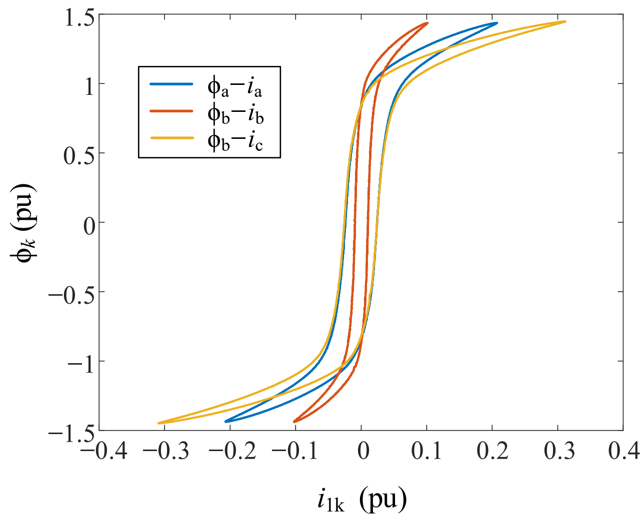

Fig. E.19. ϕ–i loops from single-phase Fuchs tests [157] of transformer T21.

Appendix F. FPGA-Based Smart Sensor to Detect Current Transformer Saturation during Inrush Current Measurement

F.1. CT saturation detection algorithm

F.1.1. Time-Domain Features

The proposed smart sensor is based on the second-order difference function to detect abrupt current changes and, therefore, when the saturation starts at each cycle.

The second-order difference of the current i_2 at the n instant, can be obtained as

$$\mathrm{d}i_2(n) = i_2(n) - 2i_2(n-1) + i_2(n-2) \tag{F.1}$$

as a function of the n current sample and the last two previous samples.

As seen in Fig. F.1, the second-order difference function has peaks every time the measured current has a steep change, so the CT saturation can be detected. However, the regular changes in inrush current due to power transformer saturation also can be incorrectly detected as CT saturation inceptions. Moreover, it also presents lower peaks as a consequence of noise. Then, to improve the use of this function, the combined use of the third-order statistic central moment is suggested, which is one of the higher-order statistics.

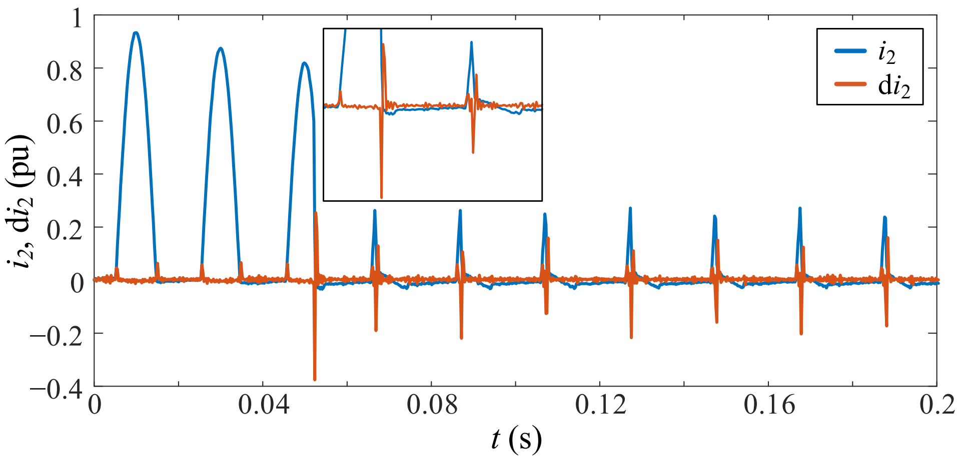

Fig. F.1. Second-order difference function of an inrush current.

A central moment is a statistic moment of a probability distribution of a random variable or discrete-time series about its mean; that is, it is the expected value of a specified integer power of the deviation of the random variable from the mean [220]. A higher-order moment relates to the spread and shape of the distribution.

The third central moment, m_3, of a time-discrete series $x(k)$ is defined as [220]

$$m_3 = \frac{1}{N}\sum_{k=1}^{N}\left(x(k)-\bar{x}\right)^3 \tag{F.2}$$

where N is the number of samples and $\bar{x}$ is the time-series mean. This definition does not take into account the normalization around the standard deviation. This paper uses a sliding window along the measured current to obtain a moving version of the third central moment. If the window has a length of L samples, the moving third moment can be calculated as

$$m_{i_2,3}(n) = m_3\left[i_2(n), i_2(n-1), \ldots, i_2(n-L+1)\right] \tag{F.3}$$

where it is considered an overlap of L–1 samples between each adjacent window. Fig. F.2 shows an example of the moving third moment for an inrush current.

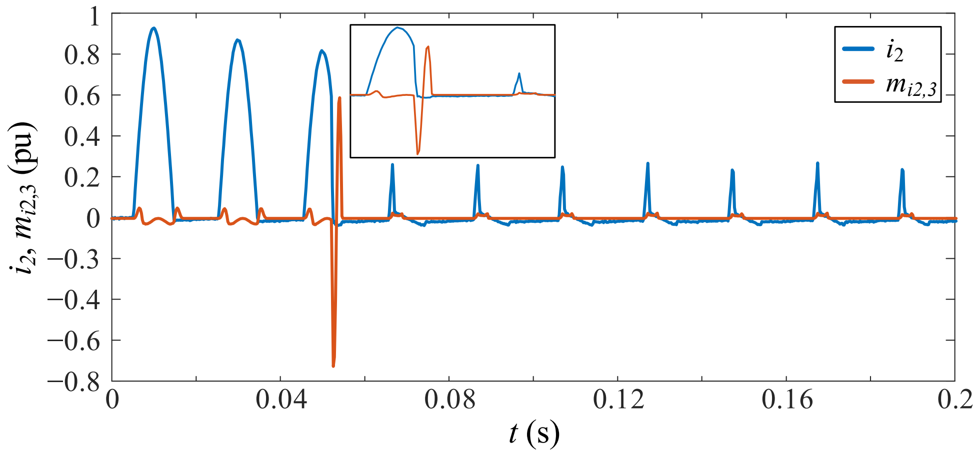

Fig. F.2. Moving third-order central moment of an inrush current.

F.1.2. Start of Saturation

In order to detect a CT saturation inception due to a transient primary current, the following algorithm has to be accomplished:

7. Set an initial threshold value, $i_{2\mathrm{TH}}$, equal to 0.05 pu.

8. Set a second threshold value, $m_{3\mathrm{TH}}$, equal to 0.003 pu.

9. Calculate in real time the two time-domain features (di_2 and $m_{i2,3}$), with (F.1) and (F.3), for the secondary CT current. To calculate $m_{i2,3}$, it must be considered an overlap L equal to 10 samples.

10. Detect maximum or minimum local peaks in $m_{i2,3}$ and compare them with the threshold value $i_{2\mathrm{TH}}$. If the absolute peak value is greater than the absolute value of existing $i_{2\mathrm{TH}}$, the latter will be updated with the peak value.

11. To detect the first CT saturation inception at n instant, it must be fulfilled that:

- If i_{2TH} is positive, d$i_2(n)$ must be negative with an absolute value greater than the threshold value.
- If i_{2TH} is negative, d$i_2(n)$ must be positive and greater than the absolute threshold value.

12. The i_{2TH} value is updated with the third part of d$i_2(n)$ value, corresponding to the first CT saturation.

13. The subsequent CT saturation inceptions are detected if:

    - If i_{2TH} is positive, d$i_2(n)$ must be positive and greater than the threshold. Also, $m_{i2,3}(n)$ or $m_{i2,3}(n-1)$ must be different from zero and with an absolute value greater than m_{3TH}.
    - If i_{2TH} is negative, d$i_2(n)$ must be negative and lower than the threshold value. Also, $m_{i2,3}(n)$ or $m_{i2,3}(n-1)$ must be different from zero and with an absolute value greater than m_{3TH}.

Fig. F.3 shows the flowchart that summarizes this CT saturation detection algorithm.

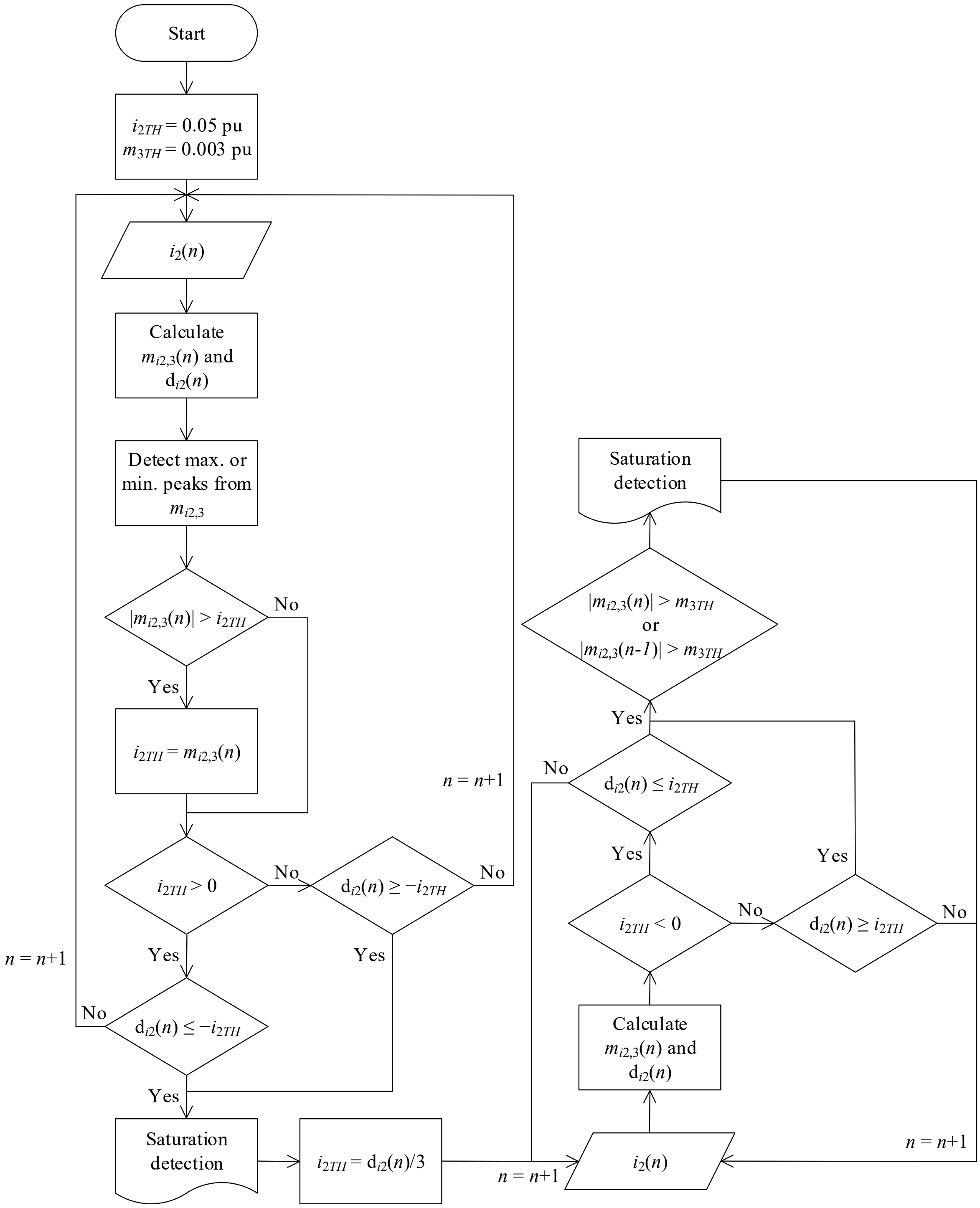

Fig. F.3. Flowchart of the CT saturation detection algorithm.

F.1.3. End of Saturation

It can be assumed that at the saturation instant, the CT core flux is the same as when the saturation ends. Neglecting the total secondary inductance, the CT flux is proportional to the integration of the secondary CT current. It is necessary to know the residual flux ϕ_R and $R_T = R_2 + R_B$ values to obtain the CT flux. Because ϕ_R only displaces the flux about the vertical axis and R_T scales the flux waveform, a pseudo-flux proportional to the actual flux can be obtained at the *n* time using the trapezoidal rule as

$$\tilde{\phi}(n) = \tilde{\phi}(n-1) + \frac{i_2(n) + i_2(n-1)}{2}\left[t(n) - t(n-1)\right] \tag{F.4}$$

Therefore, the end of the saturation interval can be determined when the instantaneous pseudo-flux magnitude falls below the magnitude corresponding to the saturation instant.

F.2. Smart Sensor

The block diagram of the general architecture of the proposed smart sensor is shown in Fig. F.4. The smart sensor is divided into three main stages: a primary sensor, a data acquisition system (DAS), and an FPGA-based processor.

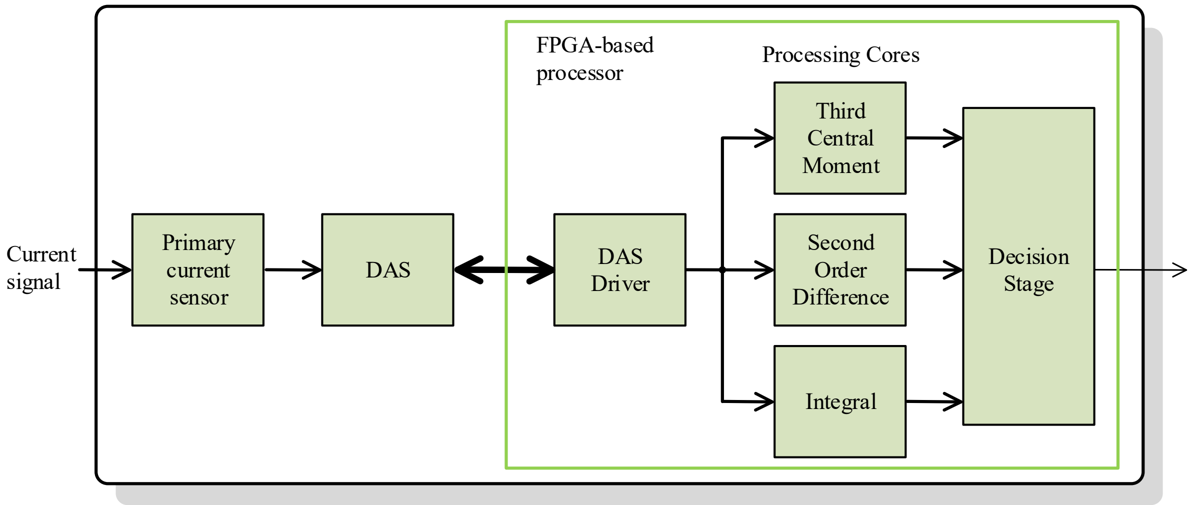

Fig. F.4. Architecture of the proposed smart sensor.

The primary sensor stage consists of a current sensor (as a Hall Effect clamp meter) connected to the secondary CT side. As explained in the Introduction Section, the smart sensor has not been tested on fully real conditions, so the primary sensor has not been included on the prototype. The CT saturation detection algorithm has been tested using Simulink computer simulations, and the smart sensor prototype (FPGA-based processor) has been implemented in a dSPACE MicroLabBox platform (which incorporates a Xilinx FPGA) and tested with the help of a HIL (Typhoon platform), which provides in real time the measured CT secondary current signal.

The MicroLabBox incorporates analog to digital converters with a 16-bit resolution, a sampling frequency of 1 million samples per second (sps), and an input range from –10 V to +10 V. In this paper, the measured signal has been resampled internally in the DSPACE to reduce the sampling frequency to 4000 sps, which is in the range of the common sampling frequencies in digital relaying systems. The signal conditioning previous to the conversion includes a fully-differential isolation amplifier to get electrical isolation and a low-pass anti-aliasing filter, allowing the correct harmonic analysis.

The FPGA-based processor is the smart sensor's final stage, responsible for the CT saturation detection, performed by the two time-domain features processing cores, an integrator core, and a decision stage. All these cores are described in detail in the following subsections. This processor delivers the saturation indicator signal, which can be sent to another device so that an optional communication interface can also be implemented in the FPGA. The FPGA-based processor also includes the necessary drivers for proper communication with the DAS and the finite state machine (FSM), which is necessary to handle the operation of all the processing cores.

F.2.1. FPGA-based Processor

The FPGA-based processor consists of two main stages. The first stage contains the two time-domain features processing cores and the integrator core, and the second stage decides whether there is saturation.

These processing cores are fully implemented on a single FPGA (Xilinx Kintex-7 XC7K325T), and the authors fully developed them under Very high speed integrated circuit Hardware Description Language (VHDL) and the standard libraries from IEEE. Commercially available processing cores and libraries have not been used.

Fig. F.5 shows the block diagram of the general architecture of the processing core for the second-order difference function, according to (F.1). There are three input signals, $x(n)$, STR, and SR, and two output signals, D2, and END. The signal $x(n)$ is the secondary CT current to be processed, a signal of 18-bit in a 2.16 fixed-point format. STR is a 1-bit indicator signal to start the calculation, and SR is a 1-bit signal to indicate to the processing core that a new $x(n)$ sample is available to be read. D2 is the result of the processing core, a 18-bit signal with the same format than $x(n)$. Finally, END is a 1-bit signal that indicates that a calculation has been finished and a new result is available to be read.

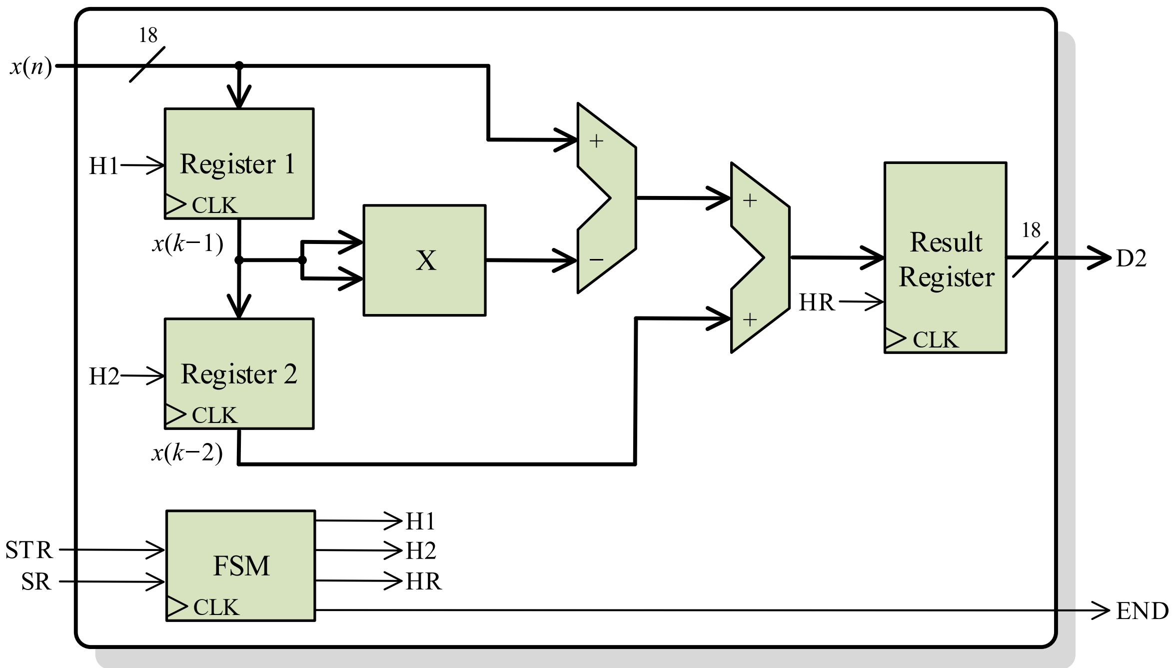

Fig. F.5. Architecture of the processing core for computing the second-order difference function.

The processing core uses two parallel registers (Register 1 and Register 2) connected in cascade to store the last two input samples, $x(n-1)$ and $x(n-2)$. Each time a new sample is available at the input $x(n)$, the two registers are enabled, so the last sample is stored, and the antepenultimate sample is discarded. There is another register to control the flow of the output result. The core also includes an FSM to control the enabling of registers and therefore the data flow. This FSM also handles the indicator signals (STR, SR, and END).

Fig. F.6 depicts the general architecture of the second processing core for computing the moving third-order central moment according to (F.2) and (F.3). This processing core has the same inputs and outputs as the previous processing core, plus a new 4-bit signal L, which indicates the length of the sliding window to the core. Again, $L-1$ parallel registers connected in cascade to store the $L-1$ last input samples. The input $x(n)$ and the registers' outputs, are connected through a multiplexor to a mean block. With the help of the multiplexor and a counter, the flow of current and past input samples can be controlled by the FSM. It is important to note that according to (F.2), the mean of L input samples has to be subtracted from each sample, so the L samples must remain available until the mean calculation is finished. This is possible with the presented core design because the used FPGA has a base operating frequency (100 MHz) much larger than the sampling frequency. With two multipliers, the third power in (F.2) is performed to get the mean again finally. The FSM handles all the indicator signals and the internal control signals for the mean blocks, registers, multiplexor, and counter.

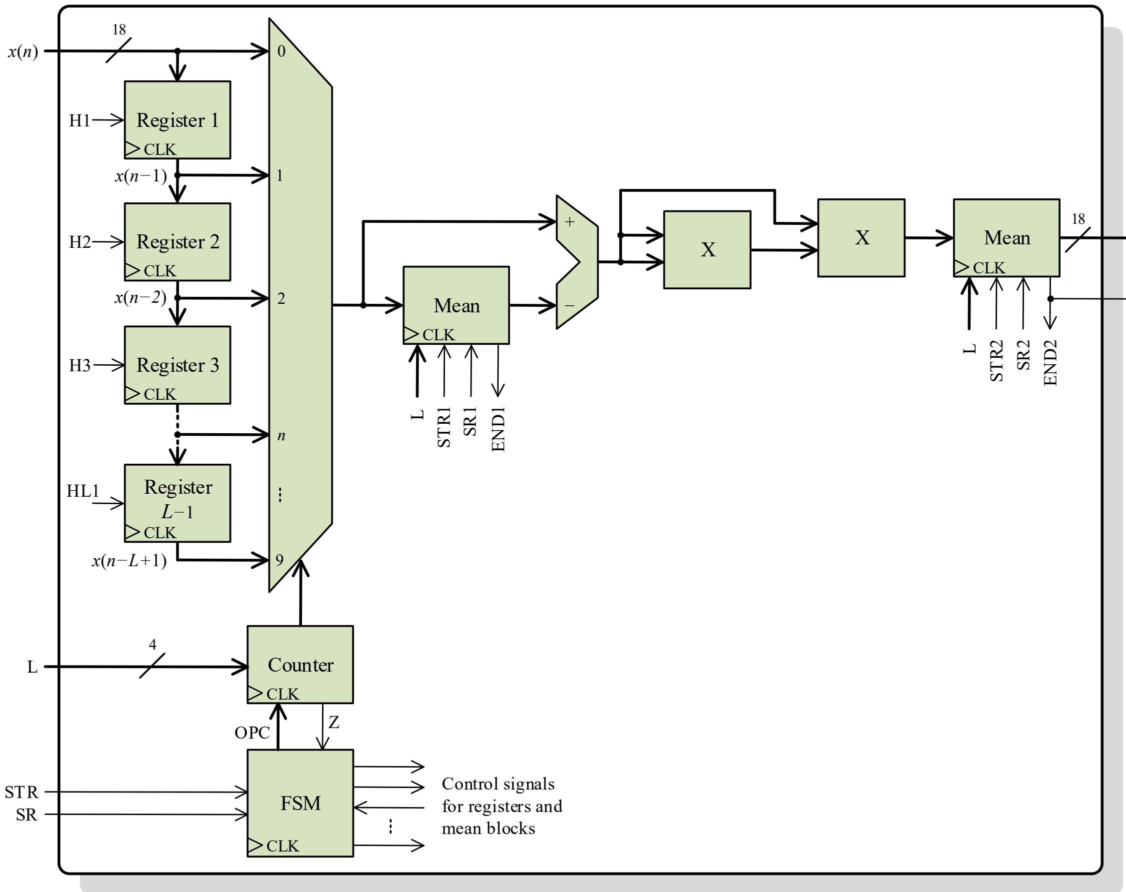

Fig. F.6. Architecture of the processing core for computing the moving third-order central moment.

The mean structure, whose basic architecture is shown in Fig. F.7, is based on a digital structure known as accumulator. An accumulator is composed of an adder and two parallel registers. Both register inputs are connected to the adder output, whereas one register output is connected in feedback to one of the adder inputs. The function of this structure is to compute successive sums using only one adder. After the accumulator, a divider structure is used to divide the sum of all samples of the input signal $x(n)$ between the number of samples L, obtaining the mean (18-bit MEAN signal). There is no division operator in the IEEE standard VHDL libraries, so it is necessary to design a digital structure for this purpose. The divider is based on a successive approximations register (SAR). This divider computes the division using a successive approximations approach. The SAR successively approximates the quotient value, comparing the quotient and divisor product, with the dividend until the product value is equal or very close to the dividend value.

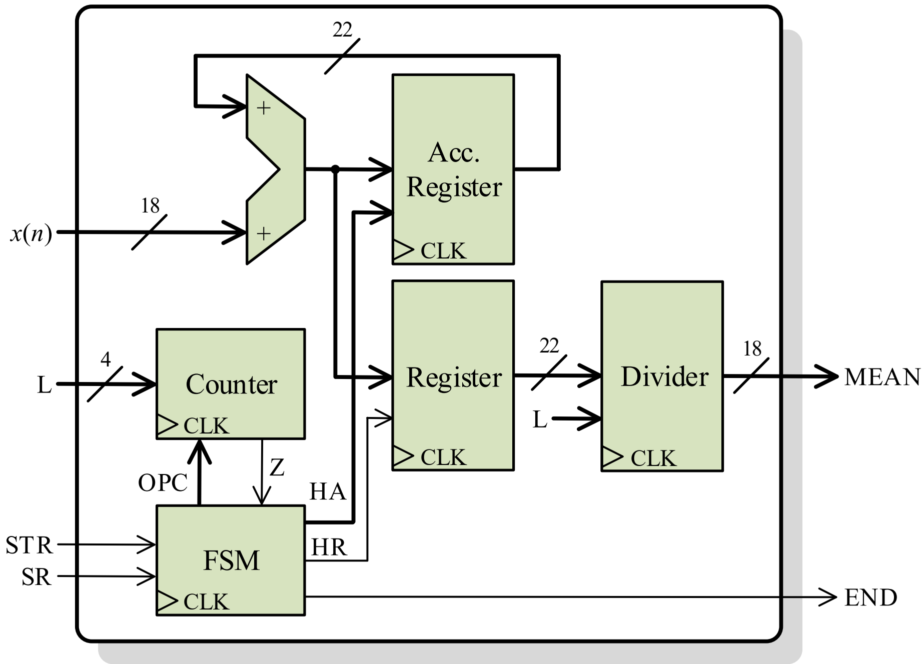

Fig. F.7. Architecture of the digital structure for computing the mean.

Fig. F.8 shows the architecture of the last processing core for computing the integral of the secondary CT current, according to the trapezoidal rule. With a register at the input $x(n)$, the processing core stores the previous sample, which is added to the current sample and then multiplied by a factor of 0.000125, which corresponds to half of the sampling period, $(t(n) - t(n-1))/2$. Finally, successive sums are computed with an accumulator to obtain the cumulative integral at any time.

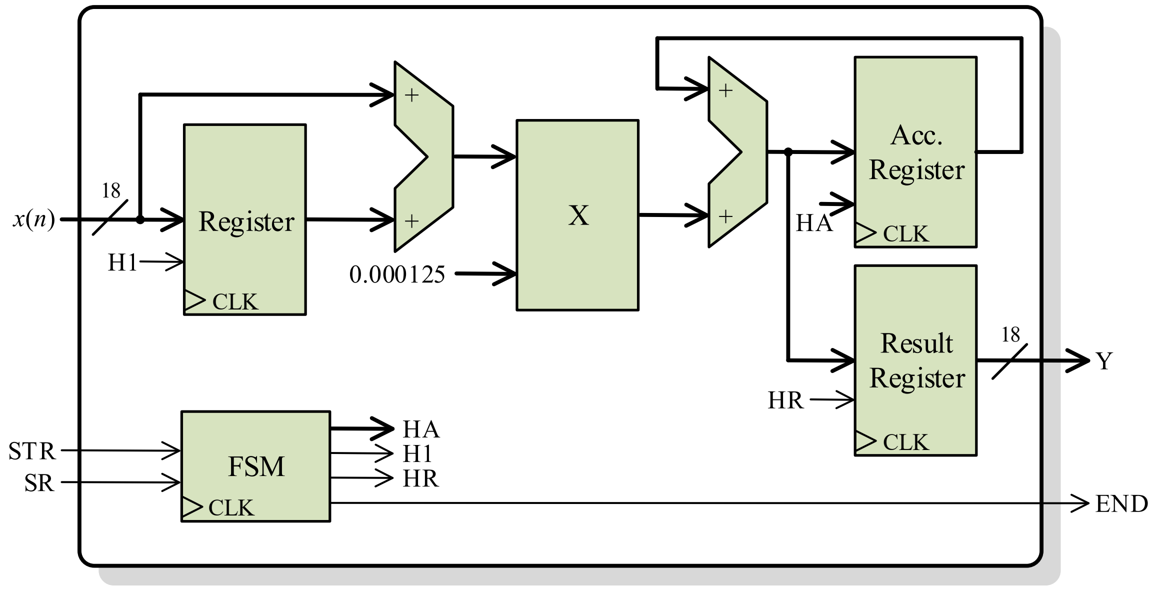

Fig. F.8. Architecture of the processing core for computing the integral.

Finally, the decision stage is compounded by a simple peak detector and if-else decisions. Fig. F.9 shows the basic architecture of the peak detector, which is based on a comparator block.

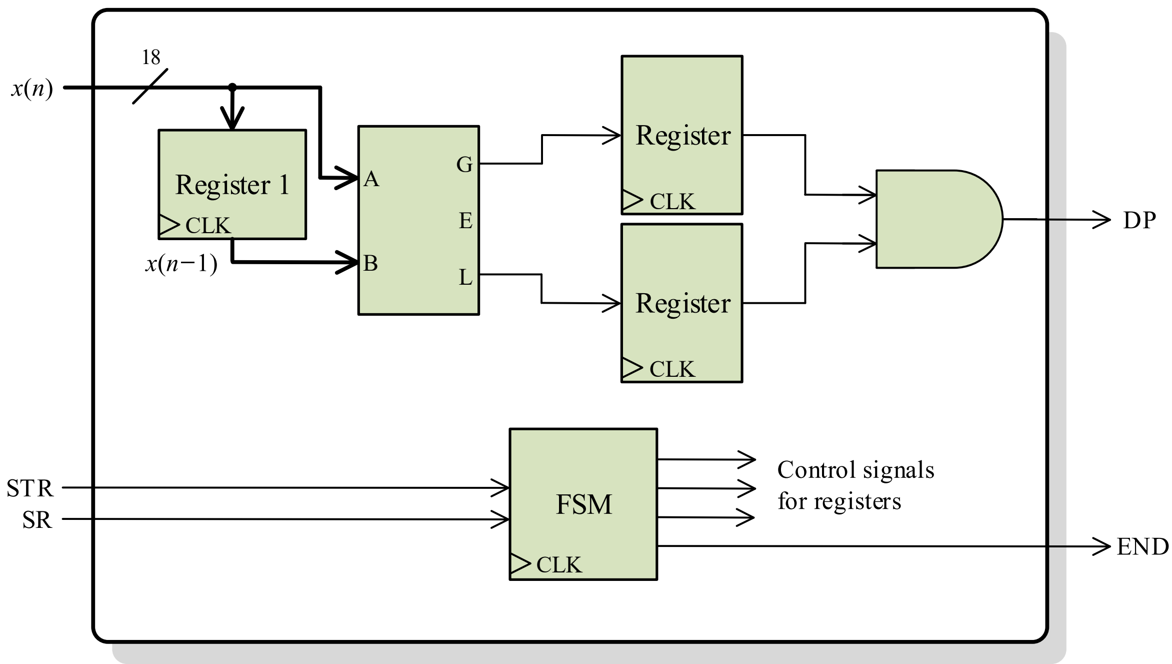

Fig. F.9. Architecture of the peak detector.

Table F.1 summarizes the resources usage of the FPGA and the processing time of each core in clock cycles, depending on the number of samples to be processed at each time (L) and the word length of the samples (i.e., e and f, which are the integer and fractional parts of each sample, respectively). For a period clock of 10 ns and a sampling frequency of 4000 sps, it is clear that the FPGA-based processor is fast enough to accomplish the real-time requirement.

Table F.1. Usage of FPGA resources.

Processing core	Logic elements	Registers	9-bit Multipliers	Memory bits	Clock Cycles
Second-order difference	480	56	2	0	2
Third central moment	1900	430	8	0	$2L+2(e+f)+1$
Integral	494	74	2	0	2
Decision stage	254	80	0	0	3

F.3. Validation and Results

The proposed algorithm to detect CT saturation has been validated by simulations using Matlab (algorithm implementation) and Simulink (CT model). It has been tested with fault short-circuit currents on a 120 kV network. The CT is rated 2000/5 A, 5 VA. The primary winding, which consists of a single turn passing through the CT core is connected in series with a shunt inductor rated 69.3 Mvar, 69.3 kV (120kV/√3), 1 kA rms. The secondary winding consisting of 400 turns is connected to a resistive burden. In the case of inrush currents, the algorithm has been tested using a 150 MVA transformer with a rated voltage of 289 kV.

Fig. F.10 shows the results during inrush current measurement with different levels of resistance burden (0.8 Ω, 1 Ω, 1.5 Ω, and 3 Ω), inside the typical range of digital relays resistance. As explained before, more burden impedance implies a larger CT core flux, so the saturation is more severe with more resistance burden. In all cases, the algorithm detects with 100% efficiency the saturation without false positive detections. The saturation inception, in all cases, is detected just when the first sample of the measured secondary current does not coincide with that of the ideal secondary current without saturation. Regarding the end of saturation, the proposal fails at most one sampling period (0.25 ms), detecting in some cases the end of saturation a period after the event, but never before. This occurs with more frequency when the burden resistance is smaller. Fig. F.11 shows the results for fault currents with the same cases of resistance burden. The results are similar to the inrush currents, detecting even the light CT saturation on the last cycles.

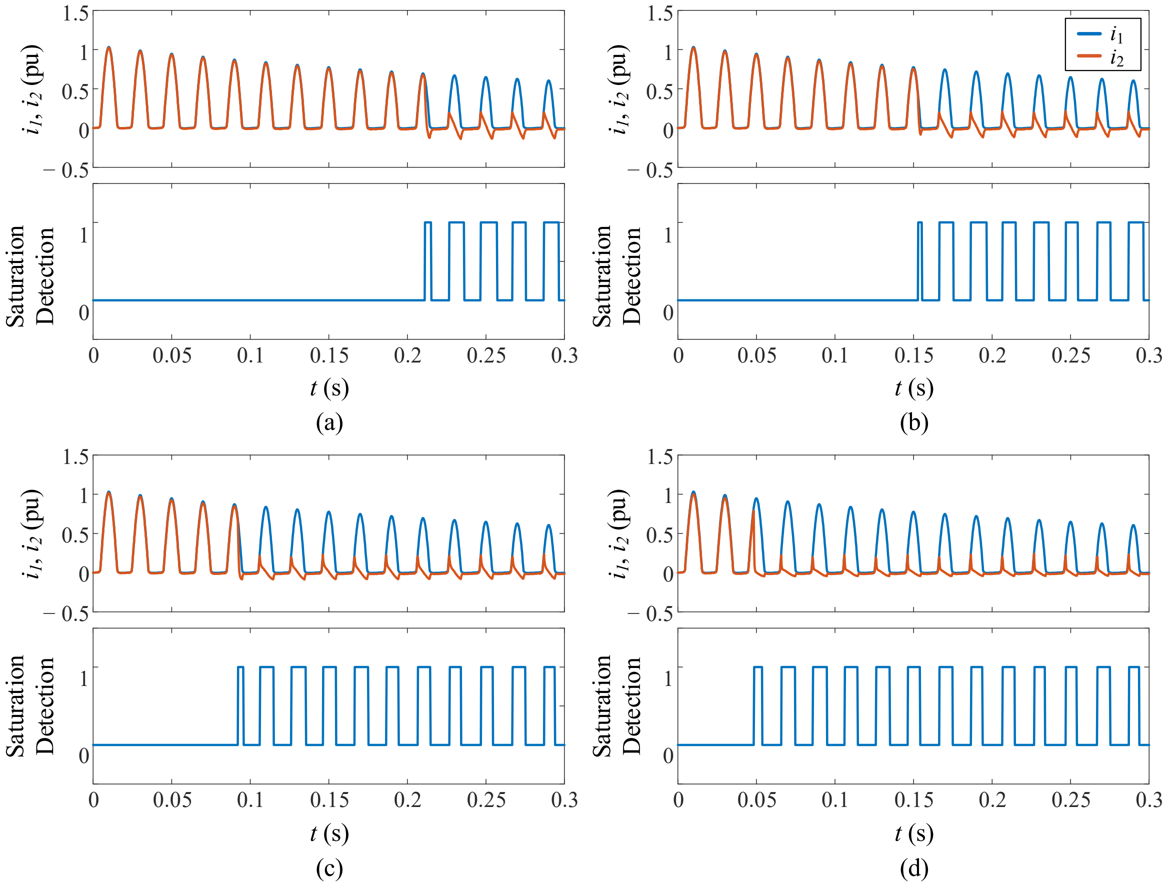

Fig. F.10. Performance of proposed algorithm on inrush currents for different resistive CT burdens: (a) 0.8 Ω, (b) 1 Ω, (c) 1.5 Ω, (d) 3 Ω.

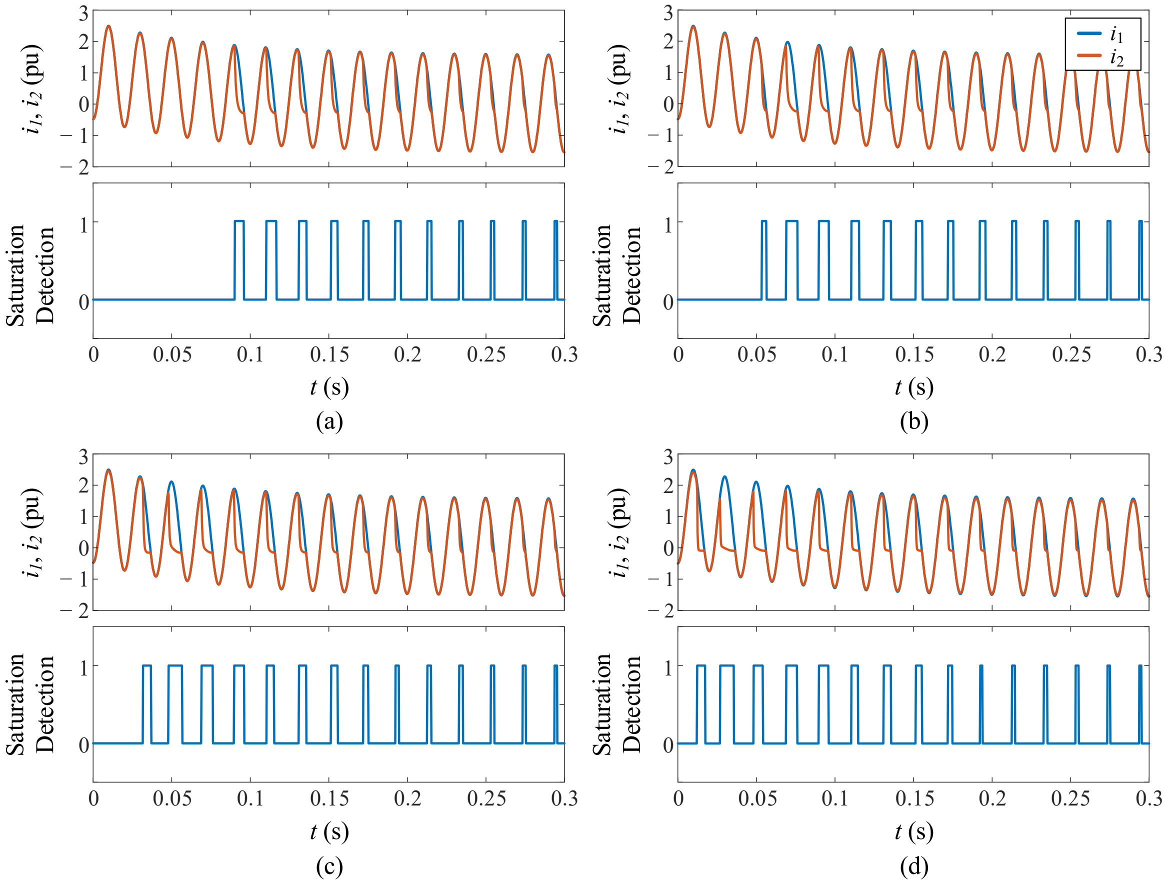

Fig. F.11. Performance of proposed algorithm on fault currents for different resistive CT burdens: (a) 0.8 Ω, (b) 1 Ω, (c) 1.5 Ω, (d) 3 Ω.

Fig. F.12 shows the results against inrush currents and fault currents measurement with different levels of Gaussian noise (signal-to-noise ratio of 35 dB and 50 dB) and a burden resistance of 1.5 **Ω**. It has been found that the algorithm ensures good results starting from a signal-to-noise ratio of 35 dB, which validates the immunity against noise of the algorithm. Fig. F.13 presents the results during inrush current measurement with different levels of CT residual flux (0.2 and 0.75 pu). More residual flux implies an earlier saturation, but not more severe saturation so the results are very similar in both cases without notable differences.

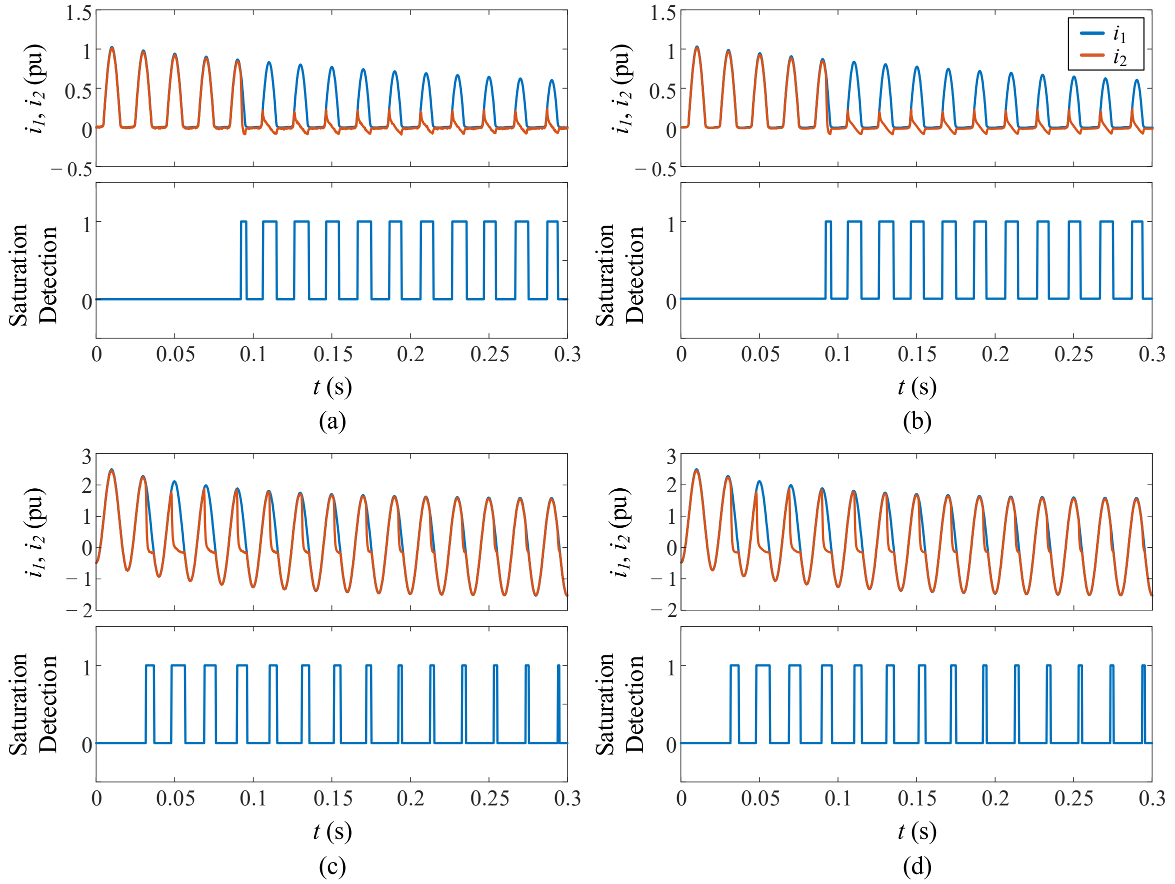

Fig. F.12. Performance of proposed algorithm against Gaussian noise. Signal to noise ratio: (a) 35 dB, (b) 50 dB, (c) 35 dB, (d) 50 dB.

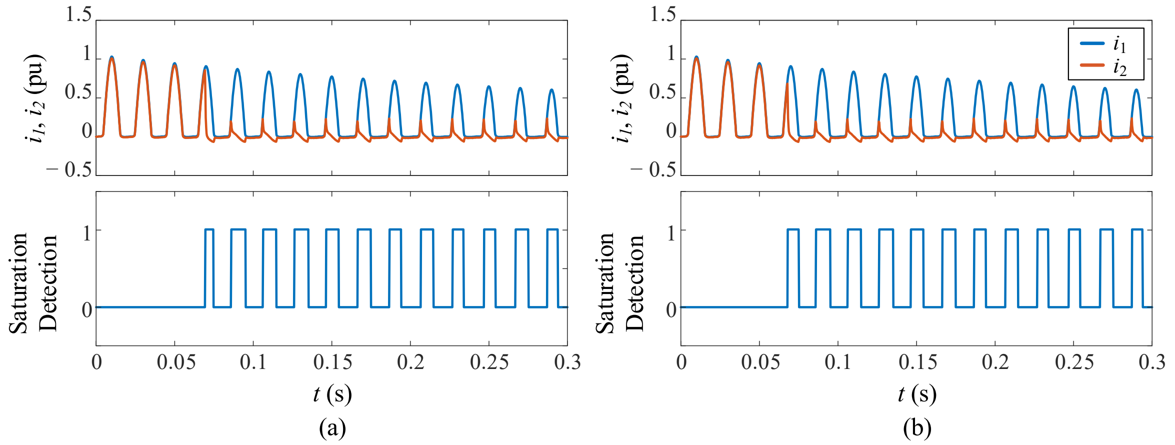

Fig. F.13. Performance of proposed algorithm against CT residual flux: (a) 0.2 pu, (b) 0.75 pu.

Finally, the smart sensor has been tested in real-time conditions. As explained, a hardware-in-the-loop platform (Typhoon HIL) has been used to emulates a power transformer energization (100 MVA, 289 kV), and the measurement with a 2000/5 CT (with a different saturation curve than the one used in the simulations), and the signals are sent to the smart sensor implemented in an FPGA in a MicroLabBox dSPACE.

In Fig. F.14, the results for the measurement of two inrush currents with different polarity are shown. The saturation inceptions have been correctly detected with 100% efficiency. Regarding the end of saturation, the proposal fails at most one sampling period, detecting in some cases the end of saturation a period after the event.

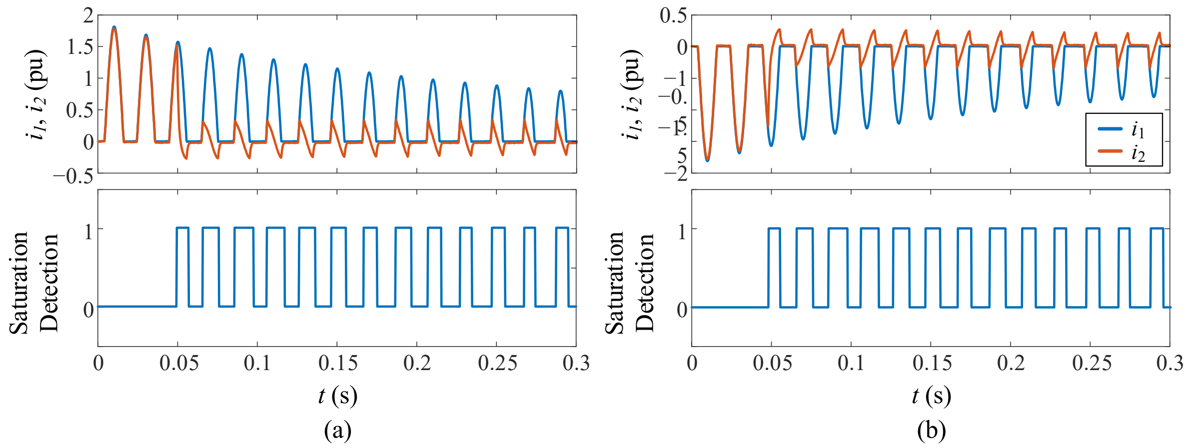

Fig. F.14. Performance of smart sensor during inrush current measurement in real time.

It has also been tested the influence of the sampling frequency (Fig. F.15). It has been found that higher sampling frequencies lead to a more accurate end-of-saturation detection. With sampling frequencies smaller than 4000 sps, the algorithm does not ensure good results because the threshold levels and sliding window length established in the previous subsection have to be changed. This is because at different sampling frequencies, the magnitudes of the two used time-domain features change, even for the same signal, as seen in Fig. F.15.

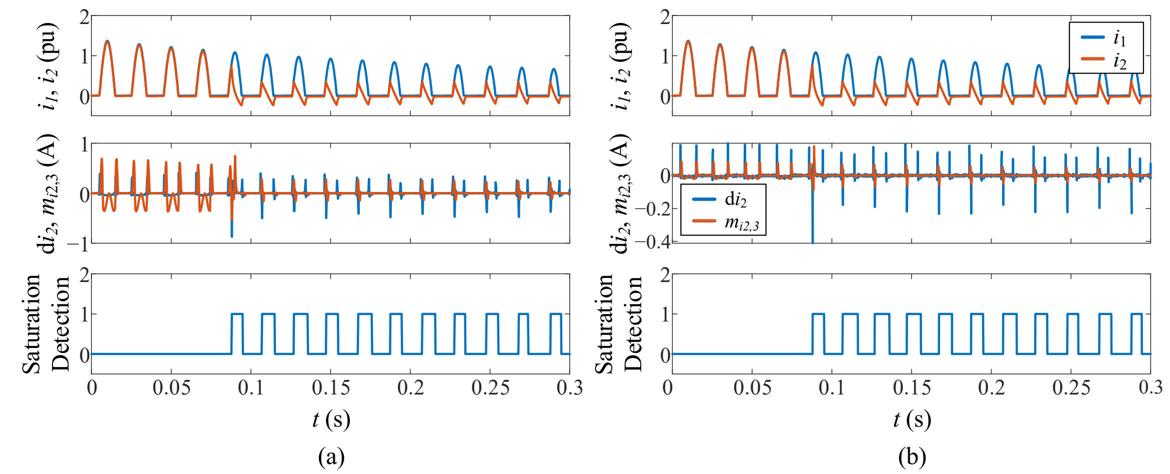

Fig. F.15. Performance of smart sensor during inrush current measurement in real time for different sampling frequencies.